Alma Mater Studiorum – Università di Bologna

DOTTORATO DI RICERCA IN

MECCANICA E SCIENZE AVANZATE DELL'INGEGNERIA

Ciclo 34

Settore Concorsuale: 09/A3 - PROGETTAZIONE INDUSTRIALE, COSTRUZIONI MECCANICHE E METALLURGIA

Settore Scientifico Disciplinare: ING-IND/21 - METALLURGIA

DEVELOPMENT, MECHANICAL CHARACTERIZATION AND QUALIFICATION IN LIQUID LEAD OF STAINLESS STEELS FOR STRUCTURAL APPLICATIONS IN THE FUTURE FISSION AND FUSION NUCLEAR REACTORS

Presentata da: Carlo Cristalli

Coordinatore Dottorato

Marco Carricato

Supervisore

Carla Martini

Co-Supervisore

Marco Utili

Esame finale anno 2022

Dedica

Questa tesi di dottorato, così come quella della laurea magistrale ottenuta 14 anni fa in questa stessa facoltà, è dedicata a Luigi Cristalli, per gli amici “Pelle”, mio padre.

Ringraziamenti

Desidero ringraziare le seguenti dodici persone che hanno contribuito, con un supporto tecnico o morale, in questo percorso di Dottorato;

Professoressa Carla Martini, supervisore del Dipartimento di Chimica industriale dell'Università di Bologna, il cui supporto è stato decisivo durante tutto il percorso del Dottorato e in particolare nella scrittura di questo documento. Auspico che la collaborazione avviata in questo Dottorato possa continuare in maniera consolidata e duratura nei prossimi anni;

Dott. Ing. Marco Utili, supervisore ENEA, il cui supporto è stato fondamentale durante tutto il percorso del Dottorato e nella scrittura di questo documento, a cui mi lega anche un rapporto di reciproca stima professionale e amicizia;

Dott. Luciano Pilloni, Primo Ricercatore ENEA esperto di materiali nucleari, dal 2020 in pensione, a cui devo gran parte degli insegnamenti ricevuti negli anni precedenti il dottorato e con cui si è creato un rapporto di sincera amicizia oltre ad una reciproca stima professionale;

La mia famiglia, nelle persone di mia madre Daniela e mia sorella Camilla, per volontà delle quali ho intrapreso questo percorso di Dottorato;

I miei collaboratori tecnici Sandro Storai, Nicola Bettocchi e Luigi Masotti, senza i quali l'esecuzione delle prove meccaniche riportate in questo documento non avrebbe avuto luogo;

Dott. Jean Henry, in qualità di revisore della tesi di Dottorato;

Dott. Ing. Mariano Tarantino, nel doppio status di Capo Divisione FSN-ING nel 2018, ai tempi dell'inizio del Dottorato, per aver consentito che questo Dottorato iniziasse, e di revisore della tesi di Dottorato;

Dott. Ing. Aldo Pizzuto, Capo Dipartimento FSN ai tempi dell'inizio del Dottorato, per aver dovuto approvare "in fretta e furia" nel 2018, durante una missione in Giappone, la documentazione che consentiva l'avvio di questo percorso, e consentire così che questo Dottorato iniziasse;

Dott. Ing. Pietro Agostini, attualmente Capo Divisione FSN-ING, per aver consentito che questo Dottorato si concludesse.

Non ho nessun altro da ringraziare.

Table of contents

Acronyms list

ADS	*Accelerator Driven System*
AISI	*American Iron and Steel Institute*
ALFRED	*Advanced Lead Fast Reactor European Demonstrator*
ALLEGRO	*European Helium-cooled Gas Fast Reactor*
ASTRID	*Advanced Sodium Technological Reactor for Industrial Demonstration*
ASME	*American Society of Mechanical Engineers*
CEA	*Commissariat a l'Energie Atomique et aux Energies Alternatives (France)*
CF	*Creep Fatigue*
CSM	*Centro Sviluppo Materiali*
CW	*Cold Working*
DACS	*Data Acquisition and Control System*
DBTT	*Ductile to Brittle Transition Temperature*
DCLL-BB	*Dual Cooled Lead Lithium Breeding Blanket*
DPA	*Displacement per Atom*
ENEA	*Italian National Agency for New Technologies, Energy and Sustainable Economic Development (Italy)*
ESNII	*European Sustainable Nuclear Industrial Initiative*
FATT	*Fracture Appearance Transition Temperature*
FEG	*Field Emission Gun*
FM	*Ferritic/Martensitic steel*
FR	*Fast Reactor*
GEMMA	*GEneration 4 Materials MAturity*
GDC	*Gadolinium-Doped Ceria*
HCLL-BB	*Helium Cooled Lead Lithium Breeding Blanket*
HLM	*Heavy Liquid Metal*
HW	*Hot Working*
LBE	*Lead Bismuth Eutectic*
LCF	*Low Cycle Fatigue*
LFR	*Lead Fast Reactor*
LME	*Liquid Metal Embrittlement*
LSE	*Lower Shelf Energy*
LSM	*Lanthanium Strontium doped Manganite*
MYRRHA	*Multi-purpose hYbrid Research Reactor for High-tech Applications*
NIST	*National Institute of Standards and Technology*
OCS	*Oxygen Control System*
PAGS	*Prior Austenite Grain Size*
P&ID	*Piping & Instrumentation Diagram*
PESR	*Pressure Electro Slug Remelting*
RAFM	*Reduced activation Ferritic-martensitic*
RC	*Ring Compression*
R&D	*Research & Development*
RCC-MRx	*Design and Construction Rules for mechanical components of nuclear installations*
Rp02	*Proof Strength at the 0.2 % plastic deformation (Yield Strength)*
RT	*Room Temperature*
SCK-CEN	*Belgian Nuclear Research Centre*
SEM	*Scanning Electron Microscopy*

SFR	*Sodium Fast Reactors*
SNETP	*Sustainable Nuclear Energy Technology Platform*
SS	*Stainless Steel*
TaC	*Tantalum Carbides*
TEM	*Transmission Electron Microscopy*
TE	*Total Elongation*
TT	*Thermal Treatment*
TMT	*Thermo-Mechanical Treatment*
TS	*Test Section*
UE	*Uniform Elongation*
UFG	*Ultrafine Grained*
USE	*Upper Shelf Energy*
UTS	*Ultimate Tensile Strength*
VAR	*Vacuum Arc Re-Melting*
VIM	*Vacuum Induction Melting*
VN	*Vanadium Nitrides*
YS	*Yield Strength*
YPSZ	*Yttria Partially Stabilized Zirconia*
YTSZ	*Yttria Totally Stabilized Zirconia*
Wt %	*Weight percentage*
WCLL-BB	*Water Cooled Lead Lithium Breeding Blanket*
WPMAT	*Work Package Materials*

Abstract

The research activity carried out in the Brasimone Research Center of ENEA concerns the development and mechanical characterization of steels conceived as structural materials for future fission reactors (Heavy Liquid Metal IV Generation reactors: MYRRHA and ALFRED) and for the future fusion reactor DEMO. Within this framework, two parallel lines of research have been carried out: (i) characterization in liquid lead of steels and weldings for the components of the IV Generation fission reactors (GIV) by means of creep and SSRT (Slow Strain Rate Tensile) tests; (ii) development and screening on mechanical properties of RAFM (Reduced Activation Ferritic Martensitic) steels to be employed as structural materials of the future DEMO fusion reactor. The doctoral work represents therefore a comprehensive report of the research carried out on nuclear materials both from the point of view of the qualification of existing (commercial) materials for their application in the typical environmental conditions of 4th generation fission reactors operating with lead as coolant, and from the point of view of the metallurgical study (with annexed microstructural and mechanical characterization of the selected compositions / Thermo Mechanical Treatment (TMT) options) of new compositional variants to be proposed for the “Breeding Blanket” of the future DEMO Fusion Reactor.
In the Fission scenario the Technology Readiness Level of the steels to be adopted is higher than in Fusion, and then we focus on the qualification of the already existing materials (the commercial austenitic steels as the 316L) in the reference environmental conditions. These materials and the related welds must be tested under the highly corrosive effects of the liquid metal with which they will come into contact in operation. The corrosive effect of these environments is markedly higher than that of the fluids (water) used in the reactors currently in operation (PWR; Pressurized Water Reactors). Therefore, suitable test procedures, which take these effects into account, must be developed with a view to updating the validation codes for the components of Generation IV reactors with respect to those currently in use (PWR). In this frame the focus is in particular on the study of the occurrence of LME (Liquid Metal Embrittlement) by means of SSRTs (Slow Strain Rate Tensile tests) and on the analysis of creep behavior in heavy liquid metal (Pb). In this frame ENEA is funded by the European program "GEMMA" (Generation IV Materials MAturity) which lasted 4 years (2017-2021).

The construction of the DEMO fusion reactor is scheduled for 2050. By that date, the strategic choices concerning the base material to be used for the “Blanket” must be made. Due to the 14 MeV neutron spectrum typical of the "Fusion" environment, for reasons related to the decay and activation of some chemical elements (Ni first of all), the choice is restricted to martensitic steels only, with limited possibilities for compositional variations compared to the EUROFER reference steel (9% Cr, 1% W). The optimization of the chemistry of the material must be carried out according to the operating conditions of the Blanket which can be substantially two, relative to the operating temperature: (i) low temperature (around 300 ° C) or (ii) high temperature (around 650 ° C).
The first option refers to water cooling (WCLL-BB-Water Cooled Lead Lithium - Breeding Blanket) and implies a minimum irradiation temperature for the blanket material in a range of 300-550 ° C. Therefore, due to the behavior of martensitic steels under neutron irradiation, in other words due to the raising of the DBTT (Ductile to Brittle Transition Temperature) under neutron irradiation, the goal to pursue is the development of a tougher alloy, with the least possible sensitivity to embrittlement at the low irradiation temperature. The target in terms of mechanical properties is to increase as much as possible the toughness and decrease the DBTT. The 3125 chemical composition, the double normalization and the recrystallization treatments are aimed at this target.
The second option refers to helium cooling (DCLL-BB-Dual Coolant Lead Lithium-Breeding Blanket) and implies an operating temperature for the Blanket material around 650 ° C. Hence the need to improve the high temperature properties of the martensitic steels employed (Eurofer and similar). In other words, this second option of blanket operating temperature implies R&D work aimed at developing martensitic steels more resistant to creep, suitable for tolerating high operating temperatures. The 3126 and 3229 chemical compositions, as well as the ausforming treatment are aimed at this target.
For activities related to research on materials for the DEMO fusion reactor Blanket, ENEA is funded by the European program "Eurofusion WPMAT" (Work Package MATerials) which started in 2014 and is currently ongoing.
Additional satellite activities reported concern the “Ring Compression” testing technique to assess the mechanical properties of the 15-15 Ti austenitic stainless steel in the frame of “TASTE” Pilot Project. Provided that fuel cladding is characterized by cylindrical geometry, it would be useful to develop simplified methodologies to assess mechanical properties and their decay under irradiation; namely; the simpler the method, the higher the possibility to implement it directly into the hot cells by automatized procedures, avoiding the contact between irradiated material and human beings.

Preliminary Introduction

The research activity proposed for the PhD program concerns the development and mechanical characterization of austenitic stainless steels conceived as structural materials for fission reactors (IV Generation reactors operating with Lead as coolant; MYRRHA and ALFRED) and ferritic-martensitic steels for the DEMO fusion reactor. Therefore, two lines of research are followed in parallel:

(i) Activities aimed at characterizing the behavior in liquid lead of steels and welds designed for Generation IV fission reactors through creep and SSRT (Slow Strain Rate Tensile) tests;
(ii) Activities related to the development and characterization of steels to be employed in the future DEMO fusion reactor.

The steels investigated for fission and fusion reactors will operate in contact with liquid metals: in the case of Fission the austenitic stainless steels for Gen IV Fast Reactor will work in contact with Lead, whilst ferritic-martensitic steels for Fusion applications will be operated in Lead-Lithium alloy. A schematic diagram showing the PhD workflow in terms of materials, tests, reference environments and demonstrators for each research line is reported in Fig. A.

In the Fission scenario the Technology Readiness Level of the steels to be adopted is higher than in Fusion, in fact the choice of the composition of the materials to be adopted is already almost definitive, and therefore we focus on the qualification of the material in the reference environmental conditions and on the definition

of the safety coefficients to be adopted for its use (modification and adaptation of the existing reference standards).

For the "Fusion" scenario, the choice of the composition of the reference steel for the “Breeding Blanket” (the structure containing the plasma confined by the magnetic fields and devoted to the interaction with the plasma itself) is still premature and the research activity in this field focuses more on the determination of the ideal steel (in terms of both composition and thermo-mechanical treatment), depending on the expected operating temperature. The qualification of the material under the effect of contact with the liquid metal will follow only later. There are currently two main options for the operation of the “Breeding Blanket”:

1. water cooling (WCLL-BB-Water Cooled Lead Lithium - Breeding Blanket) and implies a minimum irradiation temperature for the blanket material in a range of 300-550 ° C;
2. helium cooling (DCLL-BB-Dual Coolant Lead Lithium-Breeding Blanket) and implies an operating temperature for the Blanket material around 650 ° C.

It should be highlighted that, whatever the final chosen configuration, both these fusion reactor prototypes have in common, in the identification acronym, the abbreviation "LL", indicating that one side of the Blanket wall will operate in any case in contact with the heavy liquid metal (the Lead Lithium, in this case). The study of this topic, namely the interaction of the structural material with the Heavy Liquid Metal coolant, represents therefore the guiding thread, let’s say the “fil rouge” of the PhD work; both in the "Fission" and in the "Fusion" environment, the material taken into consideration must in any case operate in contact with Lead (or one of its alloys).

The doctoral work represents therefore a comprehensive report of the research carried out on nuclear materials both from the point of view of the qualification of existing materials for their application in the typical environmental conditions of 4th generation fission reactors operating with Lead as coolant, and from the point of view of the metallurgical study (with annexed microstructural and mechanical characterization of the selected compositions) of new compositional variants to be proposed for the breeding blanket of the future DEMO Fusion Reactor.

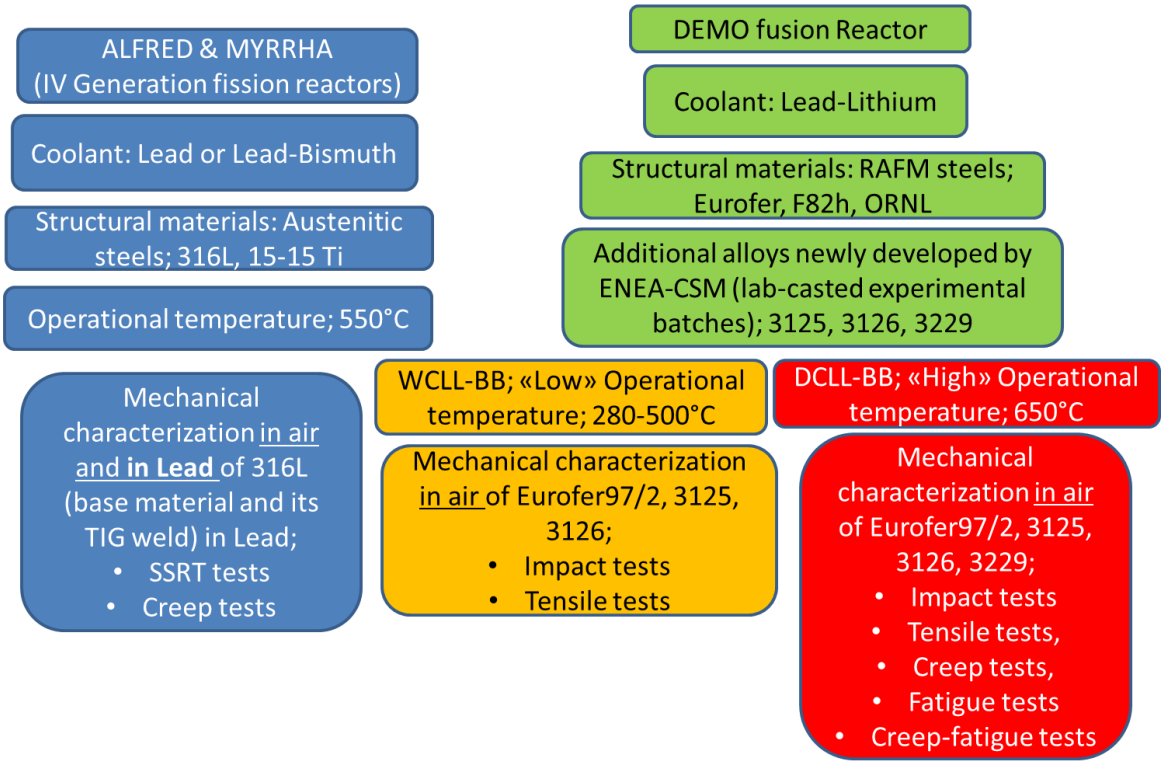

Fig. A: Diagram showing the workflow of the doctoral thesis.

Summary of the contents of each chapter

1.1; Introduction on The Heavy Liquid Metal cooled 4th Generation reactors

Among the various concepts of Generation IV reactor, the lead cooling option represents the most convincing alternative and implies advantages in terms of passive safety and potential modularity. The development of four main prototypes of Generation IV reactors is carried out in Europe; the related projects are financed and coordinated by ESNII (European Sustainable Nuclear Industrial Initiative);

- ASTRID, SFR (Sodium Fast Reactor) prototype;
- ALFRED, LFR prototype (Lead Fast Reactor), whose construction is scheduled for 2025-2030;
- ALLEGRO, GFR (Gas Fast Reactor) prototype, whose construction is scheduled for 2025-2030;
- MYRRHA, prototype of an ADS (Accelerator Driven System) accelerator for the minimization of nuclear waste, whose configuration is very similar to the LFR one, given that a Pb-Bi eutectic alloy is used as a coolant. The construction of the accelerator is scheduled for 2024, that of the annexed reactor after this date.

The components of all these demonstration reactors are made of austenitic steels and Ni-based superalloys. These materials and the related welds must be tested under the effect of highly corrosive environments such as liquid metal (Pb or Na) with which they will come into contact in operation. The corrosive effect of these environments is markedly higher than that of the fluids (water) used in the reactors currently in operation (PWR; Pressurized Water Reactors). Therefore, suitable test procedures, which take these effects into account, must be developed with a view to updating the validation codes for the components of Generation IV reactors with respect to those currently in use (PWR). In this context, actions aimed at characterizing the thermomechanical properties of materials are envisaged, including in particular the study of LME (Liquid Metal Embrittlement) and creep behavior in heavy liquid metal (Pb). In this frame ENEA is funded by the European program "GEMMA" (Generation IV Materials MAturity) which lasted 4 years (2017-2021). Several references reporting the current state of research regarding the effects of contact with the heavy liquid metal (Pb and its alloys; Pb-Bi and Pb-Li) are reported and discussed in this chapter.

1.2; Introduction on Reduced Activation Ferritic Martensitic (RAFM) steels for DEMO fusion reactor

The construction of the DEMO fusion reactor is scheduled for 2050. By that date, the strategic choices concerning the base material to be used for the “Blanket” must be made. Due to the 14 MeV neutron spectrum typical of the "Fusion" environment, for reasons related to the decay and activation of some chemical elements (Ni first of all), the choice is restricted to martensitic steels only, with limited possibilities for compositional variations compared to the EUROFER reference steel (9% Cr, 1% W). The optimization of the chemistry of the material must be carried out according to the operating conditions of the Blanket which can be substantially two, relative to the operating temperature; the low temperature; around 300 ° C, or the high temperature; around 650 ° C.

The first option refers to water cooling (WCLL-BB-Water Cooled Lead Lithium - Breeding Blanket) and implies a minimum irradiation temperature for the blanket material in a range of 300-550 ° C. Therefore, due to the behavior of martensitics under neutron irradiation, in other words due to the raising of the DBTT (Ductile to Brittle Transition Temperature) due to the effect of neutron irradiation and helium embrittlement, the goal to pursue is the development of a tougher alloy, with the least possible sensitivity to embrittlement at the low irradiation temperature.

The second option refers to helium cooling (DCLL-BB-Dual Coolant Lead Lithium-Breeding Blanket) and implies an operating temperature for the Blanket material around 650 ° C. Hence the need to improve the high temperature properties of the martensitic alloys employed (Eurofer and similar). In other words, this second option of blanket operating temperature implies R&D work aimed at developing martensitic steels more resistant to creep, suitable for tolerating high operating temperatures.

For activities related to research on materials for the DEMO fusion reactor Blanket, ENEA is funded by the European program "Eurofusion WPMAT" (Work Package MATerials) which started in 2014 and is courrently ongoing.
An overview of the “Status of the Art” concerning the RAFM (Reduced Activation Ferritic Martensitic) steels is reported in this chapter.

1.3; Introduction on additional satellite activities concerning the assessment of tensile properties by means of RC (Ring Compression) tests (TASTE pilot project)

Additional activities hereby reported concern the “Ring Compression” testing technique to assess the mechanical properties of the 15-15 Ti steel in the frame of “TASTE” (Testing and ASsessment methodologies for material Characterization of fuel cladding TubEs in relevant environmental conditions) Pilot Project. Provided that fuel cladding is characterized by cylindrical geometry, it would be useful to develop simplified methodologies to assess mechanical properties and their decay under irradiation; namely; the simplest the method, the highest the possibility to implement it directly into the hot cells by automatized procedures, avoiding the contact between irradiated material and human beings. Several references dealing with the Ring Compression technique are reported in this chapter.

Chapter 2; Experimental methods

Chapter 2.1; Description of the procedures adopted to run SSRT (Slow Strain Rate Tensile) and creep tests in lead in the frame of GEMMA Project

The PhD activity is focused on the execution of tests in liquid lead at different temperatures; namely SSRT (Slow Strain Rate Tensile) and creep tests, with appropriate control of oxygen and the levels of impurities in the liquid metal, in order to evaluate the compatibility of the HLM (Heavy Liquid Metal) coolant (lead) with the structural material taken into account (316L). The TIG weld on a plate of this material will be characterized as well with specimens extracted both in the longitudinal and in the transverse direction. In particular the mechanical characterization is aimed at excluding the susceptibility of the base materials and the welded joint to the LME (Liquid Metal Embrittlement) in HLM. All the details concerning the adopted experimental procedures to run SSRT and creep tests in liquid lead under controlled Oxygen atmosphere are reported in this chapter.

Chapter 2.2; Description of the experimental procedures adopted to characterize the RAFM steels taken into account in the frame of Eurofusion WPMAT Project

Several plates with different chemical compositions (within the specification of the RAFM steels) and Thermo-mechanical treatments have been fabricated at Rina-CSM (Centro Sviluppo Materiali); Rina CSM is the ENEA LTP (Linked Third Party) in the frame of the Eurofusion WPMAT Project. These alloys have been characterized in ENEA aiming at a screening of the mechanical properties relevant for the corresponding foreseen scenario of the DEMO fusion reactor. Therefore the description of the considered RAFM steels (in terms of chemical compositions and applied Thermo Mechanical Treatments) as well as the procedures adopted to run impact (by means of KLST samples, according to DIN 50115), tensile, fatigue and creep-fatigue tests are reported in this chapter.

Chapter 2.3; Description of the experimental procedures adopted to characterize the 15-15 claddings by means of Ring Compression tests

The 15-15 Ti claddings (outside diameter 6.5 mm, thickness 0.45 mm) have been supplied to ENEA in two manufacturing conditions; namely 24 % and 46 % cold working ratio. The procedures adopted to run ring compression tests on these claddings, as well as to extract the meaningful parameters (collapse load) from the load displacement curves are described in this chapter.

Chapter 3; Results

Chapter 3.1; Outcomes of the SSRT and creep tests in lead in the frame of GEMMA Project

The Outcomes of the SSRT and creep tests in lead are presented in this chapter; in addition to the tensile and creep curves some meaningful parameters (Yield Strength, Ultimate Tensile Strength and creep rate) are presented and compared.

Chapter 3.2; Outcomes of the SSRT and creep tests in lead in the frame of GEMMA Project

The screening on the mechanical properties of the considered RAFM steels is reported and discussed in this chapter, in light of the following alternative scenarios according to the operational temperature of the DEMO Breeding Blanket;

- The “low temperature option”, namely the WCLL, implying a reference temperature of 300°C, the target is to increase as much as possible the toughness and decrease the DBTT. The 3125 chemical composition, the double normalization and the recrystallization treatments are aimed at this target.
- The “high temperature option”, namely the DCLL, implying a reference temperature of 650°C, the target is just to maintain an acceptable DBTT, just in order to grant safe manufacturing and assembling processes at room temperature; (-20°C could be sufficient) pursuing the highest possible creep resistance (20000 hrs at 100MPa / 650°C as a “wishful thinking”) and a LCF (Low Cycle Fatigue) resistance in the range of 10000 cycles at 650°C. The 3126 and 3229 chemical compositions, as well as the ausforming treatment are aimed at this target.

Chapter 3.3; Outcomes of the Ring Compression tests

The UTS values, assessed by means of RC tests, reveal a softening effect due to aging as well as a hardening effect due to the cryogenic temperature (-196°C). No effects related to embrittlement are noticeable in any of the investigated conditions.

1 Chapter 1; Introduction

1.1 Introduction on The Heavy Liquid Metal cooled 4th Generation reactors

1.1.1 The 4th Generation reactors

Aiming at cutting greenhouse gas emissions and facing the large foreseen energy demand, the EU has launched in 2007 a coordinated strategy to deliver new safe, competitive and low-carbon technologies to the European market. The Strategic Energy Technology Plan (SET-Plan) was defined by the European Commission to speed up the development of clean, efficient and low-carbon energy technologies between now and 2050 [1]. The energy technologies, that have been identified by EU as a priority, are six: wind, solar, smart electricity grids, bioenergy, CO_2 capture and storage and nuclear fission [1]. In the framework of the European SET-Plan, the Sustainable Nuclear Energy Technology Platform (SNETP) was launched to support the nuclear fission research and innovation [2]. Within SNETP, the European Sustainable Nuclear Industrial Initiative (ESNII) constitutes one of the three structural pillars. The purpose of ESNII is to support the technological development of the Fast Reactor (FR) and Accelerator Driven System concept [3]. Thanks to a closed-fuel cycle and a high efficiency of fuel use and burning, these technologies possess high sustainability, safety and reliability features, making them completely innovative. The reactor concepts considered within ESNII are the following [3]:

• Sodium-cooled Fast Reactor (SFR), fast neutron reactor cooled by liquid sodium. The reactor concept is represented by ASTRID reactor (Advanced Sodium Technological Reactor for Industrial Demonstration), to be built in France and whose development is supported by a consortium led by CEA (Commissariat à l'Énergie Atomique et aux Énergies Alternatives, France) [3,4].

• Lead-cooled Fast Reactor (LFR), fast neutron reactor cooled by liquid lead. The reactor concept is represented by ALFRED reactor (Advanced Lead Fast Reactor European Demonstrator), which shall be built in Pitesti (Romania). The development is supported by the FALCON Consortium (Fostering ALfred CONstruction), which is composed of ANSALDO NUCLEARE, ENEA (Italy), ICN (Institutul de Cercetari Nucleare, Romania) and CVR (Centrum Výzkumu Řež, Czech Republic) [3,5].

• Accelerator Driven System (ADS), critical or sub-critical reactor cooled with LBE aimed at demonstrating the feasibility of transmutation of long-lived radioactive waste. The European irradiation facility MYRRHA (Multi-purpose hYbrid Research Reactor for High-tech Applications) should act as a pilot plant for LFR and a demonstrator for ADS, being able to operate both in critical and sub-critical mode. MYRRHA will also support the technology development of the fast reactor concept, in particular for material, components and fuel irradiation tests. MYRRHA is developed under the leadership of SCK-CEN (Belgium) [3,6,7].

• Gas-cooled Fast Reactor (GFR), fast neutron reactor cooled by helium and represented by the small-power demonstrator ALLEGRO supported by Slovakia, Czech Republic, Hungary, Poland and CEA [3,8].

SFR, LFR and GFR concepts are included in the “Generation IV”, which constitutes the future generation of nuclear systems aimed at replacing previous generation II and III of thermal neutron reactors cooled by water. Among the various concepts of Generation IV reactors, that of Sodium cooling represents the most developed and mature technology. The lead cooling option, on the other hand, represents the most convincing alternative and implies advantages in terms of passive safety and potential modularity. Finally, gas cooling represents the longer-term alternative that opens the way to higher operating temperatures and, consequently, to higher yields. Besides the three FR concepts, Generation IV includes also thermal reactors

such as the Molten Salt Reactor (MSR), the Supercritical Water-cooled Reactor (SWCR) and the Very-High-Temperature Reactor (VHTR) [9-11]. Generation IV nuclear systems are supported by the Generation IV International Forum (GIF), an initiative founded in 2000 and that today has 13 members worldwide (among which EU through the European Atomic Energy Community, EURATOM) [9]. Important R&D activities on FRs and other innovative thermal reactors are currently coordinated worldwide through GIF. Europe, through SNETP and ESNII, has defined its own strategy based on FRs, considered the most likely to meet Europe's energy needs in terms of safety, sustainability, proliferation resistance and economic competitiveness. In this framework, Italy is involved in the development of Lead alloy-cooled systems, i.e. MYRRHA and ALFRED, being Italy among the first to join the FALCON Consortium through ANSALDO NUCLEARE and ENEA for the design of LFR. Several R&D activities in support of the design and development of MYRRHA and ALFRED are performed in the context of European projects as well as the Italian Framework Program between ENEA and the Italian Ministry of Economic Development (MiSE).

1.1.2 Lead and Lead-Bismuth Eutectic (LBE) properties

The study of lead as nuclear coolant started in 1950s at the Institute of Physics and Power Engineering (IPPE) in the USSR. In those years, USA and USSR concurrently began the development of a liquid metal cooled nuclear power facility to be employed as a propulsion system for nuclear submarines [12]. In USSR LBE was chosen as coolant, while in USA sodium was chosen for the superior thermal-hydraulic properties. The research carried out by the Russians led to the operation of the 27/VT LBE-cooled reactor prototype in 1958 [13]. Following that success, eight nuclear submarines cooled with LBE were built afterwards. "Project 645" was commissioned in 1963. "Project 705" was commissioned in 1977-1981. The latter submarines were also known as "Alpha class" according to NATO designation. Thanks to the use of titanium and lead technology, these submarines were and are still the fastest submarines ever developed [13]. Conversely the operation of sodium-cooled nuclear submarines (known as "Sea Wolf class") led to several accidents caused by the contact of sodium with water and air. Sodium-cooled reactors were so quickly dismantled by USA and replaced by pressurized water ones [12].
Sustainability and safety features of the LFR are mainly due to neutron, physical and chemical properties of lead and LBE (eutectic composition: 45.5% Pb, 55.5% Bi), some of which are listed in Tab.1.1.1 [14-16]. The properties of sodium coolant are reported for comparison. The physical and chemical features of coolants determine the maximal potential non-nuclear energy per volume unit stored in the system (including thermal energy, coolant compression energy and chemical energy) which may be released in case of accident [16]. Lead and LBE have a significantly lower maximal potential energy factor (around 1) compared to sodium and water coolant (equal to 10 and 21.9 respectively), which means higher intrinsic safety for lead and LBE cooled nuclear plants and simplification for safety measures [16].

Tab. 1.1.1: Neutron, physical and chemical properties of lead, LBE and sodium coolants [14-16].

Coolant	**Pb**	**LBE**	**Na**
Melting Point (°C)	327	125	98
Boiling Point (°C)	1745	1670	883
Relative Moderating Power	1.0	0.8	1.8
Neutron absorption cross-section (1MeV)	6.00	1.42	0.23
Density at 450°C (kg/m^3)	10520	10150	845
Heat Capacity at 450°C (kJ/kg·K)	147.3	146	1.3
Thermal Conductivity at 450°C (W/m·K)	17.1	14.2	68.8
Kinematic Viscosity at 450°C (m^2/s)	1.9×10^{-7}	1.4×10^{-7}	3×10^{-7}
Chemical Reactivity with O_2 and H_2O	negligible	negligible	very high
Maximal Potential Energy (GJ/m^3)	≈ 1.1	≈ 1.1	≈ 10

Lead and LBE coolants have low neutron absorption cross-section and moderating power (unlike water), which allows to design reactor cores working with fast neutron spectrum. Fast neutrons increase the sustainability of the nuclear fuel usage thanks to the conversion of fertile uranium into fissile material (formation of Pu-239 from U-238 by neutron capture) and also to the improvement of the performance of fuel burning and transmutation of long-life fission products and minor actinides (MAs) when compared to current Generation II and III reactors [13,17,18].
LFRs also contribute to the reduction of radioactive waste volume thanks to a closed-fuel cycle. Pu and MAs (mainly Np, Am and Cm) are the main responsible for the high radiotoxicity of nuclear waste in Generation II and III, requiring storage times in geological sites of million years. In a closed fuel cycle, nuclear wastes produced in LFRs do not contain Pu and MAs as they are recycled and reused [7,18,19]. Thanks to the closed-fuel cycle and the high transmutation performance, the waste volumes from a LFR and the relative radiotoxicity are significantly reduced, allowing the storage for only 300-400 years [7].
From the point of view of safety, lead and LBE are characterized by high thermal conductivity and heat transport capability which provides an excellent heat transfer efficiency during normal operating conditions, transient regimes, as well as during decay heat removal [13,17]. Lead and LBE have also high boiling point and low vapour pressure even at high temperatures. These features allow the operation of a LFR at atmospheric pressure (unlike current water-cooled reactors, working at hundreds of bar) [12,18-21]. Moreover, the high boiling point of lead alloys excludes the probability of voids formation within the core (probability as not to exclude in SFR) [17,18,20,21]. The high density of lead and LBE significantly reduces the risk of fuel compaction in the case of core melting (even if unlikely) [18,21]. Conversely, this scenario is not negligible for water and sodium cooled reactors, for which the risk of partial or complete core melting is less reduced than for a LFR. Lead has also the capability to shield γ radiations and trap volatile fission products such as Iodine and Cesium reducing the risk of exposure for operators [21]. At last, lead and LBE have very low chemical reactivity with air and water (unlike sodium) excluding strong criticality such as fires and explosions in case of coolant leakage from the primary system [19-21]. This aspect introduces also an economic advantage since an intermediate coolant circuit is not needed for the heat removal [19-21].
Concerning the proliferation resistance and the public safety, the use of mixed U and Pu oxides (MOX) and MAs in the fuel makes the LFR unemployable for the production of weapon-grade plutonium [19]. The neutron properties of lead allow also the design of long-live cores hindering the Pu production. In addition, the use of a coolant with high boiling point, operating at low pressure and chemically inert with air and water increases the physical protection of the population living in the surrounding areas of the nuclear site, thus reducing the need for complex protection systems in case of terrorist attacks [17,19].
Comparing lead and LBE, the latter has a lower melting point (125°C), which reduces the problems connected with freezing [18,20]. A critical drawback with the use of LBE is the formation of Po-210 from Bi-209 by neutron capture. Po-210 is toxic and a strong α emitter (T1/2 = 138 days) and forms volatile compounds when in contact with air or water [12,17]. This issue requires specific devices for Po treatment and safety systems in case of leakage. Lead instead is more available on the earth's crust, is less expensive and produces lower amount of Po-210 (by a factor of 104) [12,17]. For this reason, most of the civil reactor projects under development (e.g. BREST, STAR, ELSY) are based on pure lead as coolant. LBE is mainly reserved to experimental reactors thanks to the lower freezing temperature and for the large power density that can be obtained even at low operating temperature [21]. The drawback of pure lead is the high melting point (327°C), which requires engineering strategies to prevent freezing anywhere in the system, particularly during reactor shut down, maintenance and refuelling steps [18,20,21].

1.1.3 ALFRED and MYRRHA

ALFRED and MYRRHA are the two reactor concepts cooled with HLM (lead and lead-bismuth eutectic) supported in Europe through ESNII. While about 80 reactor-years of experience and feedback have been

accumulated during operation of lead-bismuth eutectic (LBE)-cooled reactors used in submarines and land-based facilities in the former Soviet Union, there is no operating experience and feedback on LFRs. ALFRED aims to be the European LFR demonstrator, with the purpose to show the viability of the LFR technology for the employment in future commercial power plants. MYRRHA aims to be the ADS pilot with the goal to demonstrate the feasibility of the transmutation of fuel and MAs but also to provide scientific support to the study of materials and components operating under a fast spectrum regime.

ALFRED has been conceptualized under the leadership of ANSALDO NUCLEARE in the framework of the European project LEADER (Lead-cooled European Advanced DEmonstration Reactor), 7th Framework Program EU [22]. ALFRED is a pool-type reactor cooled with lead. The primary coolant (lead) operates in the cover gas at atmospheric pressure. The pool-type concept involves the containment of all the primary coolant in the reactor vessel, thus excluding issues related to circulation of the coolant outside the main vessel. Consequently, the configuration provides that all the components of the primary loop (fuel assemblies, pumps, steam generators, etc.) are introduced in the main vessel [5,22]. The design of ALFRED reactor (as conceptualized during the LEADER project) is shown in Fig. 1.1.1.

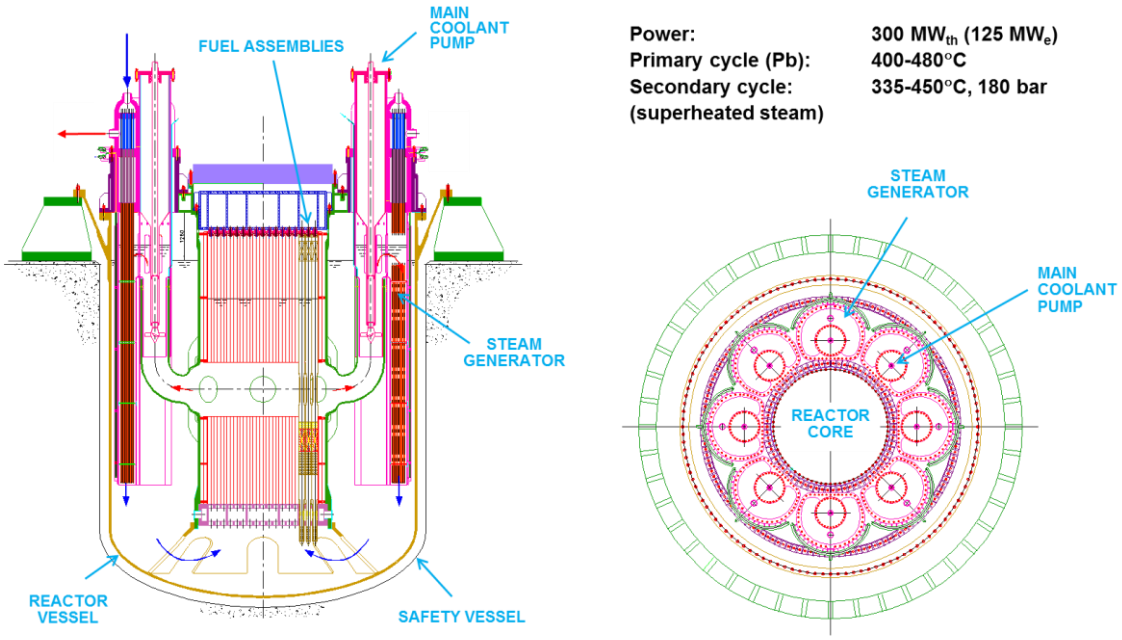

Fig. 1.1.1: Configuration and specifications of ALFRED LFR. Power: 300 MWth; Core inlet-outlet temperature: 400-480°C; max. fuel cladding temperature: 550°C [5,22].

MYRRHA ADS consists of a high-power proton accelerator, a HLM spallation target able to produce neutrons when bombarded by a high-power proton beam, and a sub-critical core [6,7]. When the proton-beam from the accelerator hits the spallation target, several spallation reactions occur, generating a large number of fast neutrons. These neutrons are in charge to sustain the nuclear chain reaction. The ADS is designed with the purpose to burn fuel containing MAs, which instability may generate problems in maintaining the critical mode. Furthermore, the ADS provides an important benefit from the point of view of safety: the power is modulated by controlling the beam current and the nuclear system can be shut down in any moment by cutting off the proton beam [6,7]. The design of MYRRHA is shown in Fig. 1.1.2: basically, it is a LBE-cooled pool-type reactor with the components of the primary loop all introduced in the main vessel. An external accelerator generates a proton-beam which is directly sent to the spallation target (consisting always in LBE) to start and sustain the nuclear chain reaction.

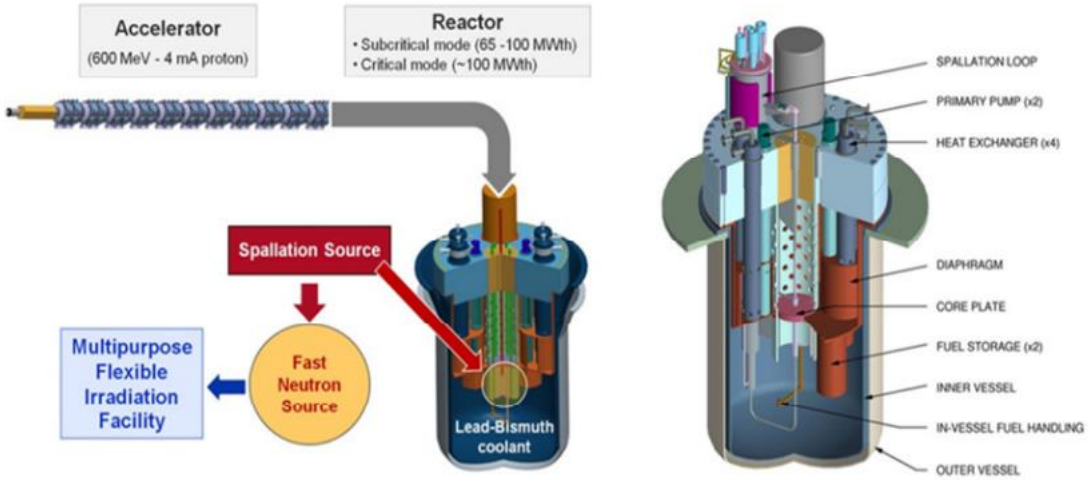

Fig. 1.1.2: Configuration and specifications of MYRRHA ADS. Power: 100 MWth; Core inlet-outlet LBE temperature: 270-410°C; max. fuel cladding temperature: 470°C [6,7].

1.1.4 The Oxygen control of the HLM coolant and the correlated issues of oxidation and corrosion of the structural materials

The chemistry of Pb and LBE is a key topic to be addressed in the development of lead-cooled nuclear reactors for two main reasons: HLM oxidation and corrosion of structural steels. Corrosion protection strategy in liquid lead is based on maintaining a controlled concentration of dissolved oxygen in the coolant, which has to be high enough to support the formation of a protective oxide layer on surfaces of structures and, at the same time, low enough to prevent the formation of large amounts of PbO precipitation, which might lead to the fouling and slagging of the primary system and subsequently coolant blockages, in particular in fuel sub-assemblies. For this reason, the concentration of the dissolved oxygen in the primary coolant has to be constantly monitored, controlled and possibly kept as low as possible.

A too high oxygen concentration in the HLM is potentially dangerous, since it may generate coolant oxides (mainly PbO) in stagnant and coldest area of the reactor. This is the case of **HLM oxidation**. Namely Pb and LBE solubilize significant amount of oxygen. When oxygen is dissolved up to the solubility level, coolant oxides formation (mainly PbO) and their consequent deposition may occur. This scenario has absolutely to be avoided since it would imply dispersion of PbO impurities into the coolant. Coolant oxides affect HLM thermal-hydraulics and cause the plugging of the structures, thus leading to potential safety risks.

On the other hand, a sufficient and optimal oxygen concentration in the HLM allows the **self-passivation of the steel structures** by formation of a double-oxide layer (external Fe_3O_4 + internal Fe-Cr spinel oxide), which is able to reduce the dissolution as well as the release of corrosion products in the HLM.

If the oxygen concentration is too low for the formation of a stable oxide layer, **steel dissolution** occurs. At low oxygen concentration, the steel becomes prone to fast detrimental corrosion.

Between the two extremes (HLM oxidation and structural steel dissolution), there is a transition zone where dissolution and oxidation are concomitant and where the overall corrosion rate is low [27]. Namely, from a mathematical point of view, in order to prevent PbO precipitation and to support Fe_3O_4 formation, the following condition must be satisfied:

$$2\,\Delta G^{o}\,PbO > RT \ln p O_2 > 0.5\,\Delta G^{o}\,Fe_3O_4$$

where ΔGº is the Gibbs energy for formation of oxides, pO_2 is the oxygen partial pressure, R is the gas constant and T is the absolute temperature. Then it derives that oxidizing / self-passivation condition region may be defined, at 550°C, as:

$$10^{-7} \text{ wt\%} \leq [O] \leq 5 \cdot 10^{-4} \text{ wt\%}$$

Experimental data [24-32] about the compatibility of steels with HLMs have shown that the three different corrosion regimes actually exist as function of the oxygen concentration (see Fig..1.1.3).
Operating in the "steel self-passivation" regime, even if the formation of a thin protective oxide layer could be seen as beneficial concerning the life of the component, a too thick oxide scale would have instead, on the other hand, a threefold negative impact; namely it deteriorates the thermal conductivity of the material and worsens the heat transfer of the component/system; it might spall off and solid oxides can plug channels in the system; and it induces metal recession which reduces the load bearing capability of the component.

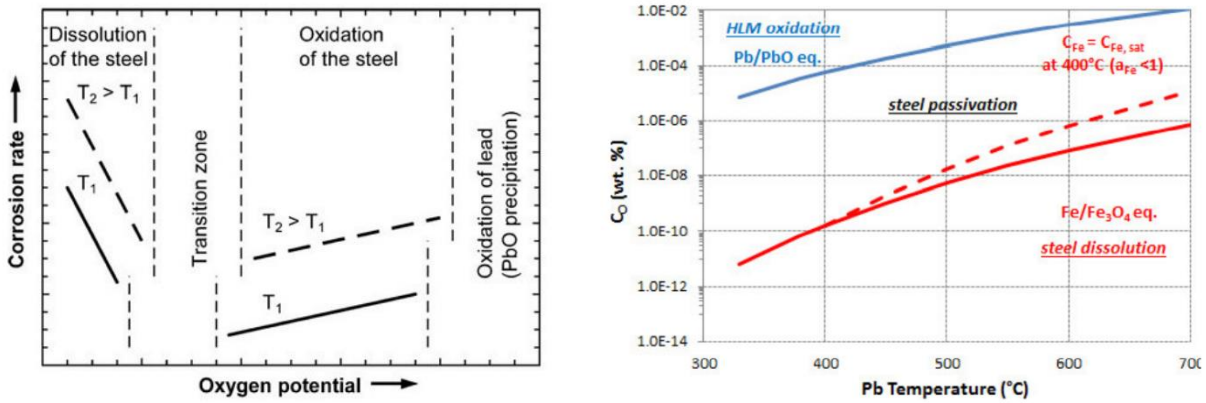

a) b)

Fig.1.1.3: a) Qualitative behaviour of steels versus oxygen potential (oxygen concentration) in Pb and LBE[27]; **b)** "Active oxygen" for a Pb-cooled system represented by the "steel passivation" area.

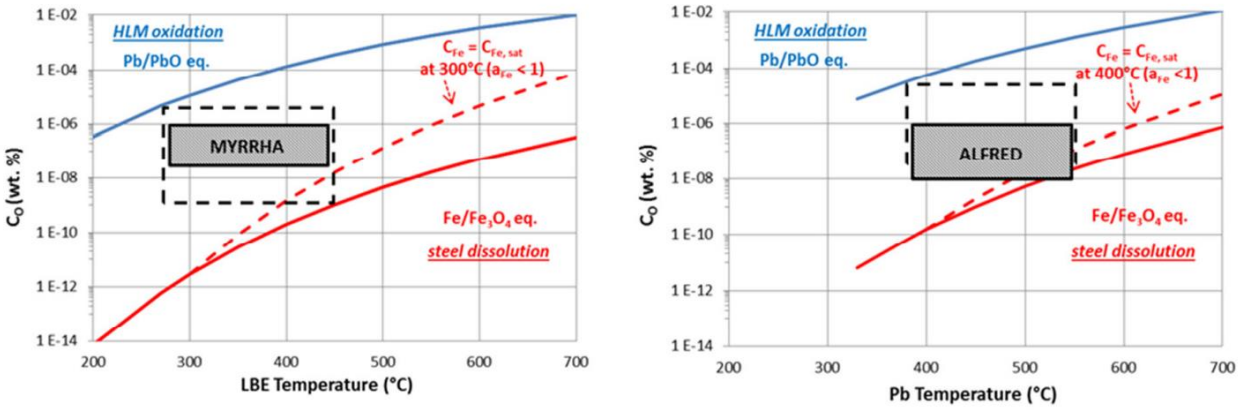

a) b)

Fig. 1.1.4: General oxygen concentration range (dashed black box) and fixed oxygen concentration (full black box) for MYRRHA (a) and ALFRED (b) operation.

Considering the contamination behaviour of oxygen and its influence on steel corrosion resistance, it is of paramount relevance to control the oxygen concentration within a well-defined range in order to reduce both the dangerous formation of coolant oxides and the dissolution of steel structures. The oxygen control technology in HLM thus constitutes a key research area in the development of Pb cooled fast reactors.

The oxygen control technology can involve different approaches about the optimal oxygen content dissolved in the coolant. However, the different strategies have the common point to work with a low oxygen content in the HLM to avoid dangerous plugging and operate in safe. This approach requires an oxygen content at least lower than the solubility at the minimum operating temperature of the reactor. At 550°C it results:

$$[O] \leq 10^{-7} \text{ wt\%}$$

The following figure (fig. 1.1.5) reports the existence of corrosion conditions as function of both oxygen content and temperature for Martensitic and Austenitic steels. The upper solid line in the diagrams indicates the border line for PbO formation as a function of temperature. The lower dashed line marks the lowest possible oxygen concentration for which protective oxygen scales occurs. The border at which dissolution occurs and that one at which PbO formation takes place depend both on temperature [24-32].

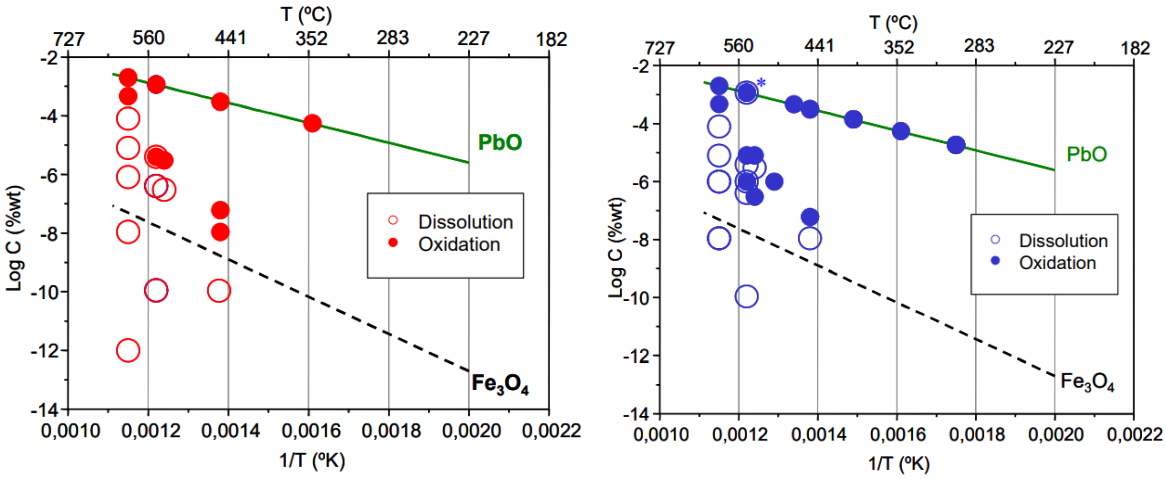

Figure 1.1.5 Martensitic (left) and Austenitic (right) steels after exposure to LBE/Pb for ≥ 2000h at temperatures ranging from 400-650°C [24].

At 550°C both martensitic and austenitic steels develop a protective scale (double layer) only when the oxidation concentration is above 10^{-5} wt%. When a duplex oxide scale is present, the inner layer is a Fe-Cr spinel while the outer layer is magnetite, Fe_3O_4. Heavy corrosion (dissolution attack) is expected above 550°C for both materials. Figure 1.1.6 is a graph taken from [24]: it shows corrosion data from the exposure of two different austenitic stainless steels to flowing liquid Pb for 3000 h at 550°C. As may be seen, a low concentration of dissolved oxygen in the liquid Pb (CO < 10-7 wt%) resulted in steel dissolution, due to the absence of a protective oxide layer.

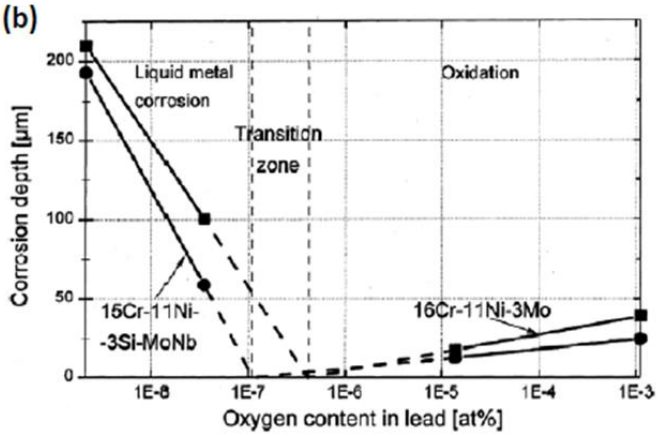

Figure 1.1.6. Effect of the liquid metal oxygen concentration on the LMC behaviour of two different austenitic steels exposed to liquid Pb for 3000 h at 550°C [24]. The y axis gives absolute values of the

corrosion depth: for oxidation corrosion, the thickness of the corrosion-affected zone is positive, and for liquid metal (dissolution) corrosion, the corrosion-affected zone thickness is negative.

Concerning the steel structures, it is important to mention that the low oxygen approach might enhance the corrosive effect if the dissolved oxygen concentration is not sufficient to ensure the steel passivation via formation of the oxide layer. In addition, the passivation cannot be considered an effective protection for steels exposed above 450-480°C. In such conditions localized depletion of Ni and Cr is anyway observed in austenitic steels and strong oxidation is detected in ferritic/martensitic (F/M) steels, both ascribable to the low protective features of the oxide above these temperatures [25,30]. This issue mandatorily requires the use of further protection strategies at least for steel structures exposed to the highest temperature in the reactor (e.g. fuel cladding and fuel assemblies at 500-550°C in LFR). For instance, the protection strategy for ALFRED LFR demonstrator consists in coatings for the fuel claddings [31]. To the opposite, the low temperature operating conditions of MYRRHA ADS (270-450°C) may not require further protection in addition to the passivation method.

1.1.5 Liquid Metal Embrittlement (LME) and Mechanical proprieties degradation

Although LME has first been observed a long time ago, the mechanism is not yet fully understood due to the complexity of the phenomenon. LME was described by Rostoker [33] as the decrease in ductility of a metal caused by contact with a liquid metal. It is characterized by a premature brittle failure of an otherwise ductile material when placed in contact with specific liquid metal. Such specificity was questioned by Fernandes and Jones [34] who suggest that it relies on particular testing conditions rather than on the actual interactions between the liquid and the solid metal. However, a crucial prerequisite for LME is direct contact on an atomic scale between the stressed solid and the embrittler. LME may depend on many parameters like metallurgical state, surface state, temperature, strain rate and oxygen concentration in liquid metal [35-38]. However, for the occurrence of LME, at least three simultaneous conditions must be applied:

- **intimate contact** between the solid and the liquid metal; a direct contact between the atoms of the solid and the atoms of the liquid is needed in order to have crack nucleation and propagation;
- **minimum strain rate**; the applied stress must be sufficient to trigger dislocation motion and then plastic deformation but slow enough to let the time dependent surface mechanisms occur; the strain rate of maximum sensitivity is not known but is often considered to result from a balance of straining rapidly enough to promote oxide fracture and crack initiation at many sites but sufficiently slowly to permit interaction of the liquid metal with the crack sites;
- **Sharp and stiff microstructure** (ex. Martensite); as we can see from the literature sources, in fact, most of the characterizations concern martensitic steels, just because these are the ones most affected by this phenomenon.

In the recent years the embrittlement effects of LBE on ferritic/martensitic steels (FMSs) have been studied by many authors. Among various mechanical tests, the slow-strain-rate tensile (SSRT) tests have been extensively used. The results reveal that the embrittlement effects of LBE on FMSs may depend on several experimental parameters such as testing temperature, strain rate and surface condition of specimens.
Several models were proposed to explain LME phenomenon [33]. All models are based on the experimental observation that LME occurs by nucleation of a crack at the wetted surface of a solid and its following propagation into the bulk until ultimate failure. With regard to metal- lead/LBE system, the more accredited model is the brittle fracture theory based one, entitled SJWK. This latter is based on a reduction of the surface energy by absorption of liquid metal atoms at the crack tip of the solid. The adsorption process relies on the specific atoms of the liquid and solid, and is often referred to as chemisorption; but the stress field at the crack tip should have an influence on the adsorption. This model is consistent with considerations made on the metallurgical parameters influencing embrittlement for ferritic/martensitic steels and austenitic stainless steels in contact with Pb or LBE.

The loss of ductility of solid metals when is in contact with liquid metal, appears to be limited to a particular temperature range known as ductility trough. It is detected following the evolution of the absorbed energy at rupture (namely the total elongation) with temperature. For T91 steel in liquid lead, a ductility trough between 350°C and 425°C was found [39]. For T91 in LBE, the more recent investigations showed that ductility trough ranges from 160°C to 425°C. During the last years, the lower limit decreased progressively until 160°C, as a result of successive modifications of experimental conditions and procedures employed. In 2006, Dai et al. [40] using micro-cracked tensile specimens in LBE with 10^{-6} wt% dissolved oxygen and at strain rate of 10^{-5} s^{-1}, found a range between 300°C and 425°C (fig. 1a). Later the ductility trough was extended [41] to the 200-425°C. Finally, the studies on crack propagation of Hadjem-Hamouche et al. [42] fixed the lower limit at 160°C. They performed tensile testing on specimens showing a center cracking in the gauged length and calculated the brittle fraction area from the analysis of the fracture surface. Brittle fracture mode was more prevalent at low temperature. Similar results were also achieved in Lead by Kashtanov [43] on a martensitic steel. A reduced necking (a lower reduction of area at fracture indicates decreased ductility) was in fact detected after the tests in lead, compared to the tests in air (fig. 1.1.7).

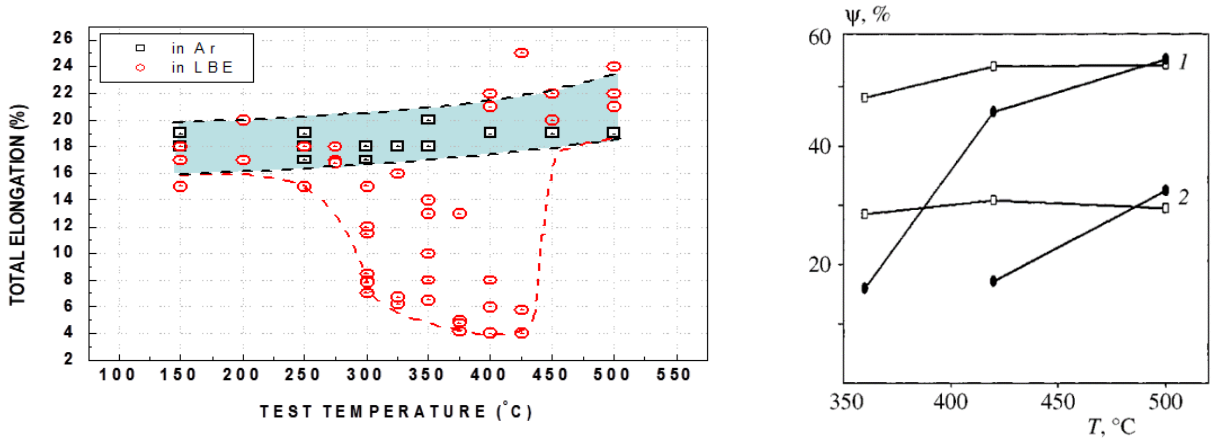

a) **b)**

Fig. 1.1.7 a) Total elongation versus testing temperature for T91 steel [41]; **b)**Temperature dependence of the relative shrinkage of notched samples of a martensitic steel after tests in lead (filled symbols) and in air (empty symbols); 1, 2) notch with radius 3 and 0.3 mm, respectively [43].

In 2008, again Hadjem-Hamouche et al. [44] carried out uniaxial tensile tests in order to study the effect of LBE both on T91 steel and on 316L steel. In particular, slow strain rate tests (SSRT) were performed on center cracked in tension specimens by varying the deformation rate from 10^{-7} s^{-1} to 10^{-2} s^{-1}. For T91 steel they observed that cracking and fracture occurred more quickly at low strain rate, while, at higher displacement rate, no LME effects were detected. In other words, the sensitivity to LBE embrittlement decreases at the increasing strain rate. Such ductility recovery behaviour can be related to the existence of an incubation period required for crack nucleation and propagation. Similar results were obtained by Long [45]. Albeit the strain rate of maximum susceptibility is not known, it is often considered to result from a balance of straining rapidly enough to promote oxide fracture and crack initiation at many sites, and sufficiently slowly to permit interaction of the liquid metal with the crack sites. Fig. 1.1.8 illustrates the effects of strain rate on susceptibility of T91 steel to LME, according to the mentioned literature sources. Instead, LME was not observed on 316L steel.

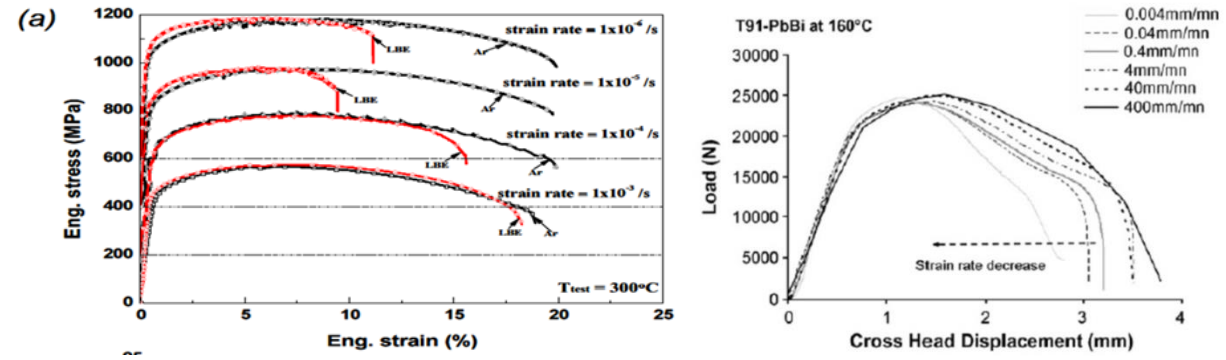

a) b)

Fig. 1.1.8 Stress strain curves of T91 tested in Pb-Bi at different strain rates; a) from [45] b) from [44].

Beside temperature and strain rate, surface state is crucial to determine the susceptibility to LME of a given solid-liquid couple. State surface shall be such as to enable intimate contact between steel and liquid metal. First, the formation of oxide layers on metal surface, for example, can be very effective to protect the steel against LME [46]. A thin oxide layer can block the initiation of any sort of degradation, including LME, because it avoids the direct contact between heavy liquid metal and steel. On the other side, long-term exposure to liquid metals or thermo-cycling and mechanical effects could damage and induce failure of oxide layers. As a consequence, either the steel is able to repair the damage by further growth of oxides or the damage starts locally and LME is observed. In this regard, several techniques have been developed to force direct contact between liquid metal and steel. As reported [47], oxide layer on T91 steel was removed by beam sputtering in an UHV (ultra high vacuum) chamber, followed by physical deposition of LBE. Tensile curves, performed at 340°C with a strain rate of 10^{-4} s^{-1} showed a decrease in strength and elongation to rupture. In addition, the rupture surface indicated a mixed ductile/brittle rupture profile and multiple cracks were observed on the gauge length. A similar "ductilization" effect in lead was also noticed by other authors on pure Iron tested at 550°C [48].

Surface cracks created by EDM cutting [40] or plastic deformation at machined notch [49] have shown to strongly increase the susceptibility of T91 steel to Pb and LBE. In particular, SSRT with strain rate of 10^{-5} s^{-1} were performed on cracked specimens in static LBE at temperatures ranging from 250°C to 425°C. Here, the results demostrated that in the temperature range of 300°C to 425°C, the T91 steel was susceptible to LBE embrittlement, and that the total elongation decreased at the increasing temperature.

Studies on the creep strength, creep damage and creep crack growth rates were conducted recently, most of which were focused on T91 ferritic-martensitic steel in contact with flowing LBE. Uniaxial creep-to-rupture tests on T91 steel in air and in flowing LBE (550°C, flow rate of 0.5 m/s, 10^{-6} wt% dissolved oxygen) were performed in 2009 by Jianu [46] and in 2012 by Weisenburger [50]. The tests [46] were performed varying operating temperature and applied stress value. Before applying the stress, the specimens were kept in contact with LBE, allowing the formation of oxide layer on the steel surface. For specimens tested in LBE and for applied stress value lower than 140 MPa, the strain rates of secondary creep stages were the same order as for specimens evaluated in air at stress value of 140 MPa. When higher stress levels were applied (above 140 MPa), the detrimental effects of LBE on T91 steel became noticeable: the rupture times were significantly reduced and the strain rate of the secondary creep stage was increased up to 53 times. The authors deduced that the dependence of the creep strength with the applied stress could be related to the stability of the oxide layer. At low stress value, the oxide layer prevented and delayed the direct contact between the steel and the liquid metal, albeit it showed the formation of few cracks. Instead at high stress, the number and the depth of the cracks increased, favoring the penetration of LBE and the direct contact with the steel. To improve creep strength of T91 steel in LBE, Weisenburger et al.[50] carried out creep-rupture tests on surface modified T91 steel in flowing LBE at varied loads. In particular, they tested T91 steel coated

with Al-rich layer having a thickness of tens of microns in a temperature range between 500°C and 550°C. If correlated to the unmodified T91 steel tested in air, no difference in secondary creep rates and in rupture time of surface modified T91 steel was noted. Creep performance of T91 steel in contact with stagnant lead with 10^{-6} wt% dissolved oxygen and at 650°C were also reported [51]. The authors declared that the creep degradation of T91 steel to stagnant lead was negligible. Indeed, the times to rupture, as well as the structure of fracture surface, of the specimens tested in lead and in air were almost similar. For 15-15 Ti(Si) austenitic steel in stagnant lead, LME effects were recently investigated [52]. Creep tests were carried out at 550°C in stagnant lead in oxidizing atmosphere (air environment) at various stress levels. Comparing creep curves of specimens tested at 560 MPa in air and in lead, a very similar performance of 15-15 Ti(Si) steel was identified. But when the load was enhanced up to 575 MPa, the specimens in lead showed a decrease of rupture time and a reduction of creep strain. Furthermore, the structure of fracture surface of the specimens tested in lead and in air, as observed by SEM, exhibited marked differences.
Concerning fatigue life, as reported in [53], the LBE seems to provide detrimental effects on the martensitic steels (T91 in the cited reference) as the number of cycles to failure results shortened if the test is carried out in LBE environment. The authors also plot the elastic strain as function of the cycles to failure, but, as expected, the liquid metal doesn't seem to affect the elastic stage of the fatigue cycling, as it just takes to a shortening of the plastic deformation (LBE environment compared to air). On the other hand, some experimental campaigns just carried out in Brasimone in the 90s [54], reveal that the fatigue life of the austenitic 316L steel isn't negatively affected by the contact with Lead Lithium; the number of cycles to failure indeed result even higher when this material is tested in Pb-17Li. The authors explain this behaviour with the slow strain rate which make the fatigue life very susceptible to the environment; concerning the inert atmosphere tests, they address the possible adverse effects that impurities present in the gas may have on the fatigue life of the material, as it seems to be indicated by the presence of thin oxide films in several areas on the samples. Nevertheless, the general conclusion is that the contact with Lead Lithium doesn't appear detrimental for the fatigue life of the 316L steel.

1.1.6 Structural materials and related kinds of damage of the components of ALFRED reactor

In the following figure (fig. 1.1.9) an overview of the components of the ALFRED reactor is presented. The corresponding operating temperatures and kinds of material damage are associated to each component as well. We can notice that the most stressed components are the ones located in the core of the reactor as long as these are subjected to both the highest temperatures (taking to big issues in terms of thermal creep and fatigue) and the highest irradiation doses (resulting in swelling and irradiation creep). In addition to temperature and irradiation effects also the issues related to the compatibility of the structural materials with the coolant (Lead for ALFRED) have to be carefully taken into account in terms of liquid metal corrosion and embrittlement. Giving its good mechanical properties at high-temperatures (in particularly as regards creep), its good irradiation resistance & wettability, and owing to the available large database and operation experience in SFRs, austenitic low-carbon steel 316LN has been selected as reference structural material for ALFRED vessel and internal components. Earlier, T91 (martensitic steel) was considered as a candidate material for steam generators, but is now also being replaced by 316LN. Hot structures wetted by liquid lead are subjected to temperatures of 480-500°C, while cold structures are exposed to temperatures of 400°C or below. Due to exposure to service conditions, including nominal as well as transient situations, primary components are subjected to ageing processes, including corrosion-erosion, thermal stripping, creep, creep-fatigue, and thermal ratcheting. The inner vessel is also subjected to low-dose irradiation damage. As we can notice from the figure, none of the steels currently chosen for the components of ALFRED reactor is martensitic (we just see 316L and 15-15 Ti as selected stainless steels alloys), and one of the main reasons is just the higher susceptibility these steels have to the insurgence of the Liquid Metal Embrittlement (LME).

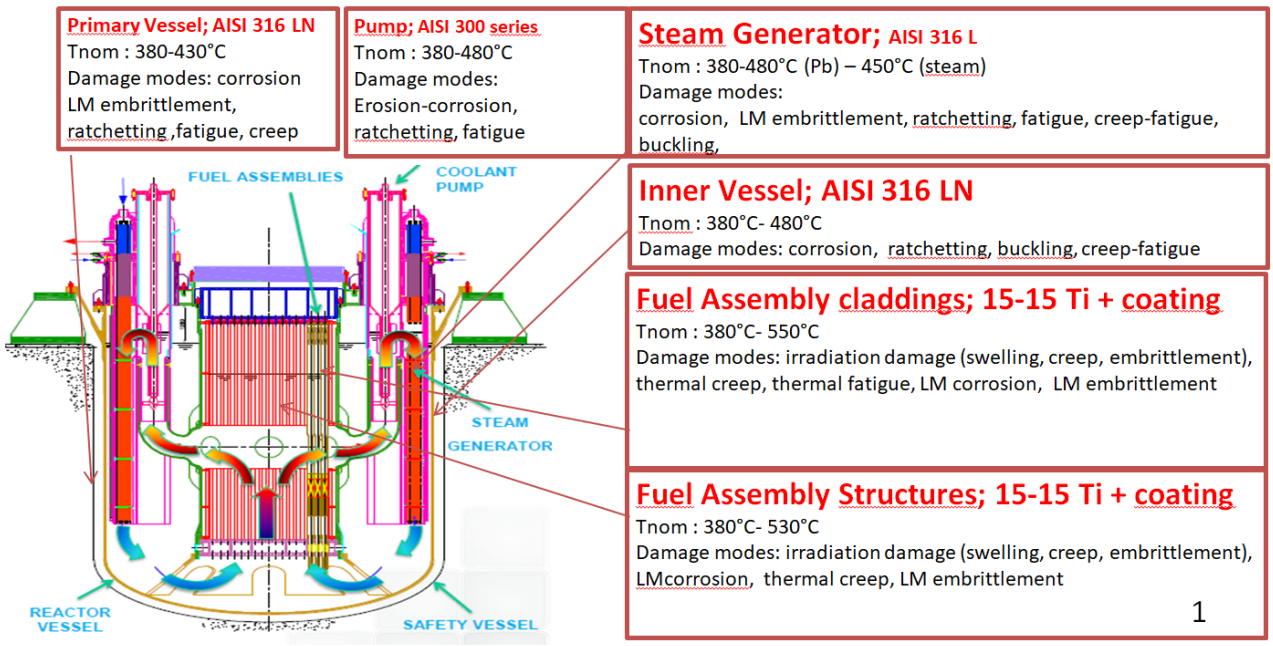

Fig.1.1.9 Overview of the materials employed for the components of ALFRED reactor with corresponding temperatures and kinds of damage

As for ASTRID SFR, the RCC-MRx Code [the French standards for the reactors design] has also been chosen for the design of ALFRED. RCC-MRx is specifically developed for Sodium Fast Reactors, and return-of-experience as well as pre-normative research in support of SFR has been incorporated. The situation is quite different for heavy liquid metal (HLM) coolants and their influence on behaviour of base material and welds are currently not treated explicitly in RCC-MRx or any other existing Design Code and Standard. Flowing heavy liquid metals are corrosive/erosive and can induce or accelerate a material failure under a static or a time-dependent loading, through embrittlement (including liquid metal induced embrittlement and irradiation embrittlement), creep (including liquid metal assisted creep), fatigue, and wear (fretting and cracking assisted by wear). New Design Rules and assessment procedures, supported by comprehensive set of test data and complemented with modelling of related degradation mechanisms, need therefore to be developed and incorporated into the RCC-MRx Design Code. This is just the aim of the current international GEMMA (Generation IV Materials Maturity) Project in which the ENEA Brasimone laboratory is involved. In the first stage of the RCC-MRx code development there will be no data in support of long-term operation. The specific long-term degradation mechanisms related to the 60-years design life will initially have a lower priority but research work has already started (Pilot Project "60+ Life Extension" in which the ENEA Brasimone laboratory is involved as well) to have it incorporated when the design of commercial reactors will start.

1.1.7 References

[1] "An energy policy for Europe", COM(2007) 1, SEC(2007) 12, 10, January 2007.

[2] EURATOM Directorate-General for Research, "The Sustainable Nuclear Energy Technology Platform. A vision report", Report n° EUR22842, 2007, available at: www.snetp.eu/wp-content/uploads/2014/05/sne-tp_vision_report_eur22842_en.pdf

[3] Sustainable Nuclear Energy Technology Platform (SNETP) Secretariat, "ESNII: The European Sustainable Nuclear Industrial Initiative. A contribution to the EU Low Carbon Energy Policy:

Demonstration Programme for Fast Neutron Reactors", Concept Paper, October 2010, available at: www.snetp.eu/publications/

[4] C. Latgé, "ASTRID (Advanced Sodium Technological Reactor for Industrial Demonstration) project: Status and main challenges", Workshop on Thermal-hydraulics and Thermo-mechanical Issues for Safety, 12-13 May 2016, Brasimone, Italy.

[5] A. Alemberti, "ALFRED: The European Lead Fast Reactor Demonstrator", 5th Annual International Conference on Sustainable Development through Nuclear Research and Education, 16-18 May 2012, Pitesti, Romania.

[6] H. Aït Abderrahim, P. Baeten, D. De Bruyn, R. Fernandez, "MYRRHA - A multi-purpose fast spectrum research reactor", Energ. Convers. Manage. 63 (2012) 4-10.

[7] M. Schyns, H. Aït Abderrahim, P. Baeten, R. Fernandez, D. De Bruyn, "The MYRRHA ADS Project in Belgium Enters the Front End Engineering Phase", Proceedings of the 2nd International Symposium on Science at J-PARC - Unlocking the Mysteries of Life, Matter and the Universe, JPS Conf. Proc. 8, 001001 (2015).

[8] P. Vácha, "ALLEGRO project: Status and perspectives", Workshop on Thermal-hydraulics and Thermo-mechanical Issues for Safety, 12-13 May 2016, Brasimone, Italy.

[9] OECD Nuclear Energy Agency for the Generation IV International Forum, "Technology Roadmap Update for Generation IV Nuclear Energy Systems", January 2014, available at: www.snetp.eu/wp content/uploads/2014/05/sne-tp_vision_report_eur22842_en.pdf

[10] T. Abram, S. Ion, "Generation-IV nuclear power: A review of the state of the science", Energ. Policy 36 (2008) 4323-4330.

[11] G. Locatelli, M. Mancini, N. Todeschini, "Generation IV nuclear reactors: Current status and future prospects", Energ. Policy 61 (2013) 1503-1520.

[12] B. F. Gromov, Yu. S. Belomitcev, E. I. Yefimov, M. P. Leonchuk, P. N. Martinov, Yu. I. Orlov, D. V. Pankratov, Yu. G. Pashkin, G. I. Toshinsky, V. V. Chekunov, B. A. Shmatko, V. S. Stepanov, "Use of lead-bismuth coolant in nuclear reactors and accelerator-driven systems", Nucl. Eng. Des. 173 (1997) 207-217.

[13] A. V. Zrodnikov, V. I. Chitaykin, B. F. Gromov, O. G. Grigoryv, A. V. Dedoul, G. I. Toshinsky, Yu. G. Dragunov, V. S. Stepanov, "Use of Russian technology of ship reactors with lead-bismuth coolant in nuclear power", Proceedings of an Advisory Group Meeting in Obninsk, Russian Federation, 20-24 July 1998, IAEA-TECDOC-1172 (2000).

[14] IAEA "Liquid metal coolants for Fast Reactors cooled by sodium, lead and lead-bismuth eutectic", Nuclear Energy Series n° NP-T-1.6, 2012, Vienna, Austria.

[15] OECD/NEA, "Handbook on lead-bismuth eutectic alloy and lead properties, materials compatibility, thermal-hydraulics and technologies", 2015.

[16] G. I. Toshinsky, O. G. Komlev, I. V. Tormyshev, V. V. Petrochenko, "Effect of Potential Energy Stored in Reactor Facility Coolant on NPP Safety and Economic Parameters", World Journal of Nuclear Science and Technology 3, (2013) 59-64.

[17] G. I Toshinsky, O. G Grigoryev, E. H. Pylchenkov, D. E. Skorikov, O. I. Komkova, “Comparative analysis of coolants for FBR of future nuclear power”, Proceeding of the 9th International Conference On Nuclear Engineering (ICONE-9), 8-12 Apr 2001, Nice, France.

[18] A. Alemberti, V. Smirnov, C. F. Smith, M. Takahashi, “Overview of lead-cooled fast reactor activities”, Prog. Nucl. Energ. 77 (2014) 300-307.

[19] A. Alemberti, “The Lead Fast Reactor: An opportunity for the future?”, Engineering 2 (2016) 59-62

[20] K. Tucek, J. Carlsson, H. Wider, “Comparison of Sodium and Lead-cooled Fast Reactors regarding reactor physics aspects, severe safety and economic issues”, Nucl. Eng. Des. 236 (2006) 1589-1598.

[21] M. Tarantino, L. Cinotti, D. Rozzia, “Lead-cooled Fast Reactor (LFR) development gaps”, IAEA Technical Meeting to Identify Innovative Fast Neutron Systems Development Gaps, IAEA Headquarters, 29 February - 2 March 2012, Vienna, Austria.

[22] M. Frogheri, A. Alemberti, L. Mansani, “The Lead Fast Reactor: Demonstrator (ALFRED) and ELFR design”, IAEA Proceedings of the International Conference on Fast Reactors and Related Fuel Cycles: Safe Technologies and Sustainable Scenarios (FR13), Vol. 1, 4-7 March 2013, Paris, France.

[23] K. Tucek, S. Hermsmeyer, L. Ammirabile, D. Blanc, E. Wattelle, L. Burgazzi, M. Frogheri, L. Mansani, S. Ehster-Vignoud, B. Carluec, Th. Aoust, C. Niculae, Zs. Elter, I. Toth, “Identification and categorisation of safety issues for ESNII reactor concepts. Part I: Common phenomena related to materials”, Ann. Nucl. Energy 87 (2016) 411-425.

[24] OECD/NEA, “Handbook on lead-bismuth eutectic alloy and lead properties, materials compatibility, thermal-hydraulics and technologies”, (2015).

[25] C. Schroer, O. Wedemeyer, J. Novotny, A. Skrypnik, J. Konys, “Selective leaching of nickel and chromium from type 316 austenitic steel in oxygen-containing lead-bismuth eutectic (LBE)”, Corros. Sci. 84 (2014) 113-124.

[26] P.N. Martynov, A.V. Gulevich, Yu.I. Orlov, V.A. Gulevsky, “Water and hydrogen in heavy liquid metal coolant technology”, 1st COE-INES International Symposium, October 31-November 4, 2004, Tokyo, Japan.

[27] C. Schroer, O. Wedemeyer, J. Konys, “Aspects of minimizing steel corrosion in liquid Lead-alloys by addition of oxygen”, Nucl. Eng. Des. 241 (2011) 4913-4923.

[28] J-L. Courouau, S. Sellier, F. Balbaud, K. Woloshun, A. Gessi, P. Schuurmans, M. Ollivier, C. Chabert, ”Initial start-up operations chemistry analysis for MEGAPIE”, 5th MEGAPIE Technical Review Meeting, 2004, Nantes, France.

[29] J.-L. Courouau, P. Agostini, P. Turroni, H. Glassbrenner, “Review of the oxygen control for the initial operations and integral tests of the MEGAPIE spallation target”, 6th MEGAPIE Technical Review Meeting, 2005, Mol, Belgium.

[30] C. Schroer, O. Wedemeyer, J. Novotny, A. Skrypnik, J. Konys, “Performance of 9% Cr steels in flowing lead-bismuth eutectic at 450 and 550°C, and 10−6 mass % dissolved oxygen”, Nucl. Eng. Des. 280 (2014) 661-672.

[31] M. Tarantino, S. Bassini, D. Rozzia, “ALFRED PROJECT. Research and Development Needs”, ENEA Technical Report LR-P-R-126 (2015).

[32] G. Müller, A. Heinzel, G. Schumacher, A. Weisenburger, J. Nucl. Mater. 321 (2003) 256

[33] Rostoker W., McCanghey J.M., Markus H. Embrittlement by liquid metals, Reinhold Publishing Cooperation, New York, **1960**, Chapman &Hall, LTD., London.

[34] Fernandes P. J. L. and Jones D. R. H., *Eng. Failure Anal.*, **1996**, 3(4), 299.

[35] Joseph B., Picat M. and Barbiera F. Liquid Metal Embrittlement: A state-of-art appraisal. *Eur. Phys. J. AP* **1999**, 5, 19-31.

[36] Wang F. Bonding Theory for metals and Alloys. Elsevier, Oxford **2005.**

[37] Glickman E. Mechanism of liquid metal embrittlement by simple experiments: from atomistics to life-time. *Multiscale Phenomena in Plasticity*, J. Lépinoux et al. (Eds.), Kluwer Academmic Publishers, **2000**, 383-401.

[38] Nicholas M. G. and Old C. F. Review Liquid Metal Embrittlement. *J. Mater. Sci.* **1979**, 14, 1-18.

[39] Nicaise G., Legris A., Vogt J.-B., Foct J., Embrittlement of the martensitic steel 91 tested in liquid lead. J. Nucl. Mater. 2001, 296, 256–264.

[40] Dai Y., Long B., Gröeschel F. Slow strain rate tensile tests on T91 in static lead-bismuth eutectic. *J. Nucl. Mater.* **2006**, 356, 222–228.

[41] Long B., Tong Z., Gröeschel F., Dai Y., Liquid Pb–Bi embrittlement effects on the T91 steel after different heat treatments. *J. Nucl. Mater.* **2008**, 377, 219–224.

[42] Hadjem-Hamouche Z., Auger T., Guillot I. Temperature effect in the maximum propagation rate of a liquid metal filled crack: The T91 martensitic steel/Lead–Bismuth Eutectic system. *Corrosion Science* **2009**, 51, 2580–2587.

[43] Kashtanov et al.; *Atomic Energy*, Vol. 97, No. 2, 2004

[44] Hamouche-Hadjem Z., Auger T., Guillot I., Dominique Gorse D. Susceptibility to LME of 316L and T91 steels by LBE: Effect of strain rate, *J. Nucl. Mater.* **2008**, 376, 317–321.

[45] Long B. Liquid Lead-Bismuth Embrittlement Effect on Un-irradiated and Irradiated Ferritic/Martensitic Steels for Nuclear Applications, Thèse EPFL, N° 4355, **2009.**

[46] Jianu A., Müller G., Weisenburger A., Heinzel A., Fazio C., Markov V.G., Kashtanov A.D. Creep-to rupture tests of T91 steel in flowing Pb-Bi eutectic melt at 550°C. *J. Nucl. Mater.* **2009**, 394, 102–108.

[47] Auger T., Lorang G. Liquid Metal Embrittlement Suscetibility of T91 steel by PbBi. *Scripta Materialia*, **2005**, 52, 1323-1328.

[48] V. V. Popovich and I. G. Dmukhovskaya "Rebinder Effect In The Fracture Of Armco Iron In Liquid Metals" UDC 532.6:539.2; 1979; Plenum Publishing Corporation (0038-5565/78/1404- 0370)

[49] Legris A., Nicaise G., Vogt J.-B., Foct J., Gorse D., Vancon D. Embrittlement of a martensitic steel by liquid lead, Scripta Materialia 2000, 43, 11, 997-1001.

[50] Weisenburger A.; Jianu A., An W., Fetzer R., Del Giacco M., Heinzel A., Müller G., Markov V.G., Kashtanov A.D. Creep, creep-rupture test of Al-surface- alloyed T91 steel in liquid lead bismuth at 500°C and 550°C. J. Nucl. Mater. 2012, 431, 77–84.

[51] Yurechko M., Schroer C., Wedemeyer O., Skrypnik A., Konys J. Creep-to-rupture of 9%Cr steel T91 ain air and oxygen-controlled lead at 650°C. J. Nucl. Mater. 2011, 419, 320–328.

[52] Strafella A., Coglitore A., Salernitano E. Creep behaviour of 15-15 Ti(Si) austenitic steel in air and in liquid lead at 550°C, Procedia Structural Integrity 2017, 3, 484-497.

[53] Verleene, A., Vogt, J.-B., Serre, I., Legris, A. Low cycle fatigue behaviour of T91 martensitic steel at 300 °C in air and in liquid lead bismuth eutectic, International Journal of Fatigue, 2006, 28(8), 843–851

[54] G. Benamati, S. Storai et al., Corrosion and low-cycle fatigue properties of AISI 316L in flowing Pb-17Li,Journal of Nuclear Materials 1994, 212-215, 1515-1518

1.2 Introduction on Reduced Activation Ferritic Martensitic (RAFM) steels for DEMO fusion reactor

1.2.1 The roadmap towards the construction of a fusion reactor and the issues related to the choice of the structural materials

DEMO is considered the last "research machine" before the construction of a commercial Fusion Power Plant. The roadmap for the construction of DEMO (foreseen towards 2050) implies that the most relevant preliminary information concerning the operation of a fusion reactor will be achieved through the current ITER experimental Reactor under construction. On the one hand ITER integrates plasma scenarios at "reactor scale" to achieve extended "plasma burn" and test or demonstrate "reactor scale" technologies. Namely its target is to fill the gaps in the physics and technology understanding and define the feasibility, in terms of Technology Readiness Level (TRL), for the adopted solutions. Instead, DEMO will have to integrate and demonstrate all relevant technology (including tritium breeding) in a prototype fusion power plant aimed at the generation of electricity. This implies that the mission of DEMO is to achieve economic and environmental acceptability.
Concerning the issues for DEMO structural materials [1–5] let's shortly say that, differently from the ones employed in the fission reactors, these are subjected to bombardment of 2 MW/m^2 from very energetic (14 MeV) neutrons. Plasma facing materials receive an additional average 500 kW/m^2 from hot particles and electromagnetic radiation (up to 20 MW/m^2 on the Divertor). This means that atoms are knocked out of place several times a year and the Displacement per Atom (DPA) is higher than 100 over the component of the reactor exposed to neutron flux. This derives from the estimation that a flux of 1 MW*year*m^2 by neutrons with a high energy spectrum (14 MeV) results in 10 DPA damage.

	ITER	DEMO	Reactor
Fusion Power	0.5 GW	2.5-5 GW	2.5-5 GW
Heat flux First wall	0.1-0.3 MW/m^2	0.5 MW/m^2	0.5 MW/m^2
Heat flux Divertor	10 MW/ m^2	15-20 MW/m^2	20 MW/m^2
Neutron Load First wall	0.78 MW/ m^2	>2MW/m^2	2 MW/m^2
Displacement per Atom (DPA)	< 3 DPA	50-80 DPA	100-150 DPA
Transmutation product rates at First Wall	10 appm He / DPA 45 appm H / DPA		

Tab. 1.2.1. Parameters of the fusion plants; ITER vs DEMO vs hypothetical future reactors [1–3]

The damage due to the displacement cascade affects the material structure in terms of both dislocation loops (resulting in hardening and embrittlement effects) and enhanced diffusion (taking to rapid diffusion of impurities to grain boundaries, irradiation swelling and creep). Moreover, some elements can transmute by nuclear reaction and this problem is much enhanced for high energy fusion neutrons. This last issue is related on the one hand to long term radioactive products (γ emission) and on the other hand to Helium and Hydrogen production in the lattice. The latter implies that Helium, which can be considered as the fusion "ash from the plasma" gets embedded in the material lattice taking to the formation of nano-sized bubbles.
Such an environment leads to a limited choice of chemical elements for the structural materials. Namely, due to reasons related to the radioactive decay and activation, the choice of the structural material is restricted to martensitic steels with limited possibilities of variation respect to the reference composition of 9% Cr, 1% W. It results that only a specific category of martensitic steels are eligible for the employment as structural

materials for a fusion reactor; the Reduced Activation Ferritic Martensitic (RAFM) steels. More specifically Nichel must be excluded due to its high γ emission and swelling tendency under the fusion high energy (14 MeV) neutron spectrum and then any kind of austenitic steel has to be avoided. As reported in the following figure (fig. 1.2.1) just the elements highlighted in green can be taken into account. The consequence is that in these steels the Mo is replaced by Tungsten as solid solution hardener and Ti and Nb are replaced by V and Ta as carbide forming elements.

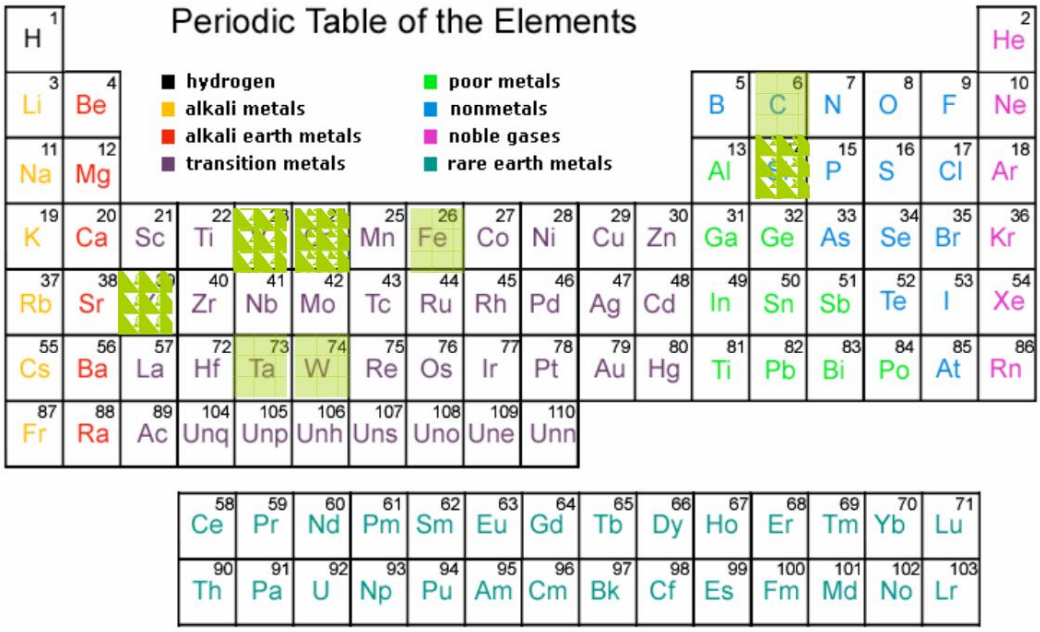

Fig. 1.2.1 Periodic Table with the elements allowed with the Fusion neutron spectrum highlighted in green

RAFM steels are being widely developed in Europe, Japan, Russia, China, the USA and India. Specifically, F82H (7,5% Cr, 2% W) is being developed by the Japan Atomic Energy Agency (JAEA), JLF-1 by Japanese universities and the National Institute for Fusion Science (NIFS), Eurofer97 (9% Cr, 1% W) is being developed in Europe within the framework of the European Fusion Development Agreement (former EFDA, currently Eurofusion) program and Fusion for Energy (F4E) program, China low activation martensitic (CLAM) steel is being developed by the Institute of Nuclear Energy Safety Technology (INEST), Chinese Academy of Sciences (CAS) and 9Cr-2WVTa (9% Cr, 2% W, 0.1% Ta) is being developed by Oak Ridge National Laboratory (ORNL). Some comprehensive reviews and comparisons among these steels concerning the mechanical properties are reported in [4,5].

The main component for which the RAFM steels are meant to be employed is the "Breeding Blanket"; it is a whole set of curved sheet metals, breeder material and pipes welded together (fig. 1.2.2) aimed at a threefold purpose;

- As it directly contains and faces the plasma it must ensure the protection of the structural components of the Tokamak Vacuum Vessel from the extremely high temperatures generated by the plasma gases, even if confined by the magnetic fields. It is just for this reason that the materials meant to be employed for the "first wall", namely the wall of the Blanket directly facing the plasma, are the high thermal energy absorbing ones, like Tungsten.
- Transform the thermal energy into vapour, to be then conveyed to the turbine for electricity production. The water contained in the pressurized tubes is used as coolant to remove the heat generated in the breeder material (Lead-Lithium) and in the structural steels.
- Ensure the self-sustenance of the fusion reactor by transforming Lithium into Tritium.

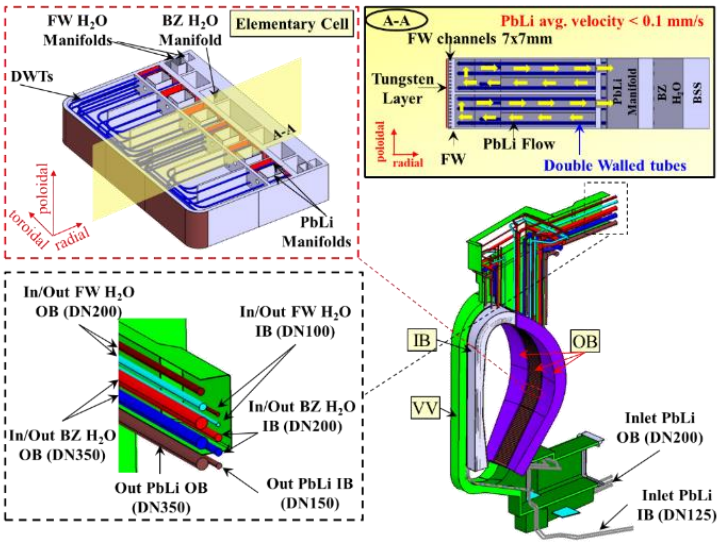

Fig. 1.2.2. Detail of the design of the WCLL Breeding Blanket

The optimization of the chemical composition and the TMT (Thermo-mechanical treatments) for the structural materials should be done according to the blanket operating temperatures that are related to two possible working conditions; the WCLL-BB (Water Cooled Lead Lithium Breeding Blanket) or the HCLL (Helium Cooled Lead Lithium) and DCLL (Dual Cooled Lead Lithium) BB. The "water-cooling" and "helium-cooled" options implies a minimum irradiation temperature for the blanket material in the range of 280-550 °C. Therefore, in light of the under-irradiation behaviour of EUROFER, namely of the DBTT (Ductile to Brittle Transition Temperature) shift under irradiation, the target of the hereby reported activities is the development of much tougher alloys, suitable to tolerate the low irradiation temperature. Moreover, several grain size reduction strategies are under investigation on RAFM steels, both at the austenitization stage, acting on the PAGS (Prior Austenite Grain Size), and at the tempering stage, acting on the tempered martensite. The "dual coolant" solutions, on the other hand, imply an operating temperature for the blanket material in the range of 280- 650°C. Therefore, the high temperature behaviour of the proposed innovative martensitic alloys should be improved. The research activities concern the development of more creep resistant martensitic alloys, suitable to tolerate such a high operating temperature.

1.2.2 Irradiation hardening and embrittlement

It is well known that the martensitic steels are characterized by a Ductile to Brittle Transition Temperature (DBTT) at a cryogenic temperature, usually in the range of -50/-80 °C. Under neutron irradiation, due to displacement cascade phenomena, the martensitic steel is subjected to a shift in the DBTT which can dangerously increase up to the operational temperature. In the following figure (fig. 1.2.3a, [6]) the shift in fracture toughness after irradiation is reported for different steels. This low temperature embrittlement has to be connected to a corresponding hardening (increase in yield stress; see fig. 1.2.3b[6]). The phenomenon of low temperature embrittlement is common to all the tested martensitic alloys and goes to saturation for a damage greater than 20 DPA (Fig. 1.2.3).

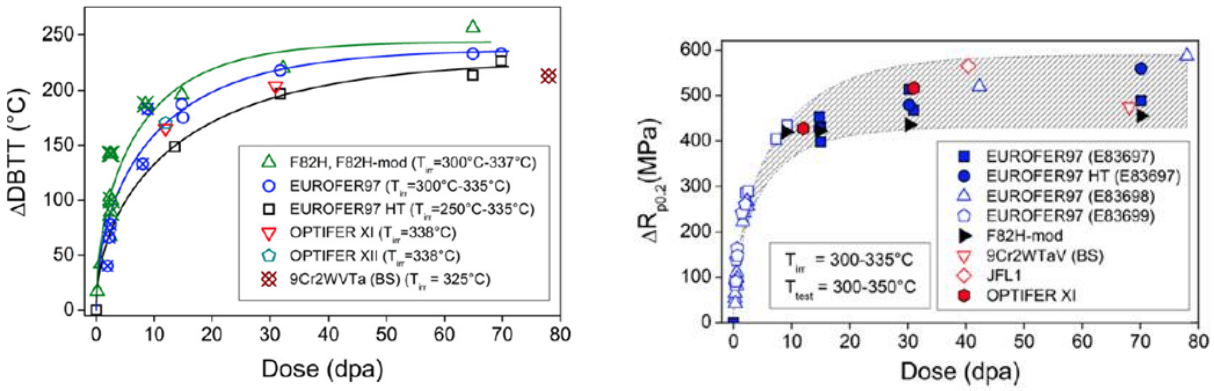

a) **b)**

Fig.1.2.3 a) Irradiation shift of the DBTT vs dose for Eurofer97 and other RAFM steels [6]; **b)Irradiation hardening vs. irradiation dose for Eurofer97 and other RAFM steels for Tirr = 300-335°C and Ttest = 300-350°C** [6]

1.2.3 Helium embrittlement

In the next graph (fig. 1.2.4, [7]) the effect of irradiation through a spallation source on several steels is reported. The embrittlement due to He generation appears even more detrimental than the one deriving from hardening, interstitial loops and displacement cascade phenomena as long as it doesn't seem to reach a saturation at the increasing dose. The trend of the DBTT shift reported in fig. 1.2.4 demonstrates how the DBTT shift increase due to Helium generation is "saturation-less" as function of the dose for the martensitic steels.

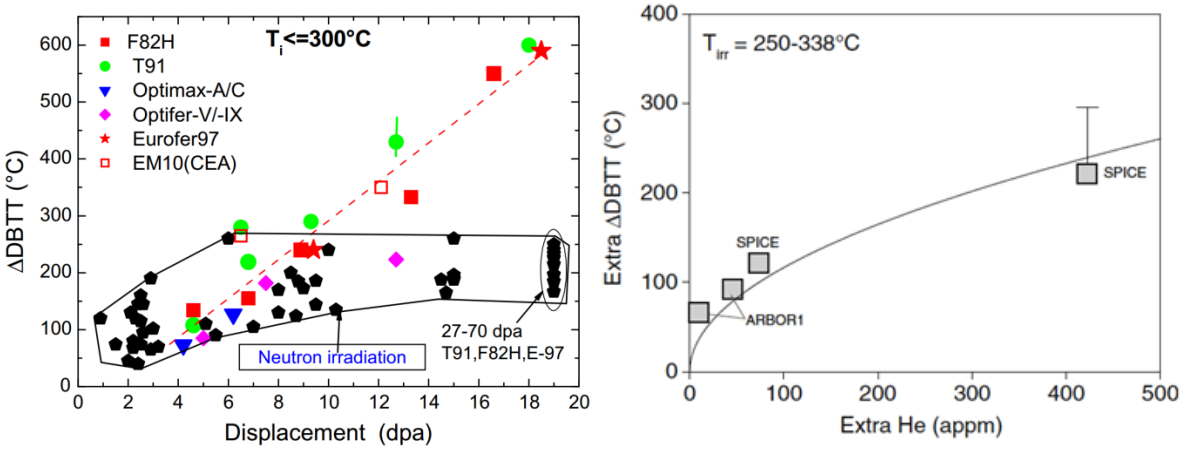

a) **b)**

Fig.1.2.4 a) Effect of the spallation source (coloured points) on the DBTT shift with respect to neutron irradiation (black points) [7] b)Helium induced extra embrittlement vs. extra helium amount for irradiated boron doped steels [8]

The other graph (fig. 4b [8]), on the other hand, shows the effect on the DBTT shift obtained by doping the steel with Boron. The material has been irradiated in a temperature range between 250 and 338 °C up to an irradiation damage of 32.3dpa. Extra Δ DBTT, on the vertical axis, means the "surplus", in terms of Δ DBTT, generated by B addition; namely DBTT shift in boron doped heat after subtraction the corresponding DBTT shift in reference EUROFER97;

$$\Delta\,\mathrm{DBTT} = \Delta\,\mathrm{DBTT}_{\mathrm{Eurofer+B}} - \Delta\,\mathrm{DBTT}_{\mathrm{Eurofer.}}$$

Extra helium, on horizontal axis, means helium amount produced in boron doped heat after subtraction of helium amount produced in Eurofer 97. The line is a $A\sqrt{p_{He}}$ type least square fitting to the data, with A as fitting parameter. Helium amount pHe produced in boron doped steels is a measure for volume fraction of

the helium bubbles, i.e. pHe proportional to $N_{He} * d_{He}^3$ with N_{He} being the bubble number density and dHe the bubble average diameter.
The shift in DBTT created by irradiation could be almost partially recovered through an annealing treatment at 550-600°C, as can be observed in the next graphs, reporting the effective recovery obtained on the 70 dpa neutrons irradiated alloys (the first, fig. 1.2.5a [6]) and the slightly less efficient one obtained on the steels irradiated in PSI by the spallation source STIP (the second, fig. 1.2.5b [7]).

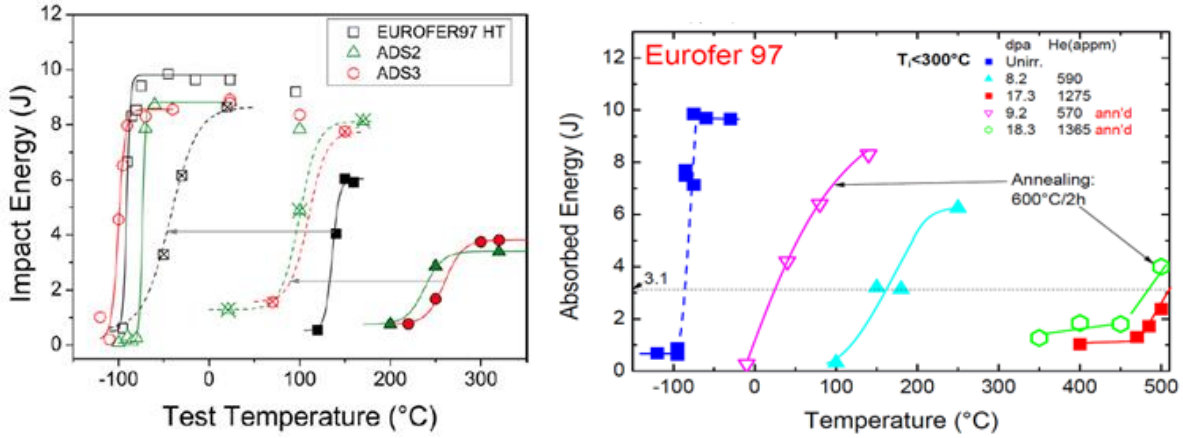

a) **b)**

Fig.1.2.5 a) Impact energy vs. test temperature for Eurofer97 HT, ADS2 and ADS3 in unirradiated (open symbols) condition, after neutron irradiation to 69.8 dpa at 332-338°C (solid symbols) and after post irradiation annealing at 550°C for 3 h (crossed symbols). The arrows indicate recovery of the impact properties after post irradiation annealing [6] **b) Charpy impact results of Eurofer 97 irradiated in STIP. The arrows indicate recovery of the impact properties after post irradiation annealing** [7]

The following microstructural observations report the effect of the irradiation on the boron doped martensitic steel (the first, fig. 1.2.6a, [9]) and the appearance of the fracture surface of the EM10 specimens irradiated at 275 °C through a spallation source (the second, fig. 1.2.6b, [10]). In the latter the irradiation damage is 18.6 dpa, with 1650 appm of He. The fracture surfaces were found to be flat and perpendicular to the specimen axis with a fully brittle appearance. The fracture mode was intergranular separation (on average, the intergranular areas made up more than 50% of the fracture surfaces) and quasi-cleavage. The percentage of intergranular areas tended to be greater at the centre of the specimens, while the amount of quasi-cleavage increased at the periphery of the fracture surfaces. The intergranular separation obviously occurred along former austenitic grain boundaries.

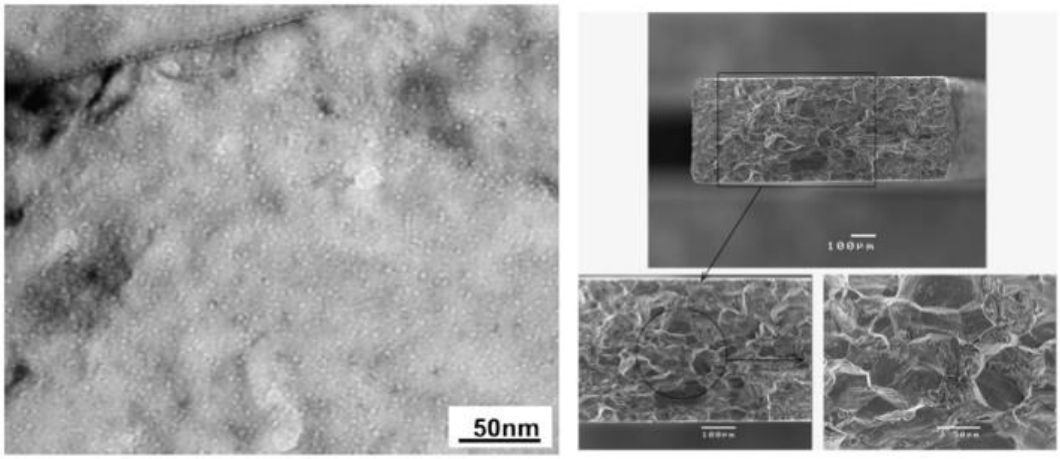

a) **b)**

Fig.1.2.6 a) TEM bright field image of the boron doped model alloy after irradiation in High Flux Reactor, Petten to 15 dpa at 250°C (approx. 432 appm He)[9] b) SEM micrographs showing the fracture surface of EM10 specimen G1 ("S"type) irradiated to 18,6 dpa and tested at room temperature [10]

1.2.4 Worldwide Development of RAFM steels

1.2.4.1 Development of RAFM steels in Europe (from Optifer to Eurofer)

A series of low activating steels (OPTIFER-Ia, Ib, II, III and IV) has been developed in Europe in the 90's as materials for the first wall and blanket structures of a future fusion device [11]. The steels have been characterized by metallurgical examinations and by tests of the mechanical properties using tensile, impact bending and creep rupture tests. This series of new 9-10% CrWVTa alloys, called OPTIFER alloys, were specified by Forschungs-zentrum Karlsruhe and produced in collaboration with the Saarstahl GmbH. Based on calculations of the neutron-induced activation and other radiological properties, the main alloying elements Mo and Nb were substituted by W and Ta with a similar metallurgical function and Ni was totally eliminated. The compositions of these OPTIFER alloys are reported in the next table (tab. 1.2.2).

Steel-grade	CETA	OP.-Ia	OP.-Ib	OP.-II	OP.-III	OP.-IV
Heat	C858	664	667	668	666	986489
Cr	9.6	9.3	9.5	9.5	9.4	8.5
W	0.81	0.96	0.97	0.01	0.02	1.2
Mn	1.35	0.50	0.49	0.49	0.49	0.6
V	0.59	0.26	0.23	0.28	0.25	0.23
Ta	0.48	0.07	0.16	0.02	1.6	0.1
C	0.17	0.11	0.12	0.13	0.13	0.10
N	0.015	0.016	0.006	0.016	0.017	0.06
B	0.008	0.006	0.007	0.006	0.007	0.004
Others	0.13 Ce [a]	[a]	0.04 Ce	1.15 Ge [a]	[a]	[a]

[a] Deoxidation with Cer; OP. = OPTIFER

Tab. 1.2.2 Chemical composition of the steels OPTIFER I-IV in weight percent [11]

In order to allow a comparison to be made among the various OPTIFER melts, all heats were subjected to the same, almost optimum heat treatment, namely at T (Austenitization) = 900 °C, 0.5 h + T(Annealing) = 730 °C, 2 h. The next graph (Fig. 1.2.7) shows the temperature dependence of the impact energy of all OPTIFER heats subjected to the heat treatment above.

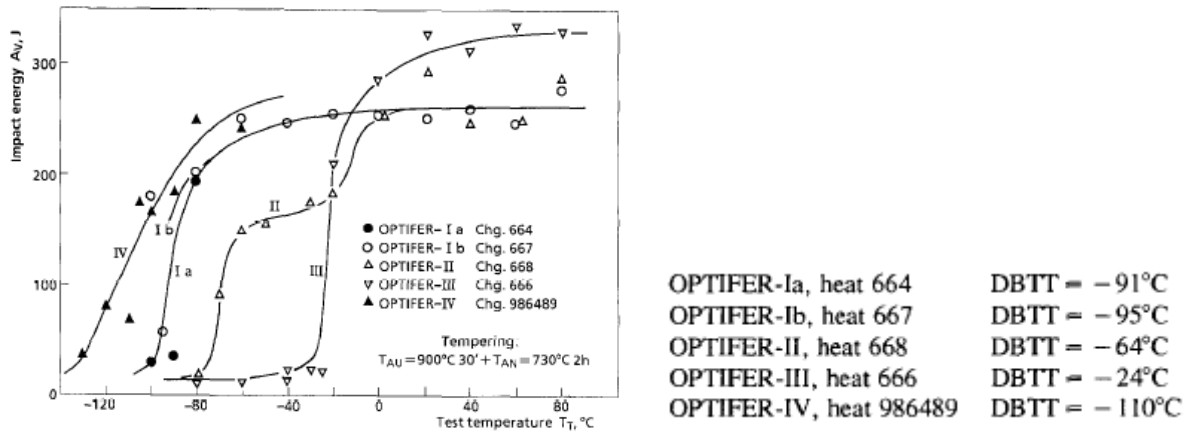

Fig. 1.2.7 Charpy impact bending energy of the OPTIFER-grade steels in dependence of the test temperature [11]

This comparison of the OPTIFER steels concerning their notch impact toughness (DBTT) made evident that with the OPTIFER-IV steel and OPTIFER-Ia steel two excellent steels were available, one of them slightly tougher (OPTIFER-IV) and the other exhibiting more high-temperature 0.2% yield strength (OPTIFER-Ia). The elevated high-temperature strength of steel OPTIFER-Ia was also noticeable from the creep-rupture

tests. It is shown that using different thermal treatment (austenitizing and annealing temperatures) the toughness and the strength of this steels can be varied in a wide range, and low austenitizing temperatures (950°C) are generally preferable (tab. 1.2.3, [12]).

	Heat treatment	Grain size (μm)	USE (J)	DBTT (°C)	Dynamic yield stress at 26 °C (MPa)
OPTIFER-Ia*	1075 °C/0.5 h + 780 °C/2 h	50	10.1	−80	543
OPTIFER-Ia	900 °C/0.5 h + 780 °C/2 h	10	10.6	−85	500
OPTIFER-V*	1040 °C/0.5 h + 750 °C/2 h	50	9.5	−80	605
OPTIFER-V	950 °C/0.5 h + 780 °C/2 h	12	9.7	−100	592
OPTIFER-II*	950 °C/0.5 h + 780 °C/2 h	55	9.2	−70	495
OPTIFER-II	900 °C/0.5 h + 780° C/2h	–	9.7[a]	−75[a]	470
OPTIFER-VI*	1040 °C/0.5 h + 750 °C/2 h	35	9.7	−56	578
OPTIFER-VI	950 °C/0.5 h + 780 °C/2 h	10	9.1	−70	540
OPTIFER-IV	900 °C/0.5 h + 750 °C/2 h	10	9.3[a]	−80[a]	519
F82H	1040 °C/0.5 h + 750 °C/2 h	35	10.7	−70	550
F82H mod.	1040 °C/0.6 h + 750 °C/1 h	55	9.8	−40	555
ORNL 3971	1050 °C/0.5 h + 750 °C/1 h	25	9.2	−80	599

[a] Values estimated from 10 × 10 mm Charpy-V results.

Tab. 1.2.3 Heat treatments and selected properties of unirradiated materials [12]

These steels have been irradiated up to 2.4 dpa in the Petten high flux reactor (HFR) [12]; their embrittlement behaviour was investigated by instrumented Charpy-V tests with subsize specimens. The aim of this mid-dose range programme was a comparison of low-activation alloys subjected to different heat treatments and with reduced B contents (down to 2 wt ppm). In the present work [12], the results of the different OPTIFER alloys (Ia, II, IV, V, VI), as obtained in the HFR-irradiation programme (2.4 dpa, at 250–450°C), are reported (fig. 1.2.8).

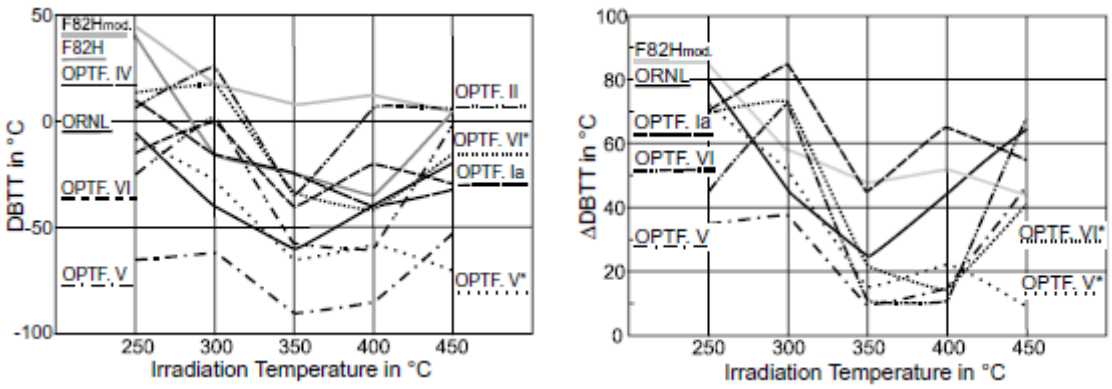

Fig. 1.2.8 DBTT vs irradiation temperature (left), irradiation-induced shifts of ductile-to-brittle transition temperature vs. irradiation temperature (right) [12]

Though the low neutron flux of this irradiation experiment didn't permit to draw any general conclusions, it can be stated that all examined low activation materials with reduced boron contents provided significantly better impact properties than the corresponding alloys with higher boron contents. Especially the results of the OPTIFER-V steel appeared very promising.
These and other results of the European effort to define a Reduced Activation Ferritic Martensitic steel (RAFM) brought to define the EUROFER97 steel [13]. The batch taken into account in the frame of this PhD (EUROFER97/2) was fabricated in a sufficiently high amount, by Saarschmiede. The chemical composition of EUROFER 97/2 is reported in the following table (tab. 1.2.4).

Table 1.2.4. Chemical composition of EUROFER 97 [13]

Heat	Producer	Chemical composition (Wt %)						
		Cr	C	Mn	V	W	Ta	N
Eurofer 97	Bohler	8.91	0.12	0.48	0.2	1.08	0.14	0.02
Eurofer 97/2	Saarschmiede	8.95	0.11	0.5	0.2	1	0.12	0.02

1.2.4.2 Development of RAFM steels in Japan (F82H and JLF)

Meanwhile, in Japan, two steels have been developed by JAEA; F82h and JLF1. The main differences between these steels are the Cr, Ta and N concentrations and heat treatment conditions as shown in Table 1.2.5 in which the composition of the Mod. JLF-1 is also shown.

	C	Si	Mn	P	S	Cr	W	V	Ta	Ti	B	N
F82H	0.093	0.09	0.21	0.004	0.0014	7.46	1.96	0.15	0.023	–	–	0.006
JLF-1	0.097	0.05	0.46	0.002	0.0020	9.04	1.97	0.19	0.073	0.001	–	0.05
Mod.JLF-1	0.10	0.042	0.53	0.002	0.0014	9.03	2.06	0.26	0.051	0.021	0.0032	0.10

F82H: normalized at 1040 °C for 30 min and then tempered at 750 °C for 1 h, AC; JLF-1: normalized at 1050 °C for 30 min and then tempered at 775 °C for 1 h, AC; Mod. JLF-1: normalized at 1050 °C for 30 min and then tempered at 760 °C for 1 h, AC.

Tab. 1.2.5 Chemical compositions and heat treatment conditions of F82h and JLF-1 [14]

The following graph (fig. 1.2.9a) reports the dependence of ΔDBTT and ΔYield Strength on the irradiation temperature in F82H and JLF-1 [14]. The fracture toughness measurement after HFIR irradiation at 300 °C to 5 dpa revealed that a much larger ductile brittle transition temperature (DBTT) shift was observed for F82H than for JLF-1. The DBTT shift of F82H is twice that of JLF-1 at all the tested irradiation temperatures, while the irradiation hardening of the steels is not significantly different, although the hardening of JLF-1 appears to be a little bit smaller than that of F82H.

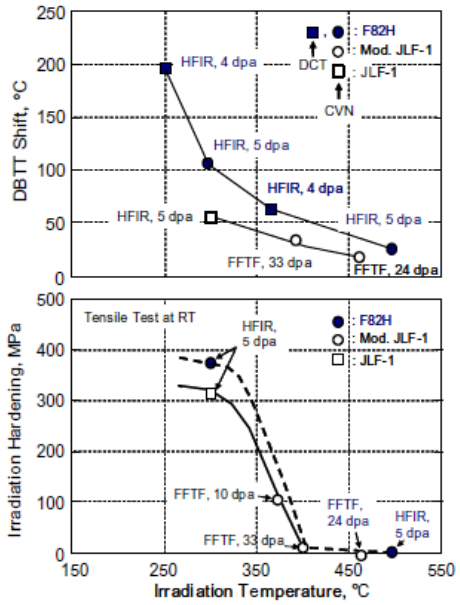

HFIR irradiation, 300 °C, 5 dpa	F82H	JLF-1
Irradiation hardening (RT)	370 MPa	314 MPa
DBTT before irradiation	215 K	190 K
Shift in DBTT	110 K	40 K
Loop density	6.64E + 23/m^3	5.91E + 23/m^3
Loop size (average)	3.5 nm	3.6 nm
Estimated from dispersed barrier model	310 MPa	300 MPa
Precipitates (extrusion residue) a measure of large precipitates	Total amount increased	Total amount decreased
Precipitates (TEM), a measure of precipitation location	Fraction of prec. Increased at block and PAG boundaries	Small $M_{23}C_6$, small MX in matrix
Main factor controlling hardening	Loops	Loops
Main factor controlling DBTT shift	Hardness and carbides	Hardness

Fig. 1.2.9 a) The dependence of Δ DBTT and Δ Yield Strength on the irradiation temperature in F82H and JLF-1 [14] **b) Summary of the results obtained for F82H and JLF-1** [14]

Since carbides may be the nucleation sites for brittle cleavage fracture that determines DBTT, the difference in their irradiation-induced precipitation behaviour was investigated for F82H and JLF-1 steels to understand the difference in the DBTT shift among the steels. The structures and chemical compositions of the extracted precipitate residues from the steels were investigated.
The main results obtained suggested that in JLF-1 steel, large MX (TaC) carbides disappeared during irradiation, while they were observed in F82H [15]. A TEM observation revealed that the volume fraction of the M23C6 that precipitated along lath block and packet boundaries to the total volume of the M23C6 was twice as large for F82H than JLF-1. It is expected that the fracture stress along lath block and packet boundaries is reduced by the precipitation of M23C6 carbides.
The larger DBTT shift observed in F82H is interpreted in terms of both the matrix hardening mechanism and reduction of cleavage fracture stress along lath block and packet boundaries, while that of JLF-1 is due to only the hardening effect. The reduction of lath block and packet boundary fracture stress is considered to be consistent with M23C6 carbide precipitation. The experimental results are summarized in Table reported in fig. 7b along with the mechanisms of irradiation hardening and embrittlement.
Each of the alloys we have dealt with up to this point of the survey appears as relentlessly affected by highly detrimental hardening and embrittlement after irradiation at temperatures lower than 380°C.

1.2.4.3 Development of RAFM steels in the USA; the Oakridge National Laboratories (ORNL) steels (Klueh, [15-18])

In the following several papers by R.L. Klueh and oth., published on the Journal of Nuclear Materials, will be taken into account. In the first [16] miniature tensile and Charpy specimens of four ferritic/martensitic steels were irradiated at 300°C and 400°C in the high flux isotope reactor (HFIR) to a maximum dose of 12 dpa. The steels were standard F82H (F82H-Std), a modified F82H (F82H-Mod), ORNL 9Cr±2WVTa, and 9Cr±2WVTa±2Ni, the 9Cr±2WVTa containing 2% Ni to produce helium by (n,a) reactions with thermal neutrons. More helium was produced in the F82H-Std than the F82HMod because of the presence of boron. Irradiation embrittlement in the form of an increase in the ductile-brittle transition temperature (ΔDBTT) and a decrease in the upper-shelf energy (USE) occurred for all the steels. The results of the mechanical tests after irradiation are reported in the following tables (tab. 1.2.6, 1.2.7). Irradiation of the two F82H steels at 300°C produced similar relatively large increases in DBTT (>150°C). After irradiation of the four steels at 400°C, the 9Cr-2WVTa developed the smallest shift in DBTT (79°C), followed by the F82HStd (117°C), the 9Cr-2WVTa-2Ni (133°C) and the F82H-Mod (146°C).

Steel	Temperature (°C)	Irradiation		Strength (MPa)		Elongation (%)	
		dpa	appm He	Yield	Tensile	Uniform	Total
F82H-Std	300			522	603	3.0	12.0
(8Cr–2WVTaB)	300	9	39	822	832	0.2	6.7
	400			464	532	2.8	11.6
	400	12	41	646	677	0.9	7.2
F82H-Mod	300			438	498	0.5	3.2
(8Cr–2WVTa)	300	5	2	765[a]	777	0.5	6.1
	400					0.8	3.5
	400					0.9	5.0
9Cr–2WVTa	400			715	817	1.6	4.5
	400	11	5	963	983	0.6	5.8
9Cr–2WVTa–2Ni	400			733	824	1.6	4.3
	400	11	114	1034	1075	0.6	5.7

[a] Data taken from another HFIR irradiation experiment.

Tab. 1.2.6 Tensile results for reduced activation Cr-W steels [16]

Steel	Irradiation temperature (°C)	Irradiation		DBTT (°C)	ΔDBTT (°C)	USE (J)
		dpa	appm He			
F82H-Std	Unirradiated			−103		12.3
(8Cr–2WVTaB)	300	10	40	56	159	7.9
	400	12	41	14	117	9.7
F82H-Mod	Unirradiated			−82		10.8
(8Cr–2WVTa)	300	9	4	70	152	8.3
	400	11	4	64	146	8.3
9Cr–2WVTa	Unirradiated			−94		10.8
	400	11	5	−15	79	6.5
9Cr–2WVTa–2Ni	Unirradiated			−113		10.8
	400	11	115	21	133	n/m

Tab. 1.2.7 Charpy impact properties of reduced activation Cr-W steels [16]

The following figure (fig. 1.2.10, [4]) demonstrates how, among the different steels taken into account, the best behaviour is the one performed by 9Cr-2WVTa steel produced by ORNL.

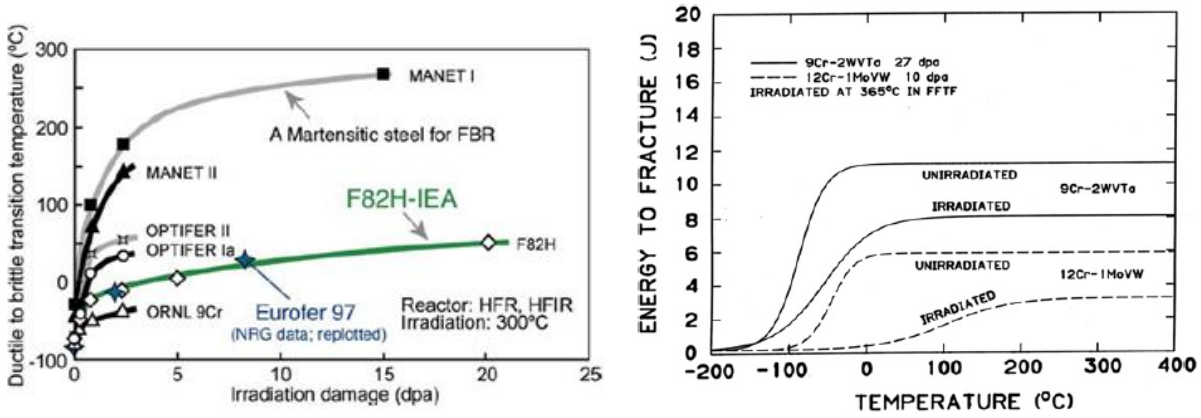

Fig.1.2.10 a) Damage level dependence of the ductile-to-brittle transition temperature after irradiation at temperatures between 300 and 400°C [4]; b) Impact behaviour of ORNL 9Cr2WVTa austenitized at 1050°Cx1h and tempered at 750°C x 1 h compared to Sandvik HT9 (12Cr–1MoVW) [17]

Therefore, let's take into account this 9Cr2WVTa steel, developed by ORNL. Its composition is reported in table 1.2.8 [18] and behaviour under irradiation in fig. 14b.

Tab. 1.2.8 Chemical composition of 9Cr2WVTa [18]

Steel	*C*	*Si*	*Mn*	*Cr*	*Ni*	*Mo*	*W*	*V*	*Nb*	*B*	*N*	*Other*
ORNL 9Cr-2WVTa	0.10	0.30	0.40	9.0			2.0	0.25			0.025	0.07 Ta

Reduced-activation Cr-W steels with chromium concentrations varying from 2.25 to 12 wt% were irradiated at 365°C to 7 dpa in the Fast Flux Test Facility [16]. In the following table (tab. 1.2.9) a list of the examined compositions is reported.

Element	Chemical composition [a] (wt%)							
	2¼Cr–¼V Heat 3785	2¼Cr–1W–¼V Heat 3786	2¼Cr–2W Heat 3787	2¼Cr–2W–¼V Heat 3788	5Cr–2W–¼V Heat 3789	9Cr–2W–¼V Heat 3790	9Cr–2W–¼V–Ta Heat 3791	12Cr–2W–¼V Heat 3792
C	0.11	0.10	0.11	0.11	0.13	0.12	0.10	0.10
Mn	0.40	0.34	0.39	0.42	0.47	0.51	0.43	0.46
P	0.015	0.015	0.016	0.016	0.015	0.014	0.015	0.014
S	0.006	0.006	0.005	0.006	0.005	0.005	0.005	0.005
Si	0.17	0.13	0.15	0.20	0.25	0.25	0.23	0.24
Ni	0.01	0.01	< 0.01	< 0.01				
Cr	2.36	2.30	2.48	2.42	5.00	8.73	8.72	11.49
Mo	0.01	< 0.01	< 0.01					
V	0.25	0.25	0.009	0.24	0.25	0.24	0.23	0.23
Nb	< 0.01	< 0.01	< 0.01					
Ta	< 0.01	< 0.01	< 0.01				0.075	
Ti	< 0.01	< 0.01	< 0.01					
Co	0.005	0.006	0.008					
Cu	0.02	0.025	0.03					
Al	0.02	0.02	0.02	0.021	0.03	0.03	0.03	0.028
B	< 0.001	< 0.001	0.001					
W		0.93	1.99	1.98	2.07	2.09	2.09	2.12

[a] Balance iron.

Tab. 1.2.9 Compositions of experimented ferritic steels [16]

In the following graphs (fig. 1.2.11, 1.2.12) the effect of the irradiations up to 7 dpa at 365 °C of the highlighted different compositions of martensitic steels is reported.

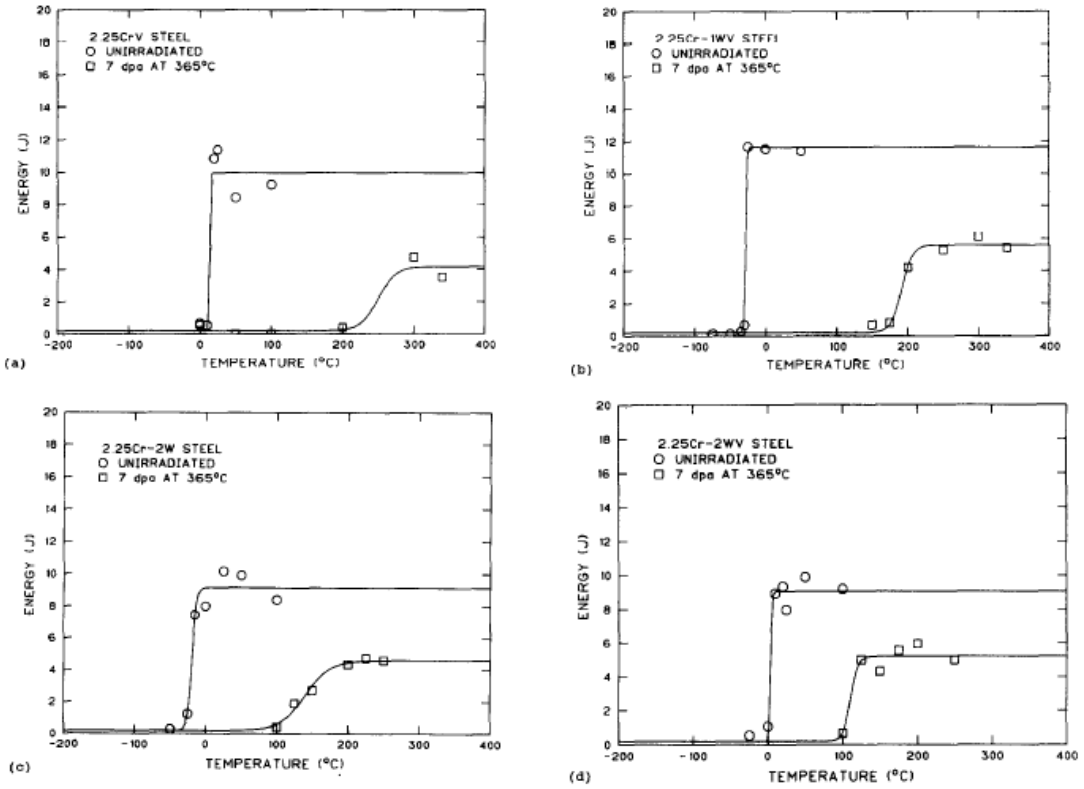

Fig. 1.2.11 Charpy impact curves of the normalized-and-tempered steel and for the steel after it was irradiated to 7 dpa at 365°C for (a) 2.25 CrV, (b) 2.25Cr-1WV, (c) 2.25Cr-2W, and (d) 2.25Cr-2WV steels [16]

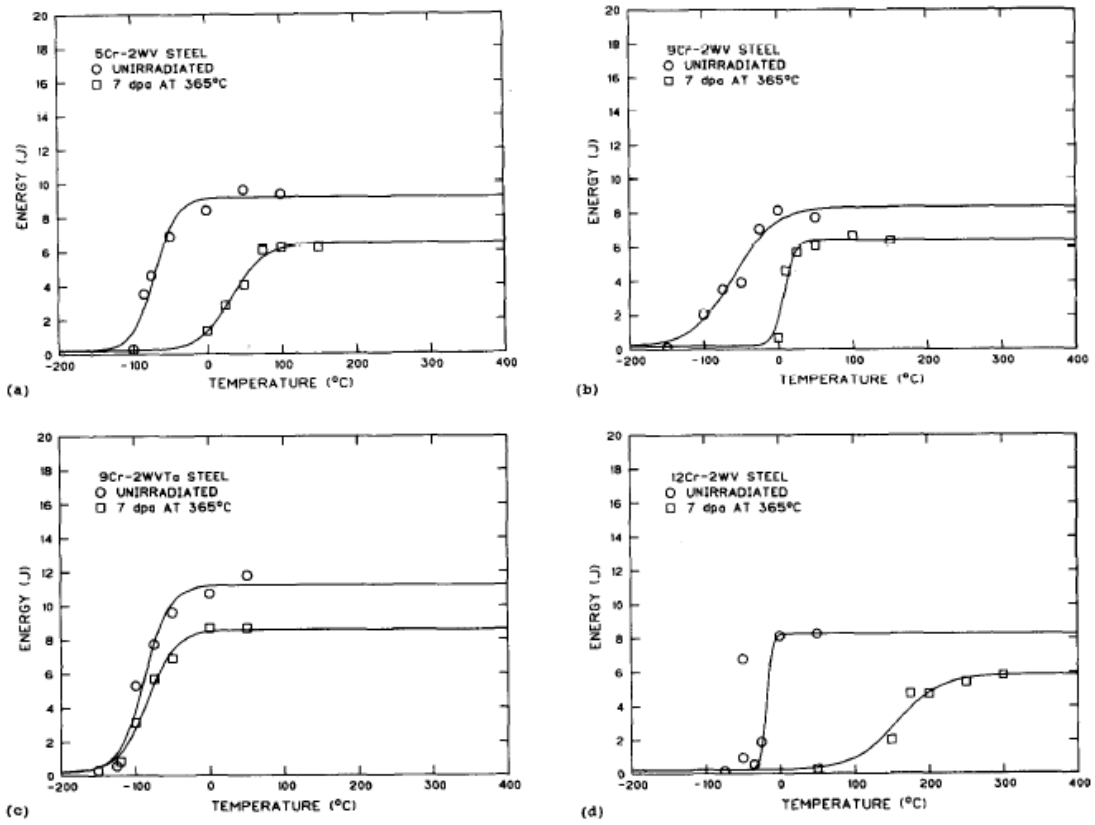

Fig. 1.2.12 Charpy impact curves of the normalized-and-tempered steel and for the steel after it was irradiated to = 7 dpa at 365°C for (a) 5Cr-2WV, (b) 9Cr-2WV, (c) 9Cr-2WVTa, and (d) 12Cr-2WV steels [16]

Irradiation caused a loss of toughness for all steels, as measured in Charpy impact tests; increases in the ductile-brittle transition temperature (DBTT) and decreases in the upper-shelf energy were observed after irradiation. Two steels with 9% Cr showed the greatest resistance to the effects of irradiation: the DBTT of a 9% Cr steel with 2% W and 0.25% V increased by 68°C during irradiation; this same composition with an addition of 0.07% Ta developed an increase in DBTT of only 4°C. These shifts in DBTT appear very successful, if compared to increases of over 100°C for the rest of the steels. Observations on the steels with 2.25% Cr indicated that a steel containing a combination of 2% W and 0.25% V was less severely affected by irradiation than steels with vanadium and no tungsten, tungsten and no vanadium, or with 1% W and 0.25% V. From observations on the 2.25 CrV, 2.25Cr-1WV, 2.25Cr-2W, and 2.25Cr-2WV, it was concluded that vanadium may exacerbate the shift in the absence of 2% W. These conclusions were complicated by differences in the overall microstructure (amount of tempered bainite and polygonal ferrite) of the steels and differences in tempering conditions. The results are summarized in the following table (tab. 1.2.10).

Alloy designation	Specimen condition [a]	DBTT (°C) [b]	ΔDBTT (°C)	Uppershelf energy (J)	ΔUSE (%) [c]	$\Delta\sigma_y$ (MPa) [d]
2¼CrV	N&T	14		10		
	I	250	236	4.2	58	301
2¼Cr–1WV	N&T	−28		11.8		
	I	192	220	5.6	53	282
2¼Cr–2W	N&T	−19		9.2		
	I	140	159	4.6	50	262
2¼Cr–2WV	N&T	4		9.1		
	I	111	107	5.2	43	183
5Cr–2WV	N&T	−70		9.2		
	I	33	103	6.5	29	192
9Cr–2WV	N&T	−60		8.4		
	I	8	68	6.4	24	161
9Cr–2WVTa	N&T	−88		11.2		
	I	−84	4	8.6	23	125
12Cr–2WV	N&T	−18		8.3		
	I	156	174	5.9	29	335

[a] N&T – normalized and tempered; I – irradiated in N&T condition.
[b] Evaluated at an energy level halfway between the upper and lower shelves.
[c] Percent change in upper-shelf energy; note that the change is a decrease.
[d] Increase in yield stress caused by irradiation calculated from data given in ref. [6].

Tab. 1.2.10 Impact properties of Cr-W steels irradiated in FFTF at 365°C [16]

From optical observations, the 9Cr-2WV, and 9Cr-2WVTa steels were 100% tempered martensite. However, the 12Cr-2WV steel contained approximately 25% delta-ferrite, with the balance being tempered martensite. The only major difference observed by optical microscopy in the tempered martensite of these latter three steels was that the 9Cr-2WVTa steel had a much finer prior austenite grain size than the other three steels [16]. For the high chromium steels, the 12Cr-2WV steel showed the largest change in properties. The 9Cr steels showed the least change, with the 9Cr-2WVTa showing only a 4°C increase in DBTT, indicating that Tantalum had a favorable effect on the properties. These results are encouraging in that they indicate that the effect of irradiation on toughness can be favorably affected by changing the composition.

1.2.5 Effects of thermal treatments on the irradiation embrittlement

Several alloys have been irradiated up to 16.3 dpa [19]. Plotting the DBTT shift as function of the irradiation temperature, the following graph is obtained (fig. 1.2.13 [19]). We can notice how the best behavior under irradiation (the minimum DBTT shift) is obtained with Eurofer WB.
The embrittlement behaviour of F82H-mod at Tirr = 300 °C is somewhat worse than that of EUROFER97 ANL, showing large scatter in the impact energy. At Tirr = 400 °C the embrittlement of EUROFER97 is lower than that of OPTIFER-Ia and F82H-mod, though the DBTTs of these materials remain below 30 °C.

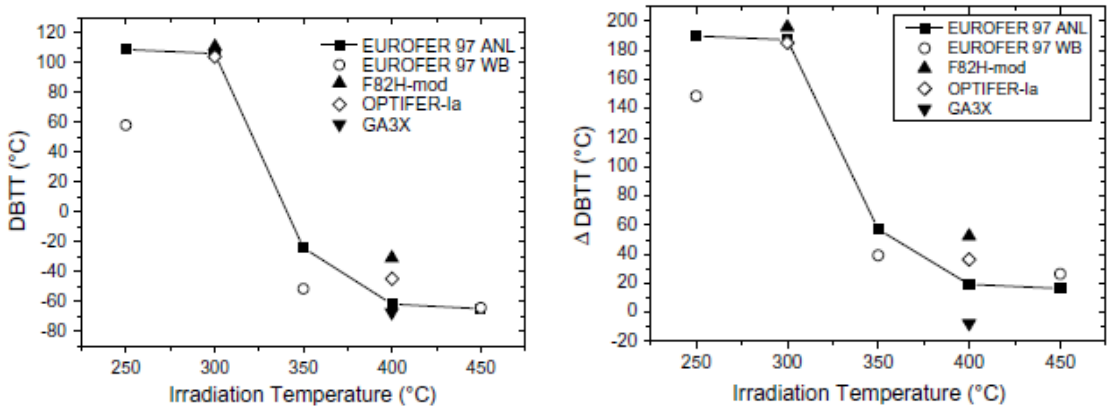

Fig.1.2.13 DBTT shift as a function of test temperature [19]

Table 1.2.11 reports the thermal treatments and the resulting DBTT of several unirradiated alloys, including Eurofer ANL and WB, taken into account in the previous graph [19].

	Heat treatment	Grain size (μm)	USE (J)	DBTT (°C)	Dynamic yield stress (MPa)
EUROFER97 ANL	980 °C/0.5 h + 760 °C/1.5 h	16 [5]	9.84	−81	543 @100 °C
EUROFER97 WB	1040 °C/0.5 h + 760 °C/1.5 h	21.4 [5]	9.84	−91	486 @100 °C
GA3X	1000 °C/1 h + 700 °C/2h	55 ± 5	9.4	−58	650 @100 °C
F82H-mod	950 °C/0.5h + 750 °C/2h	55	9.7	−86	446 @100 °C
OPTIFER-Ia	900 °C/0.5h + 780 °C/2h	10	10.6	−81	482 @23 °C
MANET-I	980 °C/2h + 1075 °C/ 0.5h + 750 °C/2h	30 ± 5	6.6	−30	670 @100 °C

Tab. 1.2.11 Heat treatments and properties of unirradiated alloys [19]

As can be seen from the experimental data, the best behaviour, from the point of view of toughness, can be found in EUROFER 97, version WB. This alloy differs from the ANL one for the heat treatment. The ANL version, namely the standard version of EUROFER, is austenitized at 980°Cx30' and tempered at 760°Cx 1.5h, exhibiting a grain size of 16 μm, while the WB version is austenitized at 1040°C, tempered at the same temperature and time and exhibits a slightly higher grain size (21.4μm). Taking into account that the error in the calculation of DBTT could be assessed in the range of 10%, we can deduce that, despite the ANL and WB version have the same toughness behaviour before irradiation, after irradiation the alloy austenitized at a higher temperature exhibits a better behaviour. The microstructures resulting from the different heat treatments undergone by the two different variations of Eurofer (namely ANL and WB) were markedly different.

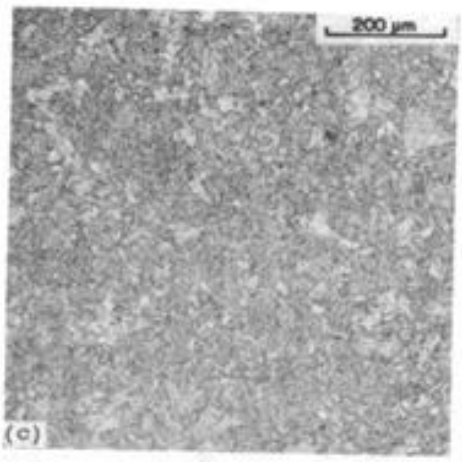

Fig. 1.2.14 Microstructure of normalized (1h, 1050°C) and tempered (1h, 750°C) 9Cr2WVTa [15]

The austenitization at the lower temperature takes to a finer grain size than the one at 1075°C. The same considerations about the better behaviour of thermally treated Eurofer WB under irradiation could be done for the ORNL 9Cr-2WV. The microstructure of this steel is reported in the previous figure (fig. 1.2.14, [15]) which reports the effect of the thermal treatments undergone by this alloy; the steel was normalized at 1050°C for 1 h, air cooled and then tempered at 750°C for 1 h. The consideration that can be drawn is that a good behavior under irradiation is obtained for sufficiently high austenitization temperature and small grain size.

Beside the grain size, also the martensite packet size is important to control the toughness; namely, as it results from some works in literature [20], the lower the martensite packet size, the better the toughness (fig. 1.2.15a [20]). A linear relation can also be found between the martensite packet size and the 50% FATT (fig. 1.2.15b[20]).

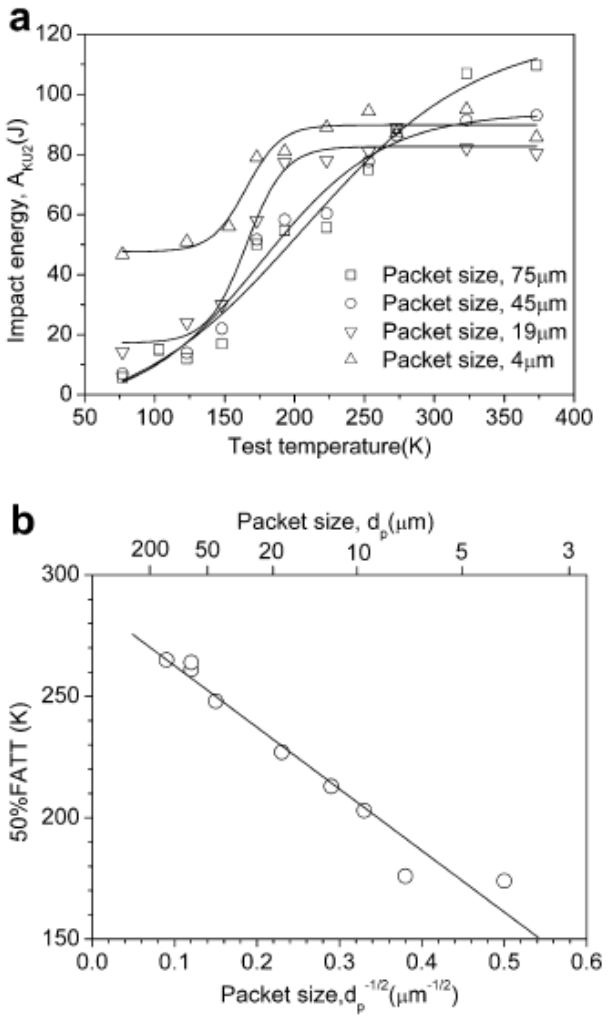

Fig. 1.2.15 (a)Variation of Charpy impact energy with test temperature in the range 77-373 K for specimens with various packet sizes and (b) 50% FATT as a function of the martensitic packet size for the steel [20]**.**

The packet size and the block width were measured by averaging about 200 packets and 120 blocks from the SEM images and orientation micrographs for each specimen, respectively. It was found that the martensitic packet size (d_p) and the block width (d_b) increased linearly with increasing prior austenite size (d_y) in the austenite grain size range studied. The following relationships between microstructural parameters d_p , d_b and d_y were obtained;

$$d_p = 0.37 d_y$$

$$d_b = 0.04 d_y$$

Further experimental results indicate that not only the grain size controls the fracture toughness but, after irradiation, it is important to have a fine primary precipitation controlling the grain size. In effect, although the normalizing treatment at 980°C, 0.5h gives a very fine grain size (about 16 μm) and the alloy exhibits the best before irradiation, after irradiation the best results are obtained from those alloys that were austenitized at higher temperature (about 1040-1050°C). When the austenitizing temperature is very low, the grain size is very fine but the volumetric fraction of primary precipitation (e,g, TaC) is high and the dimension of precipitates is relevant too. Increasing the austenitizing temperature, the volumetric fraction and mean dimension of primary precipitation decreases. So it would be important to have, at the same time, the finest

grain size and the finest primary precipitation. This effect can be obtained performing multiple austenitization treatments [20–22] at temperatures higher than the minimum austenitization temperature. To give reference of this fact the experimental work reported in [21] has been taken into account. In order to maximise fracture toughness, several normalization treatments in the temperature range 970 ± 1040°C were performed. In the following figure (fig. 1.2.16) the mean grain diameter is plotted versus the temperature of the ultimate normalization treatment for double normalized steels (BATMAN II type) as well as for the single normalized ones.

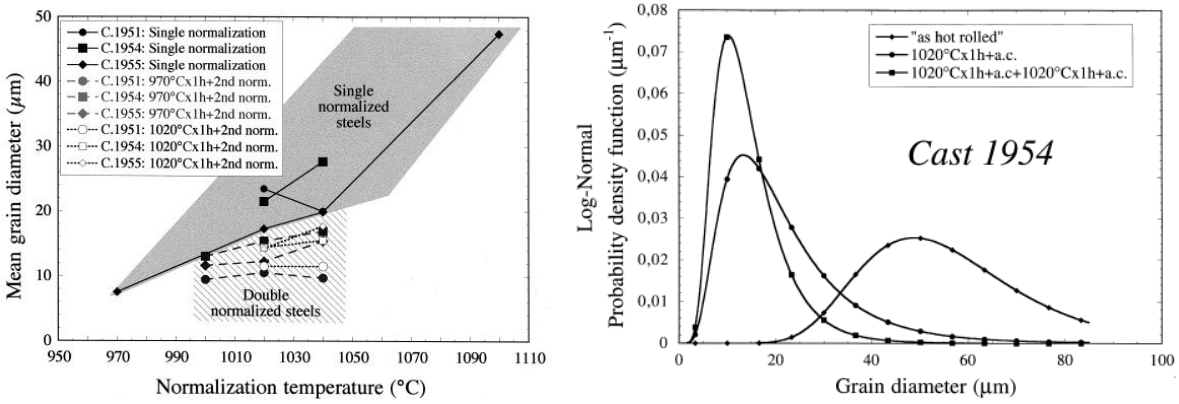

Fig. 1.2.16 Grain size as a function of normalization temperatures (Casts 1951, 1954 and 1955). Grey and white markers represent double normalized steels previously normalized respectively at 970°C and 1020°C [16] b) Fitted Grain diameter distribution function of Cast 1954 for different normalization conditions [21]

These results indicate that a second normalization before tempering is very effective as refining treatment, at least for the temperature range here investigated. The second normalization treatment does not only reduce drastically the mean grain diameter but also sharpens the grain size distribution. This behaviour is enhanced by the increase in titanium content. Moreover, the grain refinement and the sharpening of distribution function increase as normalization temperatures decrease. Within the experimental error, the second heat treatment seems to dominate these effects. The impact test results obtained from micro-Charpy specimens are reported in Fig.1.2.17 They show that normalization treatments greatly influence impact resistance while cooling rate seems to have only a minor effect (more accentuated in cast 1953). This behaviour is related to the grain size.

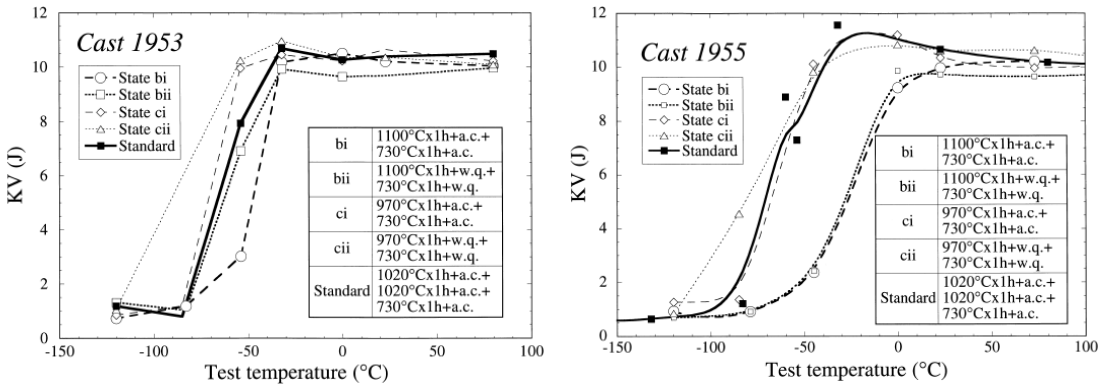

Fig. 1.2.17 Impact properties of Cast 1953 and 1955 (Batman II) for different heat treatments [21]

Prior austenite grain size control is one of the way to increase fracture toughness and to have a low ductile brittle transition temperature. Single or double normalization treatment slightly higher than AC3 greatly improves the impact resistance. In addition to this, a reduction in titanium and nitrogen contents would be sufficient to obtain at the same time a very fine structure and further decreased DBTT.
Some other references can be found in literature about the improvement of toughness properties by multiple austenitization treatments. Considering the experimental campaign carried out on the Japanese steel F82h [22] and summarized in the following table (tab. 1.2.12) we can notice the beneficial effect of the multiple austenitization on the toughness (K_{jc}) after irradiation (fig. 1.2.18). Improvement of hardening/toughness behaviour was obtained for F82H subjected to various multi-step heat treatments (including a tempering step at higher temperatures).

	Normalizing	Tempering	Heat treatment 1	Heat treatment 2	Heat treatment 3	Heat treatment 4
IEA	1040 °C × 40 min	750 °C × 1 h	–	–	–	–
Mod3	1040 °C × 0.5 h	740 °C × 1 h	–	–	–	–
Mod1-E	1040 °C × 40 min	750 °C × 1 h	1100 °C × 2 h	960 °C × 0.5 h	750 °C × 1.5 h	–
-F	1040 °C × 40 min	750 °C × 1 h	1100 °C × 2 h	960 °C × 0.5 h	700 °C × 10 h	–
-G	1040 °C × 40 min	750 °C × 1 h	1100 °C × 2 h	960 °C × 0.5 h	800 °C × 0.5 h	700 °C × 1 h
-H	1040 °C × 40 min	750 °C × 1 h	960 °C × 0.5 h	700 °C × 10 h	–	–

Tab. 1.2.12 Several combinations of heat treatments carried out on F82H [22]

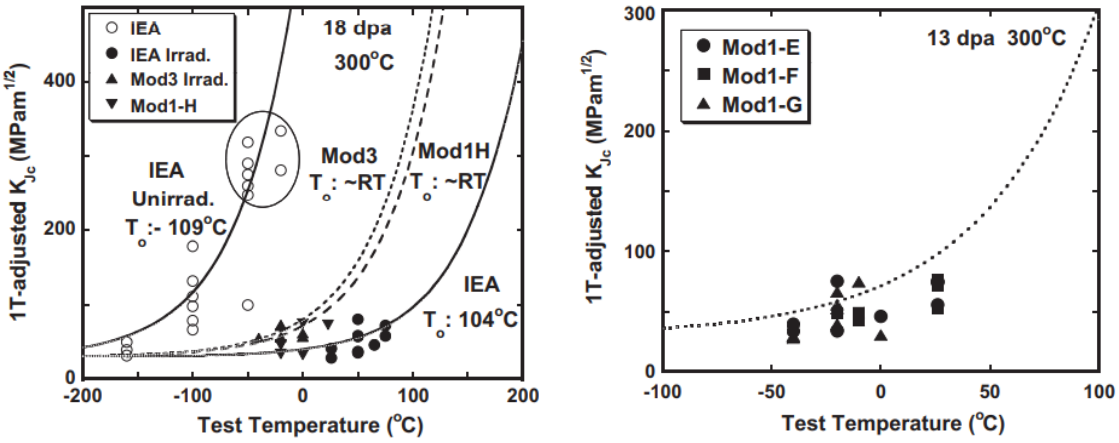

Fig. 1.2.18 Effect of the combinations of thermal treatments on the behaviour after irradiation [22]

1.2.6 Development of RAFM steels for high temperature applications

The ferritic/martensitic steels considered for fast reactors in the 1970s and for fusion reactors in the 1980s were developed by the steel industry for use in conventional power-generation systems and in the petrochemical industry [23]. Development of elevated-temperature ferritic/martensitic steels began in the 1920s with the introduction of Cr–Mo steels for conventional power-generation applications. The 2.25Cr–1Mo steel, designated by ASTM as Grade 22, was introduced in the 1940s and is still widely used today. Along with Grade 22, 9Cr–1Mo (Grade 9), an Fe–9.0Cr–1.0Mo–0.6Si–0.45Mn–0.12C composition, was an early development, the additional chromium being added for corrosion resistance. Since then, there has been a continual push for increased operating temperatures in the power-generation and petrochemical industries. Following the introduction of 2.25Cr–1Mo (T22) and 9Cr–1Mo (T9) steels, three ‘generations’ of elevated-temperature steels were introduced. The T22 and T9, termed the ‘zeroth’ generation, had 100000 h creep-rupture strengths at 600 °C of about 40 MPa with a maximum operating temperature of around 538 °C. First generation steels developed during the 1960s (e.g., HT-9 and EM-12) introduced carbide-forming elements

such as V, Nb and W. A significant increase in creep strength was achieved in going from first-generation steels to second-generation (1970-1985) compositions. This involved the addition of the strong carbide-forming element niobium and the addition of nitrogen, in order to produce more finely dispersed precipitates, thus increasing the maximum use temperature to 593 °C and increased the 105 h rupture life at 600 °C to 100 MPa from 60 MPa for the first-generation steels. Second-generation steels include modified 9Cr–1Mo. At 650 °C, the difference in creep-rupture properties of the first-generation HT9 and second-generation 9Cr–1Mo is quite large at long rupture times-low stresses [24].

Based on creep-rupture properties, which is the method used to qualify the 'generation', the reduced-activation steels could be classified as generation 1.5. This is logical, for although the reduced-activation steel compositions contain the strong carbide former tantalum, which is analogous to niobium in modified 9Cr–1Mo, the nitrogen present in second-generation steels is missing.

Generation 3 steels (1985-1995) were modifications of generation 2 obtained by substituting tungsten for some or all of the molybdenum and the addition of boron. The further improved third generation steels included NF616 (Grade 92) with 9%Cr and HCM12A (Grade 122) with 10.5–12%Cr. These steels had operating conditions dictated by the 105 h creep-rupture strengths at 600 °C of 140 MPa and maximum operating temperature about 620 °C. The generation 3 steel that shows the most promise is NF616 (T92), which like modified 9Cr–1Mo has received ASME code approval for pressure-boundary applications. In essence, NF616 is a variation of modified 9Cr–1Mo in which most of the molybdenum was replaced by tungsten and B, N, and Cu were added in order to improve creep strength. Development of the reduced-activation steels proceeded by replacing all molybdenum by tungsten, and there was no indicated negative effect of the tungsten during irradiation. Then the difference between Mod. 9Cr-1Mo and NF616 involves the presence of boron in the latter. It has been concluded that boron stabilizes M23C6, which in turn stabilizes the subgrain structure that is partly responsible for the improved creep strength of NF616.

A problem with boron in steel for nuclear applications is that natural boron contains 20% ^{10}B and 80% ^{11}B, and when irradiated, the ^{10}B undergoes an (n,a) reaction to produce helium and lithium in the steel, both of which could influence the mechanical properties. For a steel containing 0.005% natural boron, 50 appm He will form. This could be avoided by alloying with 11B instead of natural boron; ^{11}B is relatively inexpensive. With the addition of 0.003–0.005% B and 0.05% N to the best reduced-activation steel, ORNL 9Cr–2WVTa, properties should be similar to those of NF616. Alternatively, NF616 could be produced using ^{11}B instead of natural boron [24].

In the fourth generation, developed around 2000, the achievement was 105 h rupture strength at 600 °C of about 180 MPa and a maximum operating temperature of 650 °C. The 12%Cr steels NF-12 and SAVE-12 contained optimized concentrations of C, Nb, Mo, V, W and Co.

The historical development of the ferritic-martensitic steels is reported in tab. 1.2.13 and fig. 1.2.19 and the achieved improvement in creep strength is reported in fig. 1.2.20.

Generation	Years	Steel modification	10^5 h Rupture strength, 600 °C (MPa)	Steels	Max use temperature (°C)
0	1940–1960		40	T22, T9	520–538
1	1960–1970	Addition of Mo, Nb, V to simple Cr–Mo steels	60	EM12, HCM9M, HT9, HT91	565
2	1970–1985	Optimization of C, Nb,V, N	100	HCM12, T91, HCM2S	593
3	1985–1995	Partial substitution of W for Mo and add Cu, B	140	NF616, E911, HCM12A	620
4	Future	Increase W and add Co	180	NF12, SAVE12	650

Table 1.2.13. Evolution of ferritic-martensitic steels for power generation industry [24]

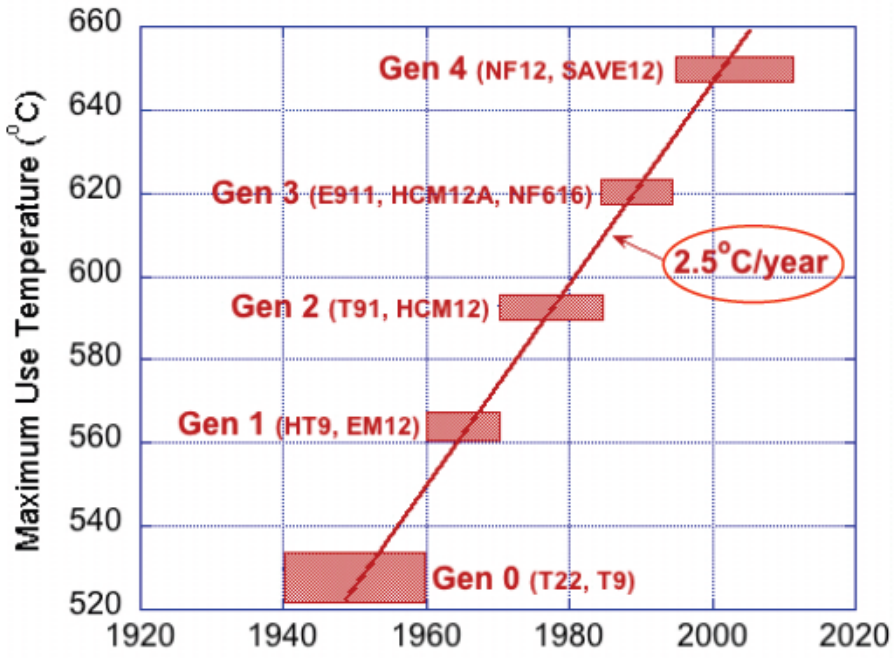

Fig. 1.2.19. Evolution of ferritic-martensitic steels for power generation industry [23]

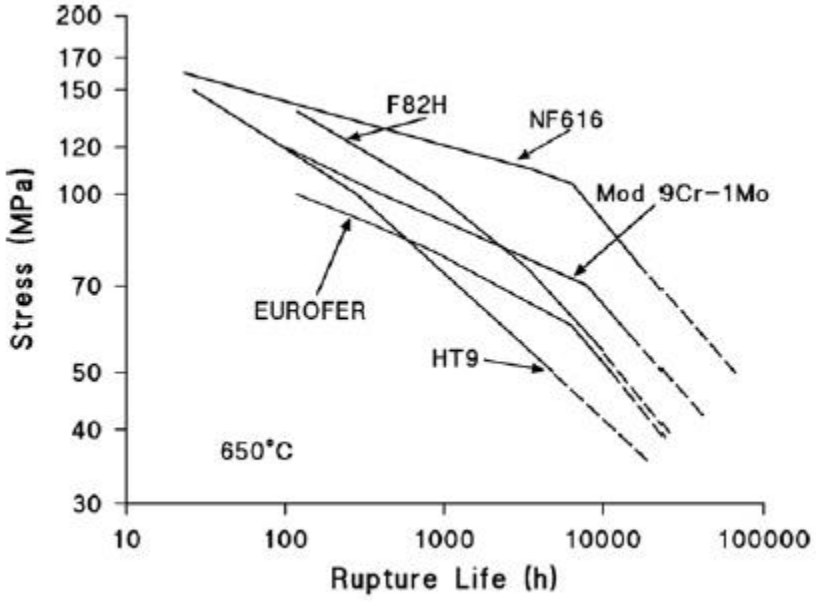

Fig. 1.2.20. Comparison of the creep-rupture curves for tests at 650 °C for commercial steels Sandvik HT9, modified 9Cr–1Mo, NF616, F82H, and EUROFER [24]

1.2.7 Thermo Mechanical Treatments (TMTs) to improve the high temperature performance of RAFM steels

1.2.7.1 Examples of TMTs; A21 steel (Klueh, [25])

Hereafter the steel A-21 is taken into account. The composition of this alloy is as follows: 9.5Cr-3Co-1.0Ni-0.6Mo-0.3Ti-0.07C. This steel isn't considered for a possible application in a fusion environment; its composition is in fact not suitable for it, because of the content in Co. We just take into account this alloy for the thermo mechanical treatments having been applied on it. The steel, in fact, has undergone austenitization, intermediate hot-working, cooling and tempering as described in literature [25]; it was austenitized at >1100°C to dissolve the carbides. Austenitization was followed by cooling to an intermediate temperature (700 ÷ 1000°C), where the steel was hot worked in the austenitic condition. After hot-working, the steel was cooled to ambient temperature to transform the matrix to martensite. Finally, the steel was tempered in the range 650 ÷ 750°C for 1 h. The resulting microstructure is reported below (Fig. 1.2.21);

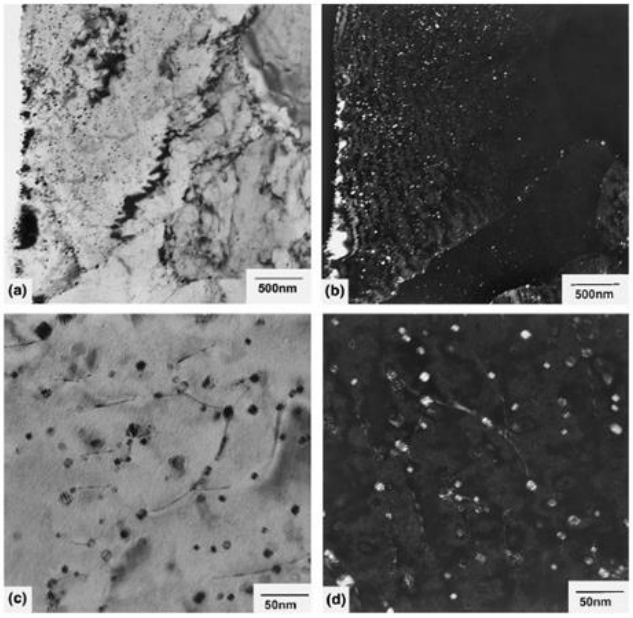

Fig. 1.2.21. Transmission electron micrograph showing high density of TiC precipitates in matrix in: (a) bright field and (b) dark field, and showing precipitates on dislocations in (c) bright field and (d) dark field [25]

As we can notice from the microstructure, an effective pinning of the dislocations through the nano-precipitation has been obtained. Consequntly, a marked increase in mechanical properties and creep strength is achieved (fig. 1.2.22).

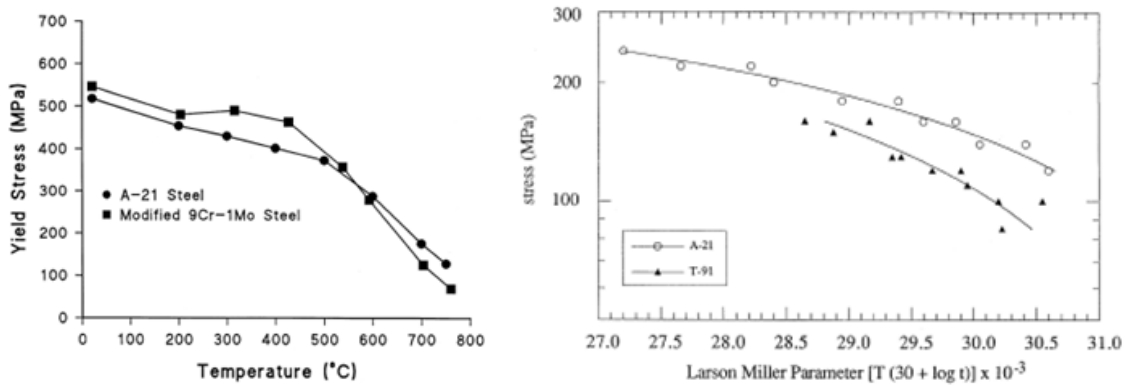

Fig. 1.2.22. Tensile properties of A21 steels compared to Modified 9Cr-1Mo steel (left) Comparison of the Larson-Miller curves of A21 and modified 9Cr-1Mo steel (right) [25]

1.2.7.2 Examples of TMTs; Grade 91 steel (Hollner, [26])

A further example of the effectiveness of the TMT is reported in [26]. The Grade 91 steel (composition reported in tab. 1.2.14) underwent TMT as in fig. 1.2.23;

C	Cr	N	Mn	Mo	Si	Nb	V	Cu	Ni	S	P	Al
0.088	8.91	0.04	0.363	0.917	0.324	0.08	0.198	0.068	0.15	0.001	0.017	0.018

Tab. 1.2.14 Chemical composition in wt% of the Grade 91 steel [26]

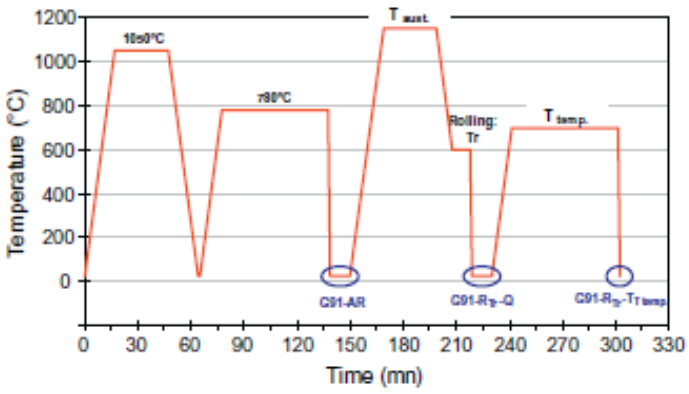

Fig. 1.2.23. Thermal cycles of the first heat-treatment and of the thermomechanical treatment under study. The different states of the material (G91) are denoted: AR = as received, R = rolled, Q = quenched, T = tempered [26].

The precipitate population evolution, as resulting from MatCalc simulations is reported in tab. 1.2.15. The temperature of the second normalisation treatment is chosen at 1150 °C in order to dissolve all the M23C6 carbides and as much MX carbides and nitrides as possible, while maintaining the same prior austenitic grain size. The VN indeed dissolve almost entirely in 1 h at 1150 °C. MatCalc results show that these remaining MX precipitates grow up during the following air quenching (≅ 1°C/s). Temperature of the warm-rolling must stay above the martensitic start temperature, avoid the ferrite stability domain, and be low enough to avoid dislocation annihilation by re-crystallization or recovery. The hot-rolling temperature can be kept between 600 and 750°C in order to allow 25% of deformation.

Notations	$M_{23}C_6$			MX		
	$\%_w$	Number/m^3	Mean diameter (nm)	$\%_w$	Number/m^3	Mean diameter (nm)
Initial "G91-AR"	1.947	9.5×10^{19}	71	0.427	1.47×10^{21}	14
Warm-rolling 600 °C "G91-R600-Q"	*0*	*n.a.*	*n.a.*	*0.195*	*3.97×10^{19}*	*44*
Warm-rolling 600 °C +1 h tempering 650 °C "G91-R600-T650"	1.955	1.86×10^{22}	12.5	0.421	9.1×10^{22}	3.5
Warm-rolling 600 °C +1 h tempering 700 °C "G91-R600-T700"	1.955	3.15×10^{21}	22	0.427	1.36×10^{21}	13.5
Warm-rolling 700 °C "G91-R700-Q"	*0*	*n.a.*	*n.a.*	*0.195*	*4.6×10^{19}*	*38*
Warm-rolling 700 °C +1 h tempering 700 °C G91-R700-T700	1.955	3.23×10^{21}	21.7	0.427	10^{21}	16.5

Tab. 1.2.15. Characteristics of the precipitates populations in Grade 91 steel after simulated thermomechanical treatments (italics letters are for rolled and quenched materials) [26]

The increase in mechanical properties achieved through TMT (warm-rolling at 600°C, 25% deformation) is shown in fig. 1.2.24 and the consequent improvement in creep strength in fig. 1.2.25.

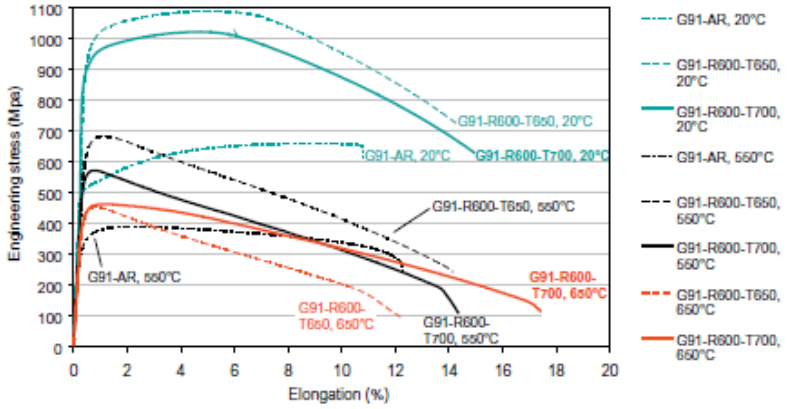

Fig. 1.2.24. Tensile tests results of G91-R600-T650 and of G91-R600-T700 compared to G91-AR [26]

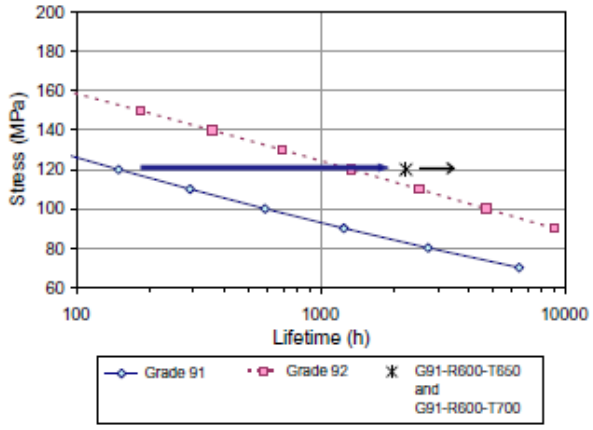

Fig. 1.2.25. Creep lifetimes versus applied stress at 650 °C of G91-R600-T650 and of G91-R600-T700 compared to G91-AR and P92-AR [26]

1.2.7.3 Examples of TMTs; NPM steel (Hollner, [27])

As last example of the effectiveness of the TMT we report the results obtained on NPM steel and described in [27]. The NPM steel (composition reported in tab. 1.2.16) underwent TMT as in fig. 1.2.26. The TMT under study consists of a normalization step of 30 min at 1150 °C, a rolling step with 25% reduction in thickness at 650 °C, and a tempering step of 1 h at 700 °C.

C	Cr	N	Mn	W	Si	Nb	V	Co	B	S	P	Al
0.09	9.26	0.01	0.51	2.92	0.299	0.05	0.199	2.88	0.0114	0.003	0.001	0.004

Tab. 1.2.16 Chemical composition in wt% of the NPM steel [27]

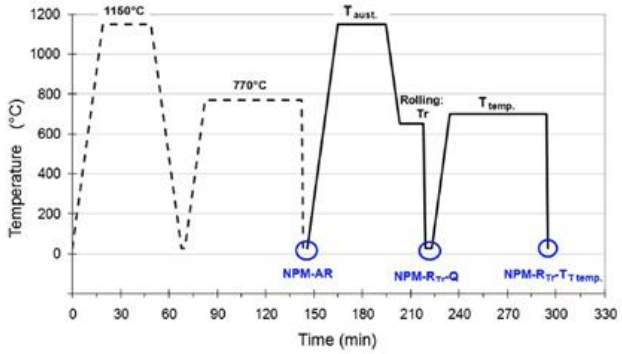

Fig. 1.2.26. Thermal cycles of the first heat-treatment and of the thermomechanical treatment under study. The different states of the material (G91) are denoted: AR = as received, R = rolled, Q = quenched, T = tempered [27]

The increase in mechanical properties achieved through TMT is shown in fig. 1.2.27 and the consequent improvement in creep strength in fig. 1.2.28.

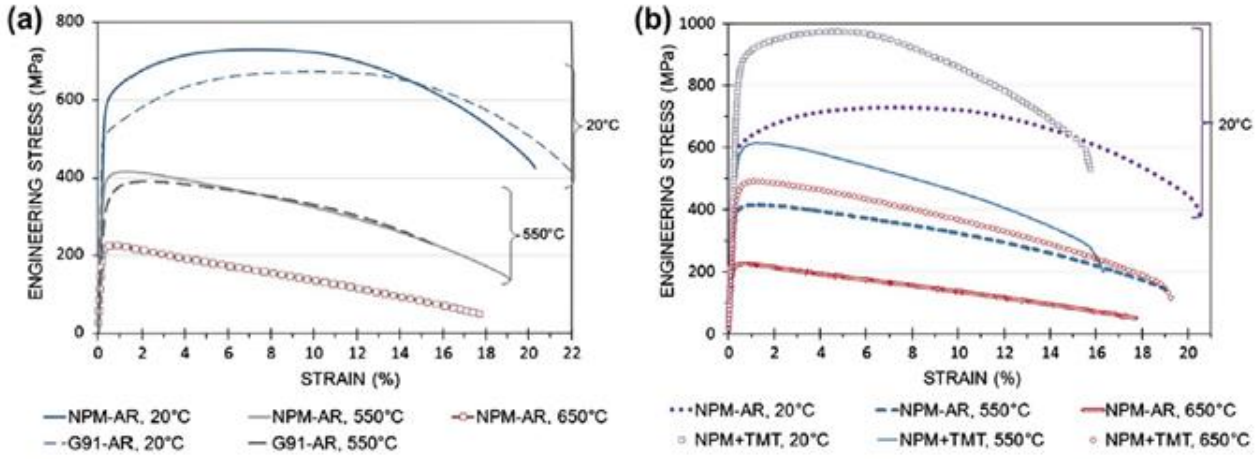

Fig. 1.2.27. Tensile results of: (a) the NPM-AR compared to the G91-AR and (b) the NPM + TMT compared to the NPM-AR [27]

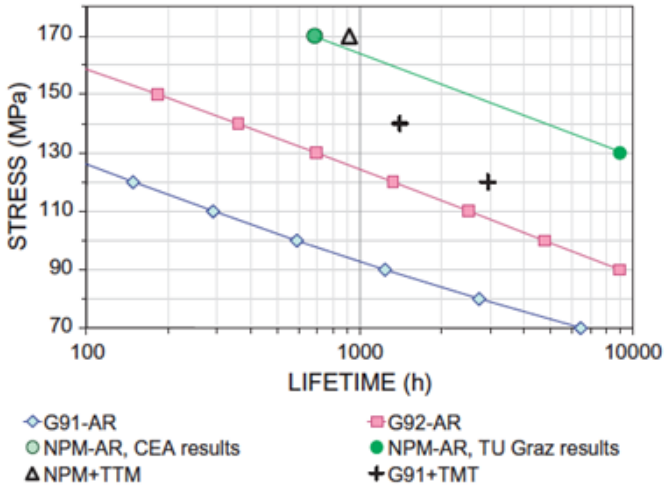

Fig. 1.2.28. Creep tests results (650°C) of NPM-AR and NPM+TMT, compared to G91-AR, G92-AR and G91+TMT [27]

Other examples of similar TMTs are reported in several works by Tan and Busby [28].

1.2.8 References

[1] D. Stork, DEMO and the Route to Fusion Power Presentation at the 3rd Intnl. School on fusion technologies, Euratom-UKAEA Fusion association, (2009).

[2] K. Lackner, R. Andreani, D. Campbell, M. Gasparotto, D. Maisonnier, M.A. Pick, Long-term fusion strategy in Europe, J. Nucl. Mater. 307–311 (2002) 10–20. https://doi.org/10.1016/S0022-3115(02)00970-4.

[3] P. Batistoni, U. Fischer, M. Angelone, P. Bem, I. Kodeli, P. Pereslavtsev, L. Petrizzi, M. Pillon, K. Seidel, S.P. Simakov, R. Villari, Neutronics design and supporting experimental activities in the EU, Fusion Eng. Des. 81 (2006) 1169–1181. https://doi.org/10.1016/J.FUSENGDES.2005.08.060.

[4] S. Jitsukawa, A. Kimura, A. Kohyama, R.L. Klueh, A.A. Tavassoli, B. Van Der Schaaf, G.R. Odette, J.W. Rensman, M. Victoria, C. Petersen, Recent results of the reduced activation ferritic/martensitic steel development, J. Nucl. Mater. 329–333 (2004) 39–46. https://doi.org/10.1016/J.JNUCMAT.2004.04.319.

[5] A.A.F. Tavassoli, E. Diegele, R. Lindau, N. Luzginova, H. Tanigawa, Current status and recent research achievements in ferritic/martensitic steels, J. Nucl. Mater. 455 (2014) 269–276. https://doi.org/10.1016/J.JNUCMAT.2014.06.017.

[6] E. Gaganidze, J. Aktaa, Assessment of neutron irradiation effects on RAFM steels, Fusion Eng. Des. 88 (2013) 118–128. https://doi.org/10.1016/J.FUSENGDES.2012.11.020.

[7] Y. Dai, J. Henry, Z. Tong, X. Averty, J. Malaplate, B. Long, Neutron/proton irradiation and He effects on the microstructure and mechanical properties of ferritic/martensitic steels T91 and EM10, J. Nucl. Mater. 415 (2011) 306–310. https://doi.org/10.1016/J.JNUCMAT.2011.04.029.

[8] E. Gaganidze, C. Petersen, J. Aktaa, Study of helium embrittlement in boron doped EUROFER97 steels, J. Nucl. Mater. 386–388 (2009) 349–352. https://doi.org/10.1016/J.JNUCMAT.2008.12.131.

[9] E. Gaganidze, C. Petersen, E. Materna-Morris, C. Dethloff, O.J. Weiß, J. Aktaa, A. Povstyanko, A.

Fedoseev, O. Makarov, V. Prokhorov, Mechanical properties and TEM examination of RAFM steels irradiated up to 70 dpa in BOR-60, J. Nucl. Mater. 417 (2011) 93–98. https://doi.org/10.1016/J.JNUCMAT.2010.12.047.

[10] J. Henry, X. Averty, Y. Dai, J.P. Pizzanelli, Tensile behaviour of 9Cr–1Mo tempered martensitic steels irradiated up to 20 dpa in a spallation environment, J. Nucl. Mater. 377 (2008) 80–93. https://doi.org/10.1016/J.JNUCMAT.2008.02.027.

[11] L. Schäfer, M. Schirra, K. Ehrlich, Mechanical properties of low activating martensitic 8–10% CrWVTa steels of type OPTIFER, J. Nucl. Mater. 233–237 (1996) 264–269. https://doi.org/10.1016/0022-3115(95)00183-2.

[12] H.C. Schneider, B. Dafferner, J. Aktaa, Embrittlement behaviour of low-activation alloys with reduced boron content after neutron irradiation, J. Nucl. Mater. 321 (2003) 135–140. https://doi.org/10.1016/S0022-3115(03)00241-1.

[13] M. Rieth et al., EUROFER 97 Tensile, charpy, creep and structural tests, 2003. http://inis.iaea.org/search/sea rch.aspx?orig_q=RN:35032617.

[14] A. Kimura, R. Kasada, A. Kohyama, H. Tanigawa, T. Hirose, K. Shiba, S. Jitsukawa, S. Ohtsuka, S. Ukai, M.A. Sokolov, R.L. Klueh, T. Yamamoto, G.R. Odette, Recent progress in US–Japan collaborative research on ferritic steels R&D, J. Nucl. Mater. 367–370 (2007) 60–67. https://doi.org/10.1016/J.JNUCMAT.2007.03.013.

[15] R.L. Klueh, M.A. Sokolov, K. Shiba, Y. Miwa, J.P. Robertson, Embrittlement of reduced-activation ferritic/martensitic steels irradiated in HFIR at 300°C and 400°C, J. Nucl. Mater. 283–287 (2000) 478–482. https://doi.org/10.1016/S0022-3115(00)00086-6.

[16] R.L. Klueh, Ferritic/martensitic steels for advanced nuclear reactors, Trans. Indian Inst. Met. 62 (2009).

[17] R.L. Klueh, D.J. Alexander, P.J. Maziasz, Impact behavior of reduced-activation ferritic steels irradiated in the Fast Flux Test Facility, J. Nucl. Mater. 186 (1992) 185–195. https://doi.org/10.1016/0022-3115(92)90333-G.

[18] P.J.M. R.L. Klueh, The microstructure of chromium-tungsten steels, Metall. Mater. Trans. A. 03 Vol. 20 (1989).

[19] E. Gaganidze, H.C. Schneider, B. Dafferner, J. Aktaa, Embrittlement behavior of neutron irradiated RAFM steels, J. Nucl. Mater. 367–370 (2007) 81–85. https://doi.org/10.1016/J.JNUCMAT.2007.03.163.

[20] J.S. Chunfang Wang, Maoqiu Wang, Effect of microstructural refinement on the toughness of low carbon martensitic steel, Scr. Mater. 58(6) (2008) 492–495.

[21] L. Pilloni, F. Attura, A. Calza-Bini, G. De Santis, G. Filacchioni, A. Carosi, S. Amato, Physical metallurgy of BATMAN II Ti-bearing martensitic steels, J. Nucl. Mater. 258–263 (1998) 1329–1335. https://doi.org/10.1016/S0022-3115(98)00199-8.

[22] N. Okubo, M.A. Sokolov, H. Tanigawa, T. Hirose, S. Jitsukawa, T. Sawai, G.R. Odette, R.E. Stoller, Heat treatment effect on fracture toughness of F82H irradiated in HFIR, J. Nucl. Mater. 417 (2011) 112–114. https://doi.org/10.1016/J.JNUCMAT.2011.05.020.

[23] J.B. S. Zinkle, Structural materials for fission & fusion energy, Mater. Sci. Mater. Today. (2009).

[24] R.L. Klueh, A.T. Nelson, Ferritic/martensitic steels for next-generation reactors, J. Nucl. Mater. 371 (2007) 37–52. https://doi.org/10.1016/J.JNUCMAT.2007.05.005.

[25] R.L. Klueh, N. Hashimoto, P.J. Maziasz, New nano-particle-strengthened ferritic/martensitic steels by

conventional thermo-mechanical treatment, J. Nucl. Mater. 367–370 (2007) 48–53. https://doi.org/10.1016/J.JNUCMAT.2007.03.001.

[26] S. Hollner, B. Fournier, J. Le Pendu, T. Cozzika, I. Tournié, J.C. Brachet, A. Pineau, High-temperature mechanical properties improvement on modified 9Cr–1Mo martensitic steel through thermomechanical treatments, J. Nucl. Mater. 405 (2010) 101–108. https://doi.org/10.1016/J.JNUCMAT.2010.07.034.

[27] S. Hollner, E. Piozin, P. Mayr, C. Caës, I. Tournié, A. Pineau, B. Fournier, Characterization of a boron alloyed 9Cr3W3CoVNbBN steel and further improvement of its high-temperature mechanical properties by thermomechanical treatments, J. Nucl. Mater. 441 (2013) 15–23. https://doi.org/10.1016/J.JNUCMAT.2013.05.018.

[28] L. Tan, Y. Yang, J.T. Busby, Effects of alloying elements and thermomechanical treatment on 9Cr Reduced Activation Ferritic–Martensitic (RAFM) steels, J. Nucl. Mater. 442 (2013) S13–S17. https://doi.org/10.1016/J.JNUCMAT.2012.10.015.

1.3 Additional satellite activities concerning the assessment of tensile properties by means of RC (Ring Compression) tests (TASTE pilot project)

Additional activities hereby reported concern the “Ring Compression” testing technique to assess the mechanical properties of the 15-15 Ti steel in the frame of “TASTE” (Testing and ASsessment methodologies for material Characterization of fuel cladding TubEs in relevant environmental conditions) Pilot Project. The proposed project has the objective to define and recommend an optimal set of tools for a comprehensive material property determination for shells with cylindrical geometries under irradiated condition. Infact, provided that fuel cladding is characterized by cylindrical geometry, it would be useful to develop simplified methodologies to assess mechanical properties and their decay under irradiation; namely; the simplest the method, the highest the possibility to implement it directly into the hot cells by automatized procedures, avoiding the contact between irradiated material and human beings. During 2020 the activities have been devoted to mechanical characterization combined with FEM simulations. More in detail the activities hereby reported concern the employment of “Ring Compression” testing technique as a possible procedure to assess hardening and embrittlement of the 15-15 Ti steel.
This Ring Compression test consists in the compression of a pipe between two parallel planes in order to achieve a characteristic curve reporting load as function of the displacement. In ring compression tests the specimen is simply compressed perpendicular to the tube axis under displacement or load control. Among the equivalent stresses distributed in the entire ring, the maximum value of these stresses is usually located close to the inner surface at the 12 o’clock position. The ring-compression test is a good ductility screening test. For determining tensile and creep properties the test method has no sensitivity to friction between the ring and the loading device. The main shortcomings are that the deformation is highly non-homogenous and undergoes simultaneously tensile and compressive deformation. The assessment is therefore very complex, in particular concerning the extraction of true stress/true strain from the force/deflection data which must be done indirectly via iterative process which may lead to non-unique solutions. Several methods have been taken into account, in literature [1-12], in order to correlate the load-displacement curve resulting from this test to the mechanical properties of the material (Yield Stress, UTS, KIC).

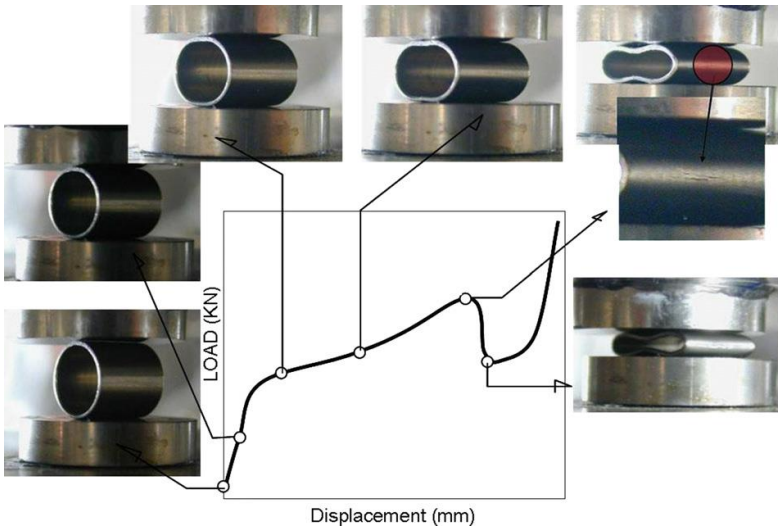

Fig. 1.3.1: Stages of Ring Compression Test [1]

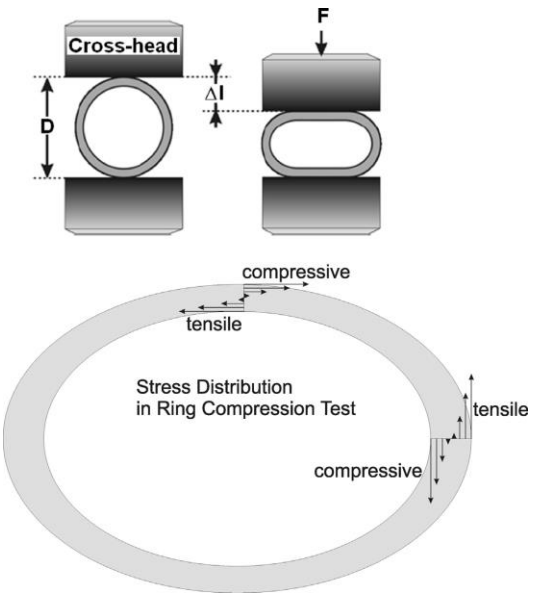

Fig. 1.3.2: Mechanics and stress distribution of RC tests [2]

Estimates of the Yield Stress, Ultimate Tensile Strength and Strain to fracture can be acquired from theoretical models which predict the shape of load-deflection characteristics of a compressed tube through standard elastic theory [3-5]. This model basically assumes that the material is rigid linear strain-hardening and gives a force-deflection relationship.
The limit load, (i.e. the load at which large plastic deformation is initiated) assuming elastic-perfectly plastic material properties is calculated as:

$$P_0 = \frac{4M_0}{R} = \frac{\sigma_0 t^2 \, l}{R}$$

where R is the initial radius of the ring, l the length of the ring and t the wall thickness. The same load can also be used with sufficient accuracy for strain hardening materials.
From these relations, the collapse stress can be obtained from the limit load P_0 as

$$\sigma_0 = \frac{\alpha P_0 R}{t^2 l}$$

where α equals 1 if rings (length not greater than a few thicknesses) are tested and 0.866 if tubes (length not less than one diameter of the tube) are tested.
The calculated collapse stress can now be linearly correlated to the yield stress ($R_{p0,2}$) and ultimate tensile strength (R_m) through the following coefficients;

$$K_{Rp02} = \frac{\sigma_0}{R_{p02}}$$

$$K_{Rm} = \frac{\sigma_0}{R_m}$$

The collapse stress can be acquired from the experimental data by applying the two-secants method [6] as shown in Fig. 1.3.3.

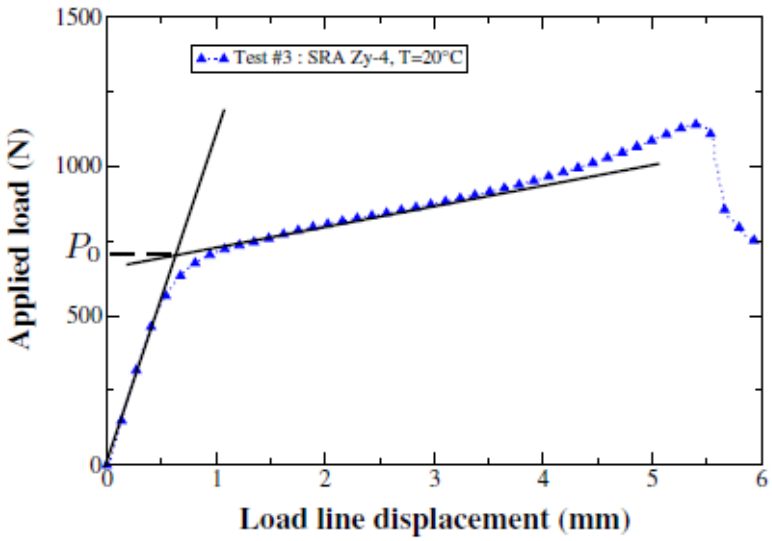

Figure 1.3.3. Extracting the collapse load P0 from experimental data [6]

A clear draw-back of this procedure is that both yield stress and tensile strength are correlated against the same calculated collapse stress.
Eventually some other references in literature focus on the possibility to exploit this technique in order to detect embrittlement effects on the latter portion of the RC curve. This kind of studies combines experimental tests with FEM simulations and reverse engineering approach. The following figure (Fig. 1.3.4) shows, for example, the approach followed by Herbs et al. [2].

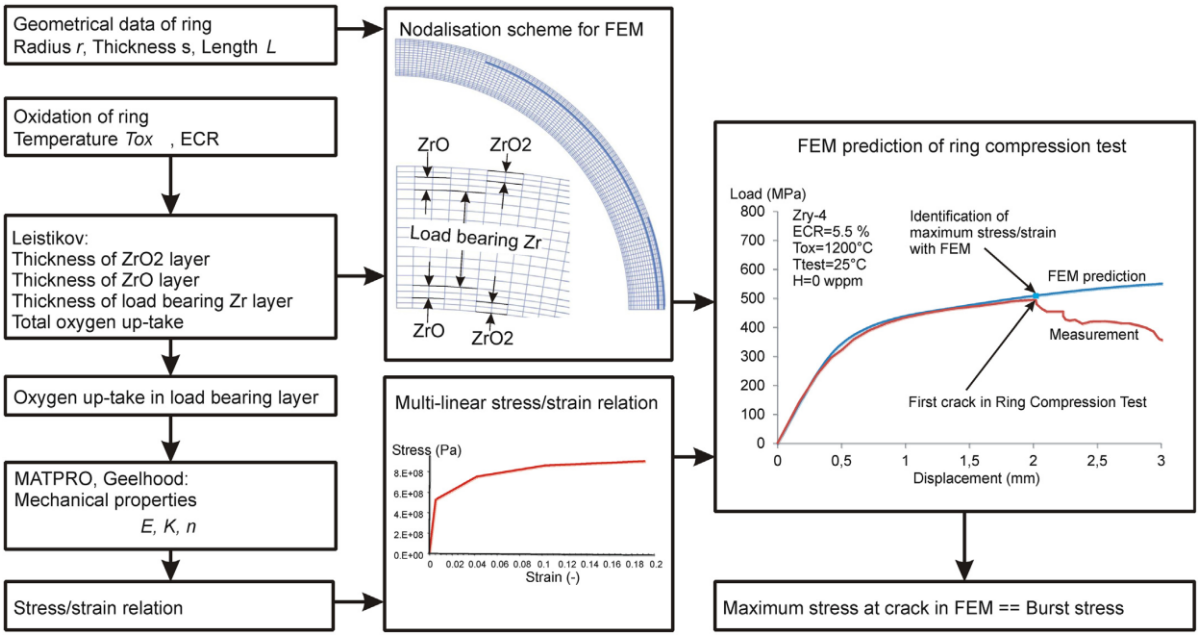

Figure 1. Quantify embrittlement by means of RC tests [2].

References

1. M.A. Martin-Rengel, F.J. Gómez Sánchez, J. Ruiz-Hervías, L. Caballero "Determination of the hoop fracture properties of unirradiated hydrogen-charged nuclear fuel cladding from ring compression tests" Journal of Nuclear Materials 436 (2013) 123–129;
2. J. Herb, J. Sievers, H.G. Sonnenburg, "A new cladding embrittlement criterion derived from ring compression tests" Nuclear Engineering and Design 273(2014)615–630;
3. T.Y. Reddy, Ph.D. Thesis, University of Cambridge (1978);
4. T. Y. Reddy and S.R. Reid "On obtaining Material Properties from the Ring Compression Test" Nuclear Engineering and Design 52 (1979) 257-263;
5. S.R. Reid and T.Y. Reddy, "Effect of strain hardening on the lateral compression of tubes between rigid plates" International Journal of Solids and Structures 14 (3), 213-225I;
6. V. Busser, M.C. Baietto-Dubourg, J. Desquines, C. Duriez, J.P. Mardon "Mechanical response of oxidized Zircaloy-4 cladding material submitted to a ring compression test" Journal of Nuclear Materials 384 (2009) 87–95;
7. R. Yamada, M. Suzuki and Y. Harayama, "Application of finite element method to ring compression test" Nucl. Eng. Des. 44 (1977) 75;
8. M.A. Martín-Rengel, F.J. Gómez, J. Ruiz-Hervías, A.Valiente, "Obtention of fracture properties of unirradiated hydrogen-charged fuel cladding from ring compression test", 2009 Water Reactor Fuel Performance Meeting, September 6–10, 2009, Paris, France, paper no. 2212, 2009;
9. Cristino, V.A.M., Rosa, P.A.R., Martins, P.A.F. "The Role of Interfaces in the Evaluation of Friction by Ring Compression Testing" 44, (2011), 134-143;
10. M. Nemat-Alla, Int. J. Mech. Sci. "Reproducing hoop stress–strain behavior for tubular material using lateral compression test" 45 (2003) 605;
11. Holmstrom B. (Stefan)., Bruchhausen, M., Nilsson K-F., Pohja, R., Altstadt, E., Serrano Garcia, M., Radu, V., Cristalli, C, Aktaa, J., Namburi, H.K., Delville, R., Courcelle A., Test methodologies for determining high temperature material properties of thin walled tubes, JRC Publication N°: JRC105586, 2017.
12. Holmström B (Stefan), Simonovski, I., De Haan, F., Lapetite, J-M., Baraldi, D., Serrano Garcia, M., Altstadt, E., Aktaa J., Radu V., Namburi, H.K., Cristalli, C. Pohja, Rami., Delville, R., Courcelle A., Determination of high temperature material properties of 15-15Ti steel by small specimen techniques, JRC Publication N°: , JRC105589, 2017

2 Chapter 2; Experimental methods

2.1 Description of the procedures adopted to run SSRT (Slow Strain Rate Tensile) and creep tests in lead in the frame of GEMMA Project

2.1.1 Material to be tested and extraction of the specimens

In the frame of this thesis the mechanical behavior of AISI 316L steel (chemical composition reported in Tab. 2.1.1) in lead was investigated since it is one of the main candidate structural material for LFR. The AISI 316 L welded plate (TIG) has been supplied by the company "Walter Tosto S.p.A".

Heat	Project	Chemical composition (wt%)									
		Cr	C	Mn	N	Ni	Mo	Co	Si	S	P
AISI 316L	GEMMA	17-18	< 0.03	1.6-2	< 0.1	10-13	2.0-2.7	< 1	< 1	< 0.015	< 0.045

Tab. 2.1.1. Chemical composition of the 316L steel

In order to perform SSRT and creep tests a set of specimens with cylindrical shape, 4.5 mm gauged diameter, 20 mm gauged length (fig. 2.1.1a), have been extracted in three different conditions (fig.2.1.1b):

- from the base material with the axis parallel to the axis of the welded joint;
- from the welded joint with the gauged length included into the weld material and the axis parallel to the one of the welded joint;
- from the welded joint with the axis perpendicular to the one of the welded joint.

In this last condition, which we will define as "cross weld", the gauged length of the specimen also includes, in addition to the weld filler material (10 mm wide, as average), also some portion of the heat-affected base material.

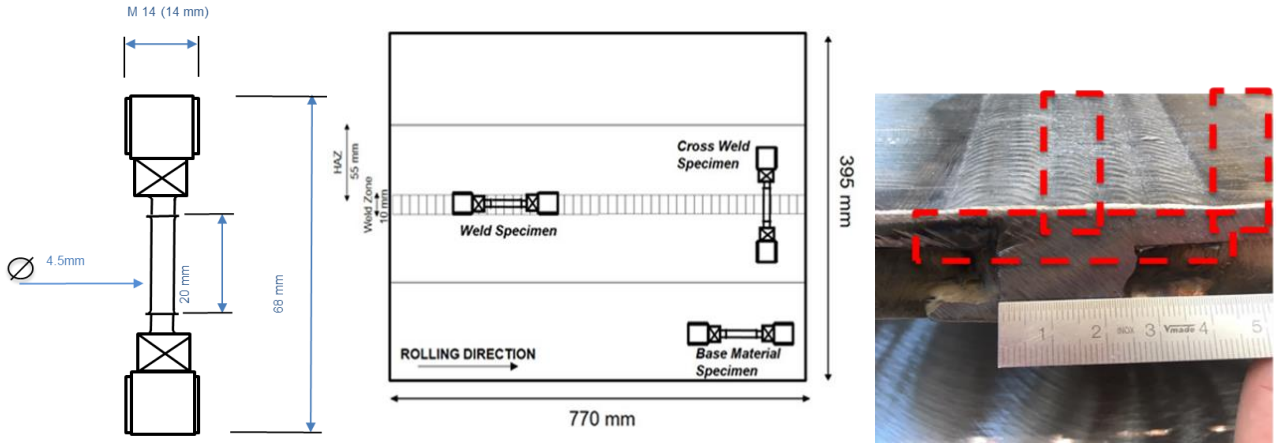

a) b) c)

Figure 2.1.1. a) drawing of the sample b) extraction of the samples from the 316L welded plate c) picture of the 316L welded joint

2.1.2 Test matrix

The test matrix to be carried out is given below (Tab. 2.1.2). Concerning the SSRT tests the strain rates selected to promote the contact between the steel and liquid metal are equal to $5x10^{-5}$ s^{-1} for the tests at 400°C, and to $5x10^{-6}$ s^{-1} for the tests at 550°C.

AISI 316L TIG 30 mm					
	SSRT in air			Creep in air	
	RT	400 °C	550 °C	500 °C	600 °C
BM	2	3	3	3	3
Weld	3	5	5	3	3
Cross Weld	3	5	5	3	3
	SSRT in Pb			Creep in Pb	
		400 °C	550 °C	500 °C	600 °C
BM		3	3	3	3
Weld		5	5	3	3
Cross Weld		5	5	3	3

Tab. 2.1.2. Test Matrix of the SSRT and creep tests in lead

2.1.3 Slow Strain Rate Tensile tests (SSRT) in air

The SSRTs have been carried out on the aforementioned cylindrical specimens. The standards taken into account are the ISO 6892-2:2011, the ASTM E8/E8M:11 and the ASTM G129-00. The tests were carried out in air and in lead in order to compare the experimental results obtained. The test temperature is controlled by means of a resistance furnace and the stress by means of a 100 kN load cell installed on a hydraulic machine. The strain is controlled on the shaft connected to the sample by a couple of Magnetostrictive Linear Position Sensor (MLPS) and measured on the gauged length of the specimen by axial extensometer (12 mm gauge). The MLPSs are the devices necessary to run the tests in lead aimed at achieving and controlling the extremely low strain rate values (in the range of 10^{-6} s^{-1}) in order to detect any embrittlement effect, if occurring. The whole instrumentation is reported in the picture below (fig. 2.1.2). The strain rate has been kept constant in a range between $5x10^{-5}$ and $5x10^{-6}$ s^{-1} according to the corresponding test condition.

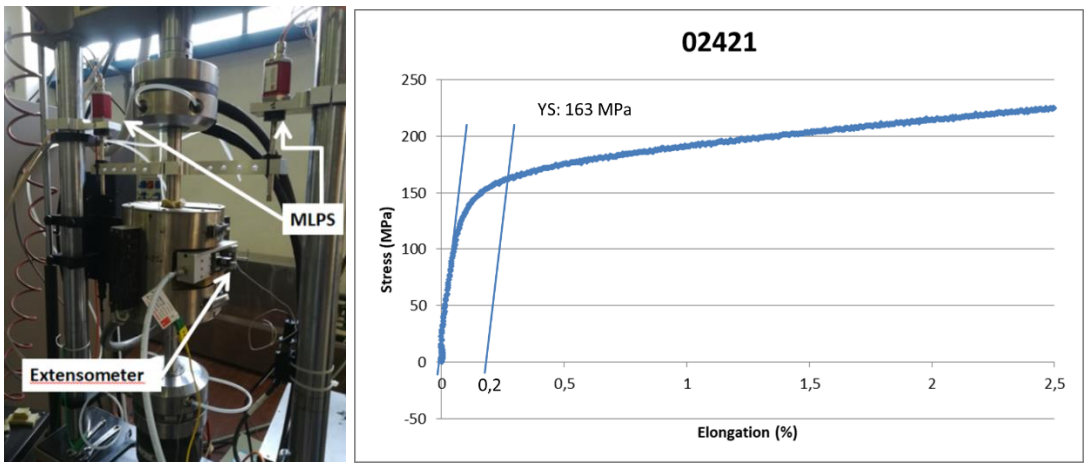

Figure 2.1.2. a) Detail of the installation of the extensometer and of the MLPS; b) YS assessment for one test carried out at 400°C, $5x10^{-5}s^{-1}$

The Yield strength (YS) has been assessed as the stress leading to a 0,2% plastic deformation (fig. 2b). In order to calculate this parameter the elastic stage of the tensile curve has been fitted by a linear function and an interval of the plastic deformation by 2nd degree polynomial (fig. 2.1.3). The intersection between the line parallel to the elastic fitting (passing through the (0,2%, 0) coordinate) and the polynomial curve has then been calculated analytically. The Yield Strength results the same, namely 163 MPa in the case of this specimen, for both the curves (one deriving from the extensometer and the other from the MLPS signal).

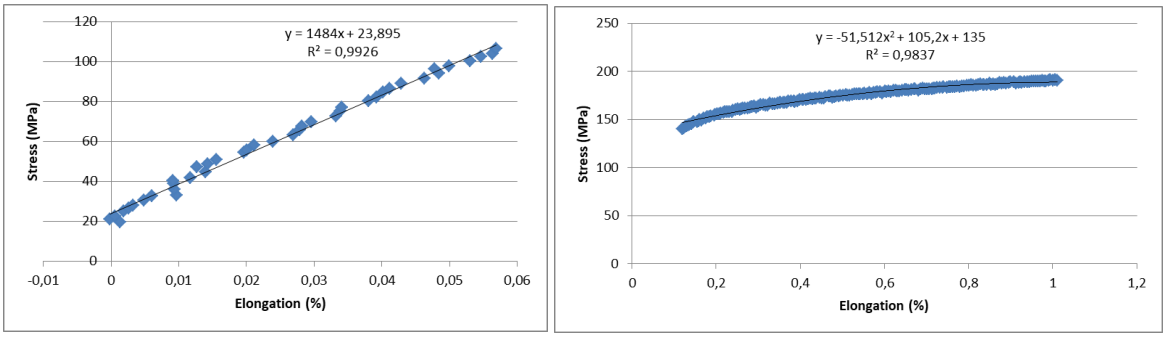

a) b)

Figure 2.1.3. Linear (a) and Polynomial (b) fitting for the elastic and plastic stage respectively of the extensometer curve of the test on one of the specimens tested at 400°C, 5x10^{-5}s^{-1}.

The Ultimate tensile strength (UTS) has been evaluated on each test as the maximum value achieved for the stress. As an example, in Figure 2.1.4, 487 MPa was achieved for the specimen whose Yield Strength resulted 163 MPa.

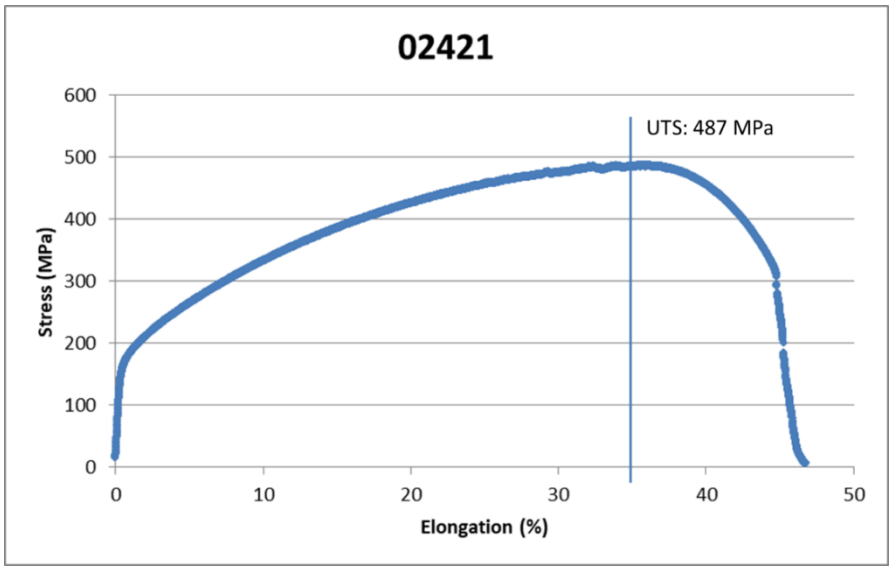

Figure 2.1.4. UTS identification on one of the tests carried out at 400°C, 5x10^{-5}s^{-1}

2.1.4 Slow Strain Rate tests (SSRT) in lead

In order to carry out the tests in lead with controlled oxygen content a devoted Test Section (TS) has been designed internally in ENEA and fabricated by an external company. The next figure (Fig. 2.1.5) shows a drawing accompanied by a picture of the test section. The chamber is provided with two channels, one for the filling with lead (in the cover) and one for the lead discharge (at the bottom). An inlet and outlet for gas is aimed at lead conditioning by inert gas (Argon/H_2 mixture) addition.

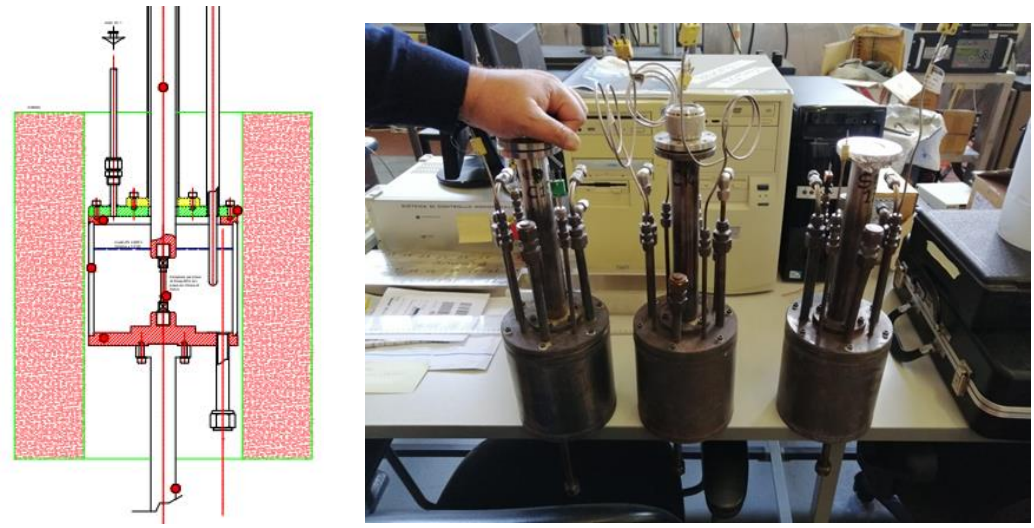

a) b)

Figure 2.1.5. (a) Drawing of the test section (b) picture of the test section

The TS for SSRT were conceptually designed by the staff of ENEA Brasimone Mechanical Testing Laboratory (FSN-ING-SMN), to be housed on the MTS 810 “Gilda” servo-hydraulic testing machine. The fabrication of the components, in AISI 321, was carried out by Lima Inox company in Ozzano dell’Emilia. Below is the schematic drawing (2.1.6-2.1.7) of the aforementioned TS and the description of the individual parts.

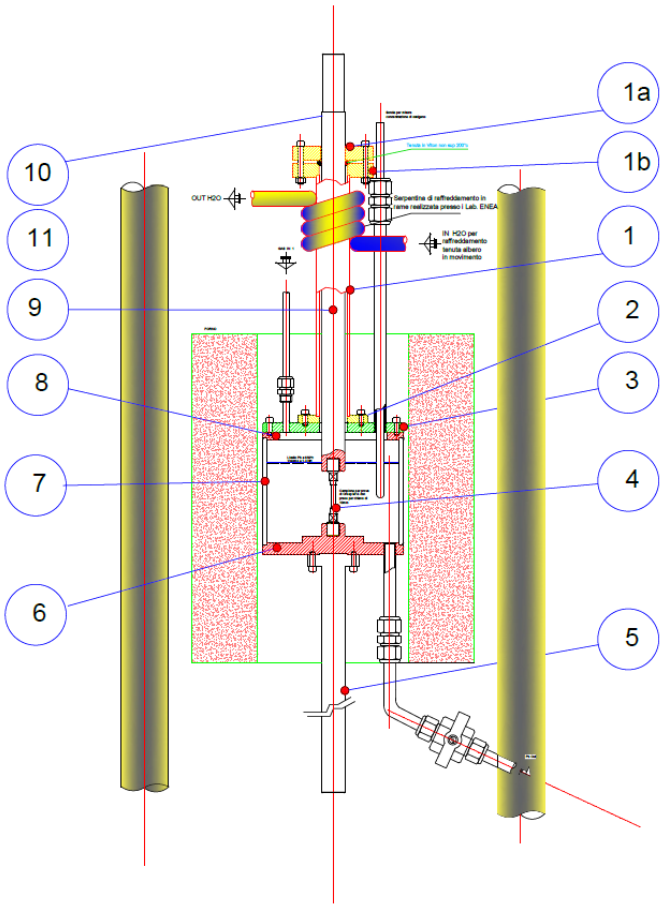

Figure 2.1.6: Schematic drawing of the test section

1 - Sleeve;

1a - Viton OR seal closing flange;

1b - Upper flange welded on component "1", for housing the Viton OR gasket;

2 - Lower flange welded on component “1”;

3 - Component “8” closing flange;

4 - Specimen;

5 - Lower shaft;

6 - Lower sample holder flange welded on component “7”;

7 - Lead containment tube;

8 - Upper flange welded on component “7”;

9 - Upper sample holder shaft.

10 - Detail not present in the SSRT test configuration

8 pass-throughs with Swagelok connections have been provided on the closing flange (detail 3) for the following purpose:

- 3 1/8 inch pass-throughs for thermocouples;
- 1 1/8 inch pass-through for the inlet of the Ar gas;

- 1 1/4 inch pass-through for the entry of molten lead;
- 1 1/4 inch pass-through for the probe for detecting the concentration of oxygen in the molten lead;
- 2 1/4 inch pass-throughs for the inlet of the Ar and H_2 gas mixture.

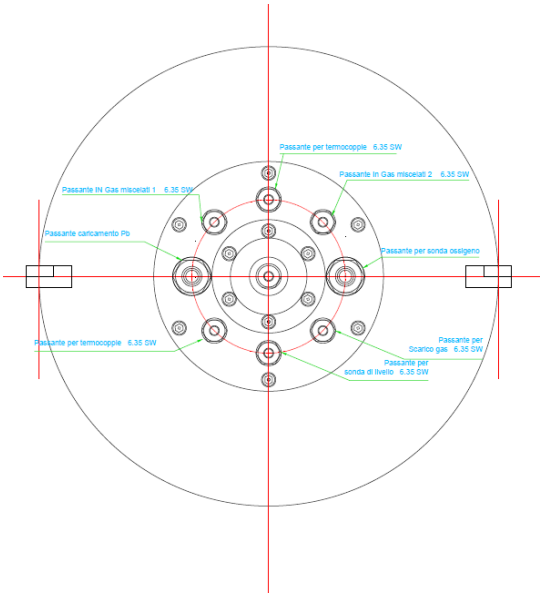

Figure 2.1.7: Schematic drawing of the closing flange

The Ar/H2 mixture is obtained by mixing pure Argon (cylinder) and pure Hydrogen (H-generator) for laboratory use. The addition of the Ar/H2 mixture to the test environment is achieved by a dedicated plant (depicted in fig. 2.1.8). In particular, the plant is equipped with 4 pressure meters and 4 mass flow meters, able to serve 4 testing machines, controlled by a specially dedicated software named "CREEP-OCS" (fig. 2.1.9), which acquires the signals generated by the following sensors:

- 3 type K thermocouples housed within each test section;
- probe for detecting the concentration of oxygen in molten lead.

The aforementioned Gas Panel is powered by a cylinder of pure (99.9%) Argon and by a Hydrogen Generator connected by means of Rilsan pipes. The connection line between the Gas Panel and the TS (Test Section) was built with ¼ inch steel pipes and Swagelok type fittings. In particular, the entry into the TS of the Ar/H_2 mixture takes place by means of two pipes placed in a bath in the molten lead, to facilitate the purification of Lead from Oxygen; furthermore, the TSs are equipped with an Ar cover flushing system.
Lead is melted in a dedicated melting system and loaded into the test section tank where conditioning (Ar/H_2 bubbling) is carried out until the achievement of the target oxygen concentration; namely **10^{-8} wt%**.

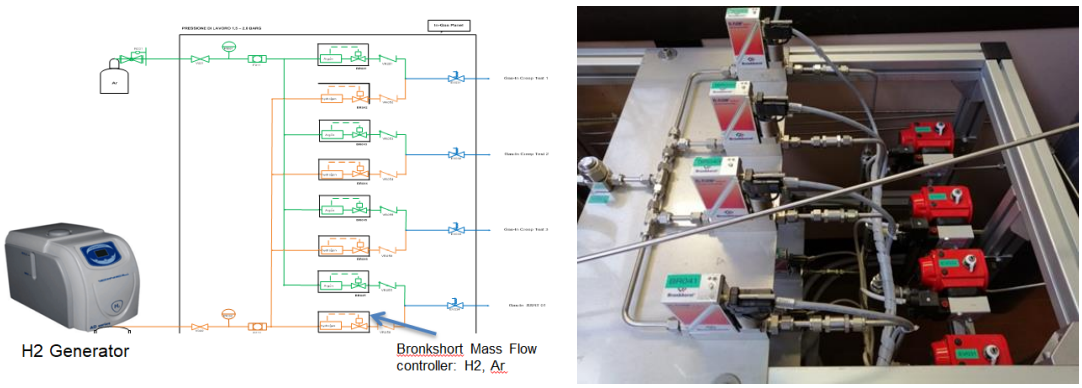

Figure 2.1.8. a) Scheme of the plant for the addition of the Ar/H2 mixture b) Picture of the components of the plant; pipes, pressure transducers and mass flow meters

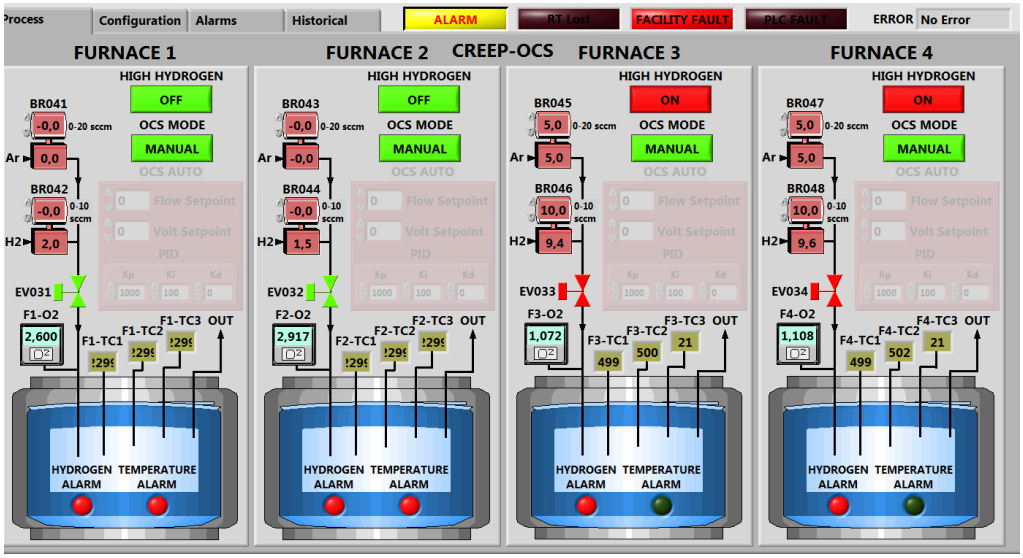

Figure 2.1.9. Dedicated software for the Oxygen control in the test sections

For the measurement of oxygen in lead, potentiometric sensors are used that measure a zero current electrical potential with high impedance. The electrical potential generated depends on the partial pressure of oxygen in the liquid metal, which in turn is related to the concentration of oxygen [1,2].
The sensor consists of a tube closed at one end made of solid ceramic material YPSZ (Yttria-partially Stabilized Zirconia) and of length 400 mm. Inside the ceramic tube, there are mixed oxide powders such as perovskite LSM / GDC (Lanthanum-Strontium-Manganite / Gadolinia-Doped-Ceria) and a 1.2 mm diameter AISI 316 stainless steel wire. The tube is open at the other end to allow independent air entry.
The YPSZ ceramic material of the tube is the conductor for oxygen ions O2- and is therefore the sensitive and selective material. The LSM-GDC powders, combined with the steel wire and the air that fills the cavity of the ceramic tube, form the reference electrode system, which has a known oxygen value (0.21 bar, the oxygen present in the atmosphere). The LSM-GDC powders are the catalyst for the dissociation and reduction of oxygen molecules in the air ($O2 \rightarrow O2^-$) while the electrode wire takes care of the current transport (almost zero due to the high impedance).
The scheme of the measurement of the oxygen concentration in lead is shown in Figure 2.1.10. The YPSZ ceramic tube wall divides two environments with different oxygen concentration. In particular, it divides the liquid metal, where the oxygen concentration is to be measured, from the air / perovskite reference system, where the oxygen concentration is always known (0.21 bar). As a result of the different oxygen concentration in the two environments, an electric potential E is generated through the ceramic element YPSZ.

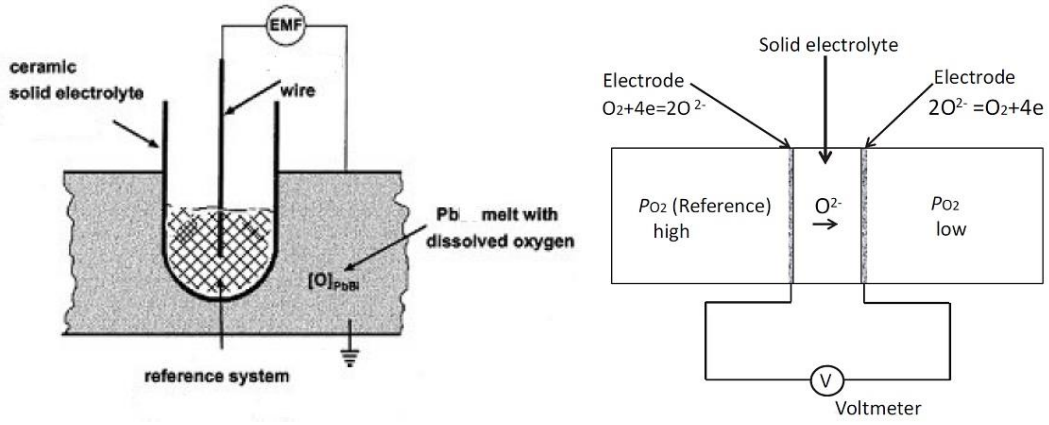

a) b)

Figure 2.1.10. a) Layout of an oxygen sensor for liquid lead [1]; b) its operation [2]

The air oxygen sensor / LSM-GDC has a minimum operating temperature of approximately 250°C in liquid metal. In liquid lead, the sensor can be used in the 350-700°C temperature range.
To calculate the dissolved oxygen concentration in lead from the electrical potential value of an air / LSM-GDC sensor, the following equation is used:

Pb: Eth, unsat (V) = 0.6340 - 0.0002293 T (K) - 0.0000431 T (K) lnCO% wt. (1)

When the oxygen concentration is equal to the solubility value (i.e. when lead is "saturated" with oxygen), equation (1) is simplified and becomes:

Pb: Eth, sat (V) = 1.1339 - 0.0005495 T (K) (2)

To operate under controlled oxygen conditions in lead, the electrical potential of the sensor must exhibit values around 1.0 V, in order to have an oxygen concentration between 10-8 and 10-6% by weight in the temperature range 350 - 700°C. From the electric potential value, it is possible to trace the oxygen concentration through equation (2).
To operate in oxygen saturation conditions, the sensor potential values follow the potential values given by the red line in the graph in Figure 2.1.11 and can be calculated using equation (1).

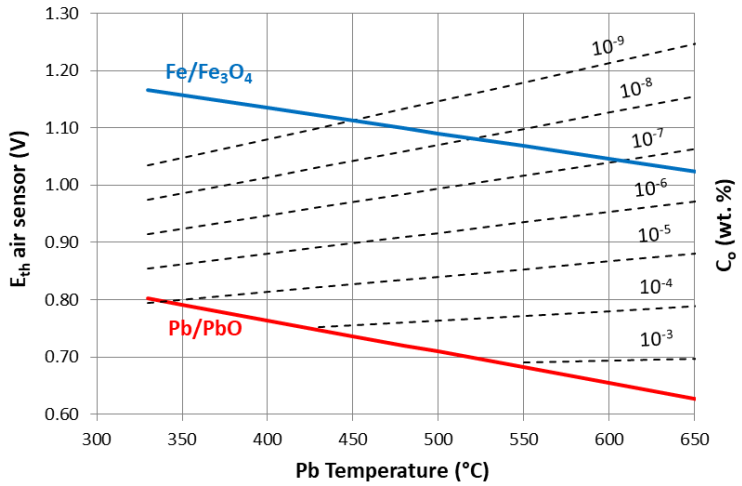

Figure 2.1.11. Potential vs Pb temperature graph for an air / LSM-GDC sensor. The red line indicates the potential for PbO formation (saturation of Pb with oxygen, maximum concentration). The blue line indicates the minimum electric potential necessary for the formation of the protective surface oxide on steels (Fe3O4, magnetite). On the right there are the oxygen iso-concentration lines (in% by weight)

The test section is operated in the oxygen concentration in the range 10^{-7} - 10^{-8} wt% in order to perform the tests with low oxygen concentration in representative LFR conditions.
The chambers are filled with lead in the ENEA lab where the crucible for lead melting is located. Lead is melted under controlled Oxygen atmosphere and the chambers, once filled, are then transferred cold (with lead solidified) to the mechanical testing lab. Here the chambers are heated again, up to the testing temperature, under controlled Oxygen atmosphere. Once the conditioning of the lead bath is achieved in terms of target Oxygen content, the test can start. The specimens are kept 20 hours in the conditioned lead bath (at 500°C for the tests at 550°C and at 400°C for the tests at 400°C) before launching the tests. This choice was agreed with the GEMMA partners in order to ensure a proper wetting of the specimen surfaces before starting the test. The test temperature is controlled by means of a resistance furnace and the stress by means of a 100 kN load cell installed on a hydraulic machine. The strain is controlled on the shaft connected to the sample by the couple of Magnetostrictive Linear Position Sensors (MLPS). The axial extensometer (12 mm gauge) attached to the gauged length of the specimen during the tests in air is removed during the tests in lead. The strain rate has been kept constant in a range between $5x10^{-5}$ and $5x10^{-6}$ s^{-1} according to the corresponding test condition.

2.1.5 Creep tests in air

In order to analyze the effect of lead on AISI 316L creep proprieties, creep tests were carried out in air and in lead at the same operative conditions and the results were compared. For the creep tests in air (testing procedure in agreement with ASTM E139:11) several frames (1:10 and 1:15 lever ratio) equipped with auto-levelling arm device and three zones P.I.D. controlled furnaces have been employed. The fixed temperature and load are applied by means of a resistance furnace and dead weights pile-up respectively. The deformation signal results from the average value of a couple of LVDTs (Linear Voltage Displacement Transducers) directly connected to the gauged length of the sample (fig. 2.1.12).

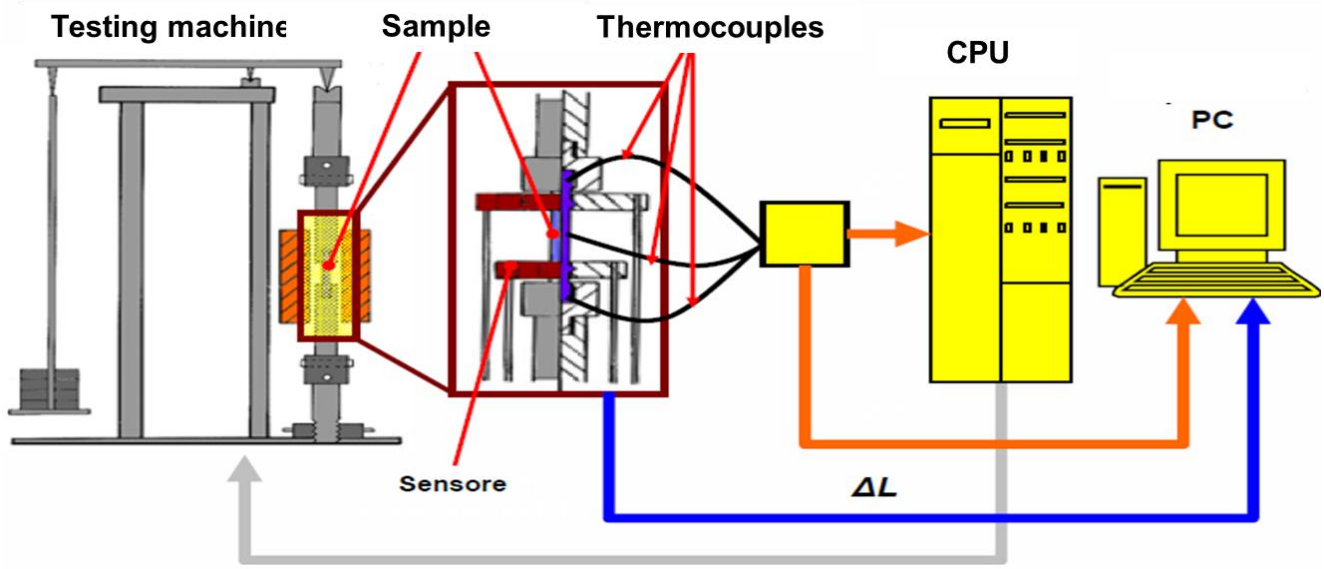

Figure 2.1.12. Schematic drawing of the creep testing instrumentation

The cylindrical geometry of the samples used in the creep tests is the same as for the SSRTs: 4.5 mm diameter and 20 mm gauged length. By means of a couple of LVDT (Linear Voltage Displacement Transducer) mounted on each specimen the deformation of the gauged length of the sample (the average of the signals from the two LVDTs) is recorded all over the duration of the test (fig. 2.1.13).

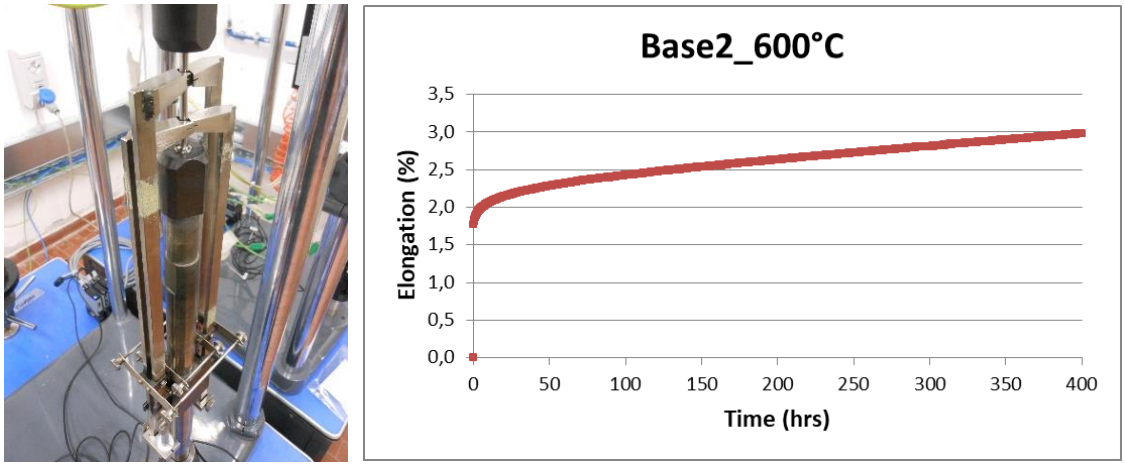

a) b)

Figure 2.1.13. a) Detail of the assembling of the LVDTs on the sample; b) Example of a recorded curve: 316L(N) base material (2nd batch) – 217 MPa 600°C

The analysis of the deformation trend recorded during the creep test implies, in addition to the ttR (time to rupture), when achieved, the calculation of the steady state creep rate. This can be achieved by fitting the "deformation (pure number) – time" plot by an exponential function as reported below;

$$\varepsilon_F = \varepsilon_0 + \varepsilon_p \left(1 - exp\left(-t/t_p\right)\right) + \dot{\varepsilon}_{ss} t$$

where $\varepsilon_0, \varepsilon_p, t_p, \dot{\varepsilon}_{ss}$ are all parameters typical of the material in the considered stress-temperature conditions and can be solved by iteration in order to achieve the "$\dot{\varepsilon}_{ss}$" coefficient, just representing the steady state creep rate. For example, applying a fitting curve of this kind to the experimental curve above by means of "Kaleidagraph 4.0" code one can obtain $\dot{\varepsilon}_{ss} = 1{,}8 \cdot 10^{-5} h^{-1}$ (fig. 2.1.14).

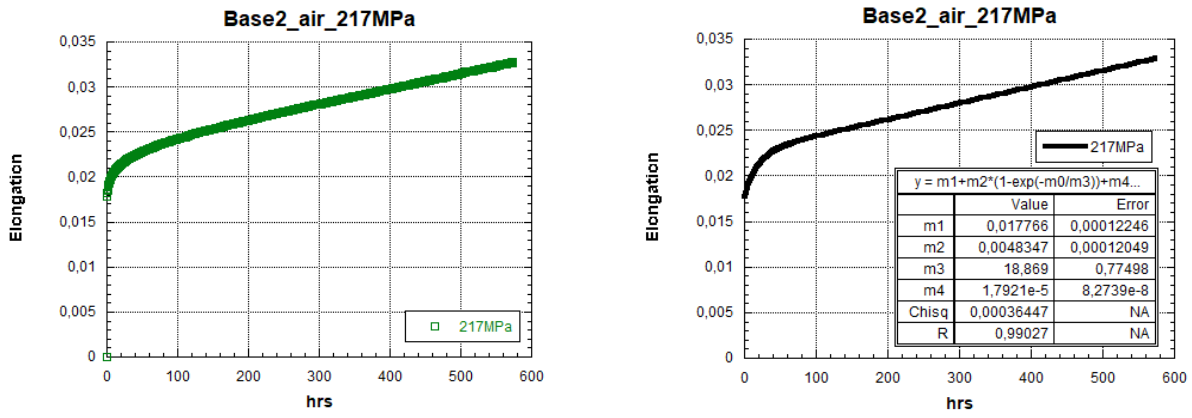

Figure 2.1.14. Fitting of the creep curve in order to obtain the $\dot{\varepsilon}_{ss}$ (steady state creep rate) value.

For the creep tests of GEMMA Project, two additional LVDTs are attached to the shaft connected to the sample (see fig. 2.1.15), mounted externally to the furnace. These are meant to record the deformation for comparison with the tests in lead, where it isn't possible to attach the LVDTs directly to the sample (flooded in lead), but only these last "external" LVDTs are left. In figure 14 we can notice that the sensor of the external LVDTs is placed at the lower left and right side; in order to bring the signal there, a rod is needed to connect the upper arm; this rod is subjected to environmental temperature variations; namely the rod lengthens and shortens according to room temperature oscillations. Then the signal is not straight, as it would be for the LVDTs directly connected to the specimens for the tests in air (fig. 2.1.16 a), but it is characterized by these fluctuations (fig. 2.1.16 b). Nevertheless, once we plot the curves from the two alternative measurements on the same graph (fig. 2.1.17), these curves appear almost superposed. Since the target is to assess the creep rate, namely the slope of the secondary creep stage, these fluctuations are considered acceptable. Moreover, a correction on the value of the initial deformation is necessary; namely, comparing the plots of figure 10, we can notice that the initial deformation is higher in the curves from the external LVDTs. This is expected as a consequence of measuring the deformation of the whole load train, which implies having higher elastic deformations related to the absorption of the jokes at the mechanical connections (threads, pins etc.). It is therefore assumed that the initial deformation is the same when comparing the trend of the external and internal (namely directly attached to the gauged length of the sample) LVDT signal.

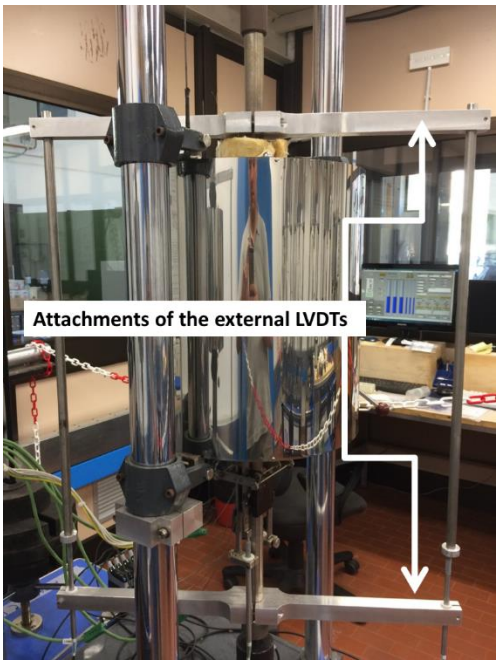

Figure 2.1.15. Detail of the assembling of the external LVDTs

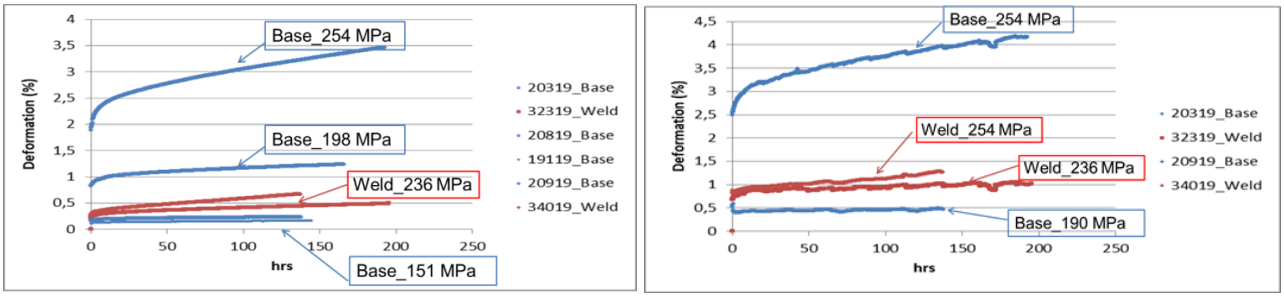

a) b)

Figure 2.1.16. (a) Creep curves from the LVDT directly connected to the sample (b) Creep curves from the LVDT connected to the external attachments

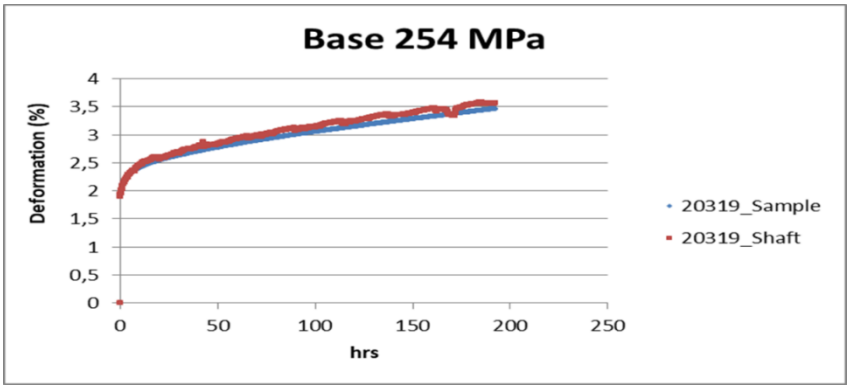

Figure 2.1.17. Superposition of the creep curves from the two couples of LVDTs for the same test in air.

2.1.6 Creep tests in lead

The equipment and the test sections used for the creep tests in Lead are the same employed for the SSRTs. The only differences rely on the acquisition of the deformation signal which is achieved by means of the couple of external LVDTs, as reported in the previous chapter. Moreover, as for the SSRTs, the specimens are kept 20 hours in the conditioned Lead bath (at 500°C for both the tests at 500°C and at 600°C) before launching the test in order to ensure a proper wetting of the specimen surfaces at the test start.

The analysis of the curves and the assessment of the corresponding creep rate, by means of the Kaleidagraph 4.0 fitting, of the Base and Weld material (600°C, 217 MPa) is hereby reported as example (fig. 2.1.18-2.1.20).

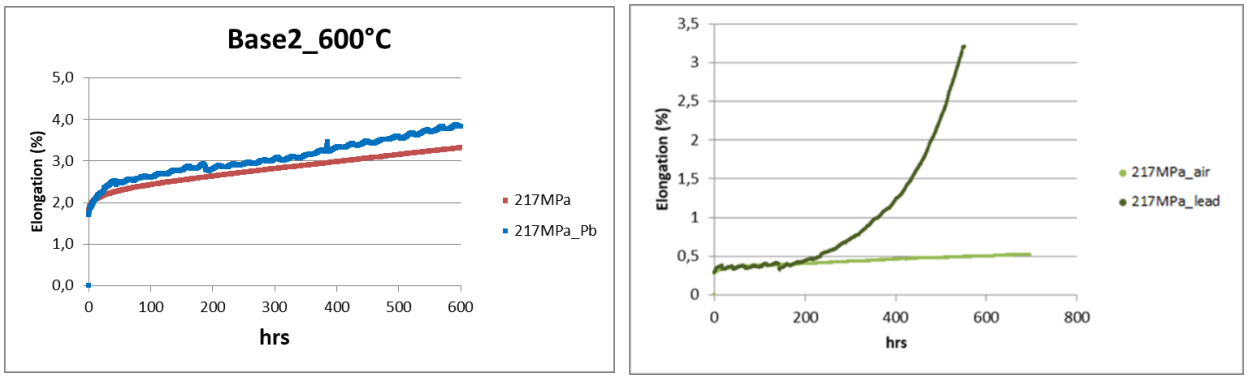

Figure 2.1.18. Comparison of the creep curves in air and in Lead for the base and weld material (600°C, 217 MPa)

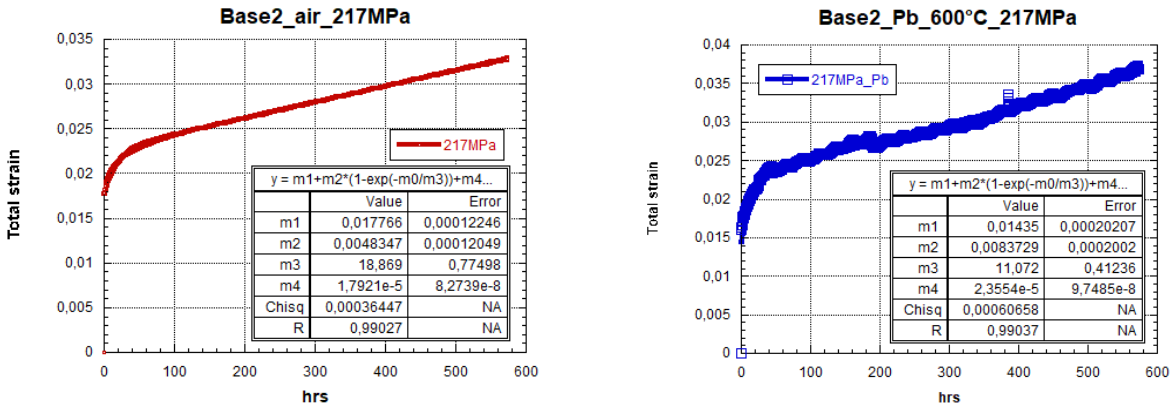

Figure 2.1.19. Comparison of the estimated creep rates (fitting parameter m4 in the tables) in air and in Lead for the base material (600°C, 217 MPa)

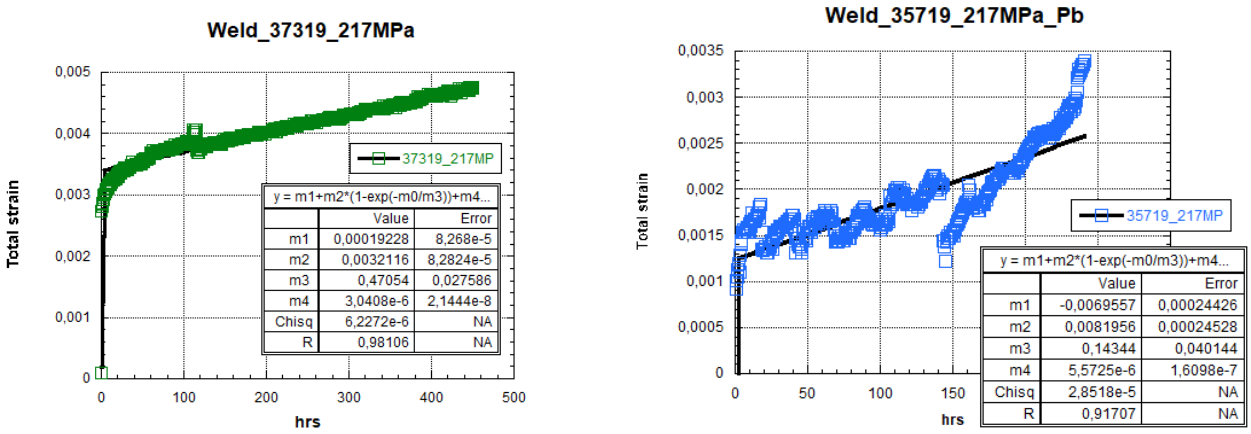

Figure 2.1.20. Comparison of the estimated creep rates (fitting parameter m4 in the tables) in air and in Lead for the weld material (600°C, 217 MPa)

2.1.7 References

[1] J. Konys, H. Muscher, Z. Vos, O. Wedemeyer, “Development of oxygen meters for the use in lead-bismuth”, J. Nucl. Mater. 296 (2001) 289-294.

[2] Y. Kurata, “Application of electromotive force measurement in nuclear systems using lead alloys”, Electromotive Force and Measurement in Several Systems (2011) Prof. Sadik Kara (Ed.), InTech, available at: http://www.intechopen.com/books/electromotive-force-andmeasurement-in-severalsystems/application-of--electromotive-force-measurement-in-nuclearsystems-using-lead-alloys

2.2 Description of the experimental procedures adopted to characterize the RAFM steels taken into account in the frame of Eurofusion WPMAT Project

2.2.1 Summary of the alloy design strategies for the choice of the compositions and the fabrication of the steels

The "water-cooled" breeding blanket option implies that the minimum irradiation temperature is around 280°C. Therefore, in the frame of Eurofusion WPMAT-AS task, in light of the under irradiation behaviour of EUROFER, namely of the DBTT shift, the target is the development of tougher alloys, able to tolerate the low irradiation temperature. The experimental evidences reported in the references cited in the introduction leaded ENEA to define the rationale for the fabrication of the new steels as follows:

- To reduce the secondary carbide precipitation at the tempering temperature (VN, TaN) in order to make the material as much tough as possible but keeping mechanical properties in an acceptable range. The content in Nitrogen and Vanadium was decreased in order to have a slightly softer matrix and to reduce secondary precipitation; a substantial reduction in the contents of those elements that foster carbide precipitation (V, N) is expected to be beneficial, as it was demonstrated in the past for EM10 and ORNL low Cr steels.
- To keep the Tantalum and Carbon concentrations at the same or slightly increased value of Eurofer and ORNL 9 Cr steel to obtain the amount of primary precipitation required to refine the PAGS (Prior Austenite Grain Size).
- To apply multiple austenitization treatments before tempering in order to have at the same time smaller PAGS and finer primary precipitation of Tantalum Carbides.

On the other hand, the "helium-cooled" breeding blanket option implies a high range of operational temperature; from the cases examined in the literature survey it appears beneficial, in terms of creep resistance, to increase Tantalum and Vanadium content. The expected outcome of this action would be an increase in the precipitation of carbo-nitrides, aimed at the dislocations pinning during the ausforming, in order to improve the creep resistance of the steel.
Concerning TMT it's worth investigating the effects of an Austenitization temperature in a range around 1180 °C in order to foster the solubility of carbides. The constraint on the small PAGS to increase toughness is in fact much less severe in the case of the steels for high temperature applications. Concerning the Ausforming temperature, a range between 650 and 750°C shouldn't result detrimental for the formation of Pearlite. This range of hot rolling temperatures, consistent with the outcomes of the literature survey concerning A21, Grade 91 and NPM alloys, is expected to better foster the mobility of the precipitates and to keep in an acceptable range the loads on the rolling machine; namely the higher the hot-rolling temperature, the lower the loads necessary to obtain a section reduction ratio in the order of 30/40 %.

2.2.2 Chemical compositions of the considered alloys

Several alloys are taken into account; either commercial, directly supplied by Project partners, like Eurofer 97/2 (Eurofusion WPMAT-AS), or also experimental, namely casted VIM (Vaacum Induction Melting) by ENEA industrial partner; RINA-CSM. The following table is meant to summarize the chemical compositions taken into account (tab. 2.2.1). The 3229 alloy is the same chemical composition (from the point of view of the chemical specifications) as the 3126 alloy. This ingot was just produced in order to supply additional material in order to perform fatigue and creep-fatigue tests.

Heat	Producer	Project	Chemical compositions (wt%)												
			Cr	C	Mn	V	W	Ta	N	Ni	Mo	Co	Si	S	P
Eurofer -97/2	Saarschmiede	Eurofusion WPMAT	9	0.11	0.4	0.2	1	0.12	0.03	-	-	-	-	-	-
3125	RINA-CSM	Eurofusion WPMAT	9	0.12	0.1	<0.05	1.8	0.15	0.002	-	-	-	-	-	-
3126	RINA-CSM	Eurofusion WPMAT	8.7	0.13	0.49	0.25	1.88	0.14	0.032	-	-	-	-	-	-
3229	RINA-CSM	Eurofusion WPMAT	8.8	0.12	0.49	0.26	1.85	0.14	0.029	-	-	-	-	-	-

Tab. 2.2.1. Chemical compositions of the steels taken into account

2.2.3 Thermo-mechanical treatments (TMT) of the considered alloys

Several kinds of TMTs have been carried out at RINA-CSM; the Recrystallization one (fig. 2.2.1), whose scope is to refine as much as possible the ferritic grain, and the Ausforming one (fig. 2.2.2) aimed at improving creep resistance by dislocation pinning through precipitation. The following tables (tab. 2.2.2, 2.2.3) are meant to summarize the TMTs taken into account.

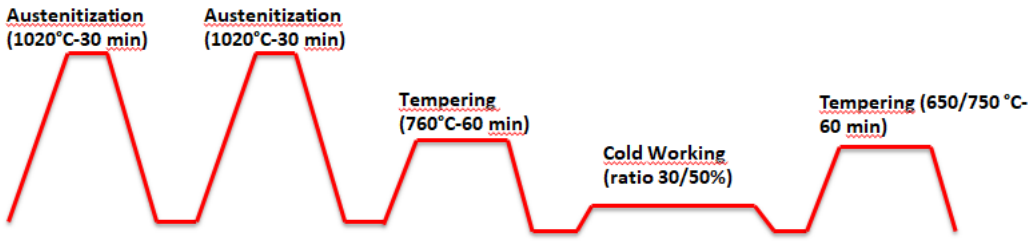

Figure 2.2.1. Typical "Recrystallization" TMT

Heat	Stages of the TMT						
	1st Austenitization	2nd Austenitization	1st Tempering	Cold working	2nd Tempering	2ndCold working	3rd Tempering
Eurofe 97/2	1020°C-30 min.	1020°C-30 min.	760°C-60 min.	30%	750°C		
	1020°C-30 min.	1020°C-30 min.	760°C-60 min.	40%	650°C		
	1020°C-30 min.	1020°C-30 min.	760°C-60 min.	50%	550°C		
3125	980°C-60 min.	980°C-60 min.	760°C-60 min.	-	-		
	980°C-60 min.	980°C-60 min.	760°C-60 min.	50%	550°C		
3126	1020°C-30 min.	1020°C-30 min.	760°C-60 min.	50%	550°C		
	1020°C-30 min.	1020°C-30 min.	760°C-60 min.	50%	550°C	50%	550°C

Tab. 2.2.1. Experimented "Normalization & Tempering" thermal treatments and "Recrystallization" TMTs

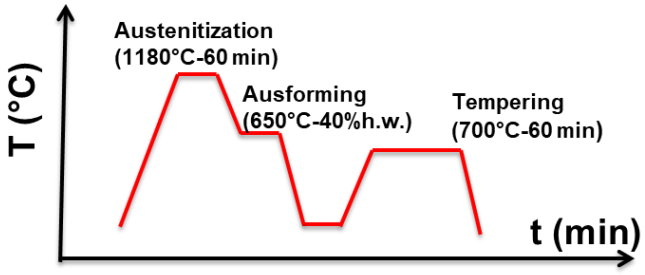

Figure 2.2.2. Typical "Ausforming" TMT

Heat	Stages of the TMT		
	Austenitization	**Ausforming**	**Tempering**
3126	1180°C-60 min.	650°C-40%	700°C-60 min.
	1180°C-60 min.	650°C-60%	700°C-60 min.
	1180°C-60 min.	-	700°C-60 min.
3229	1180°C-60 min.	650°C-40%	700°C-60 min.

Tab. 2.2.2. Experimented "Ausforming" TMTs

Let's consider the issue of the possible Pearlite transformation during hot-rolling. The following graph (fig. 2.2.3) shows the TTT curves for Eurofer, obtained by JMat-Pro code, demonstrating how (even considering an over-estimation of 1 order of magnitude in the code with respect to the experimental) the Pearlite transformation is not reached during Ausforming at a temperature around 700°C. Therefore, in order to foster the mobility of the precipitates and to avoid too high loads on the rolling machine, the Ausforming temperature has been kept in this range.

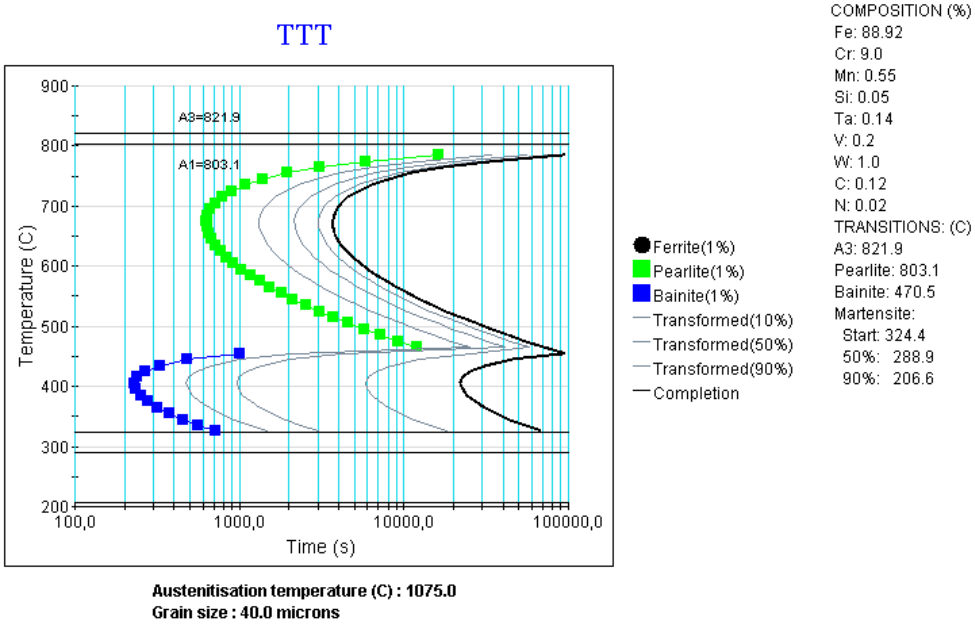

Fig. 2.2.3. TTT curves for Eurofer obtained with Jmat-Pro code**.**

2.2.4 Rationale for the mechanical characterization reported in the following chapters

The screening on the mechanical properties of the considered RAFM steels reported and discussed in the following chapters is carried out in light of the following alternative scenarios according to the operational temperature of the DEMO Breeding Blanket;

- The "low temperature option", namely the WCLL, implying a reference temperature of 300°C, the target is to increase as much as possible the toughness and decrease the DBTT. The 3125 chemical composition, the double normalization and the recrystallization treatments are aimed at this target.
- The "high temperature option", namely the DCLL, implying a reference temperature of 650°C, the target is just to maintain an acceptable DBTT, just in order to grant safe manufacturing and assembling processes at room temperature; (-20°C could be sufficient) pursuing the highest possible creep resistance (20000 hrs at 100MPa / 650°C as a "wishful thinking") and a LCF (Low Cycle Fatigue) resistance in the range of 10000 cycles at 650°C. The 3126 and 3229 chemical compositions, as well as the ausforming treatment are aimed at this target.

2.2.5 Impact tests at cryogenic temperatures

The specimens taken into account are the KLST ones; these differ from standard Charpy ISO-V in terms of dimensions; 4x3x27mm^3 (KLST) instead of 10x10x54mm^3 (Charpy ISO-V). The reference standard for these particular impact tests is the DIN-50115. While the Charpy ISO-V specimens are tested by means of a big size pendulum (360 J capacity), the KLST ones have to be tested on a small size pendulum (75 J capacity). The small size pendulum located in ENEA Brasimone laboratory is equipped with three hammers; 15, 25 and 50 Joule respectively. The 25 J size one has been calibrated by means of a set of calibrated specimens provided by NIST (National Institute of Standards and Technology, USA). The set of 9 calibrated specimens consists of three batches of 3 samples, each one of these meant to test one range of energy in particular, namely the "Low", "High", and "Super-High Energy". The certificates corresponding to each one of these 3 batches are hereby reported (fig 2.2.4).

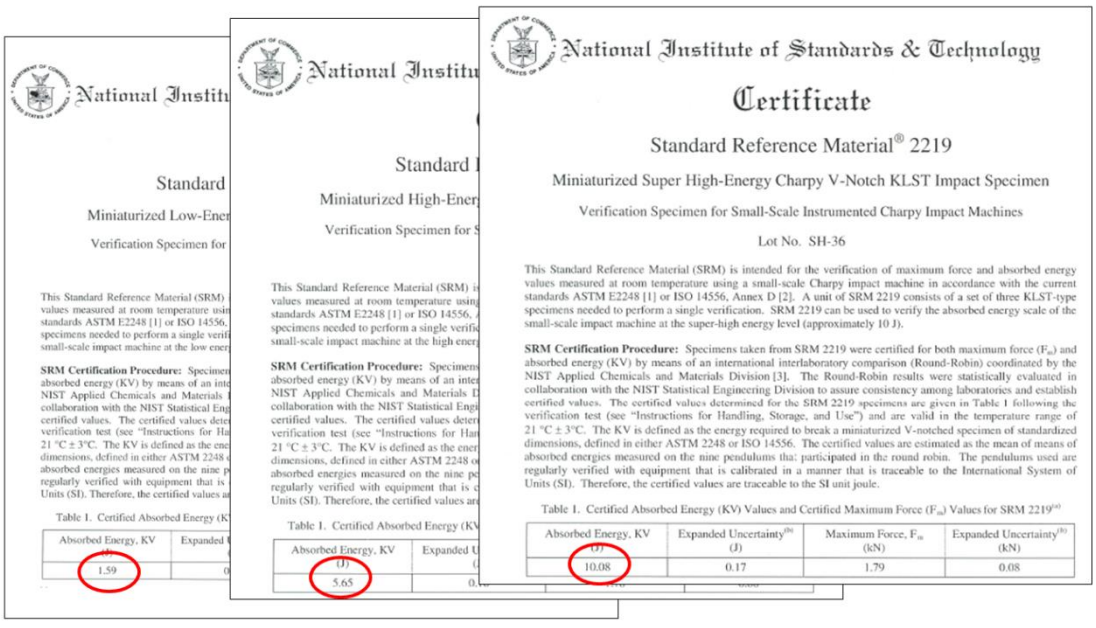

Figure 2.2.4. Certificates for the calibration of the Low, High and Super- High energy values from testing of V-notch KLST Impact Specimens

Once the specimens have been broken on the pendulum located at ENEA Brasimone, the energy values have been recorded and fitted by a function representing the correction coefficient to be applied on the achieved values of energy every time a set of specimens is tested. The achieved NIST values of energy as function of the achieved BRASIMONE values and the corresponding fitting function are reported in the next picture (fig. 2.2.5).

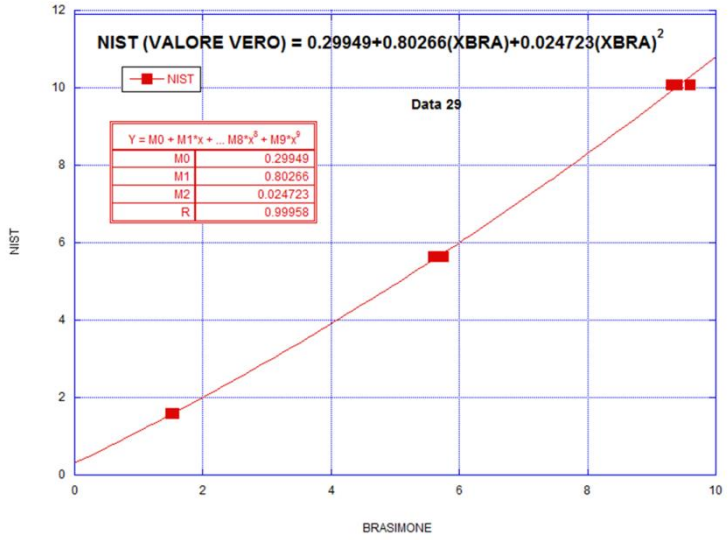

Figure 2.2.5. Fitting function correlating the values reported in NIST certificates to the ones achieved in ENEA Brasimone

In order to draw the trend of the DBTT (Ductile to Brittle Transition Temperature) it's necessary to test the specimens at cryogenic temperatures; namely in the range between 0°C and -196°C. In order to fulfill this target an instrumentation just aimed at the management of the cryogenic temperatures has been bought and installed in ENEA Brasimone. This conditioning device (fig. 2.2.6 b) is able to set and control the temperatures even under the solidification point of alcohol (the fluid used in traditional instrumentations of this kind, which solidifies at 90°C approx.), down to the liquefaction temperature of Nitrogen (-196°C).

a) b)

Figure 2.2.6. a) 60J capacity pendulum (CEAST) installed at ENEA Brasimone b) Conditioning device for the cryogenic temperatures

In order to assess the temperature increase due to the transfer of the sample from the conditioning device to the pendulum, a sample has been instrumented with a "T" thermocouple. The temperature increase has then been measured during the transfer of the specimen from the conditioning device to the pendulum. The duration of the transfer has then been recorded each time by means of a digital stopwatch. The measurement has been repeated three times for each temperature and the measured increase of temperature with time has been fitted by a 3rd degree polynomial function. Some examples of the achieved fitting functions at different temperatures are reported in the next figure (fig. 2.2.7).

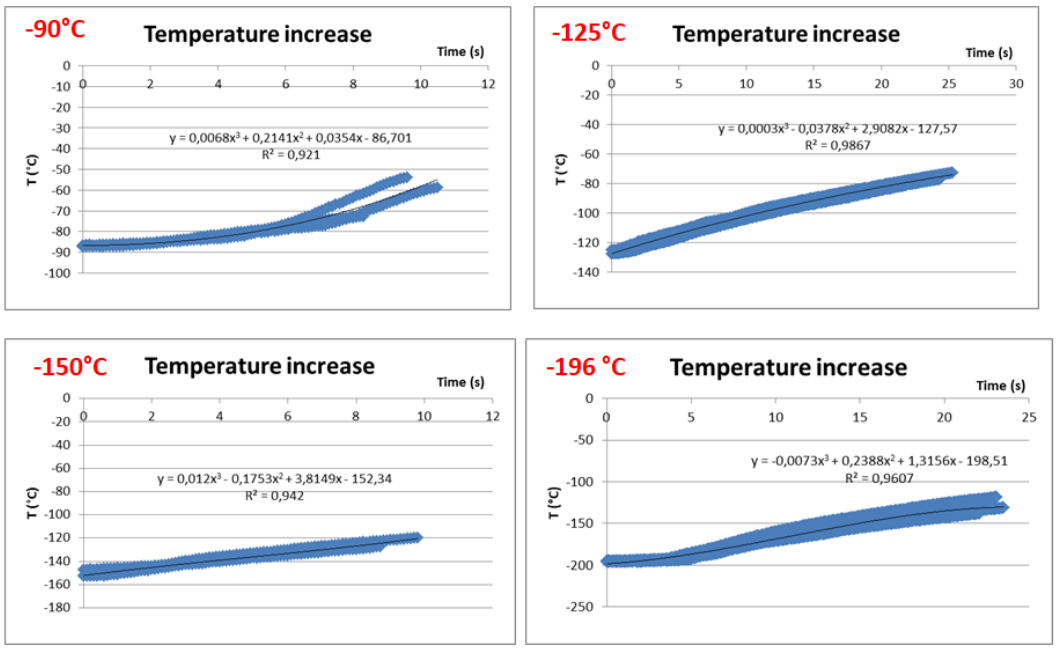

Figure 2.2.7. Fitting functions for the temperature drop at each experimental temperature

For each specimen tested the time delay due to the transfer of the sample is recorded and the temperature assessed by means of the fitting functions previously drawn.

Once the experimental points (absorbed energy as function of temperature) are achieved, the fitting function is drawn according to the following function (hyperbolic tangent);

$$E = \frac{USE + LSE}{2} + \frac{USE - LSE}{2} * \tanh\left(\frac{T - DBTT}{A}\right)$$

Where E is the absorbed energy, USE the Upper Shelf Energy, LSE the Lower Shelf Energy, T the temperature (variable), A a coefficient representing the smoothness of the transition, and DBTT is the Ductile to Brittle Transition Temperature. An example of DBTT fitting is reported below (fig. 2.2.8).

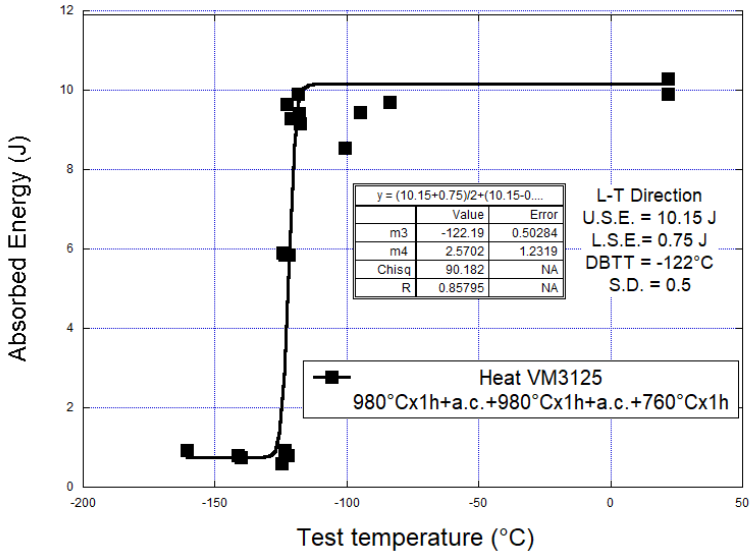

Figure 2.2.8. Fitting Curve for the impact tests of Heat VM3125

2.2.6 Standard tensile tests on cylindrical and flat specimens

In the frame of the "Eurofusion WPMAT-AS" project, tensile properties (Rp02-Yield Strength, UTS-Ultimate Tensile Strength, UE-Uniform Elongation and TE-Total Elongation) have to be measured on each of the proposed combination of chemical compositions with Thermo Mechanical Treatments. Tensile tests (according to ASTM E8/E8M:2013) have been carried out on an electro-mechanical machine equipped with a 50 kN load cell; the cylindrical geometry of the samples used in the tensile tests is the following: 6 mm gauged diameter and 33 mm gauged length (according to ASTM E8/E8M:2013). Tensile tests have been carried out controlling the crosshead displacement. An extensometer is applied on the gauged length of the sample during the tests in order to record the strain all over the test duration both at room temperature and at high temperature. The strain rate is kept equal to 0,015 mm/mm/min to determine the Yield Strength and further, up to the achievement and exceeding of the UTS.

One of the treatments considered for the development of RAFM steels as structural materials for DEMO Fusion Reactor is the "Recrystallization" treatment which implies heavy cold-working ratios and then very narrow thicknesses for the final sheet metal. Therefore, in order to test the tensile properties of these particular products, a flat sample (thickness equal to 3 mm extracted from a 5 mm thick plate) is required. The tensile tests on the flat samples have been carried out according to UNI-EN ISO 6892-2: 2011; the flat geometry of the samples used in the tensile tests is the following: 3x12,5 mm^2 gauged section and 48 mm gauged length (again according to UNI-EN ISO 6892-2: 2011). An extensometer is applied on the gauged length of the sample (fig. 2.2.9) during the tests in order to record the strain all over the test duration both at room temperature and at high temperature (300°C).

Figure 2.2.9. Details from the tensile tests on flat samples

2.2.7 Low Cycle Fatigue (LCF) tests and Creep Fatigue (CF) tests

LCF (low cycle fatigue) properties have then been investigated on the 3126 alloy (2wt.% W RAFM steel) with standard (normalization, air quenching and tempering) and ausforming (normalization, air quenching, hot rolling and tempering) heat treatment. The experimental set-up (Fig. 2.2.10 a) used to perform LCF and CF (creep fatigue) tests consists of the following components: hydraulic press (MTS), load cell (operation range: ± 100 kN), extensometer (12 mm gauged length) and induction furnace (6 kW). An extensive optimization process has been carried out on the induction furnace shape in order to keep the temperature profile constant along the gauged length, achieving a tolerance within ±2 °C. A Control Unit with embedded software allows great flexibility in mixing fatigue cycling with creep hold times. The samples for the tests were manufactured according to ASTM 2714-09 and have undergone statistic quality controls after production in order to verify their fulfilment to specifications in terms of surface roughness and dimensional tolerances. Fig. 2.2.10 b) illustrates a detail of the installation of the specimen for low cycle fatigue testing on the hydraulic machine together with the annexed equipment; induction furnace (the red coils surrounding the sample); axial extensometer (the white rods connected to the sample); pyrometer for the optical assessment of the temperature of the specimen (in the background).

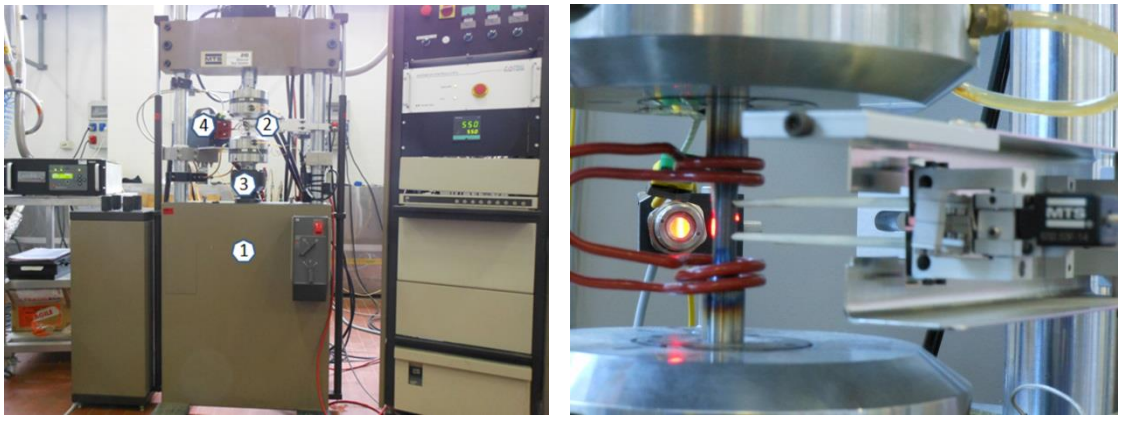

a) b)

Figure 2.2.10. (a) Experimental instrumentation; 1) MTS machine, 2) Extensometer 3), Load cell, 4) Induction furnace (b) detail of the assembling of the sample

The fatigue strain was controlled in terms of total strain (elastic + plastic), which was measured and controlled by the extensometer. The wave shape was triangular and the parameters of the test (total strain amplitude and frequency) are listed below:

- $\Delta\varepsilon_{tot}$ =1%, 0.6%, 0,4%, 0,3%
- Frequency = 0.1 Hz

The Creep fatigue (CF) tests differ from standard LCF tests by the interposition of hold-times within the cyclic testing. During CF tests, the stress level is held constant during holding periods. The strain is the controlled parameter in tensile and compressive peaks and it becomes the feedback signal during the hold-time. The load, on the other hand, is the feedback signal in tensile and compressive peaks and becomes the controlled parameter during the hold-time (Fig. 2.2.11).

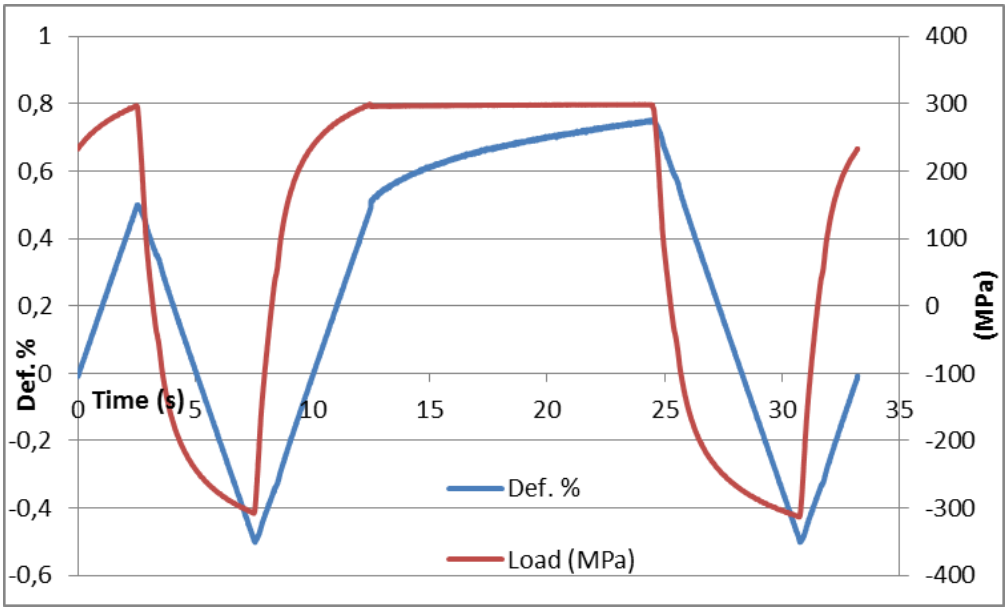

Figure 2.2.11. CF cycle; HT tension 12 s; stress-strain behaviour.

2.3 Experimental methods concerning the assessment of tensile properties by means of RC (Ring Compression) tests

The investigated material is 15-15 Ti austenitic steel. It has been produced by Sandvik and manufactured in the shape of tubes (outside diameter 6,5 mm, thickness 0,45 mm). The tubes have been supplied to ENEA by SCK-CEN (Belgian Nuclear Research Centre) in two manufacturing conditions; namely 24 % and 46 % cold working ratio. The following table (tab. 2.3.1) report the chemical composition of the 15-15 Ti austenitic steel. The results of the tensile tests carried out by the manufacturer (Sandvik) on the two batches of 24% and 46% cold worked material revealed a Yield Strength in the range of 700MPa and a UTS in the range of 800 MPa, quite high values, as expected for this cold worked steel filled with Titanium carbides precipitates.

Table 2.3.1 – Chemical composition of the 15-15 Ti steel.

Heat	Project	Cr	C	Mn	B	P	Ti	N	Ni	Mo	Co	Si	S
15-15Ti	TASTE	14-16	0.08-0.1	1-2	0.004	0.04	0.3-0.5	<0.015	14-16	1.3-1.7	<1	0.7 - 0.9	< 0.015

The Ring Compression tests were carried out at room temperature and at -196°C (liquid Nitrogen) inside the laboratory of ENEA Brasimone with electro-mechanical tensile testing machine MetroCom E50 (Fig. 2.3.1, a). equipped with a 50 kN Load cell. Each test has been performed keeping the speed of the crosshead constant to 0,2 mm/min. The test has been stopped when the tube resulted completely flattened. The typical curve resulting from the ring compression test is reported in the following graph (fig. 2.3.1, b).

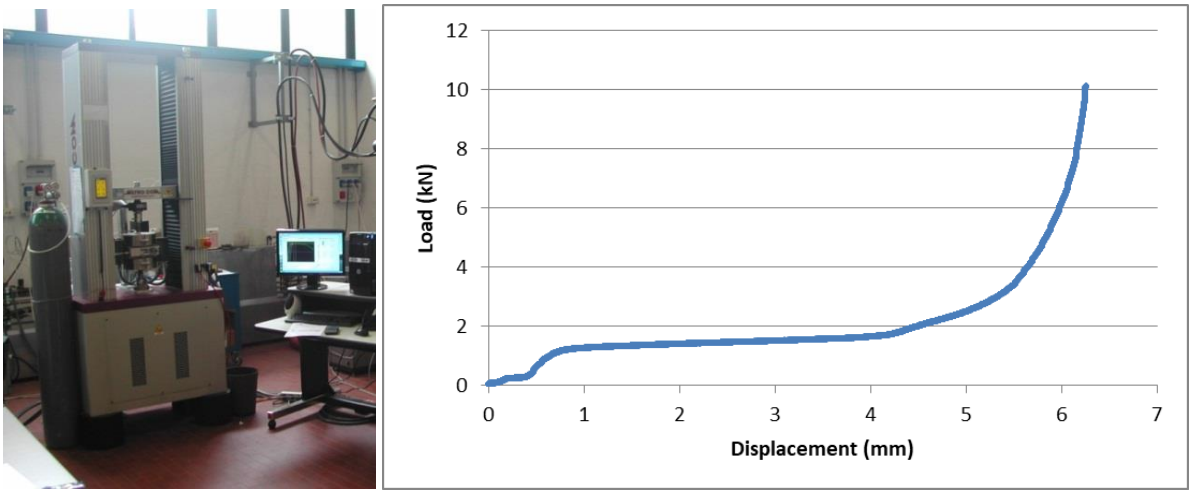

a) b)

Fig. 2.3.1: a) Metrocom E50 Machine; b) Deformation curve of the 20 mm length tube (24% c.w.)

The obtained curve can be approximately divided into three stages. In the first stage the load remains almost constant at the increasing deformation; this means that, during this phase, the plays in the crosshead grip assembly are being exhausted. This portion of the curve will be neglected in the analysis aimed at the determination of the tensile properties of the material. In the following portion of the curve the load increases rapidly with the deformation up to an elbow corresponding to the collapse load (see further). Once exceeded

this elbow, the load increases again with a linear and then parabolic law up to the complete crushing of the tube. A bilinear fitting has been performed on the linear stages (fig. 2.3.2) in order to determine the collapse load according to [6].

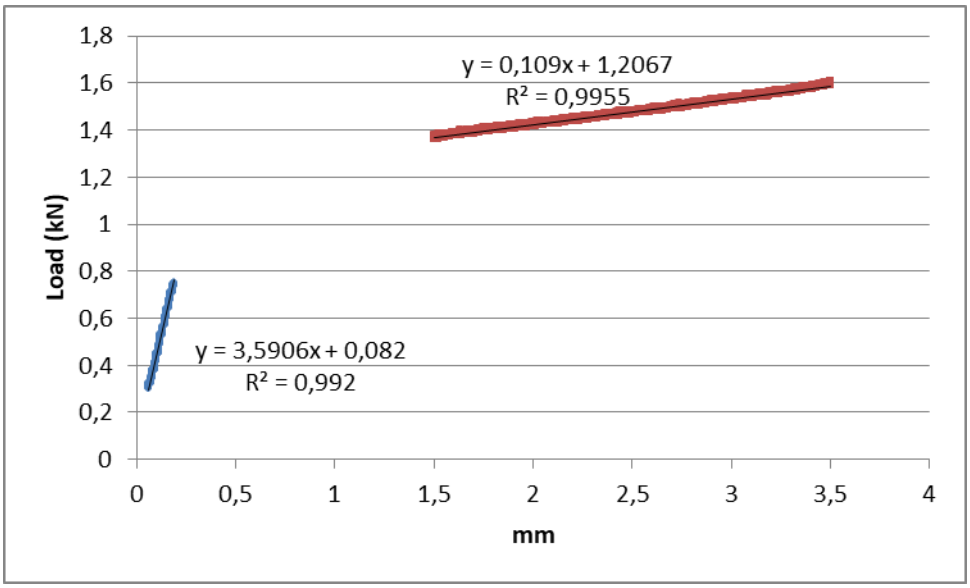

Fig. 2.3.2: Linear Interpolation to determine Collapse Load (20 mm; 24% c.w. tube)

The Collapse Stress has been calculated, in agreement with [3-6], according to the following formulation:

1) $Collapse\ Stress = \frac{\alpha P_0 R_0}{t_0^2 l}$

With:

α = 0,866 for tubes (longer than one diameter) or 1 for rings (length shorter than one diameter);

R_0 = initial outer radius;

t_0 = tube thickness;

l = length of the ring;

P_0 = initial collapse load, obtained by the graphical intersection between the linear interpolation of the first and second stages of the load-displacement curve.

The Collapse Stress has been correlated to the Ultimate Tensile Strength (UTS) through the following coefficient;

2) $K_{UTS} = \frac{Collapse\ Stress}{UTS}$ = 1,18 [15]

This calibration coefficient has been chosen according to the results reported in the final report of the former TASTE Pilot Project [15-16]; The Collapse Stress and the corresponding assessed UTS have then been identified for each c.w. ratio and environmental condition.

Tab. 2.3.2: Calculated parameters for one specimen (24% c.w., aged condition, room temperature)

Coefficient	Value	Unit
α	0,866	-
R_0	3,25	mm
t	0,45	mm
L	20	mm
Collapse Load	1,24	kN
Collapse Stress	863	Mpa
KUTS	1,18	-
UTS	731	Mpa

To reach the goal of assessing the UTS in different conditions, an aging heat treatment (700°C, 3000 hrs, inert atmosphere) has been carried out on several 15-15 Ti claddings, with different cold-working ratios (24 and 46 %). The aged and the "as received" claddings have then undergone a Ring Compression (RC) test in order to assess the UTS and detect any embrittlement effect, if occurring, both at room temperature and at -196 °C (liquid Nitrogen; fig. 2.3.4 b,c). The test matrix for the two C.W. conditions is hereby reported (tab. 2.3.3, 2.3.4).

a) b) c)

Figure 2.3.4 a) Aging of the claddings inside a sealed capsule filled with Argon b) RC test running in liquid Nitrogen c) Acquisition interface with the thermocouple reading of the cryogenic temperature

Cladding condition		Test Temperature	
		Room Temperature	-196°C
24 % Cold Working	As received (SCK-CEN)	2 tests	2 tests
	Aged (3000 hrs – 700°C)	2 tests	2 tests
46 % Cold Working	As received (SCK-CEN)	3 tests	2 tests
	Aged (3000 hrs – 700°C)	2 tests	2 tests

Tab. 2.3.3. Test matrix for the RC tests on the C.W. claddings

3 Chapter 3; Results

3.1 Outcomes of the SSRT and creep tests in lead in the frame of GEMMA Project

3.1.1 Technological issue on the first batch of base material

Hardness measurements and tensile tests were carried out on a set of samples derived from 316L plates (chapter 2.1.1), The first tensile curves achieved by SSRTs on the AISI316L base material didn't comply with the specifications of the RCC-MRx code [1]; namely the code defining the mechanical properties of the structural materials and the safety coefficients to be applied to the components of the French nuclear reactors. The mechanical properties resulted much higher than expected for a 316L(N) steel; at room temperature, for example, according to the RCC-MRx, the average value of the Yield Strength is 283 MPa, and the minimum value is 220 MPa; the average value of the Ultimate Tensile Strength is 584 MPa, and the minimum value is 524 MPa. The corresponding properties of the material we received resulted 350 MPa (YS) and 640 MPa (UTS) respectively.

Moreover, a detailed investigation was carried out in terms of hardness measurements on both the sides of each sample, as reported in the next figure (fig. 3.1.1).

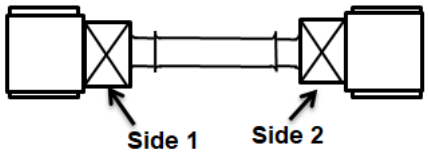

Figure 3.1.1. Position of the hardness measurements on the samples

The hardness measurements, reported in the next table (tab. 3.1.1), revealed a much higher value (290-300 HV) compared to the one that is expected for a 316L(N) steel (180-200 HV).

Sample code	HV_1 Side 1	HRC Side 1	HV_1 Side 2	HRC Side 2
18619	295	29,1	311,1	31,1
19319	294,4	29	301,7	29,9
19419	304,6	30,3	324,9	32,7
19519	316	31,7	301	29,8
19719	308,9	30,8	290,1	28,5
19919	298,4	29,5	292,5	28,8
20019	282,9	27,5	294,3	29
20219	297,2	29,4	286,8	28,1
20519	320,2	32,2	305	30,4
20719	293,4	28,9	309,7	30,9
21019	280	27,1	321	32,3
21219	275,1	26,4	267,1	25,1
21319	293	28,9	315,6	31,7

21519	265,5	24,9	286,3	28
21719	291	28,6	303	30
21819	283,8	27,6	282,8	27,5
22019	287,1	28,1	312,8	31,3
22119	300,2	29,7	286,6	28
22219	237,3	19,8	241	20,6
22319	305,3	30,4	310,8	31,1
22519	292,7	28,8	312,4	31,3
22719	299,9	29,7	279,7	27,1
22919	286,1	28	265	24,8

Table 3.1.1. Hardness measurements (HV_1 and HRC) on both sides of the first batch of base material (316L(N)).

The material properties reported in the certificate of the "virgin" plate (i.e. before welding) were in agreement with the specifications of the RCC-MRx. This lead us to think that something went wrong with the fabrication of the welded joint. Then it resulted that the manufacturer had welded additional transverse plates in order to avoid distortions during the fabrication of the main longitudinal weld (fig. 3.1.2).

Figure 3.1.2. Additional welded plates added by the manufacturer to avoid distortion during the fabrication of the main weld

Unfortunately, the effect of this action was the creation of additional HAZs (Heat Affected Zones) that modified the properties of the base material. Then we decided to fabricate new base specimens from the base material,using manual indentation data in order to identify the area of the plate not affected by heat treatment (Heat Affected Zone-HAZ) due to additional welded transverse plates. After the fabrication of the specimens from the base material they were tested in air. The difference between the tensile curves of the first and second batch of base materials are reported in the next plots (fig. 3.1.3, 3.1.4). The tensile properties from the second batch resulted compliant to the RCC-MRx specifications for the 316L steel. At last it's worth noticing the typical fluctuation of the plotted curve at the increasing temperature and decreasing strain rate; this behaviour is known as the "dynamic strain aging" phenomenon.

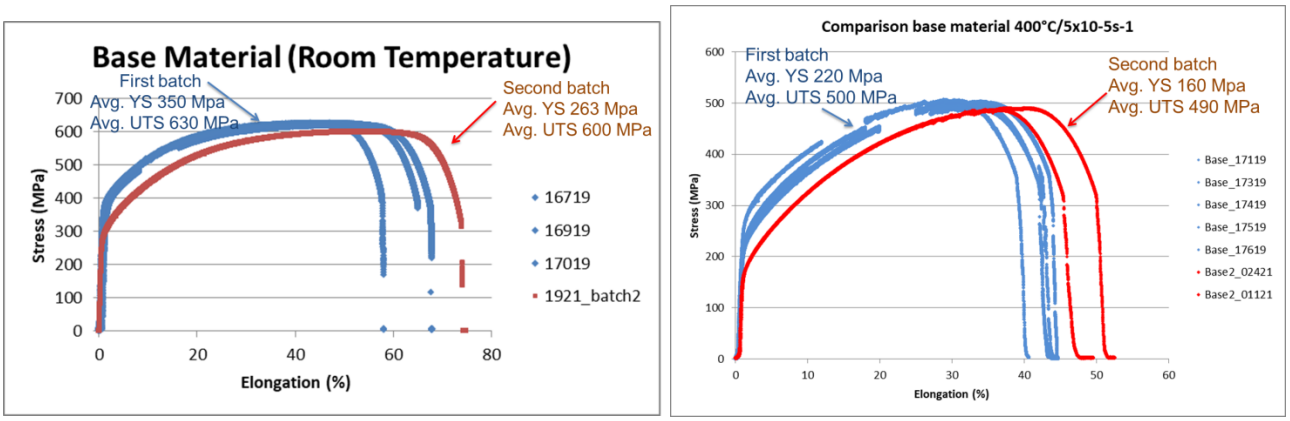

a) b)

Figure 3.1.3. Comparison between the tensile curves from the first (heat affected; blue curves) and the second ("virgin"; red curves) batch of base material specimens at $5x10^{-5}$ s^{-1} strain rate; a) at room temperature; b) at 400°C

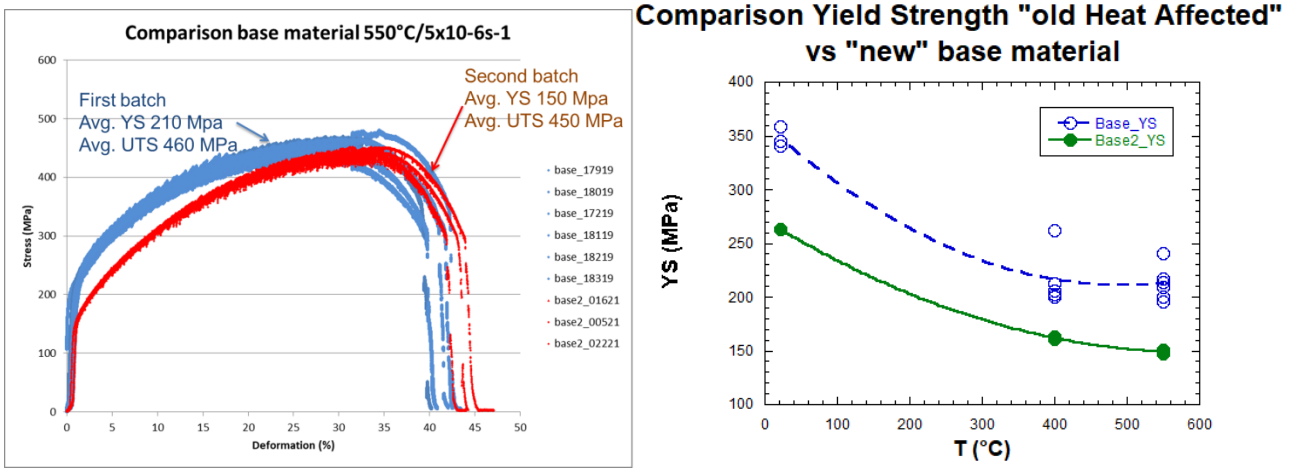

a) b)

Figure 3.1.4. a) Comparison between the tensile curves from the first and the second batch of base material specimens at 550°C / $5x10^{-6}$ s^{-1} strain rate; b) Trend of the Yield Strength as function of temperature for the two batches of base material

3.1.2 Slow Strain Rate Tensile tests (SSRT) in air

The tensile curves achieved by SSRTs on the AISI316L base material and on the weld material are hereby reported (fig. 3.1.5, 3.1.6); these tests are the benchmark for the characterization in liquid lead which will be described in the next chapters.

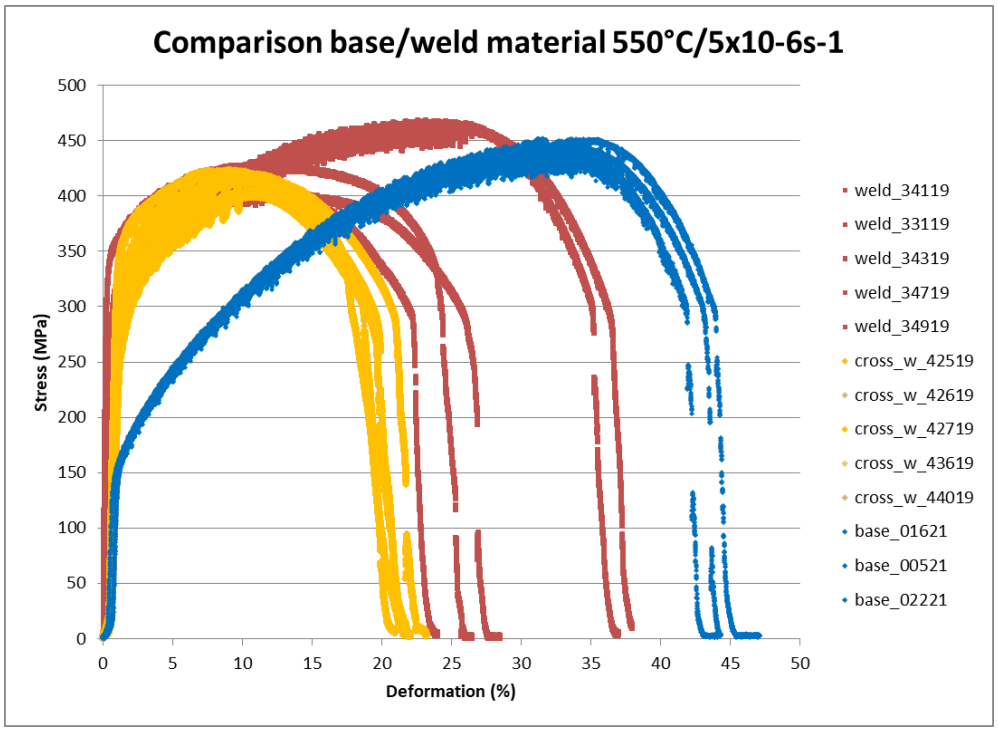

Figure 3.1.5. Tensile curves of the SSRTs carried out on AISI 316L base and weld material at 550°C ; $5x10^{-6}s^{-1}$

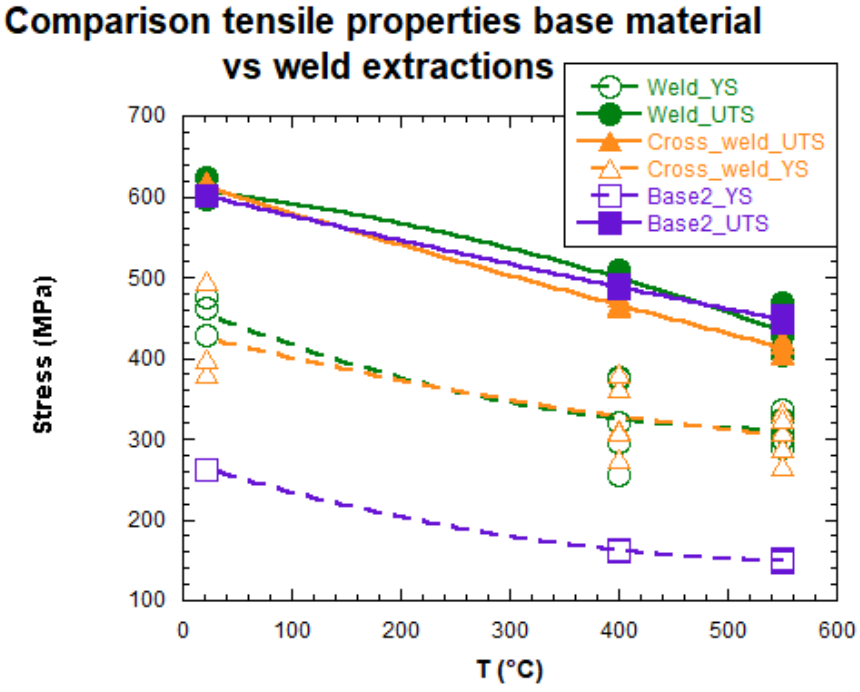

Figure 3.1.6. Trend of the tensile properties YS (Yield Strength) and UTS (Ultimate Tensile Strength) as function of temperature

We can notice the higher scatter in the curves from the weld material compared to the ones from the base material. By the way, we can state that the Yield Strength results markedly increased in the weld respect to the base while the deformation values (uniform and total elongation, as resulting from the deformation signal) appear averagely shorter. Namely the weld proves harder and less ductile than the base material. The UTS (Ultimate Tensile Strength) remains more or less the same.

3.1.3 Slow Strain Rate Tensile tests (SSRT) in Lead

The tensile curves achieved by SSRT in lead at 550°C/5x10^{-6}s^{-1} on the AISI316L base material are compared to the corresponding tests in air in Fig. 3.1.7. Apart from some little scatter within the statistical spread of the results related to the material, we can notice a different nature of the curves in HLM (Heavy Liquid Metal) respect to those in air; a sort of "plateau" corresponding to slightly lower values of the UTS appears in the tests in lead. Moreover, a higher total elongation (as it results from the recorded deformation signal) is symptomatic of an actual increase in ductility in the HLM. Therefore, we can state that the 316L base material doesn't seem to be affected at all by LME (Liquid Metal Embrittlement), but it appears indeed prone to increased ductility at 550°C/5x10^{-6}s^{-1}. This effect is consistent with some other evidences from literature, reporting the effect of liquid Lead on pure Iron [2]. At the temperature of 400°C and at 5x10^{-5}s^{-1} strain rate this effect is no longer visible; the tensile curves achieved in lead almost perfectly overlap with those obtained in air, with a very limited scatter in the tensile properties (Fig. 3.1.8).

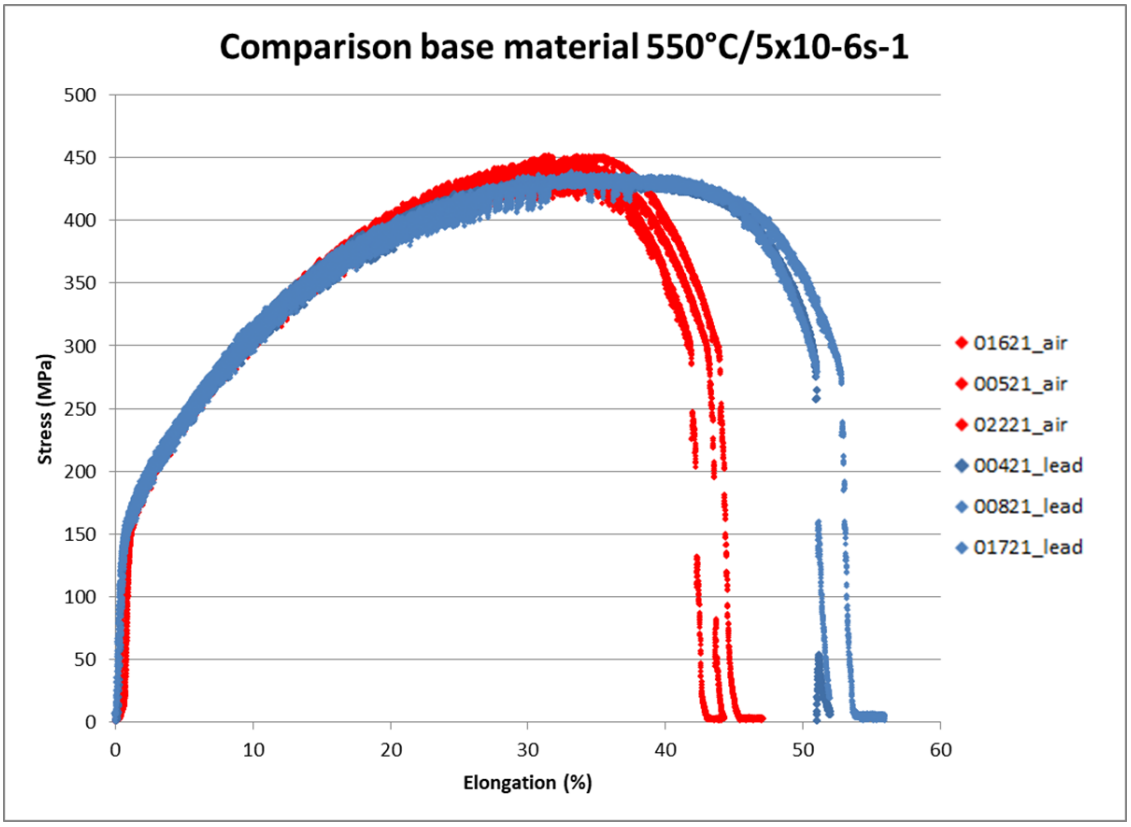

Figure 3.1.7. Comparison air / lead tensile curves resulting from the SSRTs carried out on AISI 316L base material at 550°C, 5*10^{-6}s^{-1} .

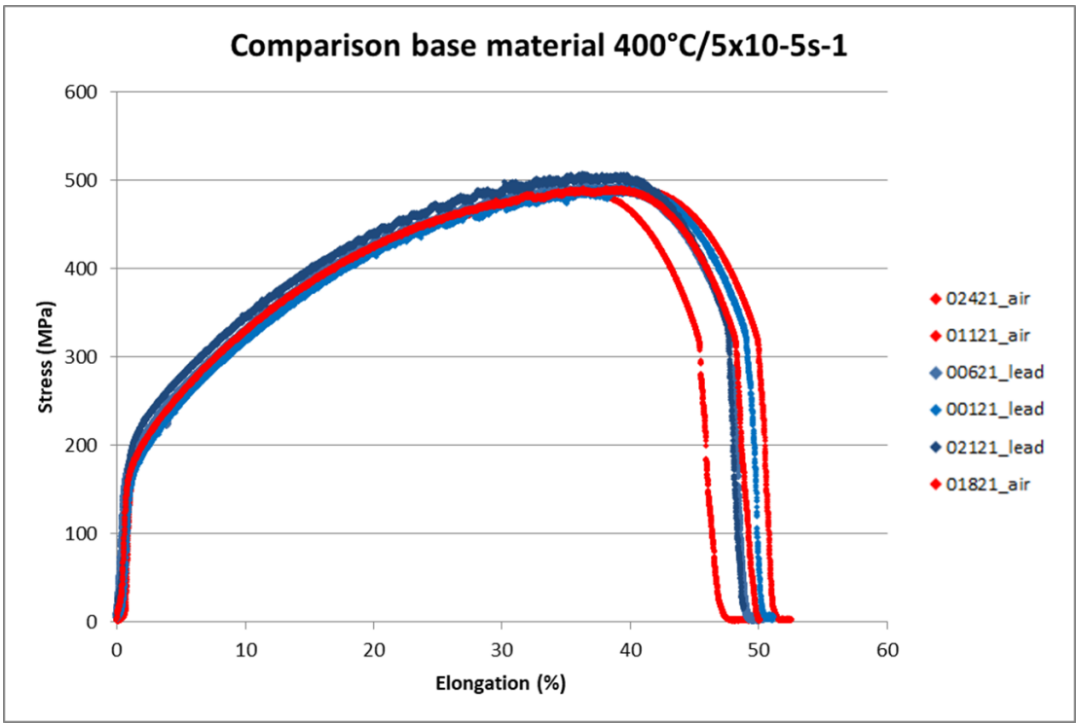

Figure 3.1.8. Comparison air / lead tensile curves resulting from the SSRTs carried out on AISI 316L base material at 400°C ; $5*10^{-5}s^{-1}$.

The achieved tensile properties are reported in the following table (Tab. 3.1.2). The trend of tensile properties, in terms of Yield Strength and Ultimate Tensile Strength (UTS) is plotted in the next graph (fig. 3.1.9). The Yield Strength has been calculated as the stress leading to 0.2 % residual plastic deformation (Rp02), as already explained in the experimental section.

Table 3.1.2. Achieved tensile properties on the 316L base material for the tests in air

Test temperature (°C)	Strain rate (s^{-1})	Air		Lead	
		Rp02 (MPa)	UTS (MPa)	Rp02 (MPa)	UTS (MPa)
RT	$5x10^{-5}$	263	601		
400	$5x10^{-5}$	163	487	158	492
		161	490	166	493
		167	491	187	507
550	$5x10^{-6}$	151	445	152	434
		147	453	145	436
		149	446	138	439

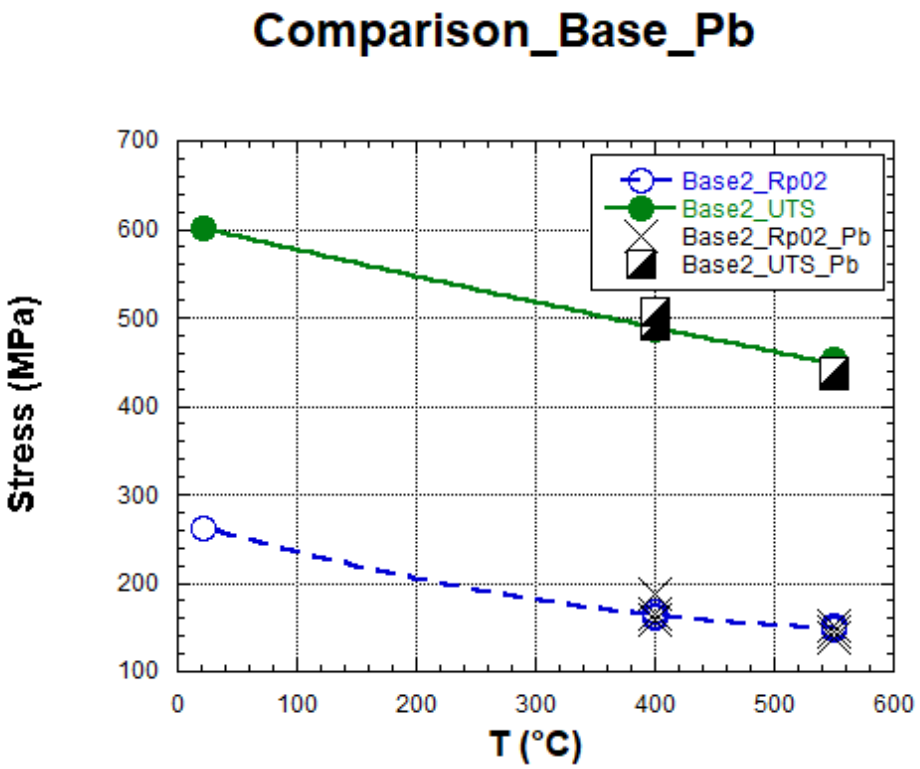

Figure 3.1.9. Trend of tensile properties as function of temperature; comparison air/lead.

The tensile curves achieved by SSRT in lead at 550°C on the AISI316L weld material (extraction of the specimen parallel to the axis of the welded joint) are compared to the corresponding tests in air in Fig 3.1.10. We can notice a relevant scatter in the results, both from the tests in air and in Lead. Therefore, no remarkable discrepancy can be found on the effect of lead on the weld material. The only effect that seems to be ascertained on each of the tests in Lead (compared to the corresponding testing conditions in air) is the appearance of the same "nature", already noticed on the base material, of the curves in lead, characterized by a slight decrease in the maximum values of the UTS with the achievement of the typical "plateau". This effect is also accompanied by an "average tendency" to increase ductility.

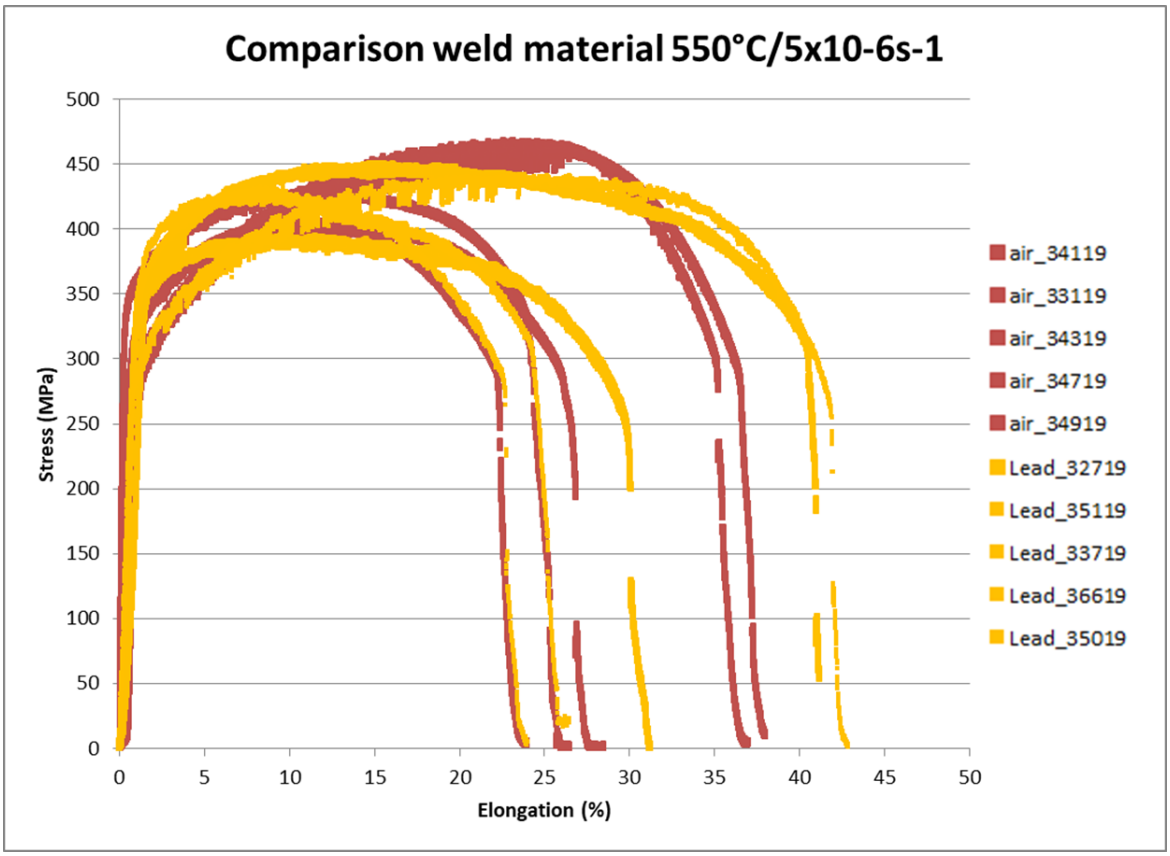

Figure 3.1.10. Comparison of tensile curves resulting from the SSRTs carried out on AISI 316L weld material (longitudinal extraction) in air and lead at 550°C, $5*10^{-6}s^{-1}$.

The achieved tensile properties are reported in the following table (Tab. 3.1.3). The trend of tensile properties, in terms of Yield Strength (Rp02) and Ultimate Tensile Strength (UTS) is plotted in the next graph (fig. 3.1.11).

Table 3.1.3. Achieved tensile properties on the 316L weld material for the tests in air and in lead

Test temperature (°C)	Strain rate (s^{-1})	Air		Lead	
		Rp02 (MPa)	UTS (MPa)	Rp02 (MPa)	UTS (MPa)
RT	$5x10^{-5}$	469	597		
		423	624		
		468	597		
400	$5x10^{-5}$	257	494	329	522
		375	484	369	499
		376	505	385	518
		285	507	304	515
		318	509		
550	$5x10^{-6}$	304	403	341	403
		333	429	355	429
		277	468	259	468
		292	463	310	463
		314	407	345	407

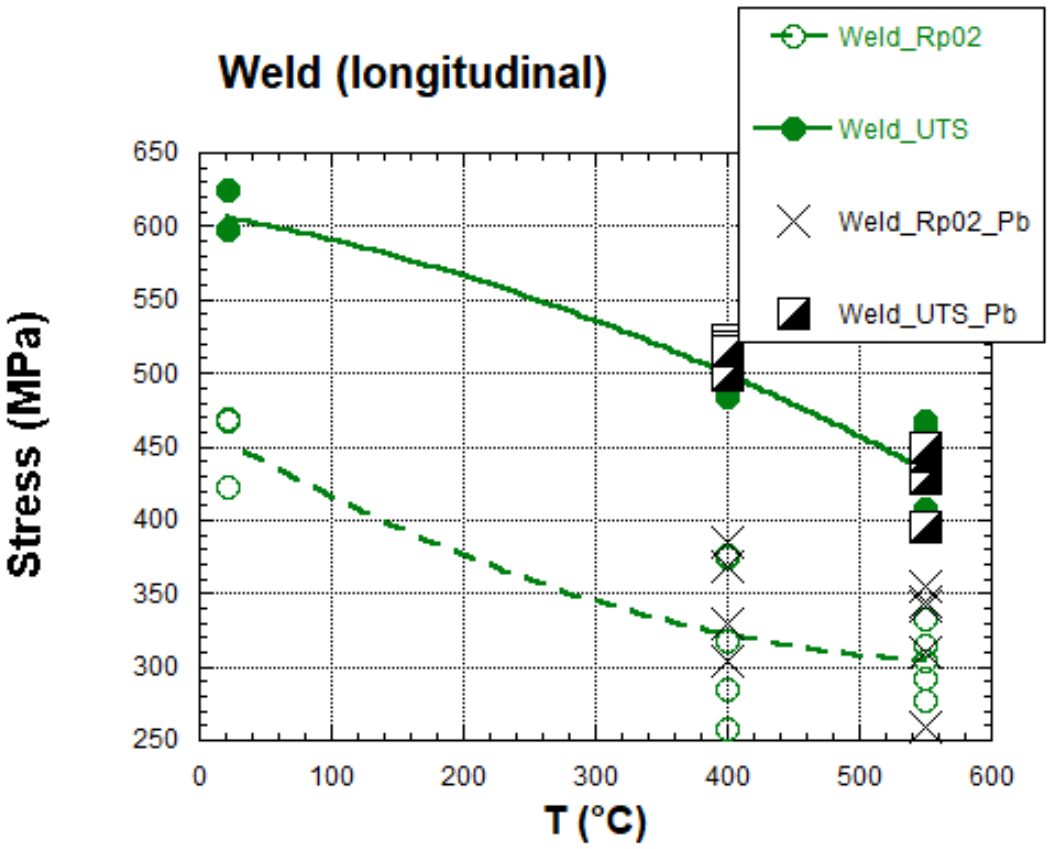

Figure 3.1.11. Trend of tensile properties as function of temperature.

The tensile curves achieved by SSRT in lead at 550°C on the AISI316L cross-weld material (extraction of the specimen perpendicular to the axis of the welded joint) are compared to the corresponding tests in air in Fig 3.1.12. As for the longitudinal extractions of the specimen, also the transverse extractions confirm the scatter in the results. This spread results a little bit less marked than for the longitudinal specimens; namely the cross-weld curves seem to be more similar to each other in groups of three or four specimens. But this just depends on the extraction of the samples; namely the cross-weld specimens, differently from the longitudinal ones, have been extracted closer to each other (pitch of extraction is the size in the direction of the diameter instead of the specimen length itself) and therefore result less sensitive, in some batches, to the longitudinal variation of the mechanical properties along the welded joint.
The achieved tensile properties are reported in the following table (Tab. 3.1.4). The trend of tensile properties, in terms of Yield Strength (Rp02) and Ultimate Tensile Strength (UTS) is plotted in the next graph (fig. 3.1.13).

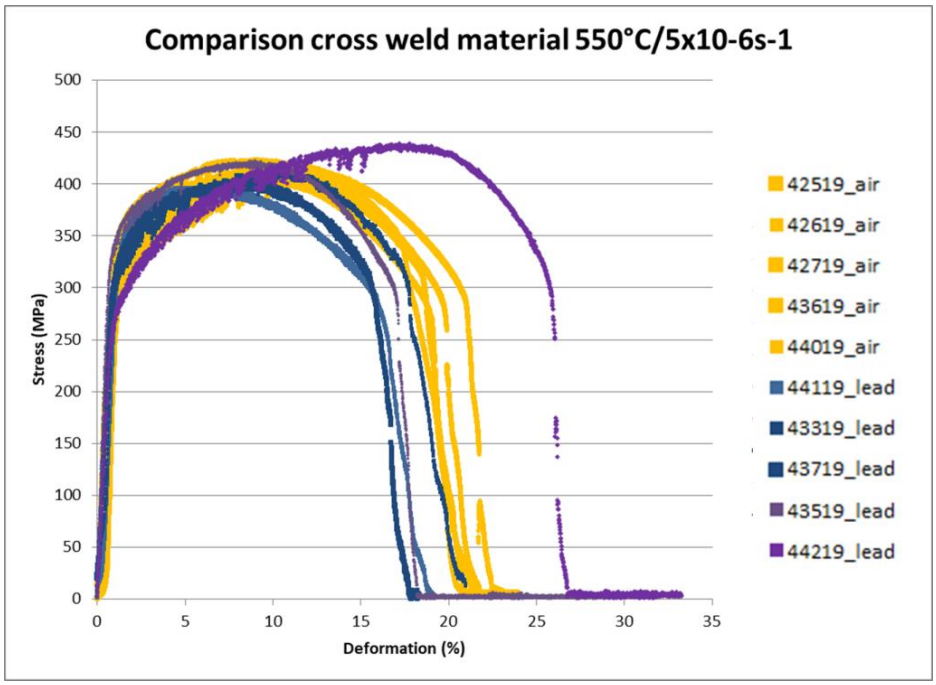

Figure 3.1.12. Tensile curves resulting from the SSRTs carried out on AISI 316L weld material (transverse extraction) at 550°C.

Table 3.1.4. Achieved tensile properties on the 316L cross weld material for the tests in air and in lead

Test temperature (°C)	**Strain rate (s^{-1})**	**Air**		**Lead**	
		Rp02 (MPa)	UTS(MPa)	Rp02 (MPa)	UTS(MPa)
RT	$5x10^{-5}$	495	604		
		380	612		
		400	619		
400	$5x10^{-5}$	312	466	295	509
		362	465	315	475
		275	463	375	516
		380	461	354	511
		310	476		
550	$5x10^{-6}$	288	406	334	398
		334	423	304	414
		267	403	296	403
		308	420	335	422
		310	417	265	439

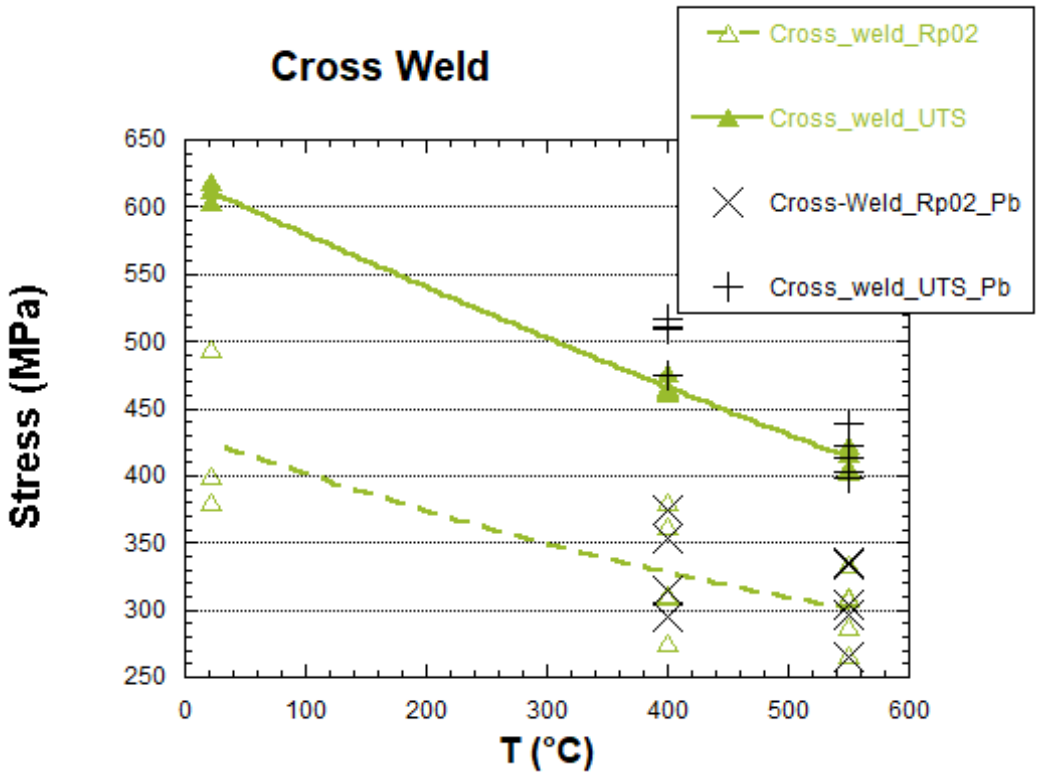

Figure 3.1.13. Trend of tensile properties as function of temperature.

3.1.4 Creep tests in lead

The following plots (fig. 3.1.14) report the comparison between the creep curves of the base material (extraction of the specimen parallel to the axis of the welded joint) and the corresponding experimental conditions (in terms of applied load and temperature) under Lead exposure. Three values of the applied load have been chosen; 150, 217 and 189 MPa, where the former represents the estimated YS (Yield Strength) at 600°C (or better the closest applied load), the second one is the lowest applied load for the specimens extracted from the weld, applied for direct comparison (see next paragraphs), and the latter is a value in between, respectively. Each curve is labeled with the corresponding value of the estimated creep rate (h^{-1}) which ranges between 10^{-5} and 10^{-6}.

There are some inconsistencies in the results; the first one is that the initial deformation of the tests in air is lower for a higher applied load. This could be likely due to a slight difference in the YS of the two tested specimens, provided that we're testing above the YS and a difference in the tensile curves would imply a marked difference in the initial plastic deformation. We have already noticed (see chapter 3.1.1) that this material can be affected by remarkable local variations of the properties. The second and more serious one is that the creep rate of the tests in lead is lower for a higher applied load (217 MPa compared to 189 MPa). This is inconsistent with common experience and further microstructural investigations are ongoing in order to find any possible explanation in terms of local inhomogeneities of the base material (for example any big inclusion that could have reduced drastically the bearing capability of the specimen cross section) or inhomogeneous oxidation behaviour on the gauged length of the specimen.

Leaving aside for the the time being the conclusions concerning the effect of lead at 189 MPa, if we just focus on the test at 217 MPa, we can notice a slight increase in the creep rate for the test in lead compared to the one in air. This increase is slightly less visible at the "YS" (150 MPa applied load). This last test seems actually affected by two kinds of fluctuations; in addition to the one (period 24 hrs) depending on the daily environmental temperature fluctuations there's another one; a sort of "hump" in the signal between approximately 50 and 170 hrs, affecting the very first stage (primary creep) of the curve. This second fluctuation seems to disappear after 200 hours, with the achievement of a sort of "saturation" in the signal at

400 hours. According to the fitting, the estimated creep rate for this test results equal to $7{,}2x10^{-6}h^{-1}$. Nevertheless, provided that the signal of this curve is affected by relevant fluctuations (whose amplitude is comparable to the value of the deformation itself) and that the "shape" of the curve doesn't correspond 100% to the one expected for a creep test, with a well defined primary stage, we conclude that only the order of magnitude for the creep rate is reliable ($10^{-6}h^{-1}$).
Eventually, a meaningful aspect that is worth highlighting concerning these creep tests on the base material is the possible correlation between the increased ductility previously recorded in the tensile tests at high temperature and low strain rate ($550°C/5x10^{-6}s^{-1}$) and the increased creep rate noticed here.

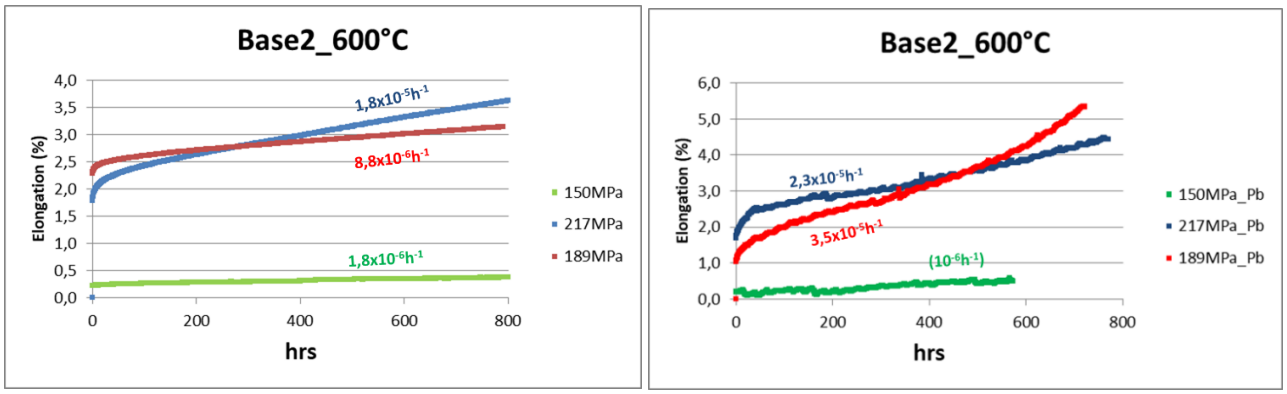

a) b)

Figure 3.1.14. Achieved creep curves for the base material (longitudinal extraction) tested in air (a) and in lead (b).

Figure 3.1.15 shows the comparison between the creep curves of the weld material (extraction of the specimen parallel to the axis of the welded joint) and the corresponding experimental conditions (in terms of applied load and temperature) under Lead exposure. Three values of the applied load are 217, 236 and 254 MPa. The rationale for the choice of these applied loads is a "tradeoff" between the need of having the applied load below the average value for the YS (in order to avoid initial plastic deformations), and the need of a sufficient creep rate to allow a meaningful comparison between the straight curve from the tests in air and the fluctuating signal from the tests in lead. Each curve is labeled with the corresponding value of the estimated creep rate (h^{-1}) which ranges from 10^{-5} to 10^{-6}. We can notice a marked increase in the creep rate in contact with the HLM in two of the three selected conditions (217 and 254 MPa) while for the third one (236 MPa) the curves, from the tests in air and in lead, appear almost perfectly superposed.

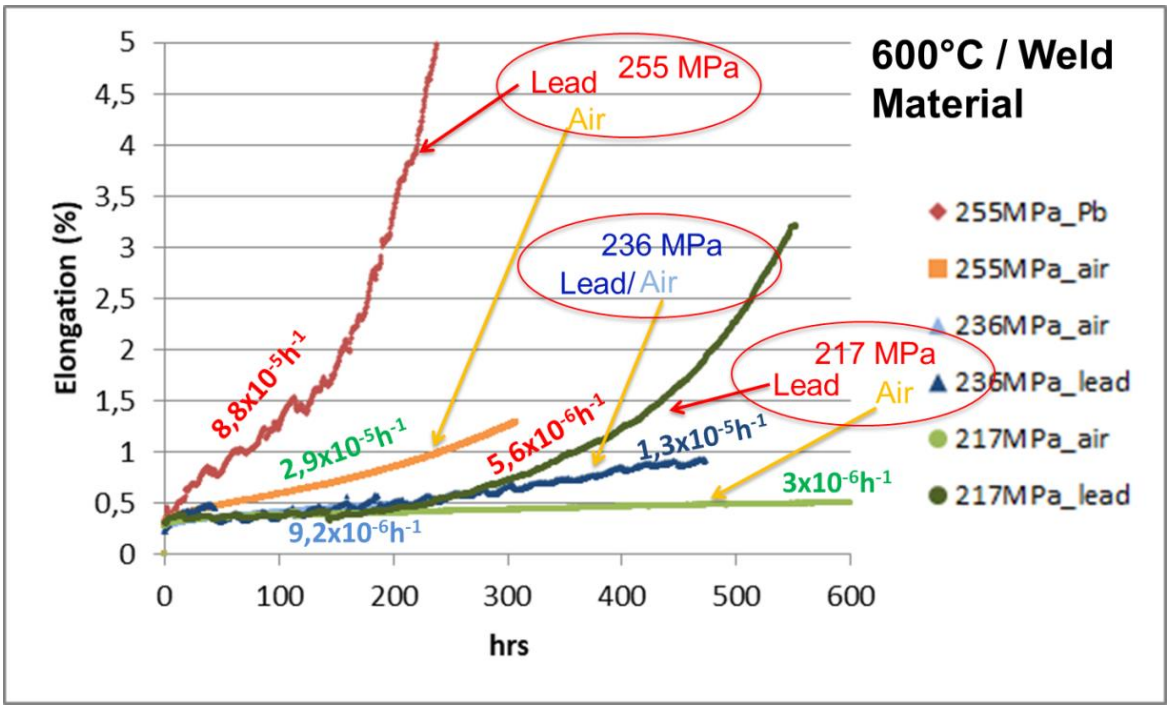

Figure 3.1.15. Achieved creep curves for the TIG welded joint (longitudinal extraction) tested in air and in lead

The following plot (fig. 3.1.16) shows the comparison between the creep curves of the cross-weld material (extraction of the specimen perpendicular to the axis of the welded joint) and the corresponding experimental conditions (in terms of applied load and temperature) under Lead exposure. Three applied loads; 217, 236 and 254 MPa, are the same as for the longitudinal weld specimens. Each curve is labeled with the corresponding value of the estimated steady state creep rate (h^{-1}) which ranges between 10^{-5} and 10^{-6}.

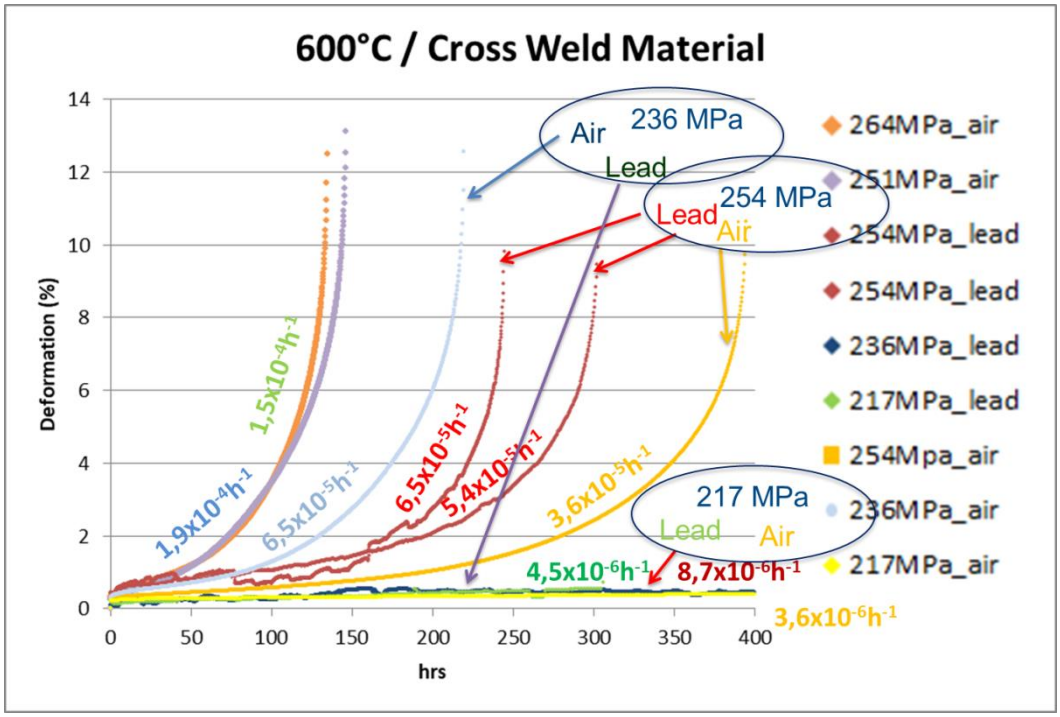

Figure 3.1.16. Achieved creep curves for the TIG welded joint (transverse extraction) tested in air and in lead.

The contact with the HLM doesn't result in any straightforward effect. It could be expected that lead exposure results in a shortening of creep life if we look at the 254 MPa tests, but, on the other hand, in an increase of creep life if we focus on the 236 MPa tests. But this is not consistent of course, a conjecture is that this unclear trend is related to the inhomogeneity of the material itself rather than on the contact with the HLM. As already noticed from the SSRT tests, the weld material is affected by a significant inhomogeneity and this is reflected in the creep curves of the cross weld material as well. In fact, if we focus on the curves from the tests in air only, we can notice that the test at 254 MPa (yellow curve on the right) lasts markedly more than the test at 236 MPa (light blue curve on the left), while exactly the other way round should be expected. However, the analysis of the results of the cross-weld material should always keep into account that, as already mentioned at the beginning, these specimens aren't extracted from a portion of uniform material, but the gauged length of these samples can be rather schematized as a "sandwich" of three different microstructures (HAZ base, weld, HAZ base). This intrinsic inhomogeneity of each of these samples could explain some of the odd trends of the mechanical properties recorded in this experimental campaign concerning this material.
Some tests have been carried out at 500°C as well. A reference applied load of 300 MPa was applied and the effect of 10% variations in this value (increase and decrease) was investigated. Figure 3.1.17 depicts the curves for the weld and the cross-weld material at 300 MPa and the effect of a 10% increase in the applied load (330 MPa).

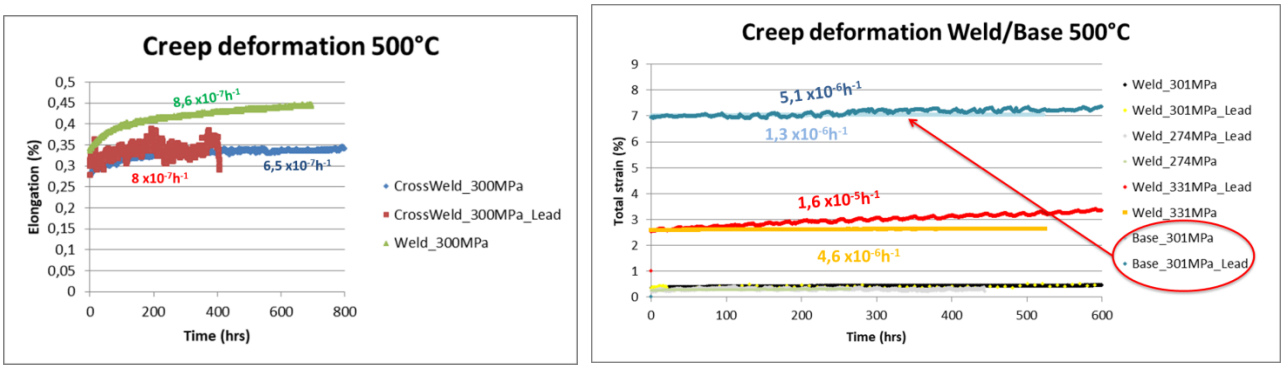

a) b)

Figure 3.1.17. a) Achieved creep curves for the weld and cross-weld specimens tested in air and in lead at 500°C; b) effect of the initial plastic deformations on the creep behaviour of the base and weld material

The achieved values of the creep rate result in a range of 10^{-7} h^{-1} for the weld and cross-weld specimens tested at 500°C, 300 MPa with an initial deformation in the elastic range. A 10% increase in the applied load (330 MPa) for the weld material or the 300 MPa load itself on the base material results in a big shift in the initial elongation and this is an evidence of exceeding of the Yield Strength, leading to a significant initial plastic deformation. We can notice an increased creep rate in the tests in HLM compared to the tests in air for these plastically deformed specimens. This is a possible clue to the hypothesis that an initial plastic deformation, associated to the provision of newly created, "fresh" surfaces to the contact with the HLM, could be necessary to trigger the effects of the HLM/steel interaction. In other words, one could be led to deduce that the initial plastic deformations could play a role in triggering the HLM/steel interaction mechanisms, as it occurs for the tensile tests where the HLM effects just become visible at the plastic stage of the curve, once YS has been exceeded.
The following plot (Fig. 3.1.18) is meant to summarize the results in terms of stress as function of creep rate for the 600°C tests. It results that the creep rate is more enhanced by the intrinsic nature of the material (weld instead of base) rather than by the environmental effect due to the contact with the Heavy Liquid Metal.

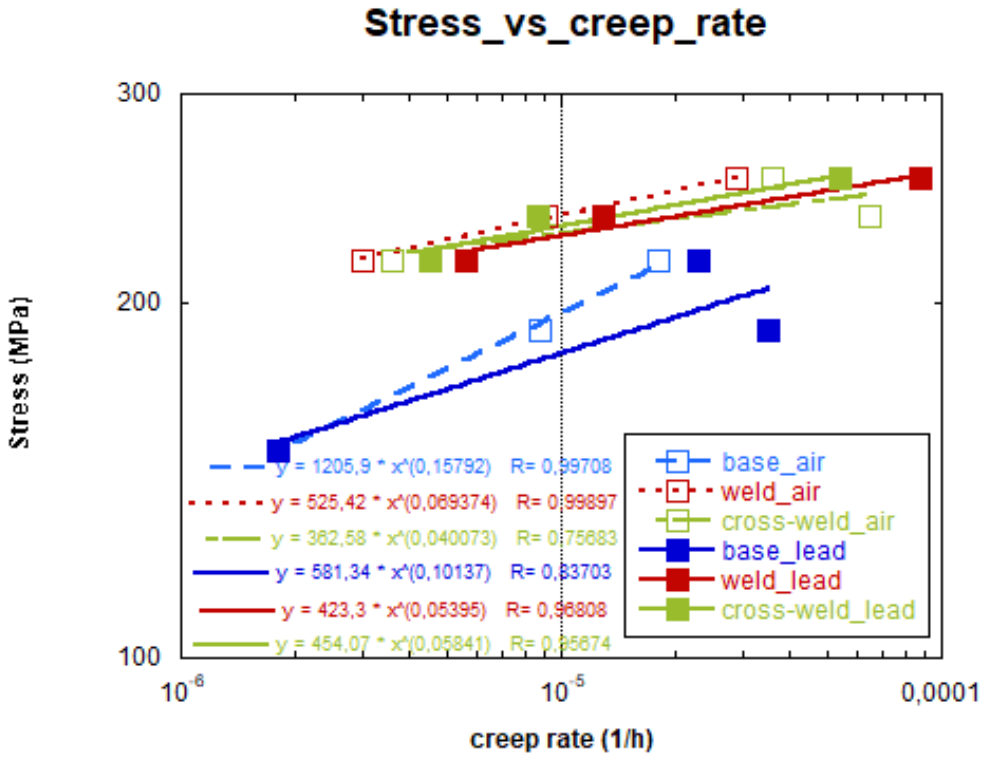

Figure 3.1.18. Stress as function of creep rate at 600°C for the three classes of materials

3.1.5 References

[1]. AFCEN RCC-MRx Code. 2012. Design and Construction Rules for Mechanical Components of Nuclear Installations.

[2]. V. V. Popovich and I. G. Dmukhovskaya "REBINDER EFFECT IN THE FRACTURE OF ARMCO IRON IN LIQUID METALS" UDC 532.6:539.2; 1979; Plenum Publishing Corporation (0038-5565/78/1404- 0370)

3.2 Results of the mechanical characterization of the RAFM steels taken into account in the frame of Eurofusion WPMAT Project

3.2.1 Impact tests at cryogenic temperatures

The results of the impact tests (KLST specimens, according to DIN 50115) carried out in 2019 on several recrystallization and ausforming TMTs on Eurofer 97/2 and on the newly produced alloys are reported in the following plot (Fig. 3.2.1) and summarized in the next table (Tab. 3.2.1).

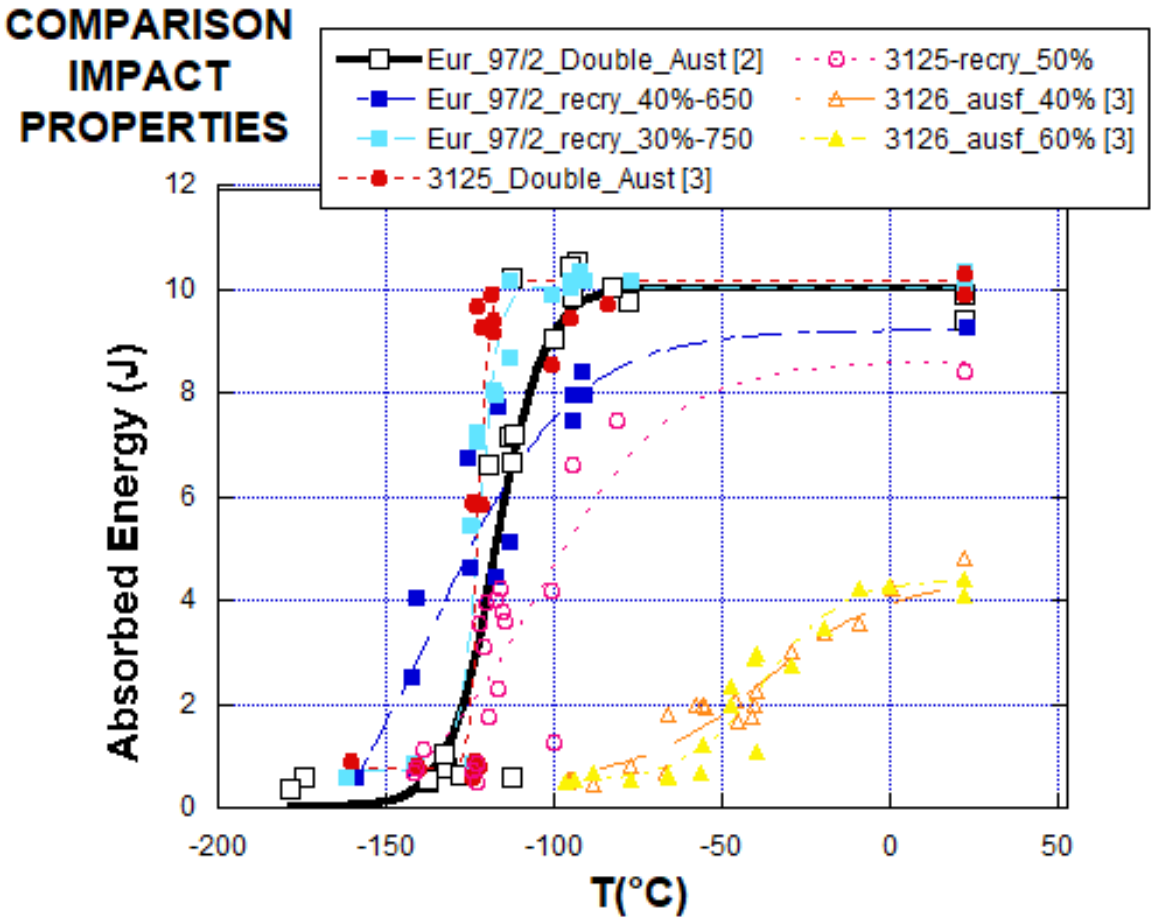

Figure 3.2.1. Impact tests on each alloy; published data [2,3].

Heat	DBTT (°C)	USE (J)	LSE (J)	Stnd. Dev. (°C)
Eurofer 97/2 Double Normalization &temp	-117	9.98	0.48	2
Eurofer 97/2 Recrystallized 30% c.w.	-122	10.2	0.9	0.8
Eurofer 97/2 Recrystallized 40% c.w.	-124	9.3	0.58	3.1
3125 Alloy – Stnd. Double Aust	-122	10.2	0.8	0.5
3125 Alloy – Recrystallized 50% c.w.	-101	8.4	0.8	4.4
3126 alloy - Ausformed 40% h.w.	-37.3	4.4	0.5	2.3
3126 alloy - Ausformed 60% h.w.	-37.3	4.4	0.5	2.2

Tab. 3.2.1. Outcomes of the impact tests on each alloy/TMT condition

Higher scatter is noticeable in the results of 3125 and 3126 alloys compared to the ones of Eurofer 97/2. This kind of scatter could be in principle correlated to the non-homogeneous microstructure of the steel and is supposed to be related to the production route undergone by the three alloys; VIM (Vacuum Induction Melting) plus VAR (Vacuum Arc Re-melting) for Eurofer 97/2, just VIM for 3125 and 3126 alloys, cast at RINA-CSM. The VAR process is just meant to reduce the non-homogeneous microstructure typical of a VIM cast batch. Nevertheless, the reported experimental campaign must be intended more as an initial screening on the effects of the variations in chemical compositions and TMTs; therefore even this presence of some in-homogeneities in the microstructure (typical of the VIM process) is considered suitable to this aim.

A marked difference between the impact properties of the ausformed 3126 alloy and the ones of Eurofer 97/2 and 3125 alloy is noticeable in terms of both DBTT and USE; the steels meant to be employed in the "low temperature" operating conditions (Eurofer 97/2 and 3125) are much more performing than 3126 alloy in terms of toughness properties. This is expected and due to the different specifications for the two operating conditions; on the one hand the "lowest possible DBTT" for the "low temperature" scenario; on the other hand a "sufficient toughness" for the "high temperature" scenario, just in order to carry out safe manufacturing and assembling processes at room temperature for the alloys meant to be used in this last one (3126 alloy).

The effect of the recrystallization treatment on Eurofer 97/2, compared to the "standard" double normalization treatment is to lower the DBTT by a few degrees and make the transition smoother; the higher the c.w. rate, the smoother the DBTT. By several microstructural observations it has been demonstrated that the recrystallization treatment provides great benefit in terms of grain size refinement; one order of magnitude decrease in grain size is achieved by means of the recrystallization TMT if we compare the 1 micron grain size (fig. 3.2.2) to the optimized 10 microns Prior Austenite Grain Size (PAGS) achieved by means of the standard normalization/tempering heat treatment.

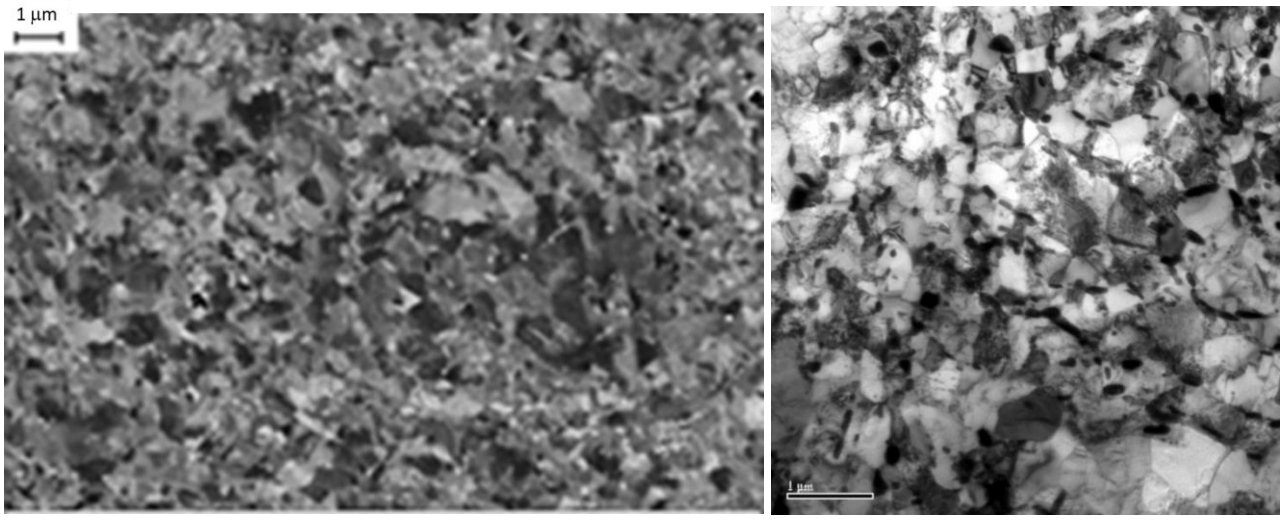

a) b)

Fig. 3.2.2. a) SEM and b) TEM analysis (thin foils) of Eurofer 97/2, 40% cold rolled and tempered (650°Cx1 h)

Nevertheless, for the composition 3125, the recrystallization TMT seems no longer effective in decreasing the DBTT. Probably the reduced content of carbide forming elements for this alloy is responsible for an inhomogeneous recrystallization but this has still to be verified by microstructural observations. In any case it has been considered more worth to focus on the alloys with increased content of carbide forming elements,

as Eurofer or 3126, for the application of the recrystallization treatment. The carbide content and distribution, in fact, is thought to play a key role in the grain size refinement by recrystallization treatment; namely the higher is the amount of the finely dispersed carbides, the higher should be the number of the nucleation sites that trigger the ferritic grain recrystallization.

Therefore, in 2020, additional impact tests have been carried out on heavily cold worked (50% c.w. or even 50+50 % c.w.) Eurofer 97/2 and 3126 plates. Hereafter the results of the impact tests (KLST specimens, according to DIN 50115) on two cold working conditions (50% and 50%+50%) on 3126 alloy are reported (Figure 3.2.3). The standard double austenitization treatment and the recrystallization (one 50% c.w. stage) treatment conditions on Eurofer 97/2 are recalled as well for comparison.

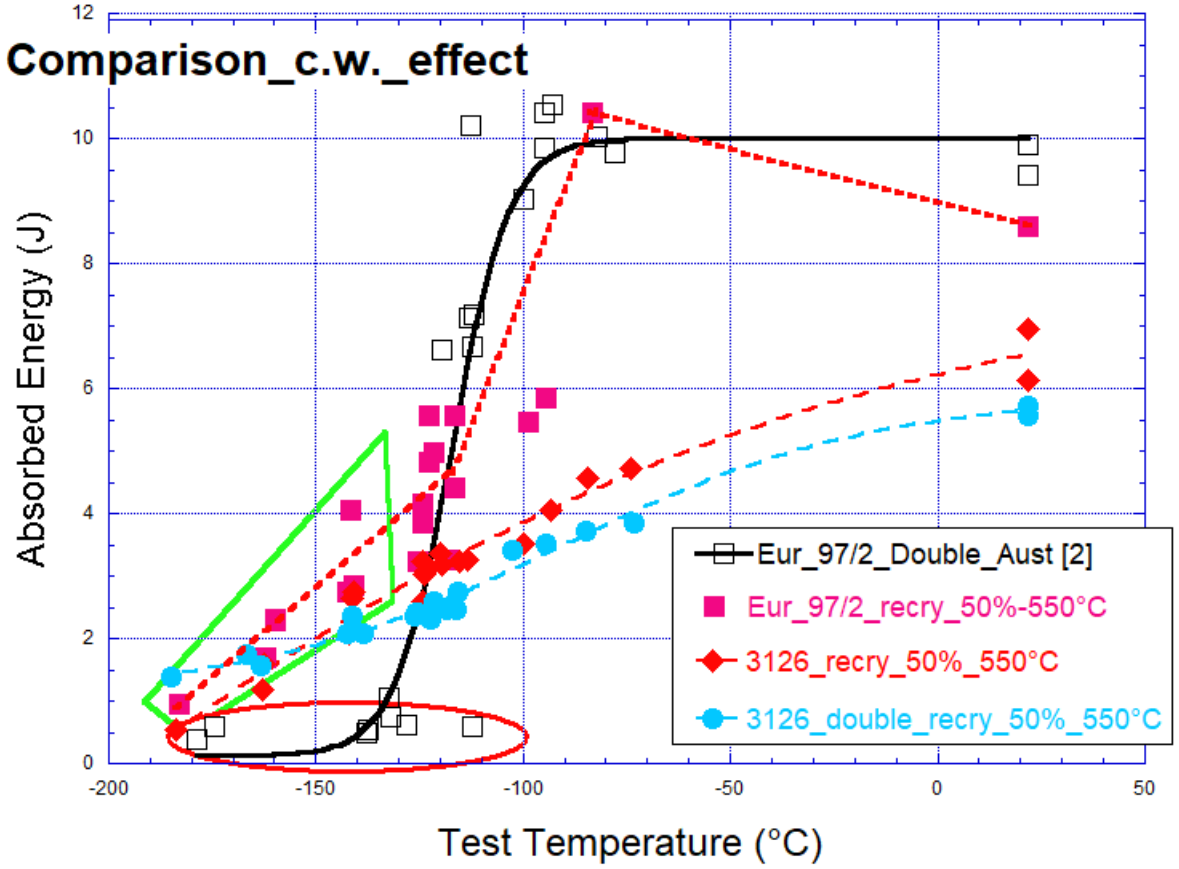

Figure 3.2.3 Comparison between the absorbed energy resulting from different cold working ratios applied during the recrystallization treatment on the 3126 alloy (KLST tests)

The results show that the Recrystallized 3126 alloy is characterized by a very smooth transition from ductile to brittle behaviour and it exhibits residual toughness at very low temperature: -150-180°C. The high C.W. deformation ratio increases the toughness of the recrystallized 3126 alloy extending the zone of "retained ductility" behaviour towards very low temperatures, down to -150-180°C: the higher the C.W. rate, the higher the Lower Shelf Energy (LSE). In addition to the out-of-pile "retained ductility", a general remark is that an UFG (Ultra-Fine Grain) steel, like this recrystallized 3126 alloy, is expected to be more radiation-tolerant, provided that grain refinement increases the surface of grain boundaries which can act as sinks for radiation-induced point defects.

3.2.2 Standard tensile tests on cylindrical and flat specimens

The results of the tensile tests referred to the high temperature applications for DEMO BB, with 650°C operation temperature, in terms of Yield Strength and Ultimate Tensile Strength are reported in the following table (Tab. 3.2.2) and plots (Fig. 3.2.4-3.2.5). The fitting functions are 3rd degree polynomials. The 3126 composition (colored symbols in the plot) seems to provide better behaviour compared to the other alloys tested during the previous years of the Eurofusion WPMAT-AS Project (black symbols in the plot) in terms of tensile properties after ausforming. The first graph (Fig. 3.2.4) is meant to provide a comparison among the yield strengths recorded all over the temperature range taken into account for each of the proposed composition / TMT condition. Each of the proposed composition / TMT condition fulfills the target requirement referred to tensile properties; namely a Yield Strength higher than 100 MPa at 650°C is obtained for each alloy. As expected, the best performances are recorded for the plates tempered at the lower temperature (720°C instead of 760°C). The different hot-working ratios applied on 3126 alloy don't make substantial differences in terms of high temperature (650°C) resistance. We can deduce that meaningful dislocation recovery presumably occurs and leads to the annihilation of the effect of the higher dislocation density of the 60% hot worked alloy. This is also confirmed by the following creep tests.

Table 3.2.2. Tensile properties of the ausformed 3126 alloy

Test Temperature (°C)	**3126_ausf_40%_temper_700**		**3126_ausf_60%_temper_700**	
	Rp02 (MPa)	**UTS(MPa)**	**Rp02 (MPa)**	**UTS(MPa)**
RT	970	1091	1022	1147
	969	1089	1039	1158
350	807	893	855	953
	809	888	856	946
450	761	831	795	877
	765	835	796	873
550	613	684	630	717
	623	702	632	717
650	447	529	442	536
	450	531	442	535

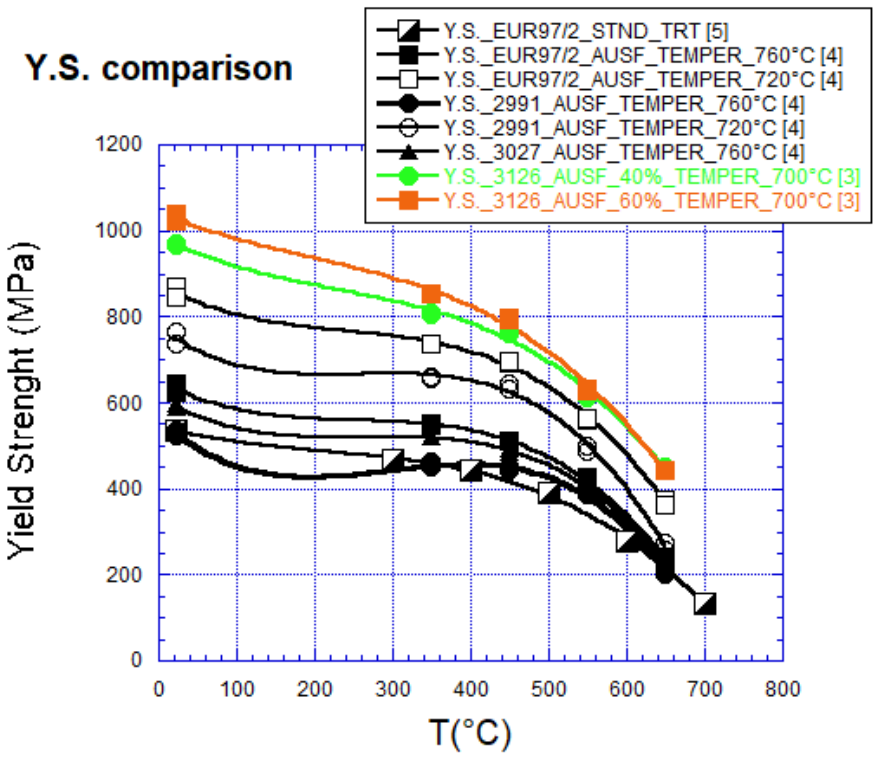

Figure 3.2.4. Comparison among the Yield Strengths obtained for each alloy (high temperature applications)

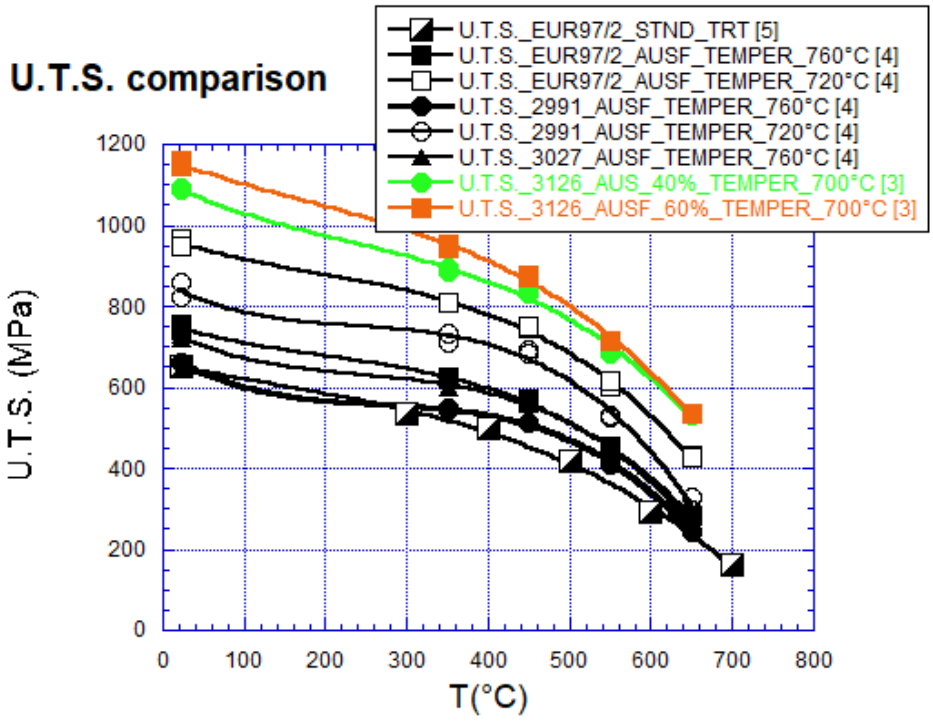

Figure 3.2.5. Comparison among the Ultimate Tensile Strengths obtained for each alloy (high temperature applications)

Concerning the low temperature applications for DEMO WCLL BB (Water Cooled Lithium Lead Breeding Blanket; 280-330°C operation temperature) the Yield Strength (solid lines) and Ultimate Tensile Strength (dashed lines) of the recrystallized (Eurofer 97/2) and newly produced (heat 3125) alloys are reported in the

following table (Tab. 3.2.3) and plot (Fig. 3.2.6). The red symbols refer to cylindrical specimens (3125 alloy) while the pink and blue symbols refer to the flat specimens (cold-worked and recrystallized Eurofer 97/2).

Table 3.2.3. Tensile properties of the alloys for low temperature applications

	3125		Recry_Eurofer_CW_40%		Recry_Eurofer_CW_50%	
	Rp02 (MPa)	**UTS(MPa)**	**Rp02 (MPa)**	**UTS(MPa)**	**Rp02(MPa)**	**UTS(MPa)**
RT	584	688	586	740	651	801
	558	689	551	740,5	577	780
300	491	589	-	636	553	683
	472	570	522	631	577	689
450	447	518				
	453	523				
500	428	469				
	418	464				
550	389	412				
	384	408				

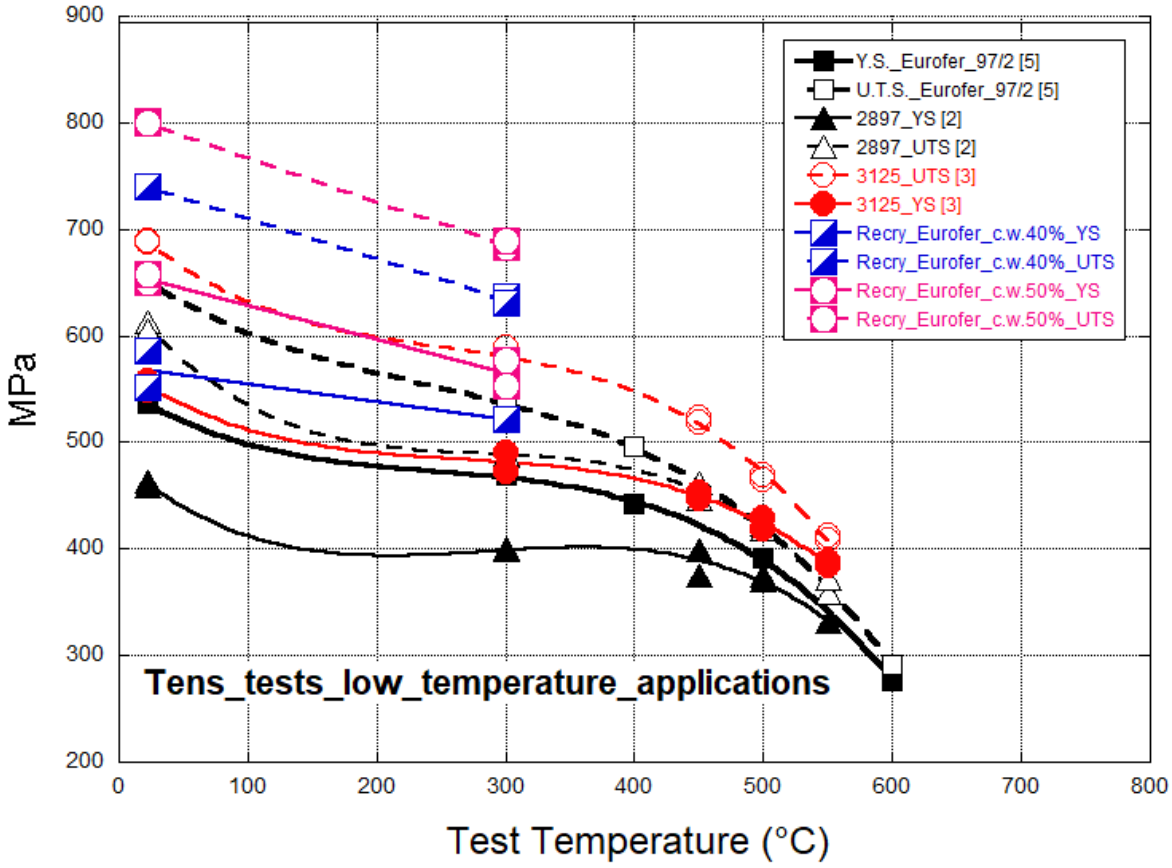

Figure 3.2.6. Comparison among the Yield and the Ultimate Tensile Strenghts obtained for each alloy (low temperature applications)

The recrystallized alloys provide markedly higher mechanical properties. This depends both on the cold working carried out at the tempering stage on these steels, but also on the Hall-Petch effect; namely the lower the grain size the higher the Yield Strength. This second effect seems indeed to be dominant since, according to some TEM (Transmission Electron Microscopy) examinations carried out, the dislocations appear almost fully recovered after the second tempering. It is instead well visible the marked reduction in grain size (one order of magnitude approximately; from the 10 microns of the optimized PAGS to 1 micron of the recrystallized ferritic grain) thought to be mainly responsible for the increased tensile properties.

Concerning the 3125 alloy (red symbols in the plot) the tensile properties are higher than the ones of Eurofer and 2897 alloy. This likely depends on the Tungsten content, that is doubled in the 3125 alloy. This element, in fact, is known to act as "solid solution" hardener.

From the point of view of the ductility, the higher toughness of the recrystallized alloys results in higher values of the Uniform Elongation (Tab. 3.2.4) compared to the standard treatment for Eurofer 97/2 (fig. 3.2.7). The alloy with double Tungsten content (3125) shows an intermediate behaviour between Eurofer with standard treatment and the best performance of 2897 alloy (an alloy with the highest reduction in carbide forming elements).

Table 3.2.4. Uniform Elongation (UE %) of the alloys for low temperature applications

	3125 UE (%)	**Recry Eurofer CW_40%**	**Recry Eurofer CW_50%**
RT	6.5	7.5	5.9
	6.4	8	5.6
300	4.1	-	3.1
	4.1	3.5	3.2
450	3.1		
	2.75		
500	1.9		
	1.75		
550	0.9		
	1.1		

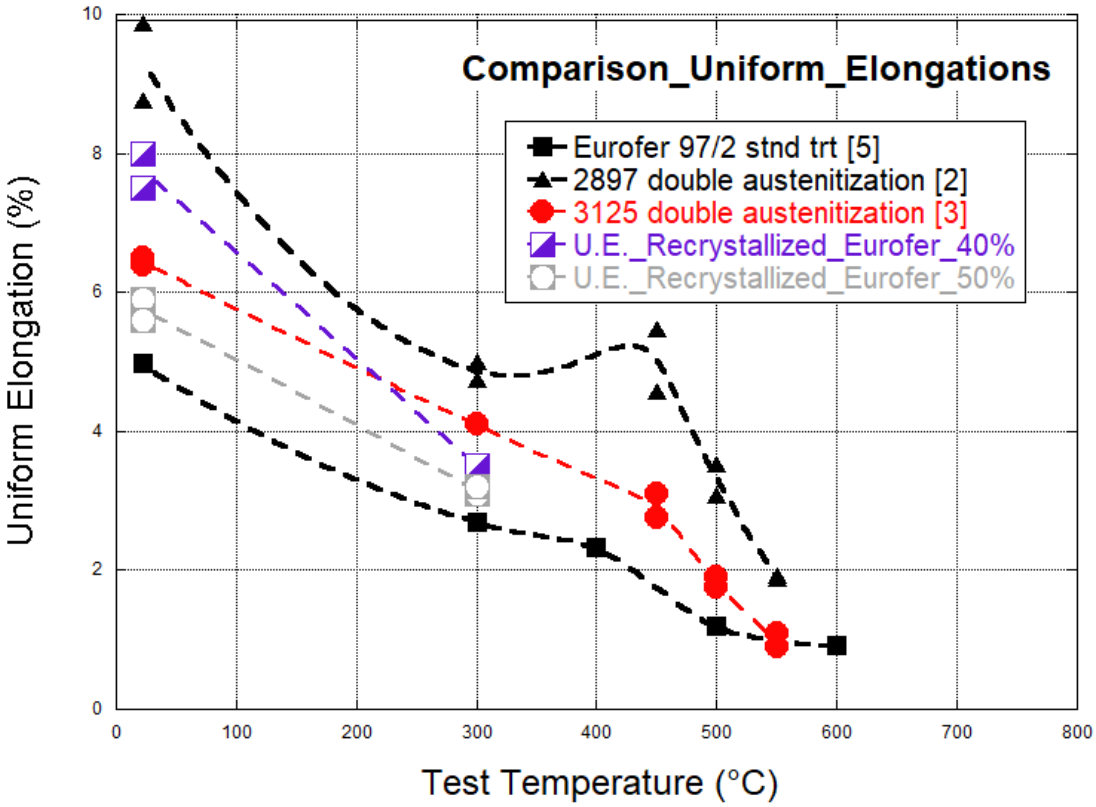

Figure 3.2.7. Comparison among the Uniform Elongations obtained for each alloy (low temperature applications)

3.2.3 Creep tests

Creep tests have been carried out on the 3126 alloy; the times to rupture of this last newly-produced casting (Tab. 3.2.5 and colored symbols in the plot; fig. 3.2.8) are compared to the results achieved on the other alloys produced and treated in the last years (black symbols in the plot, referring to previously published results). As we can observe, the creep resistance of this last alloy results very good, comparable to the one of the ausformed Eurofer 97/2, tempered at 720°C; this alloy appears to be the best one, up to now, concerning creep resistance.

Table 3.2.5. creep resistance (times to Rupture) of the ausformed 3126 alloy

	Applied Load (MPa)	**ttR (hrs)**
3126_ausf_40%_temper_700°C	120	1942
	100	3825
3126_ausf_60%_temper_700°C	120	1712
	100	3525

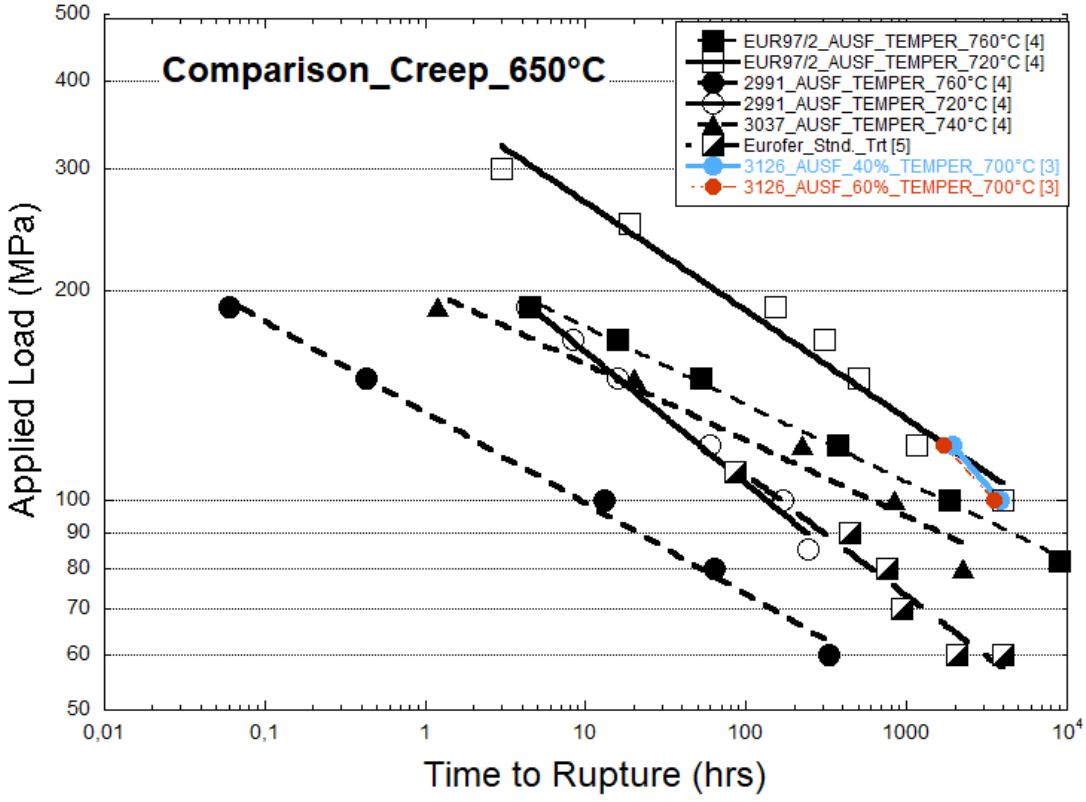

Figure 3.2.8. Comparison among the times to ruptures of several recently produced RAFM steels

We can also notice that the different hot-working ratios applied on 3126 alloy don't lead to substantial differences in creep resistance; namely the higher amount of dislocations induced by plastic deformation in the 60% h.w. (hot worked) material doesn't provide meaningful improvements in terms of times to rupture; then we can assume that the dislocation network undergoes remarkable recovery at 650°C and the difference between 40 and 60% h.w. becomes no longer relevant.

3.2.4 Low Cycle Fatigue (LCF) tests

A series of LCF tests has been carried out at 650°C on the 3126 alloy with standard treatment and on the 3126 alloy with ausforming treatment (named 3229) varying the total strain amplitude (from 1 to 0.3 %). The R value has been kept constant and equal to -1 ($\sigma max=-\sigma min$). Some examples of the achieved hysteresis cycles are reported in the next plots (Fig. 3.2.9). The trend of the stabilized load (peak stress recorded at each cycle) is reported as well in the next plots (fig. 3.2.10, 3.2.11). It's worth noticing, concerning the 0.3 % strain amplitude tests, that an initial hardening is followed by softening. In the alloy with "standard" normalization-tempering treatment, the initial hardening lasts only a few cycles; in the ausformed alloy, in one of the two performed tests, the initial hardening ends at about 5000 cycles. The fatigue life is determined as 25 % stabilized load drop according to ASTM E 606-92. The goal of fatigue life around 10000 cycles at 650°C is reached with a total strain amplitude lower than 0.4%, for both the "standard" normalized-tempered and the ausformed alloy. The alloy with "standard" treatment seems to have longer fatigue life, but this should be confirmed by enhanced statistics on the experimental conditions (just two tests per experimental point in this "screening"). The statistical spread is in fact known to be more significant in fatigue tests than in the other kinds of tests. The not perfectly linear trend of the stabilized load for the ausformed alloy as well as the averagely shorter fatigue life compared to the alloy with standard treatment is probably symptomatic of a not fully homogenous microstructure induced by the ausforming treatment.

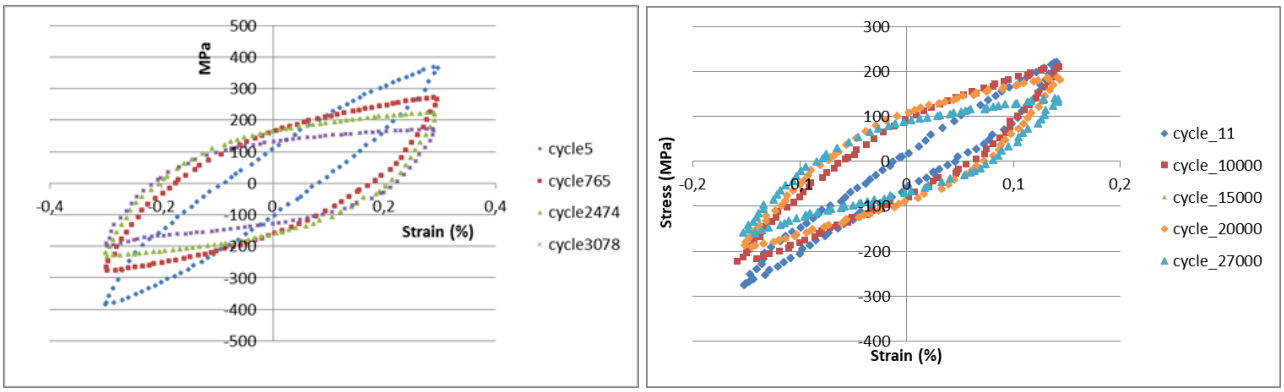

a) b)

Figure 3.2.9. a) Hysteresis cycles recorded for the tests at 650°C with 0.6 % strain amplitude; b) with 0.3 % strain amplitude

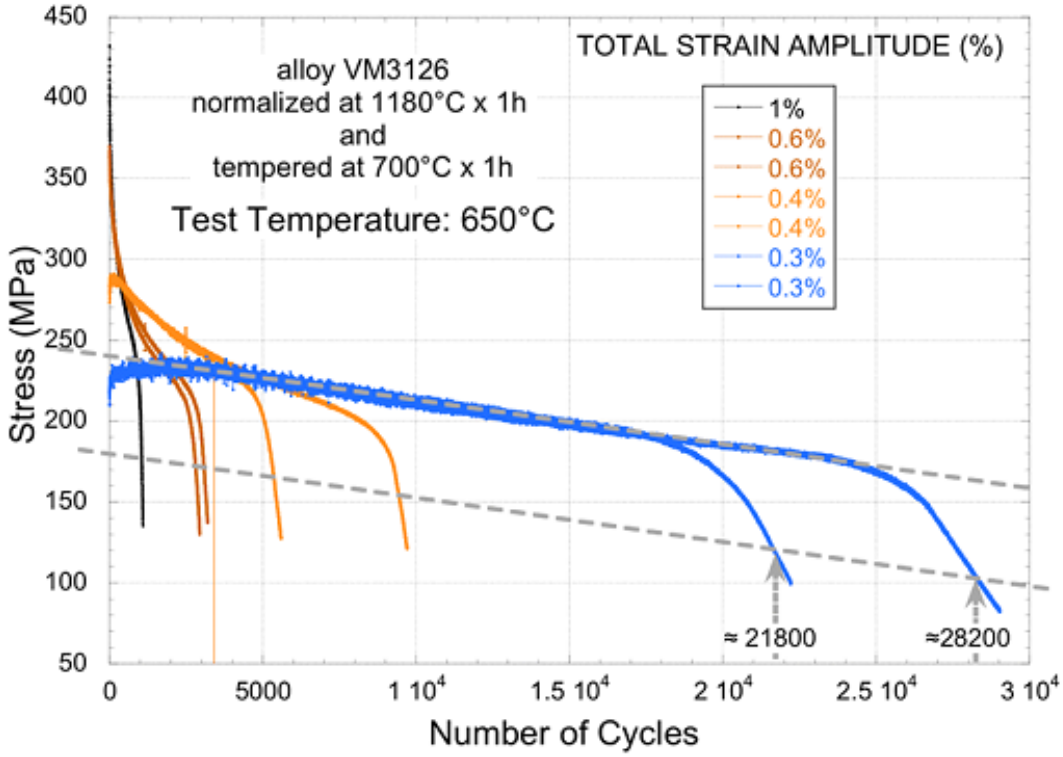

Figure 3.2.10. Trend of the stabilized load recorded in the performed LCF tests at 650°C for the 3126 alloy with standard treatment (normalization + tempering)

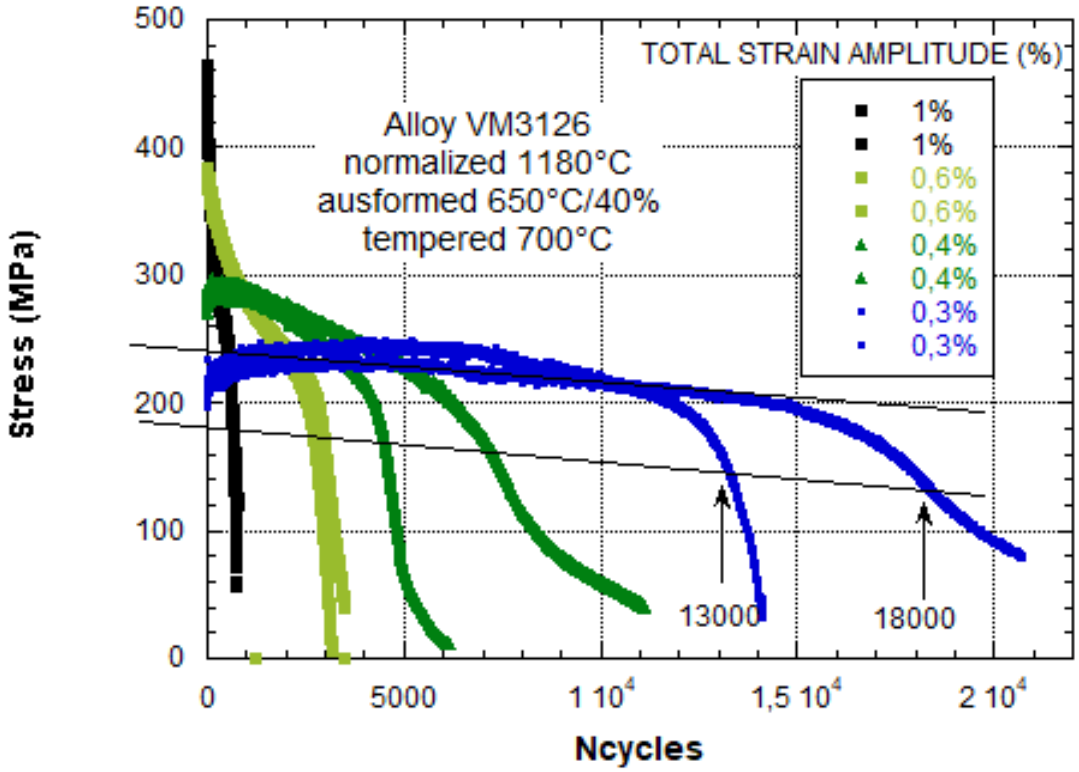

Figure 3.2.11. Trend of the stabilized load recorded in the performed LCF tests at 650°C for the ausformed 3126 alloy

3.2.5 Creep Fatigue (CF) tests

At 0.3 % strain range, three HT (hold time) durations have been selected (40s, 80s and 200s) for the tests in Creep Fatigue (CF) condition at 650°C. The stress-controlled creep-fatigue hold times are expected to be more detrimental than the strain controlled relaxation-fatigue hold times. The durations of the hold times have been chosen in order to balance the detrimental effects of creep and fatigue for the considered value of the strain range; furthermore, the choice was made in agreement with the shortest durations of the hold times (200 s) selected for the scheduled extensive testing campaign of Eurofer for TBM (source: Roadmap for extensive characterization of Eurofer as structural material for the Tritium Breeding Module). In the following figures (fig. 3.2.12-3.2.13) the recorded stress and deformation signal for one cycle is reported as well as the trend of the hysteresis cycles. In the hysteresis plot it's worth appreciating the enlargement of the deformation at constant load at the increasing number of cycles.

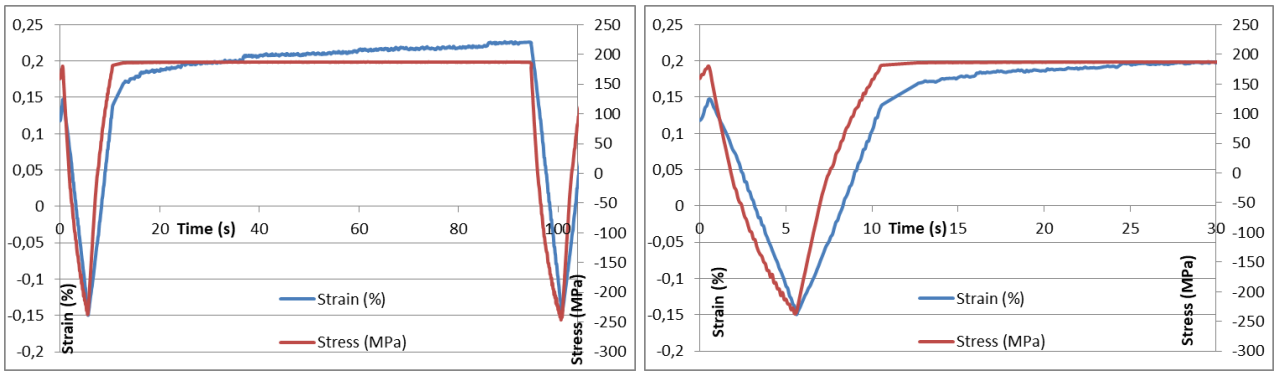

Fig. 3.2.12 CF cycle 2200; HT tension 80 s; stress-strain behaviour.

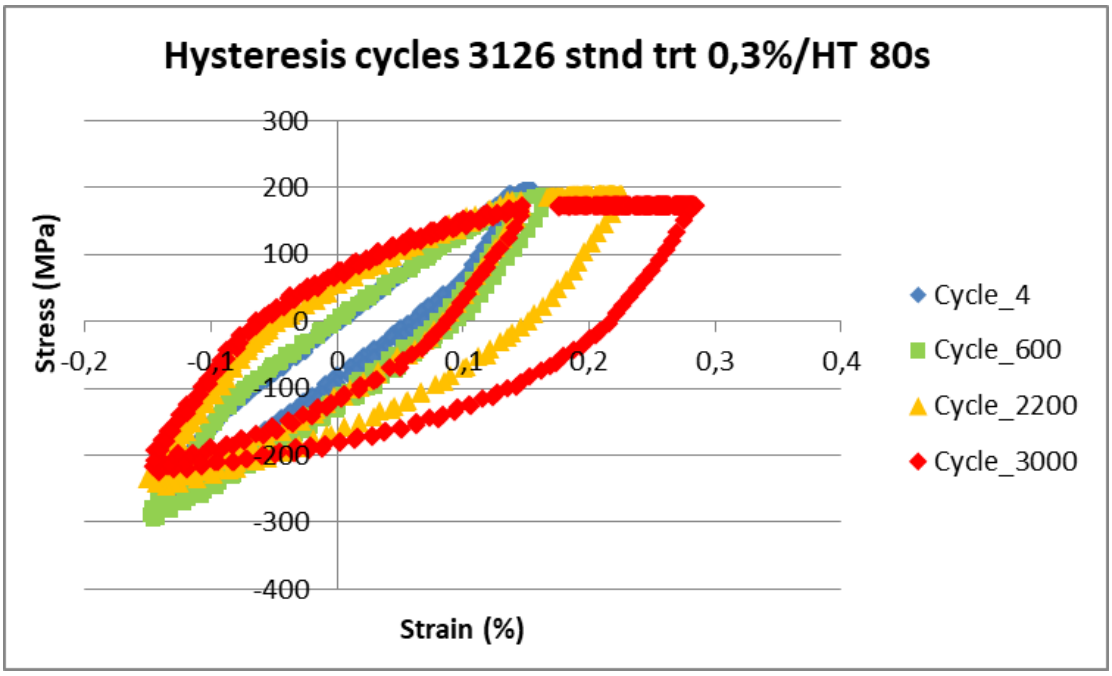

Fig. 3.2.13 Trend of the hysteresis cycles (HT 80s)

In the following figures (fig. 3.2.14-3.2.17) the effect of the hold time application on the trends of the stabilized load and of the deformation (recorded at the end of each hold time) is shown for each material. It is well noticeable the marked decrease in the stabilized load due to the hold time application as well as the reduction in fatigue life. Furthermore, it's worth noticing the harsh increase of the deformation as "end-life" creep effect.

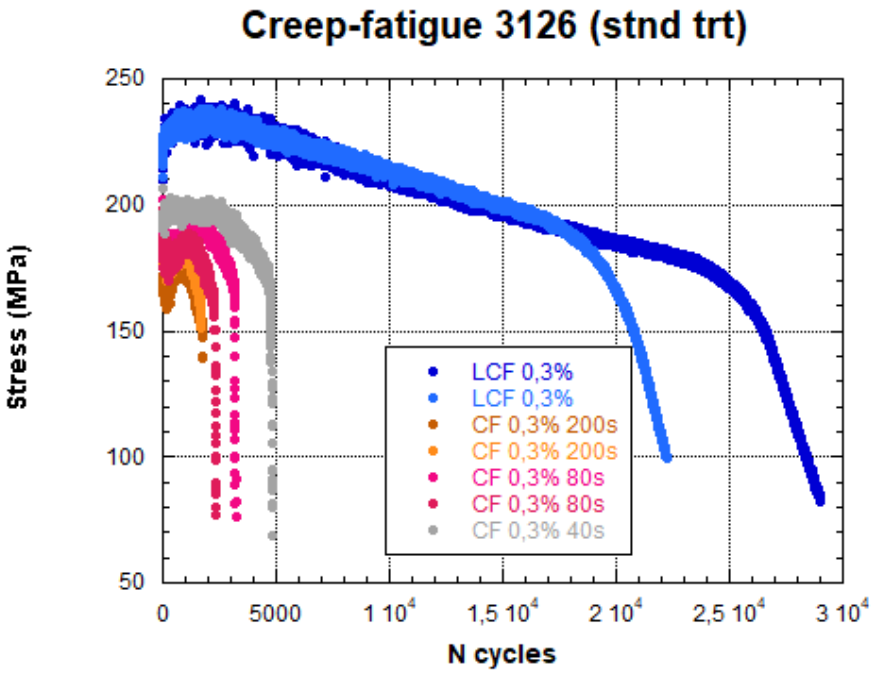

Fig. 3.2.14 Trend of the stabilized load for the performed Creep-fatigue tests (3126 alloy; stnd. trt.)

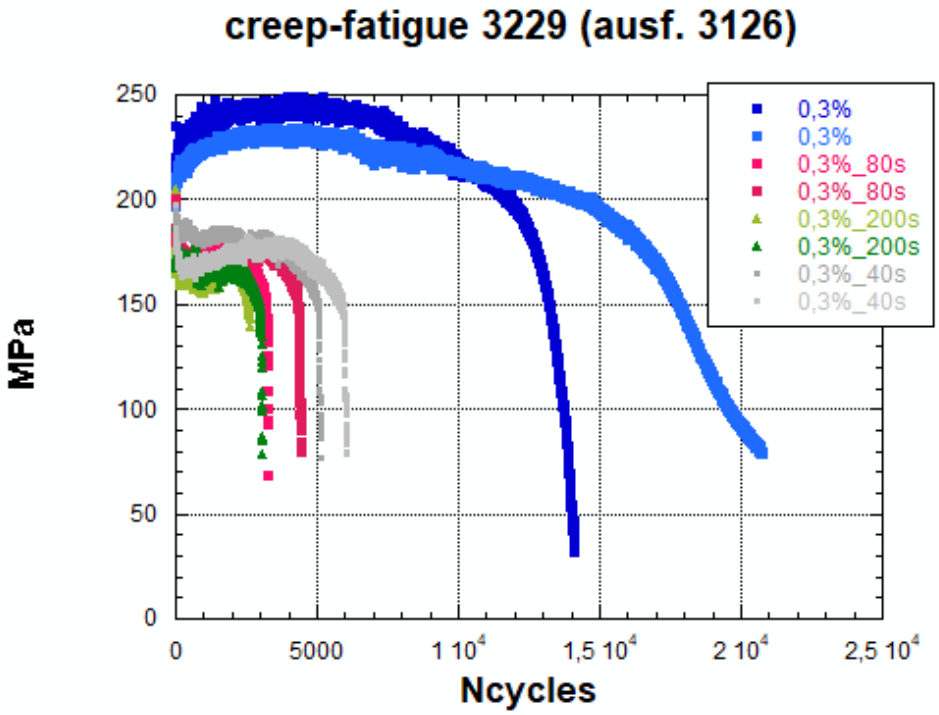

Fig. 3.2.15 Trend of the stabilized load for the performed Creep-fatigue tests (3229 alloy; ausf. trt.)

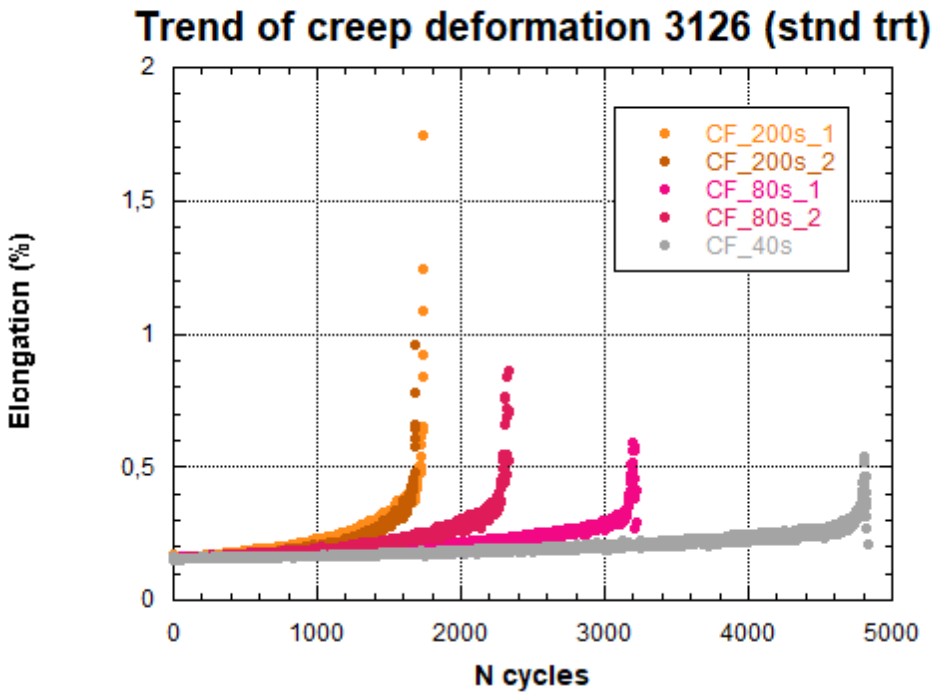

Fig. 3.2.16. Trend of the elongation at the end of the Hold time for the performed Creep-fatigue tests (3126 alloy; standard. treatment)

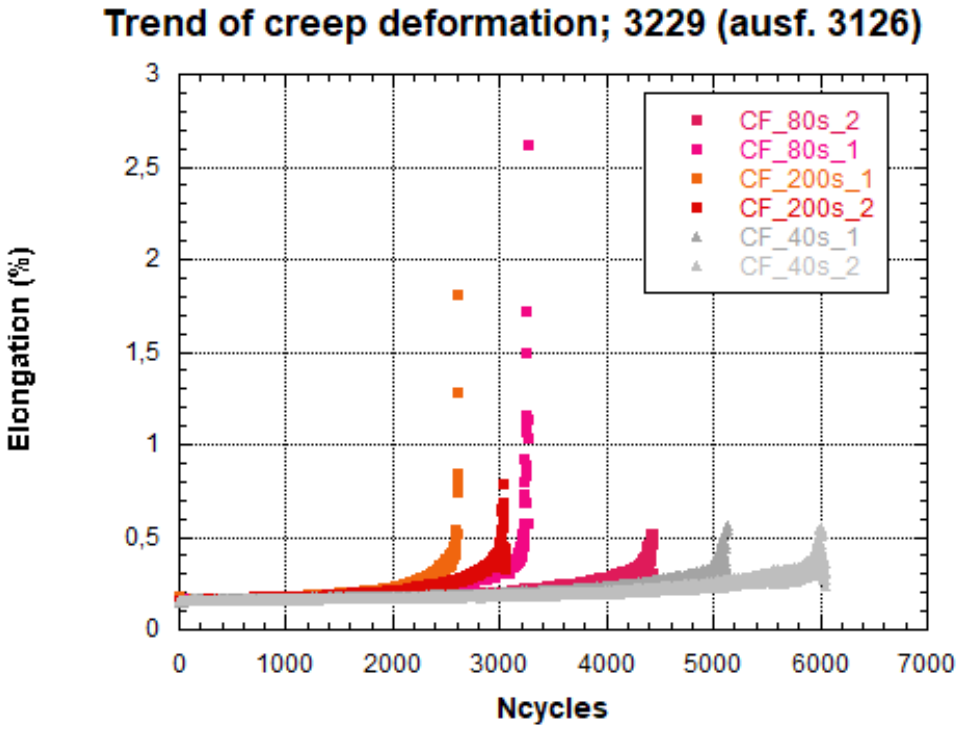

Fig. 3.2.17. Trend of the elongation at the end of the Hold time for the performed Creep-fatigue tests (3229 alloy; ausforming treatment.)

A picture of the fractured sections of the specimens broken in LCF mode and in CF mode (200 s HT) are reported in Fig. 3.2.18. The appearance of the fracture surface is smooth for the LCF specimen with a visible crack initiation at the bottom and uneven for the CF specimen characterized by a coarse nature, evidence of the porosities developed during creep hold times.

Fig. 3.2.18 Appearence of the fracture surface; a) specimen from ausformed 3229 alloy broken after LCF test; b) specimen from the same alloy broken after CF test (200s Hold Time)

The adopted criterion to estimate the cycles to failure was that of 25% load drop, according to ASTM 2714-09. The test conditions and the corresponding results are summarized in Table 3.2.2 in terms of cycles to failure, corresponding fatigue damage and creep damage. Details of the calculations are reported in the following paragraphs.

Table 3.2.2 Test matrix with number of cycles to fracture and relative damage achieved in each experimental condition.

Alloy #	$\Delta\epsilon_{tot}$ [%]	Type	Testing temperature (°C)	Hold Time duration in tension (s)	Number of cycles to failure N_f	Fatigue damage	Creep damage
3126	0.3	CF	650	40	4800	0.22	0.1
3229	0.3	CF	650	40	5100	0.33	0.07
3229	0.3	CF	650	40	6000	0.39	0.07
3126	0.3	CF	650	80	3200	0.15	0.12
3126	0.3	CF	650	80	2200	0.1	0.07
3229	0.3	CF	650	80	3120	0.2	0.07
3229	0.3	CF	650	80	4400	0.29	0.1
3126	0.3	CF	650	200	1742	0.08	0.1
3126	0.3	CF	650	200	1688	0.08	0.12
3229	0.3	CF	650	200	2612	0.17	0.12
3229	0.3	CF	650	200	3000	0.2	0.15

3.2.5.1 The Fatigue Damage

The fatigue damage has been evaluated through the following formulation:

$$\boldsymbol{D_f = \frac{N_f}{N_{max}}} \qquad \textbf{(1)}$$

where,

N_f = Number of cycles to obtain 25% of load decrease in each test, according to ASTM E2714-09 [14];

N_{max} = Maximum number of allowable strain cycles, should_be determined on the best fit experimental fatigue curve deduced by the RCC-MRx design fatigue curve at 650 °C multiplied by a factor of 2 in the strain range or a factor of 20 in the number of cycles whatever is the most conservative condition. Provided that we don't have such design information concerning this material, it's probably more worth to consider the number of allowable cycles as the value resulting from the best fit (power law) of the number of cycles to failure (25% drop in the stabilized load) recorded in the LCF tests. As it can be observed in the following plots (fig. 3.2.19) this value almost coincides with the minimum experimental value achieved in the LCF mode with the same amplitude of the performed CF tests (0.3 %,).

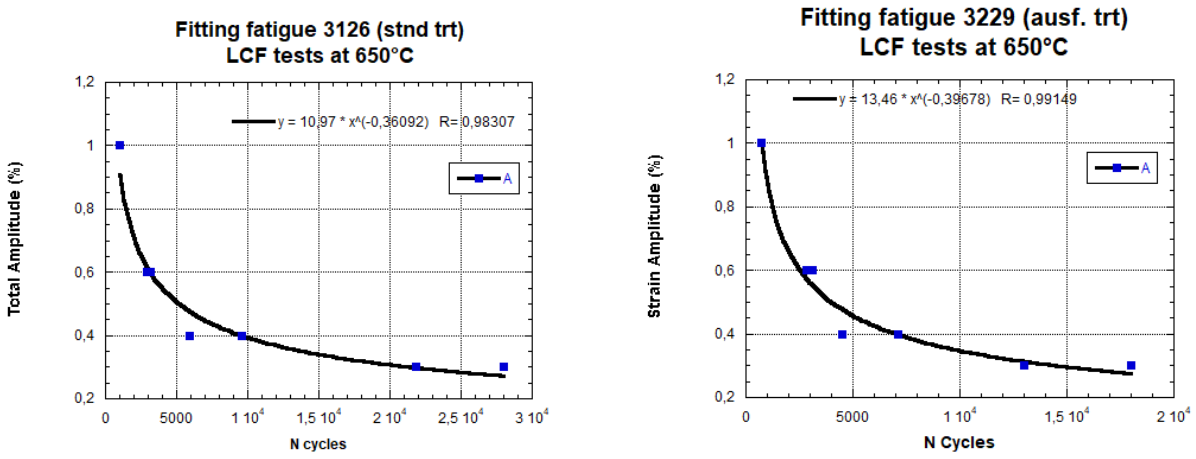

a) b)

Fig. 3.2.19 Best fit (power law) of the number of cycles to failure recorded in the LCF tests; a) 3126 (stnd. trt. Alloy); b) 3229 (ausforming TMT) alloy

3.2.5.2 The Creep Damage

The creep damage has been evaluated through the following formulation:

$$\boldsymbol{D_C = \sum_{i=1}^{N_f} \frac{T_{ht}}{T_i}} \qquad \textbf{(2)}$$

where,

T_{ht} = Duration of the hold time period in each considered kind of test, ranging from 40 s to 200 s;

T_i = Time to rupture corresponding to the load level recorded at each hold time of the test. A power function has been used to fit the time to rupture experimental values achieved at Rina-CSM (fig. 3.2.20).

N_f = Number of cycles to obtain 25% of load decrease in each test, according to ASTM E2714-09 [14].

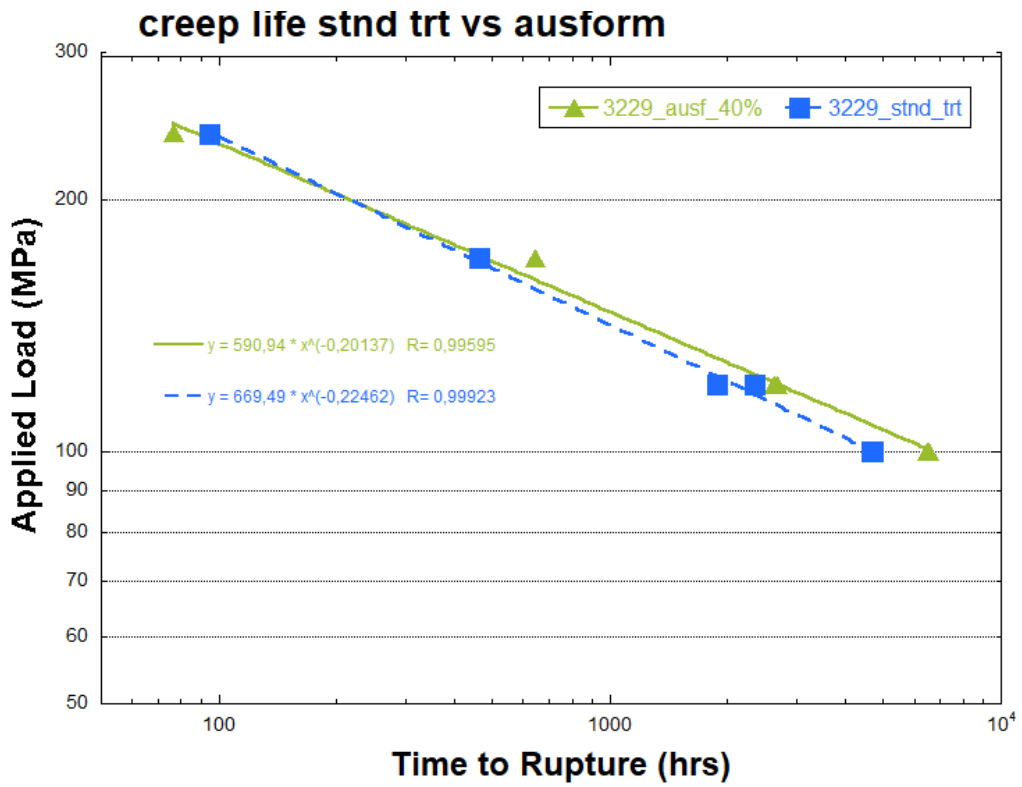

Fig. 3.2.20. Best fit (power law) of the Times to Rupture recorded in the creep tests (Rina CSM)

3.2.5.3 The Interaction Diagram

The calculated damages corresponding to the CF experimental points are plotted in the creep-fatigue interaction diagram in Fig. 3.2.21-3.2.23 in order to define the "safe" and "unsafe" zone, namely the portion of the diagram area standing respectively below and above the "interaction" curve. The interaction curve is plotted according to the existing ones up to now, namely from RCC-MRx [6] and ASME [7] in fig 3.2.22. As we can observe, all the experimental points fall below the RCC-MRx interaction curve; therefore, this curve doesn't seem conservative in defining a "safe" zone for the employment of these steels at this temperature. The ASME curve, on the other hand, seems more suitable as almost all the points fall above this curve. Nevertheless two points, namely the ones corresponding to the 200 s hold times on the 3126 alloy, still fall in the safe zone predicted by this curve, even if very close to the boundary. Therefore it seems a bit premature to define at present a safe zone on the creep-fatigue interaction diagram from the design point of view for these alloys. This steel seems in fact prone to failure for a very low application of creep damage and therefore the "safe zone" could result extremely narrow. The current activities must just be considered as a "first tentative" effort in this direction but deeper investigations and, above all, extensive testing campaigns with much wider statistics should follow in the next future.

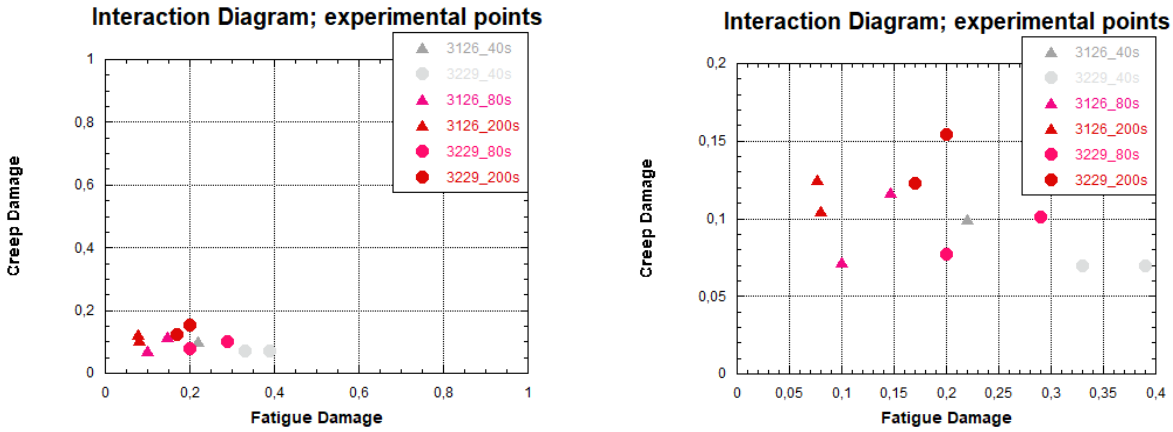

Fig. 3.2.21 a) Creep-fatigue interaction diagram with plotted experimental points b) Enlargement of the bottom left region of the Diagram

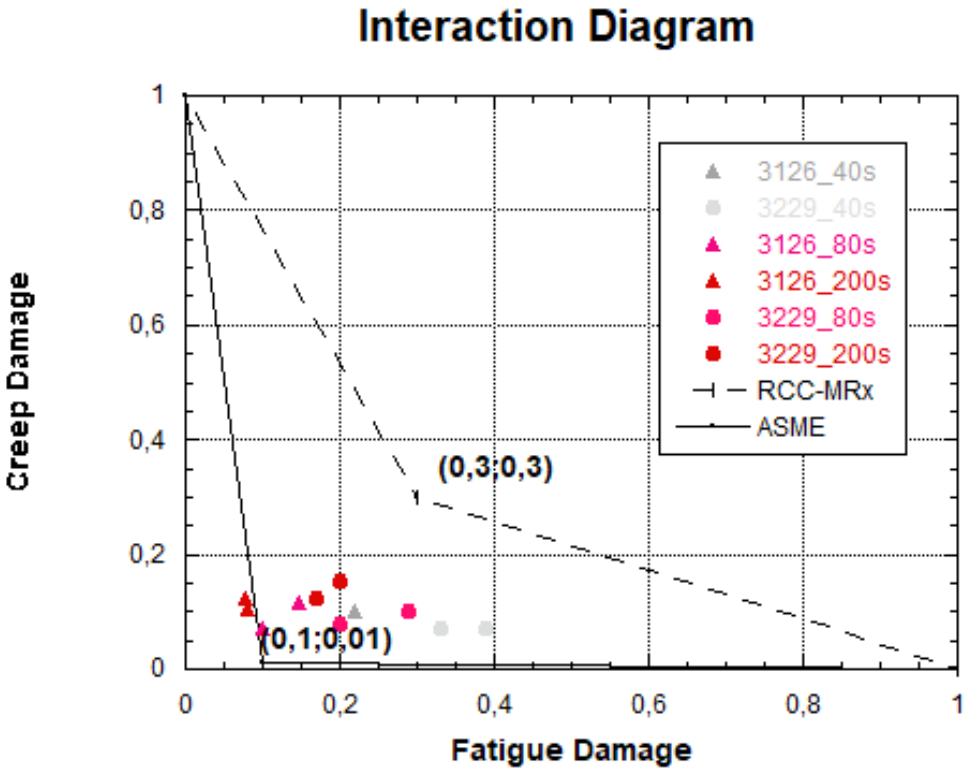

Fig. 3.2.22 Interaction diagram with plotted design curves according to RCC-MRx and ASME

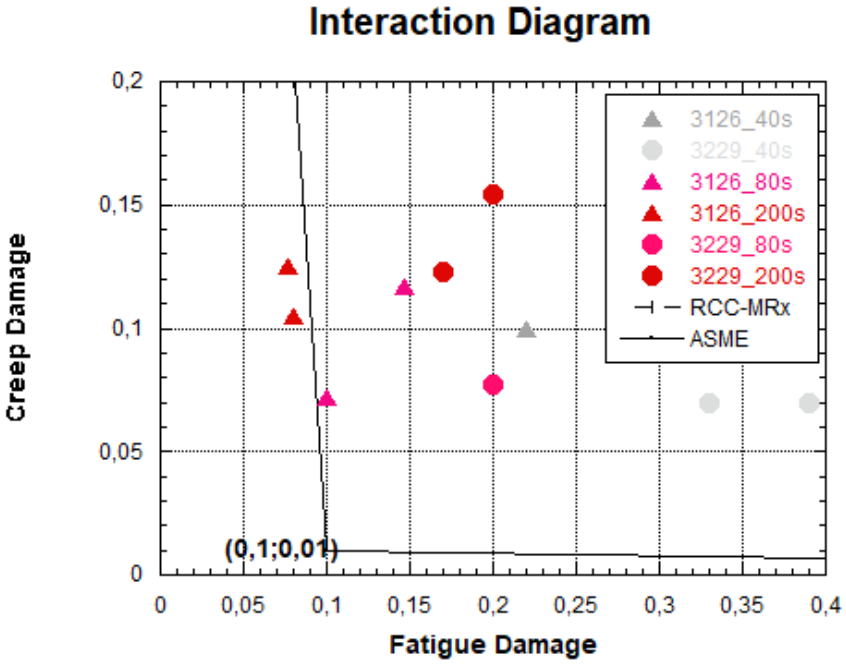

Fig. 3.2.23 Enlargement of the bottom left region of the Diagram

3.2.6 References

[1]. V. V. Popovich and I. G. Dmukhovskaya "REBINDER EFFECT IN THE FRACTURE OF ARMCO IRON IN LIQUID METALS" UDC 532.6:539.2; 1979; Plenum Publishing Corporation (0038-5565/78/1404- 0370)

[2]. L. Pilloni, C. Cristalli, O. Tassa, L. Bozzetto, E. Zanin, N. Bettocchi; *"Development of innovative materials and thermal treatments for DEMO Water Cooled blanket"*; NME (Nuclear Materials and Energy) 19 (2019) 79-86

[3]. C. Cristalli, L. Pilloni, O. Tassa, L. Bozzetto; "*Mechanical properties of several newly produced RAFM steels with Tungsten content in the range of 2 wt.%"* NME (Nuclear Materials and Energy) 25 (2020) 100793

[4]. C. Cristalli, L. Pilloni, O. Tassa, L. Bozzetto, R. Sorci, L. Masotti; *"Development of innovative steels and thermo-mechanical treatments for DEMO high operating temperature blanket options"* ; NME (Nuclear Materials and Energy) 16 (2018) 175-180

[5]. P. Fernández, A.M. Lancha and oth. EUROFER 97, Metallurgical Characterization […] Scientific Report, CIEMAT 1048, 2004

[6]. AFCEN RCC-MRx Code. 2012. Design and Construction Rules for Mechanical Components of Nuclear Installations.

[7]. ASME boiler and pressure vessel code. 2007. Section III Div. 1 Sub-Section NH. New York, USA: ASME.

3.3 Results of the assessment of tensile properties by means of RC (Ring Compression) tests

The RC curves achieved in the different experimental conditions are reported in the following figures (fig. 3.3.1, 3.3.2). The resulting UTS values, assessed by means of RC tests, are reported in Fig. 3.3.3. The softening effect due to aging is noticeable as well as the hardening effect due to the cryogenic temperature (-196°C). The spread of the experimental values seems to be higher for the heavy c.w. condition (46%) rather than for the "light" c.w. one (24%). No effect is noticeable in the latter stage of the curves, in order to identify any possible embrittlement effect by means of the same methods reported in Herb's paper [1]. It seems that 15-15 Ti is prone to hardening at the cryogenic temperature, but not to embrittlement at all. Thermal aging, on the other hand, just results in softening of this steel, likely due to dislocations recovery.

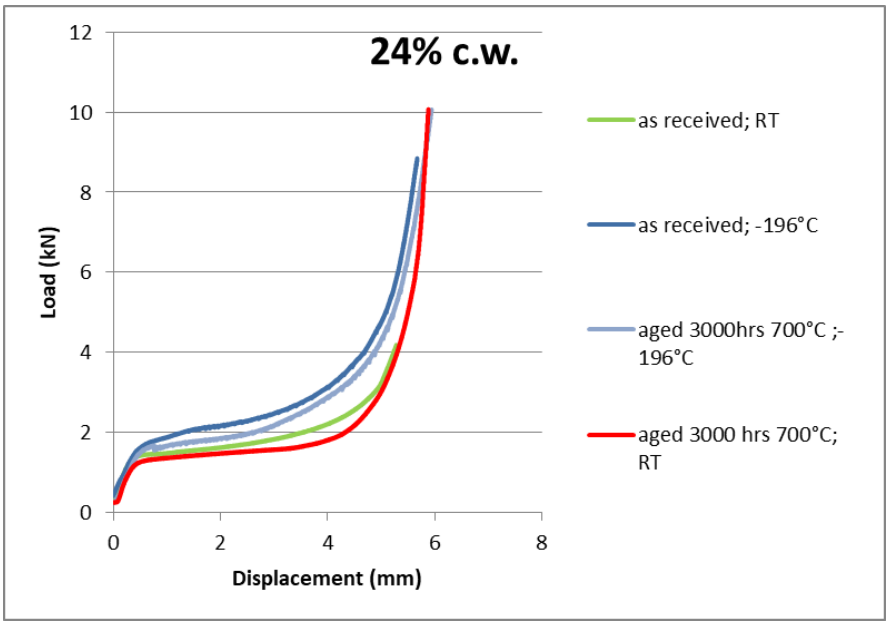

Figure 3.3.1. RC curves for the 24% c.w. condition of the claddings

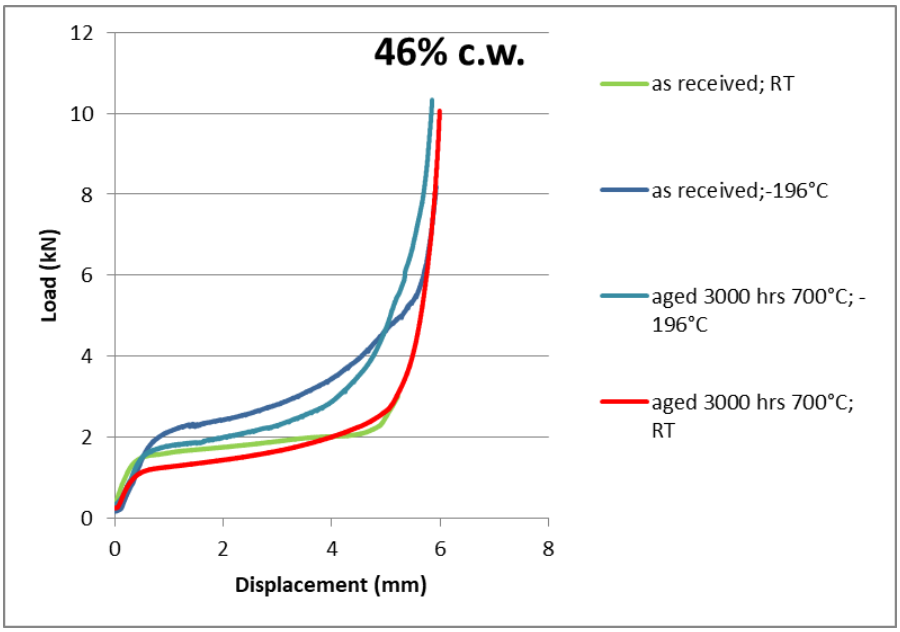

Figure 3.3.2. RC curves for the 46% c.w. condition of the claddings

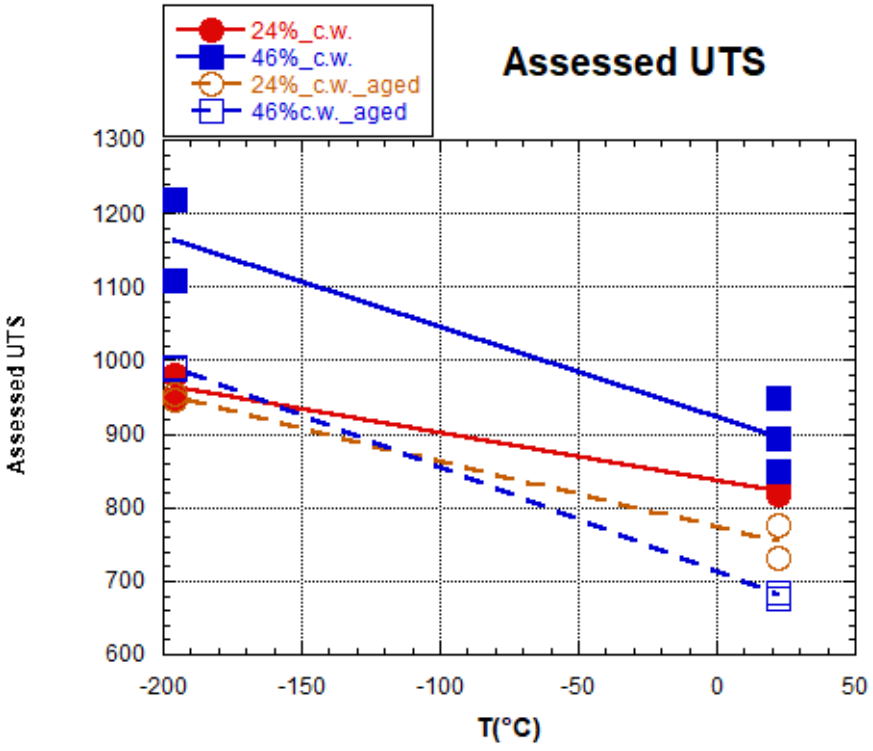

Figure 3.3.3. Estimated UTS values of 15-15 Ti claddings by means of RC tests

References

1. J. Herb, J. Sievers, H.G. Sonnenburg, “A new cladding embrittlement criterion derived from ring compression tests” Nuclear Engineering and Design 273(2014)615–630

4 Chapter 4; Conclusions

4.1 AISI 316L for Lead Fast Reactor

In the frame of the GEMMA Project, several SSRTs (Slow Strain Rate Tensile tests; strain rate maintained at $5x10^{-5}$ s^{-1} or $5x10^{-6}$ s^{-1} according to the testing condition) have been carried out in air, at different temperatures (room temperature, 400°C, 550°C), on the AISI316L base and weld material. The weld material is characterized by very high inhomogeneity of the tensile properties; both the longitudinal and the transverse ("cross-weld") extractions of the specimen confirm the scatter in the results. Nevertheless, a comparison between the tensile properties of the base and weld material reveal that the Yield Strength (YS) results markedly increased in the weld respect to the base, while the deformation values (Uniform and Total Elongation) appear averagely shorter. Namely the weld appears harder and less ductile than the base material. The tensile curves achieved in air represent the reference for the equivalent tests performed in liquid lead environment.
The 316L base material doesn't seem to be affected by LME (Liquid Metal Embrittlement); at the temperature of 400°C and with a strain rate of $5x10^{-5}s^{-1}$ the tensile curves achieved in lead almost perfectly overlap with those obtained in air, with a very limited scatter in the tensile properties. Increasing the temperature to 550°C and decreasing the strain rate to $5x10^{-6}$ s^{-1}, the steel even shows increased ductility. This effect is consistent with some other results from literature. Unfortunately, concerning the tests in lead of the weld material, it isn't possible to draw any general conclusion due to the inhomogeneity of the tensile properties already recorded in the tests in air and confirmed by the tests in lead. The only effect that seems to be ascertained, by comparison of the curves, is the appearance of the increased ductility at 550°C / $5x10^{-6}$ s^{-1}.
The creep results seem to suggest a slight increase in the creep rate for the tests in lead compared to the ones in air. On the one hand the increase of creep rate in lead for the tests carried out on the weld material (high applied loads, but below the average Yield Strength threshold) is likely related to creep-corrosion mechanisms. On the other hand, on the base material, a slight increase in creep rate is ascertained when the applied load exceeds the Yield Strength threshold. The creep tests carried out up to now at 500°C on the weld material seem to provide an overall indication in this direction as well. Therefore, a possible mechanism deduced at this stage is that the initial plastic deformations could play a role in triggering the HLM-steel interaction in creep, as it occurs for the tensile tests where the HLM effects can just be noticed at the plastic stage of the curve, once Yield Strength has been exceeded. Moreover, another aspect that's worth highlighting is the possible correlation between the increased ductility recorded in the tensile tests at high temperature and low strain rate (550°C/5x10-6s-1) and the increased creep rate in lead noticed in several creep tests up to now.

4.2 RAFM steels

In the frame of the Eurofusion WPMAT Project, the screening of the mechanical properties of several newly produced RAFM (Reduced Activation Ferritic-Martensitic) steels has been carried out and is still currently ongoing. The impact properties of the VIM lab-cast batches suffer a marked spread in the results compared to the industrially cast reference batch (Eurofer 97/2). Some meaningful improvements are however noticeable both by means of chemical composition (3125 alloy) and thermo-mechanical treatment (recrystallized Eurofer 97/2) variations. On the one hand, from the point of view of the chemical composition, the Tungsten content in the range of 2 wt%, accompanied by an increase in Ta content (whose precipitation in Tantalum Carbides is expected to contribute to PAGS refinement), proves beneficial in improving the toughness behaviour (in terms of lower DBTT) as resulting from impact tests on KLST specimens. On the other hand, from the point of view of the Thermo-mechanical Treatments (TMT) we have shown that, by means of a "tempering-coldworking-tempering" treatment, it is possible to achieve a fully recrystallized microstructure. Although the grain size distribution of TMT alloys was not measured, from a qualitative point of view, we can state that for a fixed CW the grain size increases with the increase in re-tempering temperature; for a fixed re-tempering temperature, the grain size decreases with the increase of

CW percentage. The grain refinement achieved by means of this recrystallization treatment is more than one order of magnitude (from 10 microns of the optimized PAGS to less than on micron of the ferritic grain after recrystallization). Impact tests on KLST showed that it is possible to extend the ductility up to about -160°C; namely this TMT, when the cold working is sufficiently high, induces a smoother transition towards very low test temperatures, eliminating the catastrophic behaviour of Ferritic Martensitic alloys at low temperatures. The conclusion of this feasibility study is that we have obtained a novel nano-structured microstructure that exhibits toughness behaviour completely different from "standard" normalized and tempered alloys. The recrystallized steels (looking in particular to the alloys 50% cold worked and re-tempered at 550°C x 1h) are much more cleavage tolerant at very low temperature. This microstructure could exhibit an improved behaviour under neutron irradiation and could be much more irradiation resistant under low temperature irradiation.

Concerning the alloys proposed for the high temperature applications, the 3126 alloy seems the most promising both concerning tensile and creep resistance. Generally speaking, the improvement of tensile properties of RAFM alloys (at room temperature as well as at higher temperatures) is associated to the hardening of the steel due to dislocation network and precipitation effects. This effect is well noticeable on the 3126 alloy, where the fraction of secondary precipitation (which we expect to be increased compared to the other alloys, according to the chemical composition and to some Thermocalc calculations carried out in the past), accompanied by heavy hot working ratios during the ausforming treatment, results in enhanced tensile properties at the expense of poorer toughness and higher DBTT. On the one hand the 3126 alloy provides excellent creep resistance but lacks impact properties (DBTT superior to -40 °C by means of KLST specimens in both hot-working conditions); on the other hand, the alloys conceived for low temperature applications provide excellent impact properties (DBTT close to −120 °C), but worsen significantly in terms of tensile properties. In both cases the Tungsten content in the range of 2 wt% appears beneficial as long as it increases the tensile strength by comparison to Eurofer 97/2 but leaves toughness unaffected or even slightly improved.

From a chemical point of view, concerning the 3126 alloy, the "solution hardening" effect of Tungsten can be well noticed in the plot reporting the tensile properties. The supposed increase of TaC (Tantalum Carbides) fraction combined with the adoption of the Ausforming TMT and the increase of the austenitization temperature are also thought to contribute to the enhancement of the high temperature resistance. The creep properties result comparable to the ones achieved with the best Ausforming TMT condition on Eurofer. The toughness is poor, as expected, but however it is thought sufficient to grant safe manufacturing and assembling processes, as long as the DBTT remains below -20 °C, at least by testing KLST specimens.

The goal of fatigue life around 10000 cycles at 650°C is reached with a total strain amplitude lower than 0.4%, for both the "standard" normalized-tempered and the ausformed 3126 alloy. The alloy with "standard" treatment seems to have longer fatigue life, but this should be confirmed by enhanced statistics in the investigated conditions.

Three combinations of hold time durations have been experimented in Creep-Fatigue mode; the longer the hold time, the shorter the fatigue life, as expected. This effect is accompanied by a marked decrease in the stabilized load, as well. Looking at the trend of the deformation, it is well noticeable the occurrence of a sort of "tertiary creep" stage as end-life effect. The main outcome of this activity concerns a possible update of the standards (namely the RCC-MRx and the ASME codes), in order to validate the creep-fatigue interaction diagram for these alloys. Every experimental condition falls very close to the horizontal axis (very low creep damage), so it's very difficult to draw with confidence a "safe zone" of the creep-fatigue interaction diagram, as it has been done for example in the past for T91 at 550°C. In the case of this 3126 alloy, in fact, the material seems prone (especially for the "standard" normalization & tempering condition) to failure for a very low application of creep-fatigue damage and therefore the "safe zone" could result extremely narrow. The reported activities should be considered as a "first tentative" effort in this direction but deeper investigations and, above all, extensive testing campaigns with much wider statistics should follow in the next future.

After this initial screening on mechanical properties the research work must be considered not concluded and further experimental activities are still ongoing with a twofold purpose; on the one hand to further optimize toughness and microstructure of the 3125 alloy by applying different TMTs which have proven successful on Eurofer 97/2; on the other hand to understand which is the contribution of each proposed modification (chemical composition, austenitization temperature, TMT) to the increase of the high temperature resistance

of the 3126 alloy. Nevertheless, as previously specified, the work devoted to mechanical characterization of all the newly produced RAFM steels is still ongoing and definitive conclusions will be drawn only in the next future.

4.3 Conclusions on the satellite activities concerning Ring Compression tests

The UTS values, assessed by means of RC tests, reveal a softening effect due to aging as well as a hardening effect due to the cryogenic temperature (-196°C). No effects related to embrittlement (as it is estimated according to several papers reported in literature) are noticeable in any of the investigated conditions. It seems that 15-15 Ti is prone to hardening at the cryogenic temperature, but not to embrittlement at all. Provided that it isn't possible in ENEA Brasimone to irradiate materials and assess irradiation embrittlement, in the future it would be worth to test some potentially "more prone to embrittlement" materials in order to understand whether or not this method could be suitable to assess such kind of damage.

5 Acknowledgements

5.1 GEMMA (Generation IV Materials Maturity)

The research leading to these results has been carried out in the frame of EERA Joint Program on Nuclear Materials and is partly funded by the European Commission HORIZON 2020 Framework Programme under grant agreement 755269.

5.2 Eurofusion WPMAT (Work Package MATerials)

This work has been carried out within the framework of the EUROfusion Consortium and has received funding from the Euratom research and training programme 2014-2018 and 2019-2020 under grant agreement No 633053. The views and opinions expressed herein do not necessarily reflect those of the European Commission.

6 Publications

1. L. Pilloni, C. Cristalli, O. Tassa, L. Bozzetto, E. Zanin, N. Bettocchi; *"Development of innovative materials and thermal treatments for DEMO Water Cooled blanket"*; NME (Nuclear Materials and Energy) 19 (2019) 79-86
2. C. Cristalli, L. Pilloni, O. Tassa, L. Bozzetto; "*Mechanical properties of several newly produced RAFM steels with Tungsten content in the range of 2 wt.%"* NME (Nuclear Materials and Energy) 25 (2020) 100793
3. M. Tarantino, C. Cristalli and oth., *"Fusion technologies development at ENEA Brasimone Research Centre: Status and perspectives"* FED (Fusion Engineering and Design) 160 (2020) 112008
4. M. Rieth, C. Cristalli and oth. "*Technological aspects in blanket design: Effects of micro-alloying and thermo-mechanical treatments of EUROFER97 type steels after neutron irradiation*" FED (Fusion Engineering and Design) 168 (2021) 112645
5. M. Tarantino, C. Cristalli and oth., "*Overview on Lead-Cooled Fast Reactor Design and Related Technologies Development in ENEA*" Energies 2021, 14, 5157
6. C. Cristalli and oth., "*Material Performance in Lead and Lead-Bismuth Alloy*". In: Konings, Rudy JM and Stoller Roger E (eds.) Comprehensive Nuclear Materials 2nd edition, vol. 4, pp. 218–241 (2020). Oxford: Elsevier.